NTNU

Norwegian University of
Science and Technology

Non-linear Irregular Wave Impact on Monopile Structures

Philipp Schöpfer

Maritime Engineering
Submission date: August 2016
Supervisor: Sigmund Kyrre Ås, IMT
Co-supervisor: Christof Wehmeyer, Ramboll Group
Stefan Hallström, KTH Royal Institute of Technology

Norwegian University of Science and Technology
Department of Marine Technology

Nordic Master in Maritime Engineering

KTH, Stockholm and NTNU, Trondheim

MASTER THESIS

Non-linear Wave Impact on Monopile Structures

Submitted by

Philipp Schöpfer,

880617-T396 (KTH), 763438 (NTNU)

Esbjerg, 4th of August 2016

In corporation with Rambøll Denmark AS, Esbjerg

Supervisors: Christof Wehmeyer (PhD, Rambøll Denmark AS)

Sigmund Kyrre Ås (PhD, NTNU)

Stefan Hallström (PhD, KTH)

Preface

The present *Master Thesis* is the result of an intensive collaboration with the Danish engineering consultancy *Rambøll Denmark AS* in Esbjerg which initially set the main topic and has kindly ensured continuous guidance, help and material throughout the entire time. Very special thanks goes to my corporate supervisor *Christof Wehmeyer* (*PhD, Chief Consultant Offshore Wind, Esbjerg*) who has contributed immensely to the outcome of this project and has always lent his support on a professional as well as personal basis.

As the main objective of the thesis, of course, has been tailored around the company's interest it is important to explain the extensive scope of this report. It has been agreed internally that the final paper shall be used as a reference document and process description for colleagues and upcoming projects. On that account, the report is clearly divided into four different parts and depending on the reader's background it is advised to disregard certain passages or to dedicate oneself to the complete content. In particular, this applies to the comprehensive literature study and associated presentation of theoretical principles concerning ocean surface waves and wave forces on cylindrical structures.

In the end, I am also grateful for the steering and helpful opinions of my academic supervisors *Sigmund Kyrre Ås* (*PhD, Professor*) from *NTNU* in Trondheim and *Stefan Hallström* (*PhD, Associate Professor*) from *KTH* in Stockholm who have always provided the profitable degree of discretionary and motivated own responsibility in the last six months.

02.08.2016, Esbjerg
Date, place


Signature

Summary

This *Master Thesis* deals with non-linear wave impacts on monopile structures by introducing a potential flow solver named *OceanWave3D* (*OCW3D*) for simulating free surface waves and their kinematics under engineering consideration. A comparison to *Rambøll's* analytical tool *WAVGEN* is conducted with the aim of providing distinct recommendations on the application and suitability of both programs for the monopile design. As *WAVGEN* applies common wave theories it is able to generate single waves in linear or non-linear form but only linear irregular sea states. In contrary, *OCW3D* includes both the non-linearity of the wave shape and the randomness of the water surface, resulting in a fully non-linear sea state due to the numerical solution. The obtained wave kinematics from both tools are read by a finite-element software which converts water particle velocities into wave loads. In order to reveal differences between both approaches an ultimate limit strength analysis of the foundation is performed, implementing wave kinematics by either *WAVGEN* or *OCW3D*. Here, the conventional approach with *WAVGEN* includes the principle of an embedded stream function wave into a linear irregular sea state to somewhat cover the non-linearity of the wave profile and the arbitrary surface elevation. As a result, the structural analysis yields a maximum overturning moment (*OTM*) which can be clearly affiliated to the inserted extreme wave represented by the stream function wave. On the other hand, the new approach with *OCW3D* generates a fully non-linear sea state in a numerical wave tank although without influencing the maximum wave. The already more realistic wave simulation by *OCW3D* is improved by activating a breaking filter which dissipates the energy of waves which would not exist in reality due to breaking. Multiple realisations give indications whether the non-linear sea state solution produces a single wave that exceeds the embedded stream function wave and the respective structural response. The final results in some cases confirm a greater *OTM* with *OCW3D* due to more aggressive and non-linear wave kinematics although the wave height of the embedded stream function wave is not surpassed. However, considering the most realistic wave and kinematics after a certain distance along the numerical wave tank when the breaking filter has removed all the excess energy a saving of almost *4.0 %* in the structural response with *OCW3D* is reached. Additionally, the work has provided an unprecedented validation of *Rambøll's* engineering procedure of defining an embedded stream function, i.e. this commonly used approach delivers representative wave loads compared to actual wave impacts induced by non-linear sea states.

Table of contents

Index of abbreviations and symbols

OCW3D	OceanWave3D	[-]
OTM	Overturning moment	[kNm]
FE	Finite element	[-]
MP	Monopile	[-]
ULS	Ultimate limit state	[MPa]
TP	Transition piece	[-]
ROSA	*Rambøll* Offshore Structural Analysis	[-]
SWL	Still water level	[m]
c	Celerity/speed of wave propagation	[m/s]
L	Wave length	[m]
H	Wave height	[m]
T	Wave period	[s]
k	Wave number	[-]
d	Water depth	{m]
ω	Angular frequency	[Hz]
T_z, T_2	Mean zero crossing period	[s]
T_c	Mean crest period	[s]
T_p	Wave peak period	[s]
T_1	Centroid wave period	[s]
H_m	Average wave height	[m]
H_s	Significant wave height	[m]
H_{max}	Maximum wave height	[m]

η_a	Wave amplitude	[m]
t	Time	[sec]
(x, y ,z)	*Cartesian* coordinate system	[m]
η	Surface elevation	[m]
α	Spreading angle of incident wave	[°]
u	x-component velocity	[m/s]
w	z-component velocity	[m/s]
m	Mass of fluid particle	[kg]
$\bar{v}$	Particle velocity	[m/s]
$\bar{g}$	Acceleration of gravity	[m/s^2]
F_v	Viscous forces	[N]
ρ	Water density	[kg/m^3]
μ	Dynamic viscosity	[kg/ms]
dx	Change in position in x-direction	[m]
dz	Change in position in z-direction	[m]
dt	Change in time	[s]
ϕ	Velocity potential	[-]
C_1, C_2	Integration coefficients	[-]
p_D	Hydrodynamic pressure	[Pa]
a_1	x-component acceleration	[m/s^2]
a_3	z-component acceleration	[m/s^2]
A_1, A_2, A_3, A_4	Integration constants	[-]
ε	Phase shift	[rad]
z_w	*Wheeler*-coordinates	[m]
N	Number of samples in a wave record	[-]

j	Wave component number	[-]
Δt	Equally spaced time interval	[s]
RMS	Root mean square value	[-]
FFT	Fast *Fourier* transformation	[-]
$\eta_{a,s}$	Significant wave amplitude	[m]
a	Probabilistic threshold value	[-]
P	Probability	[-]
$m_{0\eta}$	Area under spectral curve	[m^2]
$m_{1\eta}$	First order or static moment of spectral curve	[m^2]
$m_{2\eta}$	Second order or inertia moment of spectral curve	[m^2]
$S_{\eta(\omega)}$	Wave spectrum	[m^2]
γ	Peakedness factor	[-]
ω_p	Angular frequency at spectral peak	[1/rad]
σ	Step function for wave spectra	[-]
o	Order number	[-]
PDE	Partial differential equation	[-]
ST	*Stokes'* finite amplitude theory	[-]
$\Delta\omega$	Angular frequency interval	[1/rad]
A_C	Crest amplitude	[m]
A_T	Trough amplitude	[m]
$\Delta\eta$	Difference in surface elevation	[m]
A, B, C	*Stokes'* coefficients	[-]
Ψ_η	Stream function	[-]
X	Stream function coefficient	[-]
Q	*Bernoulli* constant	[-]

E	Error quantity	[-]
k_0	Linear deep water wave number	[-]
λ_0	Linear deep water wave length	[m]
U_R	*Ursell* number	[-]
S	Wave steepness parameter	[-]
μ	Shallow water parameter	[-]
D	Diameter of cylinder	[m]
A	Cross-sectional area of cylinder	[m^2]
V	Volume of cylinder	[m^3]
S	Surface of cylinder	[m^2]
r_0	Radius of cylinder	[m]
m	Mass of cylinder	[kg]
m'	Hydrodynamic mass	[kg]
C_m	Hydrodynamic mass coefficient	[-]
C_M	Inertia coefficient	[-]
C_{DS}	Drag coefficient in steady flow	[-]
C_D	Drag coefficient in oscillatory flow	[-]
Ψ	Wake amplification factor	[-]
U	Outer-flow velocity of water particles	[m/s]
$\mathring{U}$	Outer-flow acceleration of water particles	[m/s^2]
v_c	Current velocity of water particles	[m/s]
v_m	Maximum orbital velocity of water particles	[m/s]
F_P	*Froude-Krylov* force	[N]
α_c	Current/wave velocity ratio	[-]
e	Relative surface roughness	[-]

k	Surface roughness	[mm]
KC	*Keulegan-Carpenter* number	[-]
Re	Reynolds number	[-]
DNV	Det Norske Veritas	[-]
API	American Petroleum Institute	[-]
ISO	International Organisation of Standards	[-]
D_c	Clean outer diameter	[m]
t	Thickness of marine growth	[mm]
PM	*Pierson-Moskowitz* spectrum	[m_2]
f_r	Replacement factor	[-]
T_r	Replacement wave period	[s]
f_0	Overlapping factor	[-]
D_Z	Common difference	[m]
R_Z	Common ratio	[-]
ESS	Extreme sea state	[-]
Δ_H	Horizontal gradient operator	[-]
GUI	Graphical user interface	[-]
CFL	*Courant-Friedrichs-Lewy*-number	[-]
T_{dur}	Time duration	[s]
L_{total}	Total length of numerical wave tank	[m]
L_{gen}	Generation length	[m]
L_{abs}	Absorption length	[m]
n_x, n_y, n_z	Number of grid points	[-]
ROSAP	*Rambøll* Offshore Structural Analysis Programs	[-]
$\mathbf{M}$	Structural mass matrix	[kg]

$\mathbf{C}$	Structural damping matrix	[kg/s]
$\mathbf{K}$	Structural stiffness matrix	[MPa]
h(t)	External forces	[N]
$\mathbf{g(x,x)}$	Internal forces	[N]
ξ	Damping ratio	[-]
ρ	Frequency dissipation value	[-]
ASCII	American Standard Code Information Interchange	[-]
DTU	Technical University of Denmark	[-]
LAT	Lowest astronomical tide	[m]
H_{max}	Maximum wave height	[m]
T_{max}	Maximum wave period	[s]
RNA	Rotor-nacelle-assembly	[-]
φ	Angle of friction	[deg]
c	Cohesion	[MPa]
i	First beam node number	[-]
j	Second beam node number	[-]
NFA	Natural frequency analysis	[-]
FLS	Fatigue life strength	[MPa]
QS	Quasi-static analysis	[-]
DYN	Dynamic analysis	[-]
BL	Boat landing	[-]
MG	Marine growth	[-]
DLC	Design load case	[-]
f_{cut}	Cut-off frequency	[1/rad]
L_{cut}	Shortest wave length	[m]

BF	Breaking filter	[m/s^2]
x_1, x_2, x_3	Extraction positions along numerical wave tank	[m]
S	Seed number	[-]
X	Position number along numerical wave tank	[-]

List of figures

List of tables

Part I – Introduction

1 Background

The growing awareness for sustainability and preservation in today's society has led to a reconsideration of the world's dependency on fossil fuels and a shift to more non-emissive energy sources like solar, hydro or wind power. The latter constitutes the most predominant alternative as wind energy has provided the greatest share compared to any other form of green power in Europe. According to [1] almost *11.41 %* of Europe's electricity demand is covered by wind energy, producing a total of *142.0 GW* whereas land based installations are responsible for *131.0 GW* and offshore farms for *11.0 GW*. The Danish government agreed in *2012* to expand their contribution of renewable energy from *18.9 %* to *50.0 %* by the year of *2020*. Here, wind energy with a significant focus on offshore turbines is listed as the main supplier, illustrating the general trend in the energy sector [2]. The current development is clearly heading towards large wind farms out in the open sea. The major advantages towards onshore installations refer to the more stable and stronger wind conditions in the oceans and the abundant amount of space which allows larger farms and even more powerful turbines, not to mention the negligible visual or noise disturbances [2].

With a total investment of *EUR 13.3* billion and a new grid connected capacity of *3019.0 MW 2015* has evolved to a record year in the offshore wind industry, resulting in 419 newly installed wind turbines [3]. By the end of last year fourteen projects were completed and six are still under progress in Germany, the Netherlands and the UK, adding another *1.9 GW* [3]. Referring to [3] Europe is the emerging stronghold of the worldwide offshore wind business in terms of conception, production, installation and operation, running *84* offshore wind parks in eleven European countries. Most of them are found in the North Sea while a minor portion is arranged in the Baltic and Irish Sea, exemplified by the status report from *2015* in Fig. 1.1 [3].

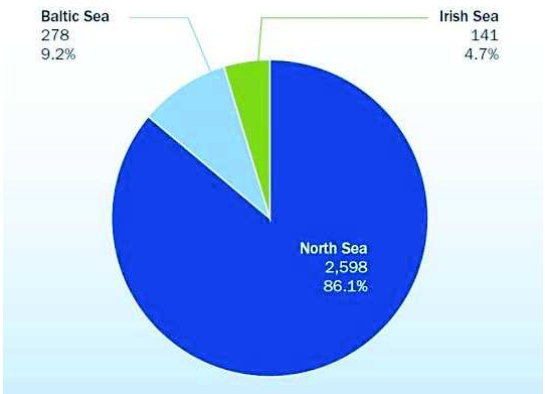

Fig. 1.1: Installation sites for the 419 newly installed turbines in 2015 [3]

But the expected progress and the associated expansion of offshore activities have triggered an increasing competition and rising demand for more cost efficient structures, more accurate assessment tools as well as alternative design approaches. Additionally, ocean structures are always accompanied with extra engineering effort due to the hostile and corrosive environment and the more complex grid connection compared to onshore installations [2]. In *2015* the average water depth for wind turbines amounted to *27.2* metres whereas the distance to the shore has increased to a mean value of *43.3* kilometres [3]. All those aspects challenge engineers once more and it becomes apparent that major improvements and the greatest optimisation potential is foreseen in determining loads concerning data recording, prediction and simulation. A reduction in engineering conservatism based on more realistic design conditions could be the solution for a profitable balance between decreasing prices and growing relevance on the energy market.

The following *Master Thesis* deals with one of those options and contains a comparison and plausibility study of two wave simulation tools. The fully non-linear potential flow solver in the open source code *OceanWave3D* (*OCW3D*) shall be tested against *Rambøll's* self-developed analytical code denoted as *WAVGEN* in terms of generating random sea states and extracting wave kinematics. The output obtained by both programs shall be read by finite-element (*FE*) software which translates water particle velocities as well as accelerations into wave loads and applies them on a monopile foundation. The final evaluation shall be based on resulting wave properties and structural responses of the offshore installation.

The work consists of four major parts dealing with the general theory of wave modelling and wave loads on cylindrical structures, the software practice and the actual comparison by means of a specifically attuned case study. Here, a monopile foundation shall be exposed to wave loads which are based on irregular sea states generated either in *OCW3D* or *WAVGEN*. In the end, the thesis shall provide general recommendations on the software handling and whether the new approach is able to complement *Rambøll's* conventional engineering procedure.

1.1 Presentation of problem

In the past *Rambøll* has invested time and effort in developing an in-house software package which should facilitate the structural analysis of major offshore installations without depending on any external experts. Gradually, the program has been advanced and supplemented, leading to the analytical wave simulation tool *WAVGEN*. As coding and interface between the *FE*-solver and *WAVGEN* constitute a one-stop process, the transfer of wave kinematics and their application on the model in form of distributed loads can be considered as approved and correct. However, this procedure lacks some validation and an understanding of the degree of conservatism. Therefore, the common ultimate limit strength (*ULS*) analysis of a monopile shall be examined more closely in the course of this *Master Thesis*.

In reality the monopile is installed on the sea bed and exposed to a varying wave loading. Its propagation and magnitude seems unpredictable as wave formation is a completely random process. Various theories and assumptions have eventually led to the simplification that one single wave can be described as a *sine* or *cosine* function. By implementing *Fourier* transformation series and signal analysis the irregular water surface can be computed as a sum of linear trigonometric functions. However, further researches and laboratory tests have revealed that the actual wave profile is dominated by a rather asymmetric shape which can only be covered mathematically by higher order solutions, introducing a certain degree of non-linearity. Hence, the main problem is that the actual water surface evolves arbitrarily and its single wave components cannot be simulated sufficiently. That means that engineers either accept the lack of non-linearity or the chaotic properties of the sea.

However, *Rambøll* has found remedy to a certain extent as they have introduced the principle of an embedded stream function wave for their *ULS* assessment. Briefly, *Rambøll* combines a single non-linear wave with a linear random sea state. On that account, it is possible to somewhat include the non-linearity of free surfaces waves and the randomness of the ocean. But, of course, this is accompanied with certain drawbacks which shall be illuminated in the following report. Generally speaking, the main problem of this procedure is the fact that it has not been validated before and that the embedded stream function wave is expected to yield too conservative results in terms of wave height and water particle kinematics. In the engineering environment this would have an effect on the monopile design in terms of general arrangement, geometry, steel weight and costs. In order to tackle this problem *OCW3D* shall be consulted as it offers the opportunity to generate sea states which

end up completely random and non-linear at the same time due to its higher order potential flow solution in contrast to *WAVGEN's* analytical approach.

1.2 Monopile design

The monopile (*MP*) is the most frequently installed foundation type in today's offshore wind industry. With reference to [3] *385* new wind turbines in *2015* are carried by monopiles compared to the construction of only *12* jacket structures, amounting to the total market distribution of last year's commissioning in Fig. 1.2.

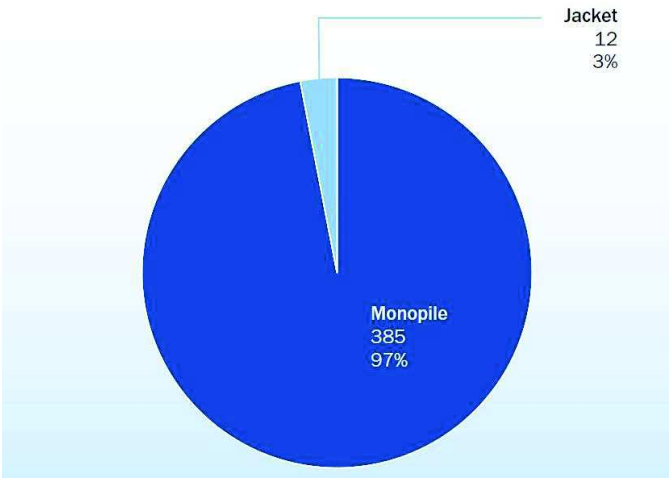

Fig. 1.2: Foundation types installed in 2015 [3]

The overall design refers to a large and thick-walled steel pile which is driven into the seafloor by forced oscillations or hammering. A transition piece (*TP*) links the bottom fixed monopile with the tower which holds turbine and rotors. Usually, the connection is made by means of grouting or bolted flanges. Additionally, the conception includes a boat landing in form of tubular bumpers, several working platforms for maintenance reasons and turbine equipment. The *J*-tubes which are externally arranged in Fig. 1.3 serve as cable tracks. Concerning corrosion the offshore structure is generally divided into three areas with different protection techniques. In the atmospheric zone a high quality and multi-layered coating is applied and for the submerged part of the monopile cathodic protection in form of sacrificial anodes are installed. In the transition or splash zone coating combined with extra corrosion allowance should redeem the problem. In order to prevent a wash-out around the pile rocks and concrete are arranged at the installation site, forming the so-called scour protection. Besides the wall thickness and the pile diameter the penetration depth is one of the most crucial design parameter for a reliable monopile as the soil-pile interaction is mainly responsible for the lateral wind and wave

resistance by opposing a sufficient horizontal pressure along the buried part of the structure.

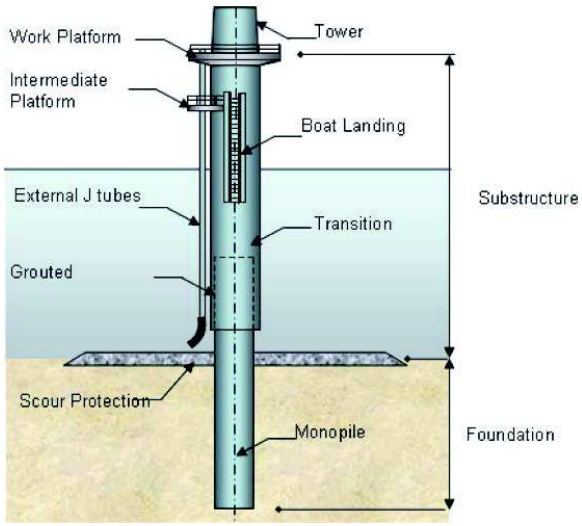

Fig. 1.3: Structural overview of a typical monopile foundation [4]

Monopile foundations are considered as slender structures with little structural stiffness and damping capabilities. That is the main reason why the design is limited to water depths between *30.0* to *40.0* metres [2]. Otherwise increased diameters and more steel would be required. Here, jacket structures are preferred to bridge larger distances to the sea floor. However, the increased stiffness of such complex frameworks is always accompanied with more expenses due to elaborate production and the amount of high quality welding along cords and braces. As the trend in the offshore wind industry aims for intermediate and shallow waters the monopile continues to convince with its simplicity and cost efficient as well as large scale production compared to other options summarised in Fig. 1.4 [2]. Among experts it is also jointly agreed that monopiles belong to the most handling-friendly ocean structures regarding transportation, installation and endurance. All major design aspects, including advantages and disadvantages are summarised as follows [4].

Fig. 1.4: Overview of possible bottom fixed foundations for wind turbines[1]

[1] Image source: *Rambøll Denmark AS*

Disadvantages:

- Unprofitable for larger water depths due to increased engineering, material and production expenditure
- Due to reached design limit extremely expensive and elaborate development beyond today's monopiles, especially in terms of transportation and installation
- In the course of de-commissioning after service lifetime a certain part of the structure remains in the ocean, being hazardous for the environment and marine life

Advantages:

- Very cost efficient due to simple design and possible large scale production
- Convenient and profitable manufacturing and installation
- Ample references and validated technology over years of engineering knowledge
- Relatively site-independent as applicable and installable in almost any soil
- Efficient and comprehensible determination of forces and their interaction, resulting in a highly advanced design

As the monopile is viewed as a structurally optimised and extremely efficient foundation type, it shall be used in the subsequent work to evaluate the difference between *OCW3D* and *WAVGEN*. Moreover, the market-leading expertise of *Rambøll* in the offshore wind foundation design and available references and data are of remarkable value for the successful completion of this *Master Thesis*.

1.3 Methods and objectives

As the thesis in principle describes the comparison between an analytical and numerical wave simulation code, the major part of the work shall be dedicated to the correct software handling and interpretation of obtained results. This, however, implies a certain pre-knowledge and thus initially the focus shall be on the theoretical background of common wave theories and wave loads on cylindrical structures. It is essential to elaborate the differences between linear and non-linear as well as regular and irregular waves. So the principle of various ocean surface waves with reference to the small amplitude wave theory, *Stokes'* finite amplitude approach and the stream function method shall be presented together with the realisation of irregular sea states. Subsequently, the idea of transferring water particle kinematics into wave loads by *Morison et al. (1950)* shall be discussed to round off the complete engineering

procedure. As a support and platform for a better understanding throughout the project *Matlab* shall gradually be used to conduct own simulations. After fundamentals are internalised, it is of great importance to test and apply all involved programs to be familiar with settings, input format, computational effort and output files. Besides *OCW3D* and *WAVGEN* *Rambøll's* *FE*-tool called *ROSA* shall be presented in more details as it is responsible for the conversion of wave kinematics into loads and their application on the model. One important aspect is the appropriate interface between *ROSA* and *OCW3D* as the latter runs in a *LINUX* environment. In order to assure a successful collaboration both software combinations, *WAVGEN+ROSA* (conventional approach) and *OCW3D+ROSA* (new approach), shall be tested and validated by means of an established wave scenario and a simple cylinder model which is composed of ordinary beam elements fixed at the bottom.

Following the main idea of the thesis a *ULS* design process shall be conducted in line with *Rambøll's* standards, including genuine conditions, realistic input parameters and a complete monopile model. Therefore, a distinct design scenario shall be defined and eventually taken as the common ground for the comparison study. That means that environmental settings, the *FE*-model, metocean and geotechnical data shall remain constant and that the preceding generation of wave kinematics shall be performed by *WAVGEN* and *OCW3D*, following the scheme in Fig. 1.5. The resulting wave properties and the structural impact on the monopile in form of the *OTM* shall be classified as the governing assessment criterion for the final evaluation.

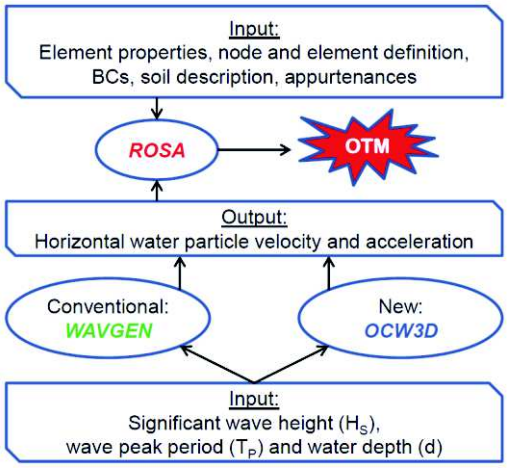

Fig. 1.5: Strategy for the upcoming comparison and plausibility study of OCW3D

Due to the different approaches within both wave codes and depending on the overall outcome the main target of the *Master Thesis* is to provide general recommendations on the application and output of *OCW3D* and/or to validate the conventional procedure with *WAVGEN*.

Part II – Theoretical principles

2 Ocean surface waves

The here described physical background constitutes one of the two main cornerstones of this *Master Thesis*. Referring to the overall objectives the theoretical knowledge about ocean surface waves shall be discussed in details as it will be retrieved consistently throughout the entire project. In the end of the work, the new software and its alternative solution approach shall be correctly implemented and efficiently assessed in a real working environment. On that account, it is of great importance to comprehend the basic theory together with its origin, application and limits, laying the groundwork to compare the current procedure with the possibilities of *OCW3D*.

Generally, scientists and engineers are interested in the kinematics and dynamics of waves, especially in their generation, propagation behaviour and their interaction with currents and the sea floor. This is seen as the foundation for any design and construction of fixed or floating structures in the marine environment as the response of those installation or even ships is mainly governed by wave loads. Consequently, this chapter shall provide an insight in the hydrodynamics of waves and how waves and their properties can be simulated and processed to eventually obtain wave induced forces. Starting with general definitions, the hydrodynamic concept shall be presented, including crucial assumptions, limitations and implementation. As ocean waves vary in shape, height, length and velocity, it is important to distinguish between regular and irregular waves as well as between linear and non-linear wave modelling. Therefore, the linear wave theory and the two most commonly deployed non-linear theories shall be outlined in the upcoming paragraphs. Additionally, the principles of an irregular sea state shall be described and eventually shall lead to the realisation of the random water surface under realistic conditions. Parallel to the literature study, *Matlab* shall be used to visualise the fundamentals and to verify them for future applications before the actual wave loads on a monopile can be determined, applied and evaluated.

2.1 Wave characteristics and terminology

In the subsequent work a *Cartesian* coordinate system (*x, y, z*) shall be used as reference where *x* points in the direction of the wave propagation, *z* is defined positive upwards from the still water level (*SWL*) at *z = 0.0* and *y* describes the spatial dimension orthogonal to *x* and *z*. The two-dimensional appearance of the wave extends over the *x-z* plane whereas the wave travels in the positive *x*-direction over a straight seabed at a constant water depth *d*, summarised in Fig 2.1. Following [5] the wave shall remain in a steady form, guaranteeing no underlying current and an uncontaminated free surface. Additional assumptions include an incompressible and inviscid fluid associated with an irrotational flow.

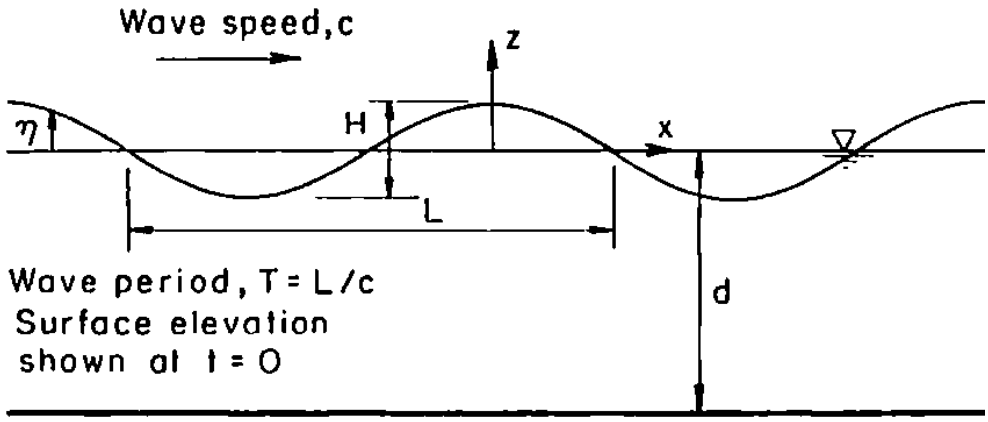

Fig 2.1: Basic definition of a regular wave train [5]

Here, the main parameters are given by the wave height *H* which is the vertical distance from the trough to the crest, the wave length *L* between two successive peaks and the wave period *T* which accounts for the time interval between two sequential crests at a particular point in space. It is common to distinguish between deep and shallow water waves. Under deep water conditions the water depth is more than half the wave length, so that the relatively short waves are not affected by the seabed. In contrary, in shallow water which covers water depth of less than *1/20* of the wave length the sea floor majorly influences the motion of those typically long waves [6].

$$Deep\ water: \quad \frac{d}{L} > \frac{1}{2} \tag{2.1}$$

$$Shallow\ water: \quad \frac{d}{L} < \frac{1}{20} \tag{2.2}$$

In case of a sinusoidal wave the amplitude η_a describes the distance from crest or trough respectively to *SWL* [6]. By simply relating wave length and period it is possible

to determine the wave celerity c through the water. The angular frequency ω as well as wave number k are determined to fully describe the above stated wave train. A design wave can clearly be defined in terms of wave height, period and water depth where it is common to deploy dimensionless parameters such as relative height or depth and the wave steepness H/L [5].

$$H = 2 \cdot \eta_a \tag{2.3}$$

$$c = \frac{L}{T} = \frac{\omega}{k} \tag{2.4}$$

$$\omega = \frac{2\pi}{T} \tag{2.5}$$

$$k = \frac{2\pi}{L} = \frac{\omega^2}{g} \tag{2.6}$$

The angular frequency and the wave number or equivalent the period and wave length form the crucial *dispersion relationship* in (2.7) which basically explains how waves spread and dissolve over time and distance. In other words it describes the process of how wave trains of the same phase velocity develop from chaos and arbitrariness induced by random winds or storms.

$$\omega^2 = kg \cdot \tanh(kd) \tag{2.7}$$

Usually, the angular frequency or the period is given but the non-linear dependence on the wave number requires an iterative solution. However, in deep water the dispersion relationship can be simplified because the hyperbolic tangent approaches *1.0* [6].

$$Deep\ water: \qquad \omega^2 = kg \tag{2.8}$$

$$T = \sqrt{\frac{2\pi}{g}} \cdot \sqrt{L} \quad or \quad L = \frac{g}{2\pi} \cdot T^2 \approx 1.56 \cdot T^2 \tag{2.9}$$

It is important to mention that the above presented relationship is relatively limited to regular waves and if applied on an irregular sea state a regular swell must prevail, accepting accuracy between *10.0* to *15.0* per cent [6]. In case of shallow water the hyperbolic tangent can be replaced by kd in equation (2.7).

$$Shallow\ water: \qquad \omega = k \cdot \sqrt{gd} \tag{2.10}$$

$$T = \frac{L}{\sqrt{gd}} \quad or \quad L = \mathrm{T} \cdot \sqrt{gd} \tag{2.11}$$

Taking account of the dispersion relationship the phase velocity can be rewritten as follows.

$$c = \sqrt{\frac{g}{k} \cdot tanh(kd)} \tag{2.12}$$

By looking at equation (2.12) it can be stated that the velocity increases with the wave length [7]. Therefore, dispersion is initiated as shorter waves are slower and thus will be overtaken by longer waves. In shallow water the phase velocity turns out to be independent of the period, resulting in non-dispersive waves. However, this critical speed is more important for ships in those waters as it determines the limit of its own speed and the rapid surge in wave resistance which however shall not be discussed further in this report [6].

$$Deep\ water: \qquad \mathrm{c} = \sqrt{\frac{g}{k}} = \frac{g}{\omega} \approx 1.25 \cdot \sqrt{L} \approx 1.56 \cdot T \tag{2.13}$$

$$Shallow\ water: \qquad c = \sqrt{gd} \tag{2.14}$$

With respect to the upcoming description of an irregular sea state in 2.5 two important parameters shall be defined beforehand. An irregular wave in Fig. 2.1 is characterised by a random surface elevation with arbitrary periods and wave heights, requiring some reasonable data handling for such a stochastic process.

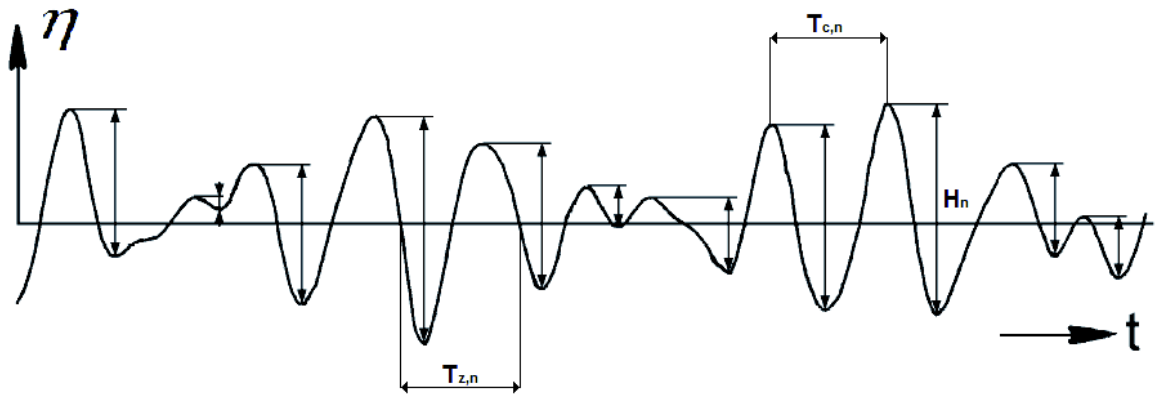

Fig. 2.1: Example of an irregular wave [6]

A convenient tool is to extract samples and compute different statistical measures such as mean values and standard deviations. For example the mean period for zero crossings T_z refers to a large number of samples of the time between two neighbouring crossings with the same slope either in up- or downward direction where N is the sum of all measurements [8].

$$\mathrm{T_z} = \frac{\sum_{n=1}^{N} T_{z,n}}{N} \tag{2.15}$$

The position in time of successive wave crests can also serve as a reference, yielding the mean crest period T_c as in Fig. 2.1. Concerning the wave height the data is additionally processed by grouping successive wave heights in different classes of specified heights [6]. After that it is possible to determine either the simple mean wave height H_m or the so-called significant wave height H_s which usually stands for the average of the highest third of the measured wave heights. This compilation is generally preferred due to a more realistic resemblance of a visually estimated wave height [8].

$$\mathrm{H_s} = \frac{\sum_{n=N-\frac{N}{3}}^{N} H_n}{\frac{N}{3}} \tag{2.16}$$

2.2 Wave generation by wind

The mean water level can be disturbed in various ways whereas severe weather conditions, sailing ships or other external perturbations belong to the most decisive triggers of ocean surface waves. There are additional wave phenomena, including internal waves which can be compared to surface waves due to their interaction between kinetic and potential energy. However, according to *Newman (1977)* [9] those waves "are found in the internal regions of density stratification beneath the sharp interface with the atmosphere". Because of the insignificant density differences in this case internal waves have majorly been recorded at lower frequencies with periods of several minutes which can be seen as irrelevant for marine structures [9]. Waves with even lower frequencies are called inertial waves caused for example by the *Coriolis acceleration* due to the earth's rotation. Those so-called *Kelvin* or *planetary Rossby waves* are mainly influenced by bottom and lateral restrictions with respect to the ocean basin. Tidal changes of the water surface trace back to the shift of the gravitational force on the earth's mass between the moon and the sun, resulting in the typical half-day or one-day

occurrence period. Tsunamis complete this group of large-scale water waves which arise in the course of underwater seismic irregularities with periods in the range of *10.0* to *60.0* minutes [10]. On the other side, capillary waves and ripples form the group of high-frequency surface oscillations but again with a rather small effect on vessels or offshore installations [9]. A summary of free surface waves, including their generating mechanisms can be found in Fig. 2.2.

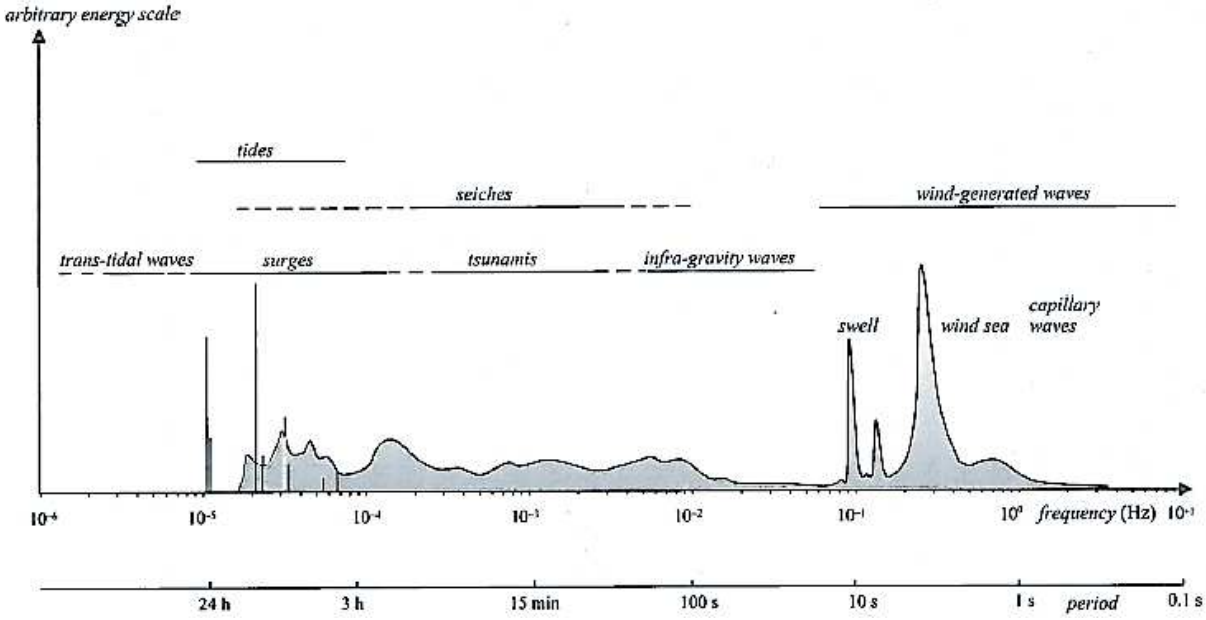

Fig. 2.2: Wave energy spectrum with generating mechanisms [11]

Thus, it can generally be stated that water waves embody periodic motions of a density interface for example between the air and the sea or completely underwater. In contrary to sound waves, water waves describe an oscillating movement around a mean level transverse to their propagation direction where the gravity force constitutes the main restoring parameter of the elevation pattern [10]. Wind generated waves cover small to medium scale waves. Here, characteristics like periods between less than a second up to *30.0* seconds, wave lengths from a couple of centimetres to approximately *1000.0* metres and wave heights which can easily reach *30.0* metres have led to the great significance for ocean and coastal engineering. The previously mentioned capillary waves represent the shortest waves among the surface motions which are mainly dominated by surface tension of the water [10]. Although this phenomenon just produces wave lengths in the order of centimetres with periods of less than one tenth of a second, capillary waves take an essential role in the generation of waves induced by wind.

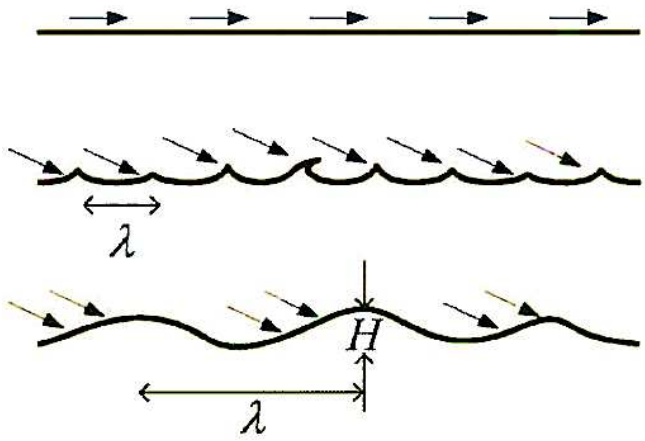

Fig. 2.3: Development of wind generated waves from calm water [8]

Fig. 2.3 schematically depicts three major stages in the generation of wind-driven water waves. In the beginning the wind starts to blow on a calm water surface, leading to friction between air and water as well as an energy transfer from the wind to the water [8]. The unsteady wind speed and direction are responsible for the evolving ripples which provide a larger target area and due to the increased pressure eventually evolve into more pronounced wave crests. The energy transfer grows and the surface elevation reaches a critical state in terms of wave height relative to wave length. In the end the ripples break, forming lower but also longer waves which are able to absorb even more wind energy. If this process of constant wind and growing wave amplitude continues the ripples turn into a more rounded and smooth appearance, describing the foundation of gravitational waves [8].

The above described wave development finds its maximum either in wave breaking or in the condition of equal velocity of wind and wave. In case of zero relative speed an energy exchange between the two densities cannot occur and a constant wave height and length over a certain time period settle in, reaching a fully developed sea state [8]. But the wave height is generally limited by a certain ratio between wave height and length where the upper boundary is commonly set at a wave height of about *10.0* per cent of its height [8].

$$\frac{H}{L} > 0.1 \tag{2.17}$$

As large-scale waves are seen as extreme conditions in terms of characteristics, magnitude and occurrence and as capillary waves are solely considered in the initial phase of generating waves the following report shall mainly focus on gravitational waves induced by wind and storms.

2.3 Hydrodynamic concept

The following paragraph shall provide a brief insight into the hydrodynamic fundamentals applied for the different wave theories, including main assumptions and approximations together with their influences on the results. Due to simplicity reasons, the description shall only refer to a two-dimensional problem where the general vector notation describes a vertical plane in ordinary rectangular coordinates along the x- and z-axis, see Fig. 2.4. Here, u and w represent the vector components of $\bar{v}$ which shall denote the particle velocity from now on [12].

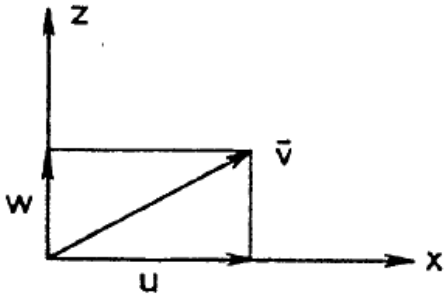

Fig. 2.4: Mathematical background for the following theory [12]

2.3.1 Physical principles

Generally, fluid mechanics follow two major principles, the conservation of mass and momentum. This relies on the consideration of water as a continuum, arguing that any volume of water holds the same properties such as density ρ and viscosity μ. If the water is also treated as homogenous and independent of temperature so that the density remains constant, it is possible to conserve the mass within the fluid flow. But this requires an establishment of an incompressible medium, resulting in the fact that the conservation of mass now equals the conservation of volume [7]. Under free surface conditions this assumption is usually accepted as the fluid particle velocity is rather small in relation to the sound velocity in the fluid [12].

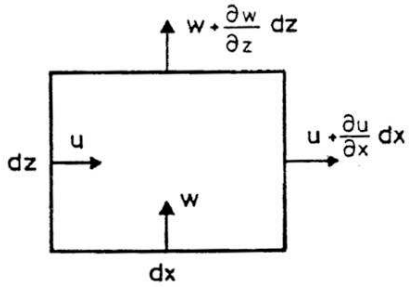

Fig. 2.5: Volume flux through fixed reference surface

By means of the above defined surface in Fig. 2.5 with infinitesimal edges *dx* and *dz* completely underwater the conservation of mass states that "the net mass flux per unit width through the surface is zero" [12], yielding the *continuity equation* in (2.18).

$$\frac{\partial u}{\partial x} + \frac{\partial w}{\partial z} = 0 \tag{2.18}$$

Additionally, any particle which is by definition "an infinitesimal part of the fluid containing the same molecules at all time" [12] must fulfil *Newton's second law*. Therefore, the conservation of momentum applies for water particles as it does for a mass particle which simply states that a force is needed to alter the state of momentum [7].

$$m\frac{d\bar{v}}{dt} = \sum \bar{F} \tag{2.19}$$

where:

m = mass of fluid particle
v = particle velocity
t = time
$\sum F$ = sum of all forces acting on the fluid particle

The fluid particle illustrated as a rectangle in Fig. 2.6 is exposed to normal, shear or tangential forces and volume forces whereas only the first two are measured on the surface of the particle. The total normal force derives from the pressure difference in the fluid plus a viscosity share which, however, can be neglected in accordance with [12]. As the shear forces depend on friction and consequently on the water viscosity, they are not considered further.

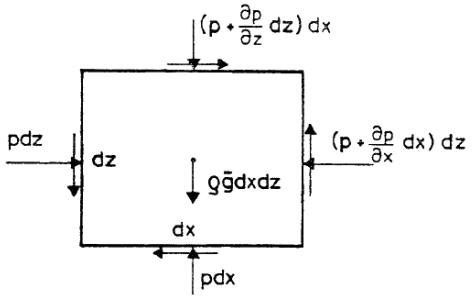

Fig. 2.6: Forces on a fluid particle [12]

In the end, only the volume force in (2.20) based on the acceleration of gravity $\bar{g}$ or centrifugal force due to the acceleration of the entire volume remains and can be inserted in (2.19), resulting in the *equations of motion* in (2.21) and (2.22) [7].

$$\bar{F}_V = \rho \, dx \, dz \, \bar{g} \tag{2.20}$$

$$x - direction \qquad \rho \frac{du}{dt} = -\frac{\partial p}{\partial x} + viscous \; forces \tag{2.21}$$

$$z - direction \qquad \rho \frac{du}{dt} = -\frac{\partial p}{\partial z} - \rho g + viscous \; forces \tag{2.22}$$

As the fluid particle is constantly moving and consequently the position is a function of time, the velocity of the fluid particle can solely be expressed with respect to time [12]. Because of that the acceleration of a particle refers to a fixed point and it shall be distinguished between *local accelerations* with respect to time and *convective accelerations* with respect to position in the following expanded *equations of motion* in (2.25) and (2.26).

$$\frac{du}{dt} = \frac{\partial u}{\partial t} + \frac{\partial u}{\partial x}\frac{dx}{dt} + \frac{\partial u}{\partial z}\frac{dz}{dt} \tag{2.23}$$

$$\frac{dw}{dt} = \frac{\partial w}{\partial t} + \frac{\partial w}{\partial x}\frac{dx}{dt} + \frac{\partial w}{\partial z}\frac{dz}{dt} \tag{2.24}$$

$$\rho \frac{du}{dt} = \rho \left(\frac{\partial u}{\partial t} + u\frac{\partial u}{\partial x} + w\frac{\partial u}{\partial z} \right) = -\frac{\partial p}{\partial x} + viscous \; forces \tag{2.25}$$

$$\rho \frac{dw}{dt} = \rho \left(\frac{\partial w}{\partial t} + u\frac{\partial w}{\partial x} + w\frac{\partial w}{\partial z} \right) = -\frac{\partial p}{\partial z} - \rho g + viscous \; forces \tag{2.26}$$

The above derived equations can be adapted and interpreted in many ways. For example the viscous forces for water can be defined as $\nu \nabla^2 u$ and $\nu \nabla^2 w$ respectively under certain conditions. With the kinematic viscosity ν it is then possible to establish the well-known *Navier-Stokes equations*. However, this cannot be solved directly as there are less equations available for more variables [7]. On the other hand, in case of turbulent flow the velocities in (2.25) and (2.26) can be extended by velocity fluctuations which account for additional stresses, forming the so-called *Reynolds equations* [12]. However, if viscous forces are completely ignored the *equations of motion* turn into a special form, named *Euler equations* in (2.27) and (2.28). Together with the continuity equation and distinct boundary conditions this approach allows a full capture of an inviscid fluid flow. Here, the problem is examined by a total velocity field and not as an individual particle travelling through space [7].

$$\frac{\partial u}{\partial t} + u\frac{\partial u}{\partial x} + w\frac{\partial u}{\partial z} = -\frac{1}{\rho}\frac{\partial p}{\partial x} \tag{2.27}$$

$$\frac{\partial w}{\partial t} + u\frac{\partial w}{\partial x} + w\frac{\partial w}{\partial z} = -\frac{1}{\rho}\frac{\partial p}{\partial z} - g \tag{2.28}$$

Eventually, the physical principles consolidating the hydromechanical wave model are chosen in a way to retain the law of mass conservation, saying that "no mass may disappear and that a change in momentum takes place only when forces are acting on the particles" [7].

2.3.2 Potential flow theory

If the flow is not only inviscid but also irrotational, then the potential flow theory constitutes a well-established method of determining the velocity field within the fluid. The absence of vorticity goes back to *Kelvin's theorem* which declares vorticity to be constant for each particle within an inviscid fluid with conservative external forces and if there is no vorticity in the beginning it will not evolve over time [12]. Thus, the irrotational assumption is seen as an initial condition for the potential flow approach, enabling an alternative definition of the velocity vector by means of a scalar which is better known as the velocity potential ϕ [12].

$$(u, w) = \left(\frac{\partial \phi}{\partial x}, \frac{\partial \phi}{\partial z}\right) \tag{2.29}$$

Generally, the potential flow idea implies the replacement of both velocity components w and u in the previously discussed *continuity* and *Euler equations* in order to reduce the number of unknowns. On that account, the modified velocity vector in (2.29) is substituted in the *continuity equation* in (2.18), resulting in the *Laplace* definition in (2.31) [12].

$$\frac{\partial u}{\partial x} = \frac{\partial^2 \phi}{\partial x^2}, \qquad \frac{\partial w}{\partial z} = \frac{\partial^2 \phi}{\partial z^2} \tag{2.30}$$

$$\frac{\partial^2 \phi}{\partial x^2} + \frac{\partial^2 \phi}{\partial z^2} = 0 \quad or \quad \nabla^2 \phi = 0 \tag{2.31}$$

If the right as well as left side of the *equations of motion* under *Eulerian* conditions in (2.27) and (2.28) are now adjusted accordingly and separately, an integration with

respect to x and z eventually reveals a new description of the velocity field in (2.35) and (2.36) [12].

$$\frac{\partial u}{\partial t}+u\frac{\partial u}{\partial x}+w\frac{\partial u}{\partial z}=\frac{\partial u}{\partial t}+\frac{1}{2}\frac{\partial}{\partial x}(u^2+w^2)=\frac{\partial}{\partial x}\left(\frac{\partial \phi}{\partial t}+\frac{1}{2}(u^2+w^2)\right) \tag{2.32}$$

$$\frac{\partial w}{\partial t}+u\frac{\partial w}{\partial x}+w\frac{\partial w}{\partial z}=\frac{\partial w}{\partial t}+\frac{1}{2}\frac{\partial}{\partial z}(u^2+w^2)=\frac{\partial}{\partial z}\left(\frac{\partial \phi}{\partial t}+\frac{1}{2}(u^2+w^2)\right) \tag{2.33}$$

$$-\frac{1}{\rho}\frac{\partial p}{\partial x}=-\frac{\partial}{\partial x}\left(\frac{p}{\rho}+gz\right) \tag{2.34}$$

$$\frac{\partial \phi}{\partial t}+\frac{1}{2}(u^2+w^2)=-\frac{p}{\rho}-gz+C_1(z,t) \tag{2.35}$$

$$\frac{\partial \phi}{\partial t}+\frac{1}{2}(u^2+w^2)=-\frac{p}{\rho}-gz+C_2(x,t) \tag{2.36}$$

The results of the integration solely differ from the arbitrary integration coefficients C_1 and C_2 and since C_2 does not depend on z, C_1 cannot rely on z neither and vice versa with respect to x. This interdependence brings along the advantage that the *equations motion* only need to be integrated once and eventually combined with the so called *Bernoulli equation*, summarised in (2.38) [12].

$$C_1(z,t)=C_2\,(x,t)=C(t) \tag{2.37}$$

$$gz+\frac{p}{\rho}+\frac{1}{2}(u^2+w^2)+\frac{\partial \phi}{\partial t}=C(t) \tag{2.38}$$

If it is assumed that the flow remains the same at ϕ and $\phi+\int C(t)dt$, the *Bernoulli equation* can be set to zero and by implementing the alternative velocity vector from (2.29) reads as follows [12].

$$gz+\frac{p}{\rho}+\frac{1}{2}\left[\left(\frac{\partial \phi}{\partial x}\right)^2+\left(\frac{\partial \phi}{\partial z}\right)^2\right]+\frac{\partial \phi}{\partial t}=0 \tag{2.39}$$

In case of sufficient boundary conditions which do not affect the pressure p the internal velocity field is just built upon the velocity potential ϕ as the only unknown. The conclusion of the presented potential flow problem involves an answer to the second

order partial differential equation in form of the *Laplace equation* in (2.31) which can then be entered in (2.39) to compute the pressure at each point. So according to *Svendson et al. (1976)* [12] "the pressure acts as a kind of reaction, the magnitude of which is scaled so that the *equations of motion* are satisfied at each point, for the velocities already determined by the solution for Φ". Accordingly, the *Laplace* and the *Bernoulli equation* valid for $-\infty \leq x \leq \infty$ and $-d \leq z \leq \eta(x, t)$ are to be developed to describe the governing model for wave simulations [7].

2.3.3 Boundary conditions

In the previous paragraph 2.3.2 it is shown that the potential theory is only applicable in case of zero vorticity and according to [12] this assumption is generally acceptable for wind generated waves as the boundary layer at the bottom is considered as thin compared to the water depth for a specific time period. That means that the turbulent region along the bottom takes up a rather inferior role. However, for the description of the free water surface the seabed is essential as it takes one boundary condition at the bottom and two at the free surface to solve the potential flow problem in (2.39). It is important to begin by saying that the following boundary conditions at the free surface refer to the surface elevation η, introducing a new unknown to the potential flow problem which now depends on the variables $\phi(x, z, t)$ and $\eta(x, t)$ [12].

Bottom condition:

This boundary condition prohibits a penetration of the water particles through the seabed, meaning that the flow must be parallel to the bottom [12], as illustrated in Fig. 2.7.

$$w = 0 \quad or \quad \frac{\partial \phi}{\partial z} = 0 \quad at\ z = -d \tag{2.40}$$

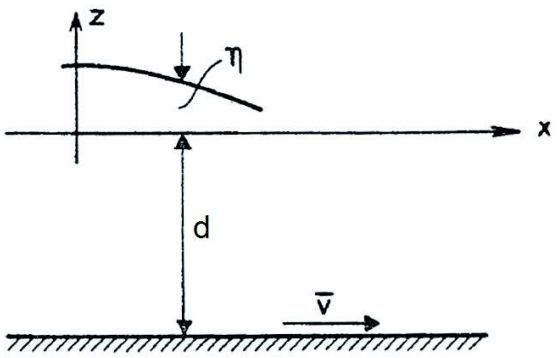

Fig. 2.7: Bottom and free surface condition [12]

Free surface conditions:

One of the free surface conditions refers to the wave kinematics on the surface and its relation to the surface level, prescribing that the fluid particle on the free surface will stay there and that the height adapts the following condition [12].

$$dz = \frac{\partial \eta}{\partial t} dt + \frac{\partial \eta}{\partial x} dx \tag{2.41}$$

$$dx = u\, dt \quad \text{and} \quad dz = w\, dt \tag{2.42}$$

Thus, the particle must follow the surface elevation but also keep its position at the free surface and cannot pass through the water surface. This implies that the fluid particle velocity normal to the free surface is the same as the velocity of the free surface itself in that direction [7]. If the kinematics are now included in (2.41) and the time step *dt* is eliminated by division, the so-called *kinematic boundary condition* in (2.43) can be postulated and explained visually in Fig. 2.8.

$$w = \eta_t + u\, \eta_x \quad or \quad \phi_z = \eta_t + \phi_x\, \eta_x \quad at\ z = \eta \tag{2.43}$$

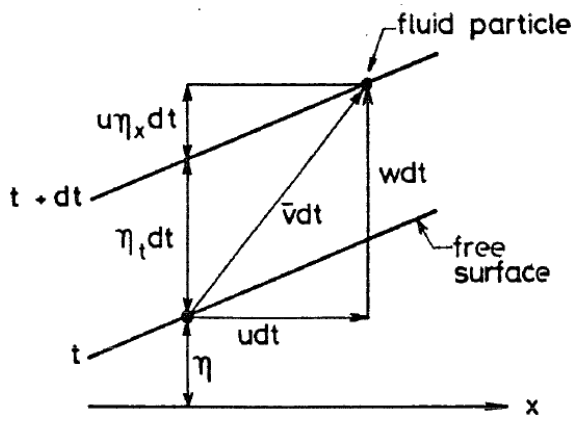

Fig. 2.8: Visualisation of the kinematic boundary condition [12]

However, unlike the clearly defined seabed the water surface can only be obtained by solving the potential flow approach and thus depends on an additional unknown in form of the surface elevation η, demanding a second condition [7]. Remedy is provided by stipulating that the free surface lacks tension and that the pressure is more or less constant along the water surface because it is expected that atmospheric air prevails above the water with a density of only *1/100* times that of water [5]. The resulting *dynamic boundary condition* at the free surface yields the subsequent expression for the *Bernoulli equation* in the potential theory.

$$g\eta + \frac{1}{2}(\phi_x^2 + \phi_z^2) + \phi_t = 0 \quad at\ z = \eta \tag{2.44}$$

Open vertical boundary condition:

This condition shall only be mentioned briefly as it concerns the edges of the considered ocean region and thus affects the type of wave motion which, however, is mainly discussed in the various wave theories separately [12]. Using the example of the wave celerity c the *periodicity condition* in (2.45) is responsible for the oscillating behaviour of a wave train with constant speed and permanent form which traces back to the absence of an underlying current [5].

$$\phi(x, z, t) = \phi(x - ct, z) \tag{2.45}$$

So far it is crucial to point out that the above described potential flow problem and its associated solution does not include any type of excitation. Thus, it does not output wave height or frequency. Obviously, the method waives any viscous or surface tension effects and the potential flow theory is also incapable of observing foam or breaking wave phenomena [7].

In the end, it is important to conclude that some of the above mentioned assumptions have to be viewed critically. In particular, the neglected underlying current, a constant depth as well as the two-dimensional and permanently shaped form of the wave train should be questioned under certain conditions but shall be accepted for now. Various theories explained in the subsequent paragraphs attempt to tackle those difficulties independently [5]. But the irrotationality default has been commonly agreed on if the very thin but complex boundary layers at the seabed and free surface are ignored respectively.

2.4 Regular waves – small amplitude wave theory

The previously described boundary conditions constitute the major challenges in defining a regular wave, in particular the *free surface boundary conditions* due to their non-linear properties. This is exacerbated by the fact that those requirements shall refer to the free surface $z = \eta$ which is not given at the moment. On that account, the small amplitude wave theory shall be introduced which simply restricts the wave height H to be much smaller than the wave length L and the water depth d [5]. Invoking $H << L, d$ the non-linear influences at the free surface with respect to the wave height can be evaded compared to the linear terms. This allows to set the reference level at the mean water level $z = 0$, yielding the principle of perturbation procedures in the following work [5]. In addition to the necessary simplifications in 2.3 and the limited wave height the linear or sinusoidal wave theory dictates a constant depth and period, two-dimensional oscillation as well as a steady form while traveling through water [12]. This simplifies the *free surface boundary conditions* to the following linearised expressions in (2.46) and (2.47) [5]. If the *dynamic boundary condition* in (2.49) is differentiated with respect to time, it can be combined with the *kinematic boundary condition* in (2.46) to form one master constraint for the velocity potential in (2.48) [9].

$$\frac{\partial \phi}{\partial z} - \frac{\partial \eta}{\partial t} = 0 \quad at\ z = 0 \tag{2.46}$$

$$\frac{\partial \phi}{\partial t} + g\eta = 0 \quad at\ z = 0 \tag{2.47}$$

$$\frac{\partial^2 \phi}{\partial t^2} + g\frac{\partial \phi}{\partial z} = 0 \quad at\ z = 0 \tag{2.48}$$

$$\eta = -\frac{1}{g}\left(\frac{\partial \phi}{\partial t}\right) \quad at\ z = 0 \tag{2.49}$$

A solution to the problem can be found by means of the *periodicity condition* in (2.45) and by separating the variables so that the velocity potential can be re-written as follows and substituted in the *Laplace equation* in (2.31).

$$\phi = Z(z) \cdot \phi(x - ct) \tag{2.50}$$

As a result two ordinary differential equations (2.51) and (2.52) are generated where the sign shift of k^2 shall ensure a periodic solution according to [5].

$$\frac{\partial^2 Z}{\partial z^2} - k^2 Z = 0 \tag{2.51}$$

$$\frac{\partial^2 \phi}{\partial x^2} + k^2 \phi = 0 \tag{2.52}$$

The general solutions of Z and ϕ are given by the subsequent expressions with the integration constants A_1, A_2, A_3 and A_4 which shall be defined with respect to the applied boundary conditions [5].

$$Z = A_1 \cdot \cosh(kz) + A_2 \cdot \sinh(kz) \tag{2.53}$$

$$\phi = A_3 \cdot \cos[k(x - ct)] + A_4 \cdot \sin[k(x - ct)] \tag{2.54}$$

With reference to [5] the time equals zero in case of a wave crest crossing the plane $x = 0$ and together with equation (2.49) it is legit to put A_3 to zero. Due to the *bottom boundary condition* in (2.40) A_2 can be related to A_1 and after inserting all constants in (2.50) the velocity potential can be obtained with $A = A_1 A_4$.

$$A_2 = A_1 \cdot \tanh(kd) \tag{2.55}$$

$$\phi = A \cdot \frac{\cosh\big(k(z + d)\big) \cdot}{\cosh(kd)} \sin[k(x - ct)] \tag{2.56}$$

The formula in (2.49) shall now be used to specify the overall integration constant A in order to include the surface elevation and the wave height. The already mentioned linear *dispersion relationship* in (2.57) and (2.58) is attained by implementing the general potential velocity in the combined *free surface boundary conditions*, expressed in (2.48) [5].

$$\omega^2 = gk \cdot \tanh(kd) \tag{2.57}$$

$$c^2 = \frac{g}{k} \cdot \tanh(kd) \tag{2.58}$$

While it links a wave speed increase to the wave length, the *dispersion relationship* additionally relates the phase velocity to the wave number, resulting in the final form of the velocity potential for the small amplitude wave theory. The wave phase angle θ is introduced which shall be used in any equation from now on [5].

$$\phi = \frac{gH}{2\omega} \cdot \frac{\cosh(k(z+d)}{\cosh(kd)} \cdot \sin(\theta) \tag{2.59}$$

$$\phi = \frac{\pi H}{kT} \cdot \frac{\cosh(k(z+d)}{\sinh(kd)} \cdot \sin(\theta) \tag{2.60}$$

$$\theta = k(x - ct) = kx - \omega t \tag{2.61}$$

The above derived velocity potential now fulfils the *continuity equation*, the sea floor requirement and the combined *free surface condition*, eventually summarised in (2.62) - (2.64) and illustrated in Fig. 2.9. In the end, this approach and the final expressions enable a precise definition of the water particle motions and the hydrodynamic pressure anywhere in the fluid. Here, the former shall be based on the velocity potential whereas the pressure refers to the *Bernoulli* approach in 2.3.2 [7].

$$\nabla^2 \phi = 0 \quad -\infty \leq x, y \leq \infty, -d \leq z \leq 0 \tag{2.62}$$

$$\frac{\partial \phi}{\partial z} = 0 \quad at\ z = -d \tag{2.63}$$

$$\frac{1}{g} \cdot \frac{\partial^2 \phi}{\partial z^2} + \frac{\partial \phi}{\partial z} = 0 \quad at\ z = 0 \tag{2.64}$$

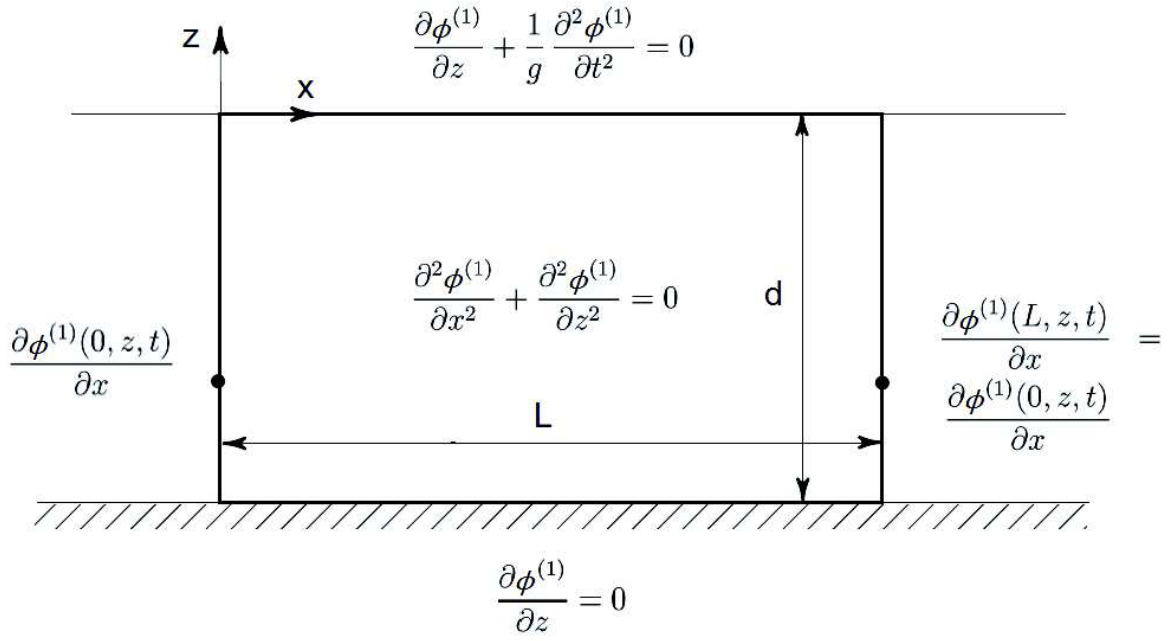

Fig. 2.9: Illustration of solution and boundary conditions of linear wave theory [13]

Referring to the *dispersion relationship* the phase velocity for linear waves only relies on the wave length and is not affected by its amplitude. Fig. 2.10 provides an overview that compares wave length and phase velocity to wave period for different water depths. At first, it can clearly be noted that the water depth has a severe effect on the general wave properties as wave length but also phase velocity increase with growing distance between sea floor and free water surface. Additionally, the continuous surge in speed and length in case of longer wave periods is striking although the slope of each rise proceeds reversely.

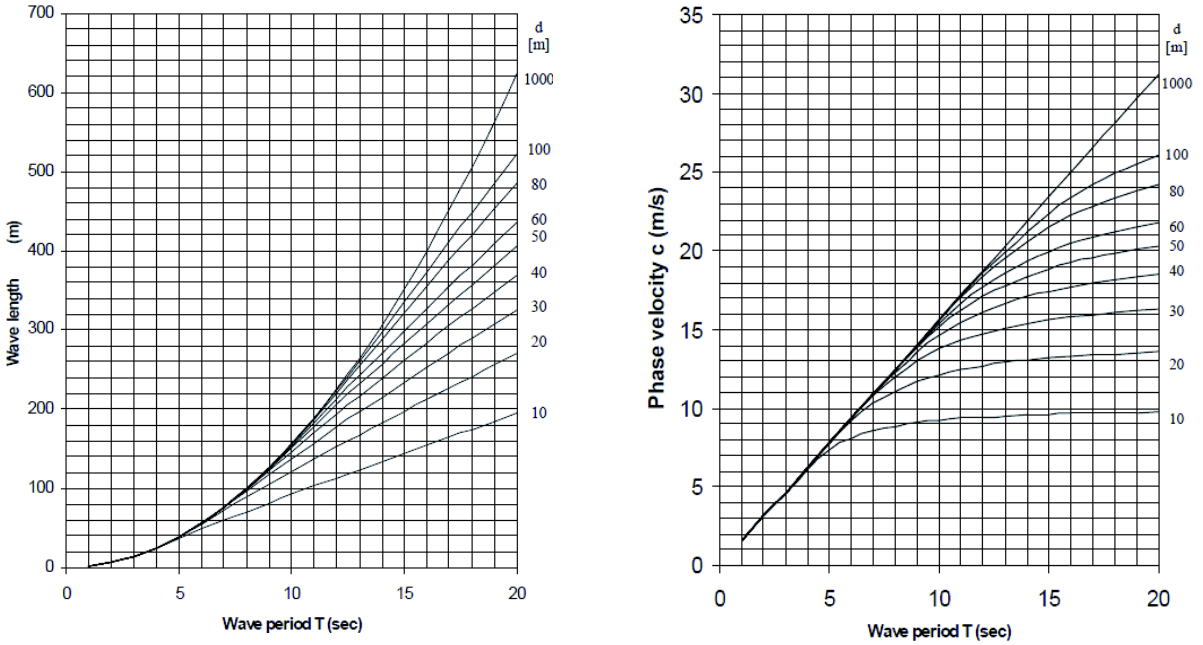

Fig. 2.10: Wave length and phase velocity as a function of wave period for different water depths [14]

In order to comprehend the here described wave theories, relationships and differences of each mathematical approach for simulating waves various *Matlab* codes are written. In the upcoming paragraph an example wave in Tab. 2.1 shall be visualised and analysed with respect to surface elevation, hydrodynamic pressure and wave kinematics. Since today's bottom-fixed structures have not yet entered water depths where the wave and its properties are independent of the distance to the seabed and floating offshore foundation for wind turbines have not gained the necessary technical relevance, the following work shall only focus on waves in finite depths. The simplifying deep water effect shall not be discussed further.

Tab. 2.1: Characteristics of exemplary wave for the following wave theories

Water depth, d [m]	*Wave period, T [sec]*	*Wave height, H [m]*	*x-position, x [m]*
10.0	10.0	5.0	0.0

2.4.1 Wave profile

The combined *free surface condition* in (2.64) can preferably be handled by a plane progressive wave train with a two-dimensional motion and a sinusoidal oscillation with the angular frequency ω. Considering a propagation in the positive x-direction with the phase velocity c and observing in line with this velocity the following general expression of the surface elevation in (2.65) describes a steady-state process [9].

$$\eta(x,t) = \eta_a \cdot \cos(\mathrm{kx} - \omega\mathrm{t} + \epsilon) \tag{2.65}$$

In general, η defines the vertical coordinate of the surface elevation with reference to *SWL* [8]. The wave amplitude η_a refers to half the wave height H while ε represents any phase angle between -π and π and x a position in space. In case of an origin at $x = 0$ for the wave system it is common to ignore the phase angle for regular waves or alternatively adjust it in a way if the wave shall be illustrated in terms of sine. The above provided surface elevation can be extended to account for any wave direction μ relative to the x-axis in the x-y-plane [8], given by (2.66).

$$\eta(x,y,t) = \zeta_a \cdot \cos[k \cdot (x \cdot \cos(\mu) + y \cdot \sin(\mu)) - \omega t + \varepsilon] \tag{2.66}$$

The equation in (2.65) yields the subsequent surface elevation in Fig. 2.11 for a regular wave with a sinusoidal shape and amplitude which refers to half the wave height in Tab. 2.1. Spreading is not considered and it is important to mention that the actual wave profile is not affected by the water depth.

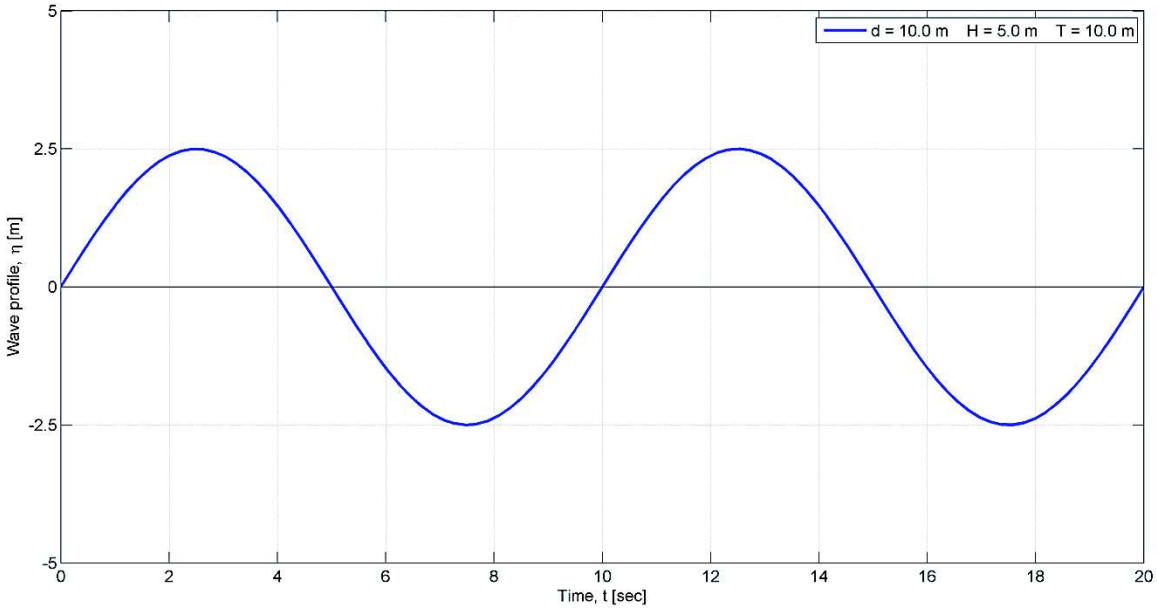

Fig. 2.11: Surface elevation of a linear regular wave

2.4.2 Water particle kinematics

For the design of offshore structures a distinct reproduction of the wave kinematics along the water column below the wave surface is inevitable since particle velocities and accelerations lay the foundation for defining wave loads by means of *Morison's* equation. Therefore, the general velocity potential in (2.60) is adjusted to give indication of the moving water particles excited by the wave and its energy transfer. The wave kinematics can simply be obtained by differentiating the general velocity potential with respect to the x- and z-direction [14], following the principles of potential flow theory in (2.29). Again, the focus shall be set on the general description of the wave characteristics for any water depths.

$$u = \frac{\partial \phi}{\partial x} = \frac{\pi H}{T} \cdot \frac{\cosh[\mathrm{k(z+d)}]}{\sinh(kd)} \cdot \cos(\theta) \tag{2.67}$$

$$w = \frac{\partial \phi}{\partial z} = \frac{\pi H}{T} \cdot \frac{\sinh[\mathrm{k(z+d)}]}{\sinh(kd)} \cdot \sin(\theta) \tag{2.68}$$

The terms in (2.67) and (2.68) allow a determination of the velocity components u and w at a fixed location *(x, z)*, representing the *Eulerian* description and thus resulting in the velocity field at each point in the wave [12]. The progression of the velocity components together with their extreme positions can be perceived in Fig. 2.12. Here, at first glance it is perceptible that due to the irrotational flow $\partial u/\partial z$ equals zero at the bottom, declaring u being independent of the z-coordinate at the sea floor [12].

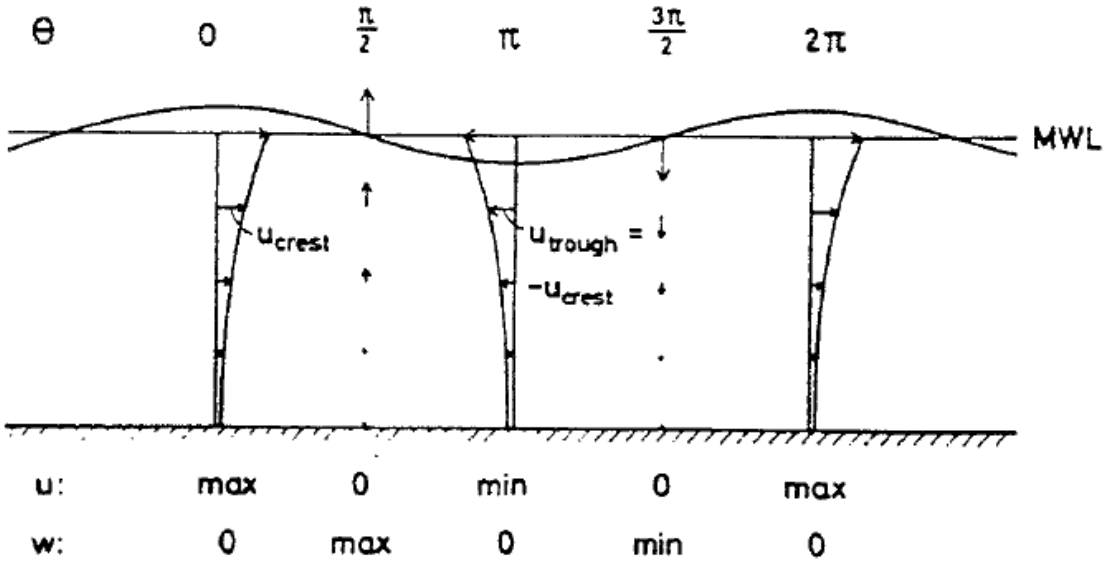

Fig. 2.12: Depiction of velocity components and its maximum values [12]

However, it is essential to point out that the results above only represent a velocity field between the bottom and *SWL* at $z = 0$ as the wave is restricted to be much smaller than the wave length. Any non-linear influences are omitted with reference to the main assumption of the small amplitude wave theory. That means that the boundary conditions refer to *SWL* and the motion of the actual free surface at $z = \eta$ is not implemented at all, neglecting wave kinematics in the region of a wave crest above *SWL* or between *SWL* and the wave profile in a trough where no water is found [12]. In order to adjust the wave kinematics to the actual surface elevation there are several profile extension methods which shall be presented in 2.4.4. Here, a consideration of the example wave in Tab. 2.1 shall be used to explain the relationship between both velocity components and their dependency on the wave profile more precisely.

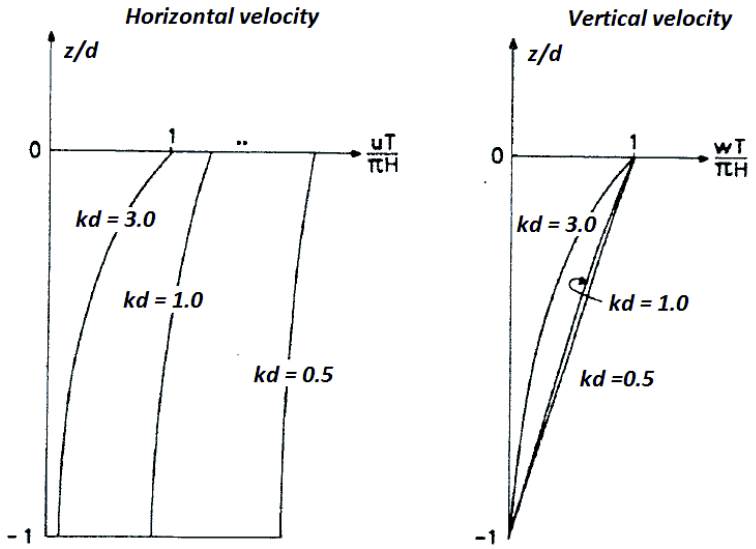

Fig. 2.13: x-component velocity under wave crest (left) and z-component velocity at z = 0 (right) for various kd [12]

But in principle Fig. 2.13 illustrates the maximum velocity components under a wave crest or in a trough respectively for the horizontal speed and at *SWL* for the vertical velocity. In case of constant depth the combination of *kd* provides different sets of wave periods and lengths. As noticeable the longer the wave the more linearly behaves the *x*-component velocity over the water depth. On the other side the vertical particle velocity *w* becomes more constant along the *z*-axis, representing shallow water waves [12]. Additionally, Fig. 2.13 reveals under the assumption of uniform wave period and height that a smaller water depth only alters the shape of the *w*-velocity field while the horizontal component *u* grows in magnitude instead [12].

The calculation of the water particle accelerations bases on the same procedure as for the velocity although with a second differentiation with respect to the *x*- and *z*-direction. But again it requires an adjustment of the results concerning the instantaneous water

level. The final results of the *x*-component acceleration a_1 and the *z*-component acceleration a_3 in (2.69) and (2.70) for the example wave can be found in 2.4.4 after applying the profile extension method. Here, it shall be noticed that the acceleration amplitudes reveal a dependency on the angular frequency ω to the second power and a 90° shift towards both directions. With respect to the orbital path the size of the acceleration does not change and is always orientated to the centre of the circular trajectory [6].

$$a_1 = \frac{\partial^2 \phi}{\partial x^2} = \frac{2\pi^2 H}{T^2} \cdot \frac{\cosh[\mathrm{k(z+d)}]}{\sinh(kd)} \cdot \cos(\theta) \tag{2.69}$$

$$a_3 = \frac{\partial^2 \phi}{\partial z^2} = -\frac{2\pi^2 H}{T^2} \cdot \frac{\sinh[\mathrm{k(z+d)}]}{\sinh(kd)} \cdot \sin(\theta) \tag{2.70}$$

Without the briefly introduced profile extension methods, it is still possible to realistically reproduce as well as plot the wave kinematics at *SWL*. Fig. 2.14 displays a typical sinusoidal wave with its alternating velocity and acceleration components along the wave propagation, mainly reasoning the circular motion of the water particles in the following explanation.

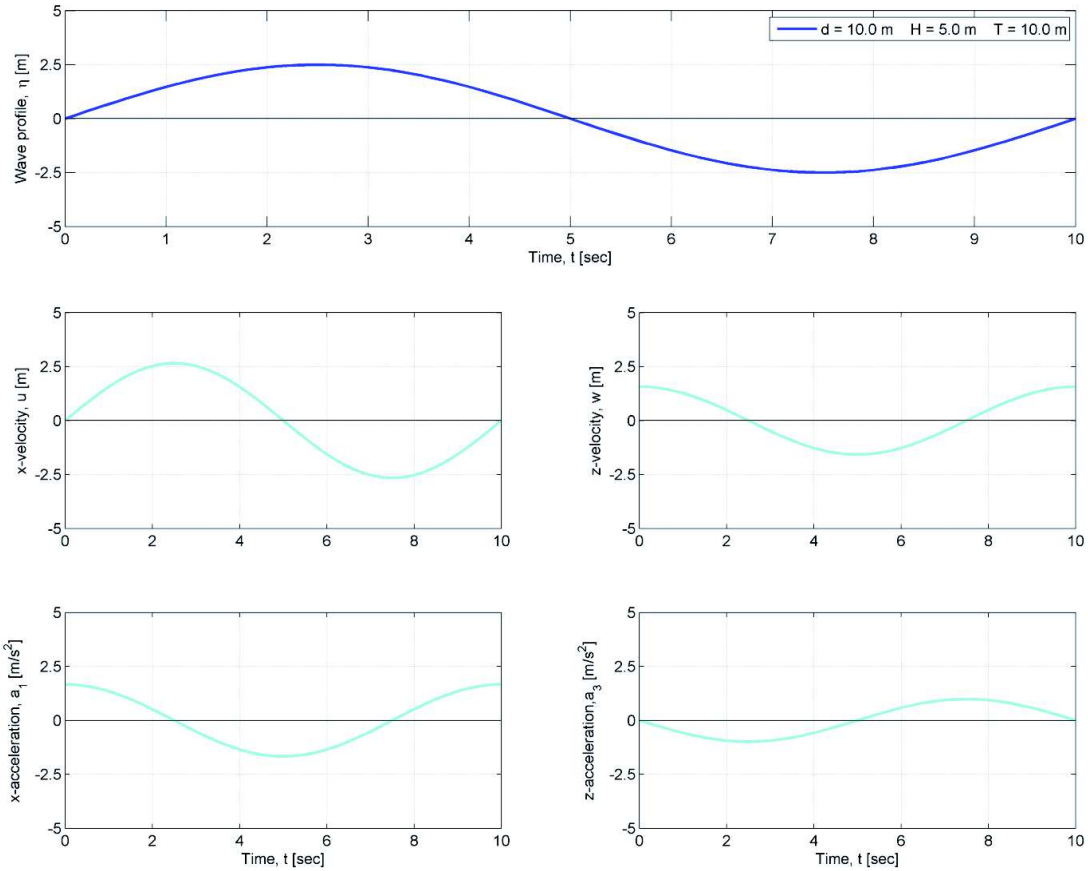

Fig. 2.14: Typical distribution of wave kinematics of a sinusoidal wave

The associated trajectory of the particles shall only marginally be discussed as they rather play an inferior role for the upcoming definition of wave loads and their structural impacts. However, it shall generally be said that according to *Svendson et al. (1976)* [12] "the instantaneous velocity at a point is tangent to the path of the particle at that point" and thus it can be argued that due to the *Eulerian* description of the velocity field the water particles must follow an orbital direction, applying the following functions with respect to time [12] which however shall not be elaborated in details.

$$\frac{dx}{dt} = u(x,z,t) \tag{2.71}$$

$$\frac{dz}{dt} = w(x,z,t) \tag{2.72}$$

But it is obvious that the water particles oscillate in the x- and z-direction about a certain position (C_1, C_2) which is simplified in the point (x_1, z_1,) according to [6]. So by using (2.73) the path of the water particle is reduced by the time factor, yielding the general function of an ellipse.

$$\sin^2 \cdot(kx_1 - \omega t) + \cos^2 \cdot (kx_1 - \omega t) = 1 \tag{2.73}$$

$$\frac{(x-x_1)^2}{\left(\eta_a \cdot \frac{\cosh[k(d+z_1)]}{\sinh(kd)}\right)^2} + \frac{(z-z_1)^2}{\left(\eta_a \cdot \frac{\sinh[k(d+z_1)]}{\sinh(kd)}\right)^2} = 1 \tag{2.74}$$

As seen in Fig. 2.15, the water motion diminishes with growing water depth and the effect of the *bottom boundary* condition is clearly visible as the vertical water displacement amplitude equals zero at the sea bottom, i.e. the water particle motions are reduced to a plain back and forth oscillation along the ground [6] whereas at the free surface $z_1 = 0$ it is the same as the wave amplitude η_a..

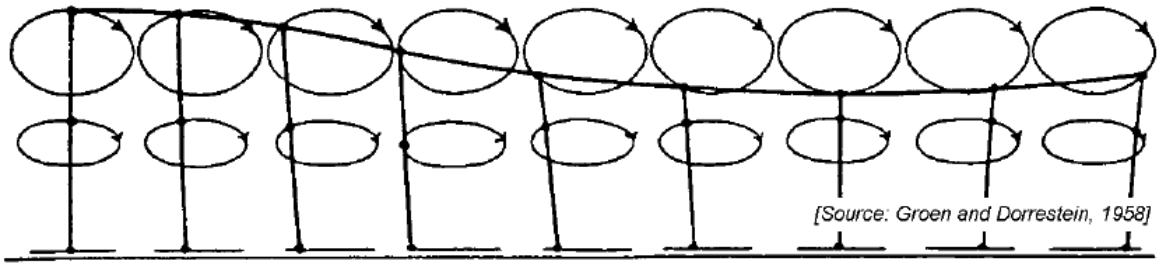

Fig. 2.15: Water particle motion under long or shallow water waves [6]

2.4.3 Dynamic pressure

The dynamic pressure induced by the wave motion changes in line with the below stated *Bernoulli* equation in (2.75) derived in 2.3.3.

$$g\eta + \frac{\mathrm{p}}{\rho} + \frac{1}{2}(\phi_x^2 + \phi_z^2) + \phi_t = 0 \tag{2.75}$$

According to [12] the still water or hydrostatic pressure $-\rho gz$ is commonly separated, introducing p_D which denotes the *excess pressure* in diverse literatures and only considers the wave generated pressure differences. Inserting this in (2.75) and again excluding non-linear contributions due to the small amplitude approach the dynamic pressure p_D can be reduced to the following expression in (2.78).

$$p_D = p + \rho gz \tag{2.76}$$

$$\frac{p_D}{\rho} + \frac{1}{2}(\phi_x^2 + \phi_z^2) + \phi_t = 0 \tag{2.77}$$

$$p_D = -\rho\phi_t \tag{2.78}$$

The differentiation of the general velocity potential with respect to time yields the hydrodynamic pressure distribution p_D in (2.79) for any water depths.

$$p_D = \frac{1}{2}\rho gH \cdot \frac{\cosh[k(z+d)]}{\cosh(kd)} \cdot \cos(\theta) \tag{2.79}$$

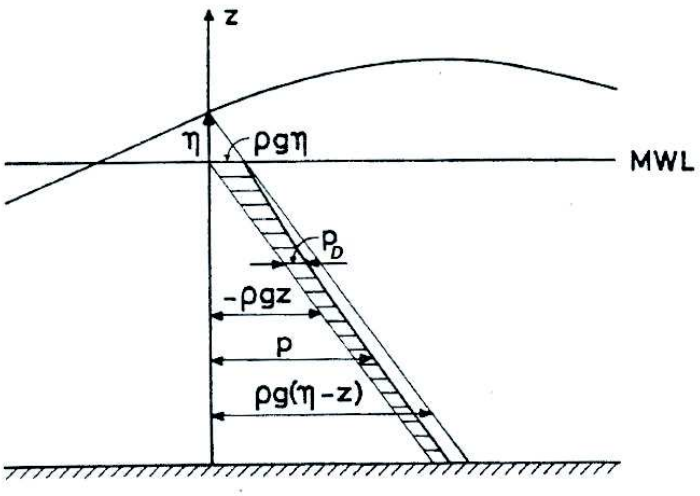

Fig. 2.16: Distribution of hydrodynamic pressure with the different contribution in a linear regular wave [12]

With reference to Fig. 2.16 the distribution of p_D over the water depth and the interactions with p and the hydrostatic pressure $-\rho g z$ again accepts the negligence of the wave data between *SWL* and the actual surface elevation by the wave, relying on the boundary conditions at $z = 0$ instead at $z = \eta$. But based on the work by *Svendson et al. (1976)* [12]"the pressure force from the small triangle between *SWL* and the dotted line will be 0" in Fig. 2.16. Consequently, the pressure variation only at the *SWL* is of importance which is shown by the example wave in Tab. 2.1 for the general depth scenario. Here in Fig. 2.17, it becomes clear how the hydrodynamic pressure simply follows the wave pattern in phase over a certain time period.

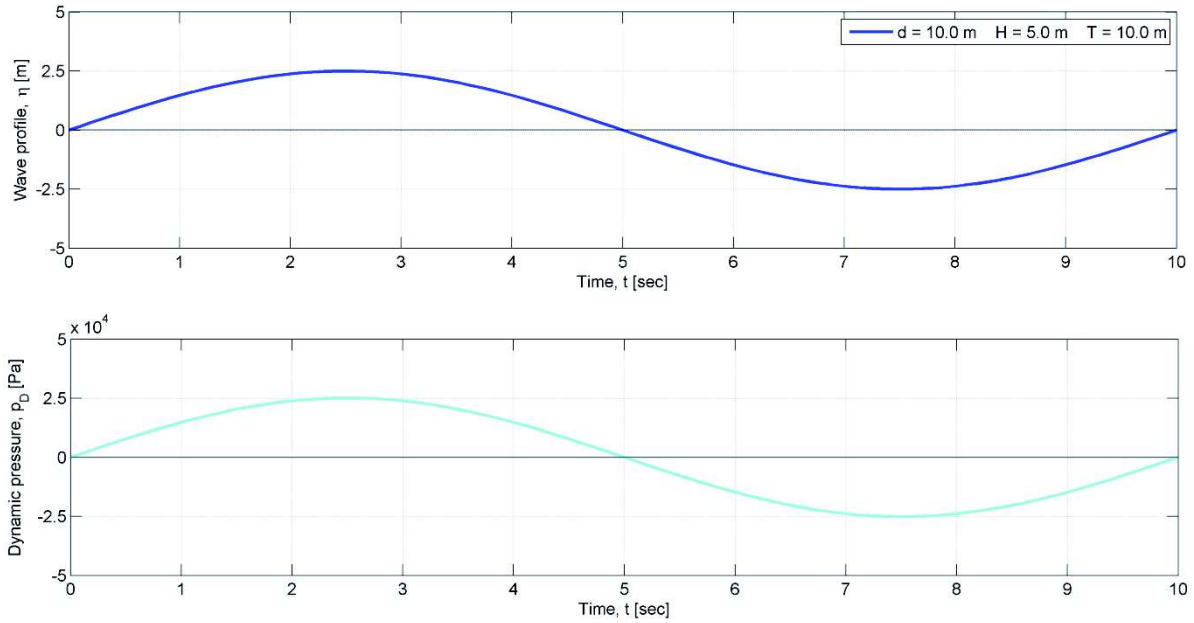

Fig. 2.17: Pressure variation in phase with wave profile on SWL

2.4.4 Profile extension methods for effective wave kinematics

As already mentioned in 2.4.2 the small amplitude wave theory and its associated linearisation is accompanied by one major drawback as it solely concentrates on wave kinematics up to *SWL*. So in theory the surface elevation literally never exceeds the water level at $z = 0$. Referring to [6] this simplification is considered to be extremely obstructive in case of splash zone hydromechanics which are usually applied to determine non-linear ship motions or to assess ultimate strength of fixed offshore structures. Thus, in case of linear wave theory it is essential to adjust the wave kinematics manually so that they fit to the actual surface elevation. There are different stretching approaches which are illustrated in Fig. 2.18 but generally the profile extensions are performed either by extrapolation, constant extension or the so-called *Wheeler* profile stretching.

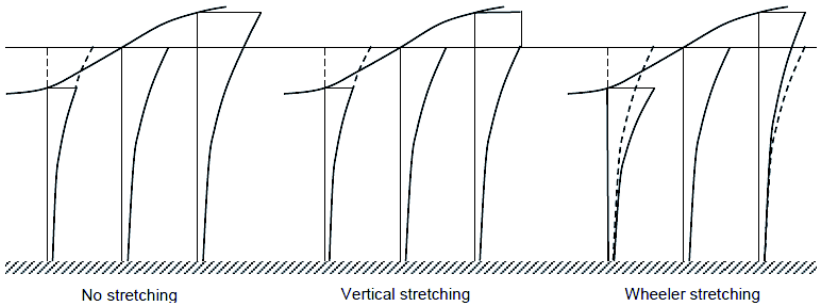

Fig. 2.18: Stretching types for sinusoidal waves [15]

Extrapolation:

This method simply refers wave kinematics obtained by linear wave theory to the instantaneous water level, so allowing positive z-coordinates in case of a wave crest. However, according to *Journeé et al. (2001)* [6] "this straightforward mathematical extension of linear theory in this way leads to an explosion in the exponential functions so that the velocities become exaggerated within the wave crest". This simply leads to over-conservatism with regards to water particle velocities and accelerations which heavily effect higher constructions of for instance monopile foundations.

Constant extension:

The constant extension or vertical stretching in Fig. 2.18 involves computing kinematics to the *SWL* and appointing the same results received at $z = 0$ for all other remaining vertical steps above zero. In case of a wave trough, the linear theory is just applied to the reduced z-coordinate below *SWL*, resulting in a commonly and handy profile extension method [6].

Wheeler profile stretching:

The *Wheeler* profile stretching implies an alternative definition of the z-axis, now reaching from the sea floor to the instantaneous water level at $z = \eta$ [6]. As depicted in Fig. 2.18, this means that the wave kinematics are initially calculated with respect to the original depth division from $-d \leq z \leq 0$. But by introducing the adjusted *Wheeler*-coordinates z_w in (2.80) and interpolating the initial results over those new z-coordinates "the kinematic profile from the bottom is mapped into a profile from the bottom to the actual water surface through the coordinate change" [15]. However, the minimum and the maximum values of particle velocities or accelerations remain the same. The *Wheeler* stretching persuades with one decisive advantage as the adjusted z-values still turn out to be negative so that the exponential functions are able to reveal reasonable results [6].

$$z_w = \frac{d(z-\eta)}{(d+\eta)} \tag{2.80}$$

In general, all of the above methods can be deployed to any position in a regular progressive wave in any water depth as well as independent of the phase angle. Due to the linear background it is possible to stretch wave kinematics of irregular waves as well as presented in 2.5.4. It shall be emphasised that the simple extrapolation reveals the largest outputs whereas the negligence of the wave crest influence and its associated vertical stretching provides a lower boundary [6]. Since the *Wheeler* approach finishes in a reasonable margin and thus does not overshoots the actual wave profile, it shall be implemented throughout the entire upcoming work, starting with the stretched z-coordinates of the exemplary wave in Fig. 2.19.

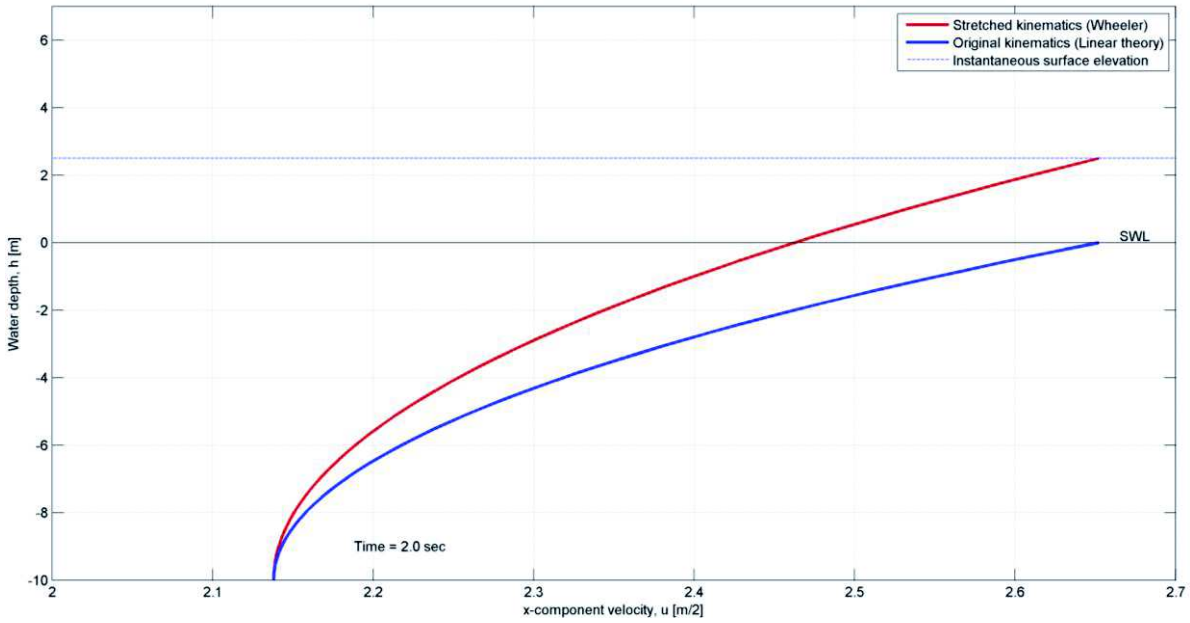

Fig. 2.19: Wheeler stretching applied to the x-component velocity of the example wave at a certain point in time

The conducted *Wheeler* stretching in Fig. 2.19 reveals a clear description of the velocity and acceleration distribution under the actual surface elevation compared to depth variations below *SWL*. The following contour plots display the entire wave kinematics below the regular wave.

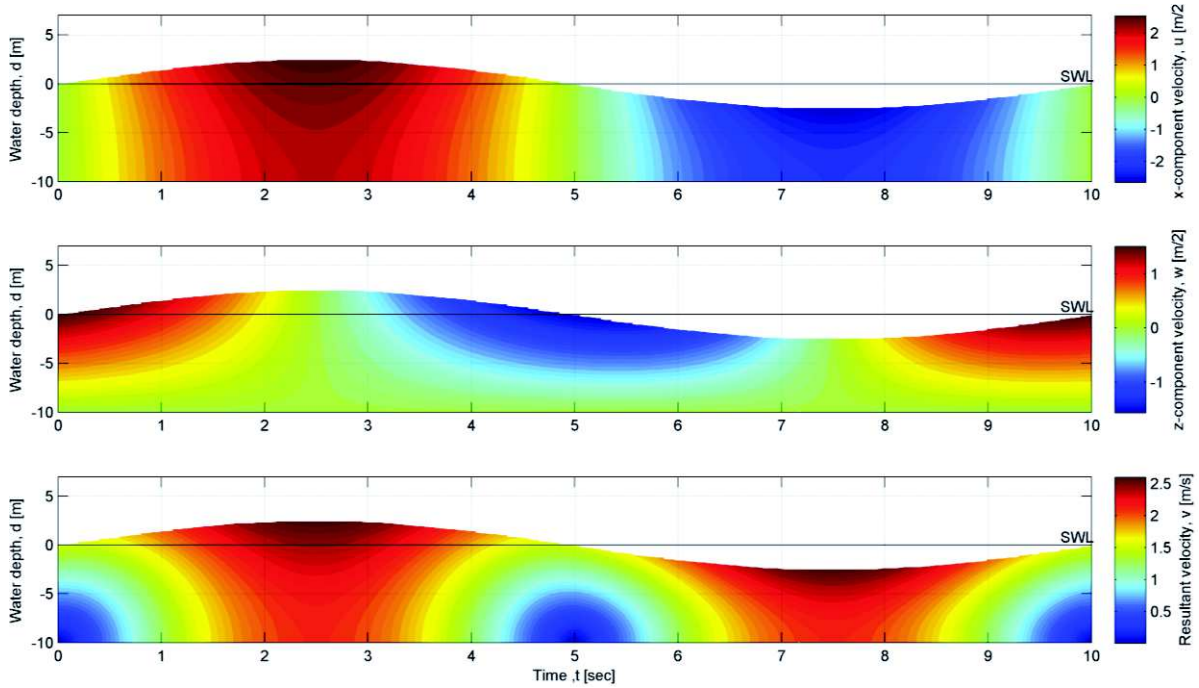

Fig. 2.20: Contour plot of particle velocity and its single x- and z-components

In Fig. 2.20 one can clearly see how the total water particle velocity shows maximum values at the free surface and decreases with the water depth. By looking at each velocity component separately one can perceive the orbital motion of the water particles. At a wave crest or in the trough the particle only moves horizontally as it cannot perforate the water surface whereas the *z*-component velocity reaches its maximum at the zero-crossings. Here, the sign shift implies the up and down movement of the water particle before or respectively after an extreme surface elevation. In comparison to the velocities, the acceleration of each water particle in Fig. 2.21 features the same depth dependency although its components act in a completely reversed manner. Now the crest and the trough are dominated by the *z*-component as this point in time initiates the change of direction for the water particles due to the wave travel.

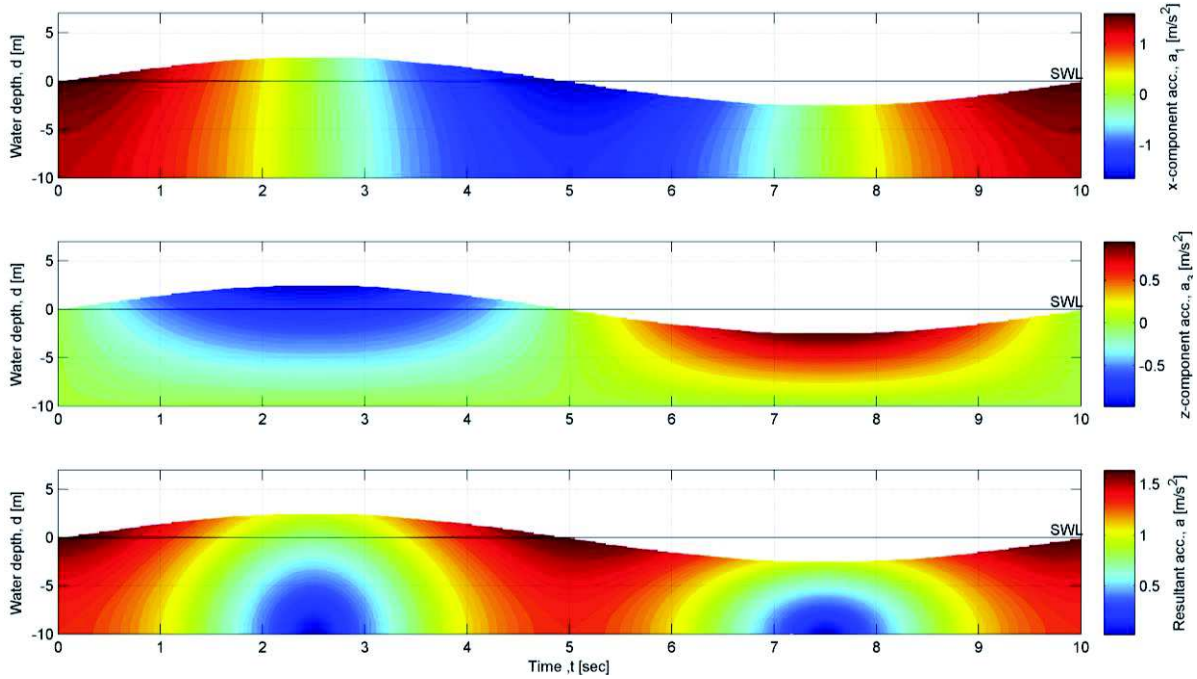

Fig. 2.21: Contour plot of particle acceleration and its single x- and z-components

The vector field in Fig. 2.22 is typically used to expose the elliptical trajectory of the water particles and to proof the depth effects as both the velocity and acceleration flatten to a horizontal line close to the seabed. It is also shown how the acceleration vector always points to the centre of the circular orbit and is perpendicular to the velocity vector which follows the wave motion in the crest but changes direction in the trough. This is because the particles are simply pushed back by the progressive characteristic of the wave.

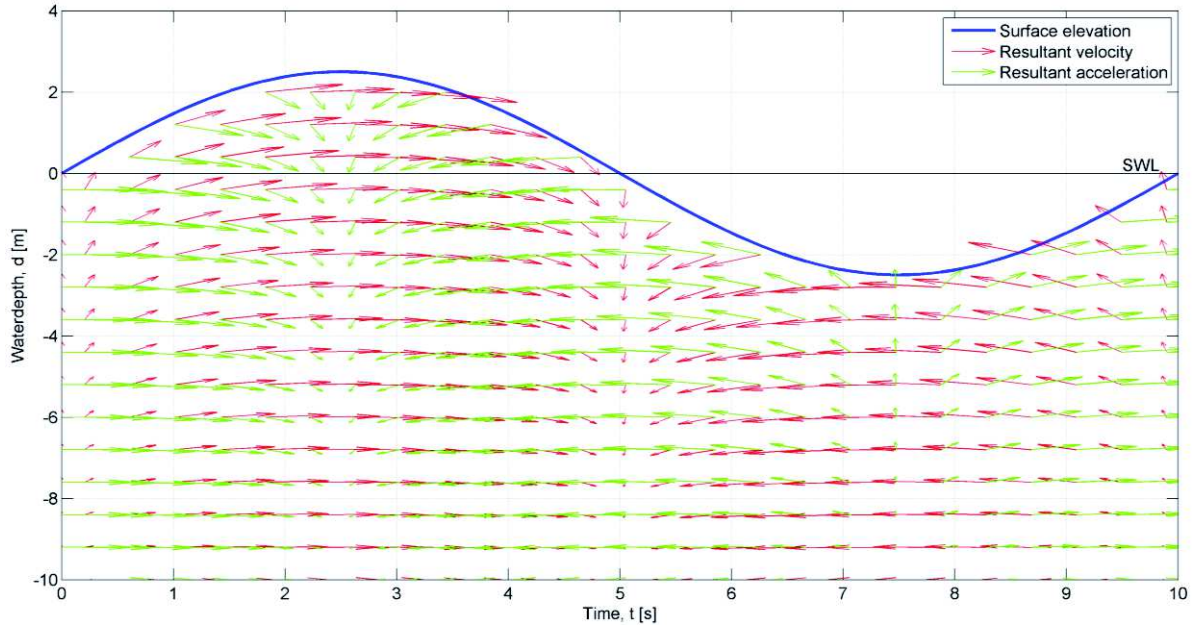

Fig. 2.22: Velocity and acceleration field of example wave

2.5 Irregular waves

In 2.4 wind-generated waves are only considered as regular and long-crested surface oscillations where wave crests and troughs alternate consistently with the same amplitude and period. However, the actual formation of gravitational waves implies a much greater degree of irregularity and randomness majorly due to the inconsistency in wind speed and direction. Thus, a more realistic capture of the sea surface demands a stochastic consideration of the wave pattern. The main concept of reproducing the surface elevation and wave kinematics of an irregular sea state propagating in the positive *x*-direction involves the superposition of a large number of regular wave components, as in (2.81) [16]. Here, the wave amplitude $\eta_{a,j}$, wave number k_j, angular frequency ω_j and the phase angle ε_j represent the characteristics of the wave component number *j*. The applied phase angle can vary uniformly although constantly over time between zero and 2π.

$$\eta(x,t) = \sum_{j=1}^{N} \eta_{a,j} \cdot \cos\left(\mathrm{k_j x} - \omega_\mathrm{j} t + \varepsilon_\mathrm{j}\right) \tag{2.81}$$

This approach bases on the *Fourier* theory which principally states that any signal over a specific time span can be decomposed into a number of individual *sine* and *cosine* functions, outlined in (2.82). The needed coefficients and associated formulas shall not be discussed further but this *Fourier* transformation demonstrates a helpful and quite efficient application [8].

$$\eta(t) = \bar{\eta} + \sum_{m=1}^{M} \mathrm{a}_m \cdot \cos(\omega_m \mathrm{t}) + \sum_{m=1}^{M} \mathrm{b}_m \cdot \sin(\omega_m \mathrm{t}) \tag{2.82}$$

As an irregular wave generally consists of a confusingly high number of regular components, it is recommended expressing the *Fourier* approach in form of energy spectra. Here, every regular *Fourier* component represents the half of its amplitude squared, resulting in an energy distribution of the signal as a function of varying frequencies. Most energy of an irregular sea state is rather limited to a relatively narrow and discrete frequency band. But in practice, it appears that the energy rather varies continuously in (2.83) over the angular frequencies [8].

$$S_\eta(\omega_m) = \frac{0.5 \cdot \eta_{a,m}^2}{\Delta\omega} \tag{2.83}$$

The continuous energy spectrum is considered as the initial situation in predicting and simulating irregular sea states on the basis of wave statistics for a certain area in the ocean. Those ocean data are collected in so-called scatter diagrams exemplified in Fig. 2.23. Here, each combination of the previously explained significant wave height H_s and mean zero-crossing period T_z describes one single sea state whereas the numbers in the cells represent the actual counts of this particular condition. By relating the number of measurements to the total number of observation in the lower right corner in Fig. 2.23 the relative occurrence, the relative frequency and the probability for that one specific sea state can be computed [8].

Signifikant	Medelperiod, Tz, [s]																Alla
våghöjd, [m]	<2	2-2.5	2.5-3	3-3.5	3.5-4	4-4.5	4.5-5	5-5.5	5.5-6	6-6.5	6.5-7	7-7.5	7.5-8	8-8.5	8.5-9	>9	perioder
6.2													1				1
6												2					2
5.8												4					4
5.6												4	1				5
5.4											2	11					13
5.2											5	8					13
5											14	5	1				20
4.8										1	14	4		1			20
4.6										4	19						23
4.4										14	17	1					32
4.2										29	17	1					47
4									1	43	14	1					59
3.8									14	60	7						81
3.6									38	56	5						99
3.4								2	79	45							126
3.2								7	123	29	1						160
3								48	149	9							206
2.8							6	150	180	16							352
2.6							14	311	96	4							425
2.4						1	75	397	62	2							537
2.2						1	317	393	42	0							753
2						33	642	253	32	5							965
1.8						207	725	138	15	5							1090
1.6					7	711	542	92	10	1							1363
1.4				1	148	1217	379	61	15	4							1825
1.2				3	852	1075	269	46	5	0							2250
1				172	1534	728	158	29	6	0							2627
0.8			6	939	1345	472	111	16	1	0							2890
0.6			270	1489	1037	377	72	6	0	4		1					3256
0.4		45	708	1067	770	263	50	17	14	5	3	3	3	1			2949
0.2	1	98	315	435	328	213	104	48	42	9	3		1			3	1600
Alla våghöjder	1	143	1299	4106	6021	5298	3464	2014	924	345	121	45	7	2	0	3	23793

Fig. 2.23: Wave statistics at a particular area in the Baltic Sea (Öland Södra grund, SSPA 1982) [8]

By means of various measurements and researches the energy spectrum has been generalised to define the energy distribution for any combination of significant wave height and mean zero-crossing period. However, before those wave spectra shall be discussed more thoroughly in 2.5.2, it is important to concentrate on probability theory and analysing stochastic processes. The following paragraph shall present common tools to conceive wave data and their corresponding distribution as well as handle samples to obtain essential statistical measures such as variance or standard deviation.

2.5.1 Statistical analysis and data processing

A time record of an irregular wave which should outlast at least *100* times the longest wave period [6] is briefly discussed in 2.1 with respect to mean or significant values for the wave height or period. Usually, a large number of sample oscillations of the water surface N within the record is extracted equally spaced in time intervals Δt over an entire duration between *30.0* minutes up to a couple of hours. According to [16] this short-term description of the sea ensures a reliable picture of this stationary random process if any impairment induced by tidal changes can be disregarded in advance. In order to obtain a clear description of the surface elevation it is necessary to refer all measured oscillations to a specific still water level which can be defined by the average level of the N samples relative to some randomly set reference [6].

The standard deviation σ is seen as an essential tool to work with a large number of statistical data and "defined as the square root of the variance which in turn can be calculated as the squares of the samples averaged over the number of samples" according to *Rosén (2011)* [8].

$$\sigma = \sqrt{\frac{1}{N-1} \cdot \sum_{n=1}^{N} \eta_n^2} \tag{2.84}$$

The expression in (2.84) also denotes the so-called root mean square value (*RMS*) of the instantaneous surface elevations but not the wave height from maximum to minimum deflection. This yields the following relationships for significant wave amplitude $\eta_{a,s}$ and wave height H_s [6].

$$\eta_{a,s} = 2 \cdot \sigma \tag{2.85}$$

$$H_{a,s} = 4 \cdot \sigma \tag{2.86}$$

It is assumed that all values within the series of water levels possess a zero mean value and thus can normally be analysed in form of a *Gaussian* distribution in (2.87) where x is an arbitrarily chosen input value.

$$f(x) = \frac{1}{\sigma\sqrt{2\pi}} \cdot exp\left\{-\left(\frac{x}{\sigma\sqrt{2\pi}}\right)^2\right\} \tag{2.87}$$

With the above it is possible to determine the probability that the surface elevation turns out to be greater than a specifically indicated value *a* by integrating the area under the *Gaussian* distribution to the right of the set threshold [6].

$$P\{\eta > a\} = \int_a^{\infty} f(x) \cdot dx \tag{2.88}$$

The wave amplitude can also be further assessed if the sea or the swell meets the previously mentioned requirement that the data lie within a relatively narrow frequency band. Together with the *Gaussian* distribution of the free surface elevation the wave amplitude can be subject to a *Rayleigh* compilation in (2.89). This again provides access to probabilities that the wave amplitude exceeds a certain boundary, expressed in the following integral (2.90) [6].

$$f(x) = \frac{x}{\sigma^2} \cdot exp\left\{-\left(\frac{x}{\sigma\sqrt{2}}\right)^2\right\} \tag{2.89}$$

$$P\{\eta_a > a\} = \int_a^{\infty} f(x) \cdot dx = exp\left\{-\frac{a^2}{2\sigma^2}\right\} \tag{2.90}$$

Concerning a more engineering or design perspective the *Rayleigh* distribution can be applied to the actual wave height, so the distance between crest to trough in (2.91). If for example the maximum wave height induced by a storm is of great interest, *Journeé et al. (2001)* [6] introduces a rule of thumb which defines the maximum wave height "that will be exceeded (on the average) once in every 1000 (storm) waves". According to [6] it can generally be said that it takes at least three hours for this amount of samples to be recorded, resulting in the maximum expected wave height H_{max} in this three hours tempest.

$$P\{H > a\} = exp\left\{-2\left(\frac{H}{H_S}\right)^2\right\} \tag{2.91}$$

$$exp\left\{-2\left(\frac{H_{max}}{H_S}\right)^2\right\} = \frac{1}{1000} \approx H_{max} \approx 1.86 \cdot H_s \tag{2.92}$$

2.5.2 Wave spectra

Due to the superposition of regular wave components the frequency characteristics of an irregular sea state become quite important with respect to the application of the *Fourier* series analysis which considerably simplifies the reproduction of a measured time record. Referring to the general expression of the irregular wave in (2.81) this decomposing approach at one location can provide a set of values for the wave amplitude $\eta_{a,j}$ and the phase angle ε_j related to a certain angular frequency ω_j. The associated wave number k_j can be obtained by using the *dispersion relationship*. However, according to [6] a precise description of the water level at some time is not of great importance and the main focus shall be put on the frequency and amplitude as those statistical evidences can be used to develop energy density spectra. On the condition of a *Gaussian* and *Rayleigh* distribution the amplitudes $\eta_{a,j}$ can be determined by the *Fourier* analysis of the oscillation, although they constantly would change for each new time step. But a mean square value of $\eta_{a,j}$ can be produced which would not vary much with frequency, resulting in a continuous function of $\overline{\eta_a^2}$ according to [6]. The variance of this input data in (2.93) can then be related solely to the wave amplitude components which are eventually summarised in the so called wave energy spectrum $S_\eta(\omega)$ in (2.94) if $\Delta\omega$ approaches zero in Fig. 2.24 [6]. The standard deviation in (2.95) can then readily be attained by the area under the spectral curve.

$$\begin{aligned}\sigma_\eta^2 = \overline{\eta^2} &= \frac{1}{N}\cdot\sum_{n=1}^{N}\eta_n^2 = \frac{1}{N\cdot\Delta t}\cdot\sum_{n=1}^{N}\eta_n^2\cdot\Delta t \\ &= \frac{1}{N\cdot\Delta t}\int_0^{N\cdot\Delta t}\left\{\sum_{j=1}^{N}\eta_{a,j}\cdot\cos\left(\mathrm{k_j x}-\omega_\mathrm{j} t+\varepsilon_\mathrm{j}\right)\right\}^2\cdot dt \\ &= \sum_{j=1}^{N}\frac{1}{2}\eta_{\mathrm{a,n}}^2\end{aligned} \tag{2.93}$$

$$S_\eta(\omega_j)\cdot d\omega = \frac{1}{2}\eta_{\mathrm{a,n}}^2 \tag{2.94}$$

$$\sigma_\eta^2 = \sqrt{\int_0^\infty S_\eta(\omega)\cdot d\omega} \tag{2.95}$$

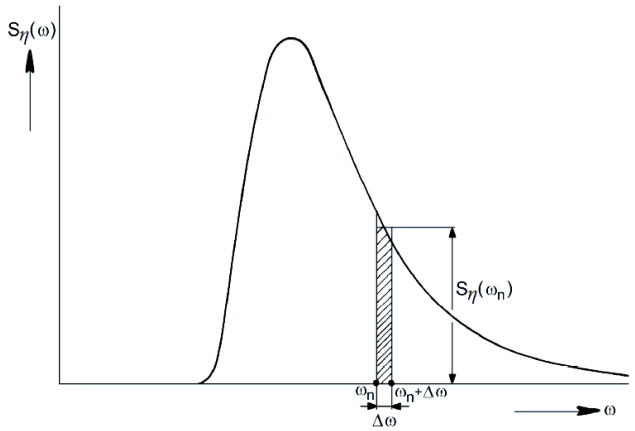

Fig. 2.24: Definition of spectral density [6]

The definition of the wave spectrum shall be illustrated in the Fig. 2.25 where the irregular wave is recorded in the time domain and eventually broken up in a number of regular wave components, including their associated frequencies, amplitudes and phase angles by means of *Fourier* series analysis. With this information the wave energy spectrum in (2.94) for each frequency step can be computed and displayed vertically in the frequency domain [6].

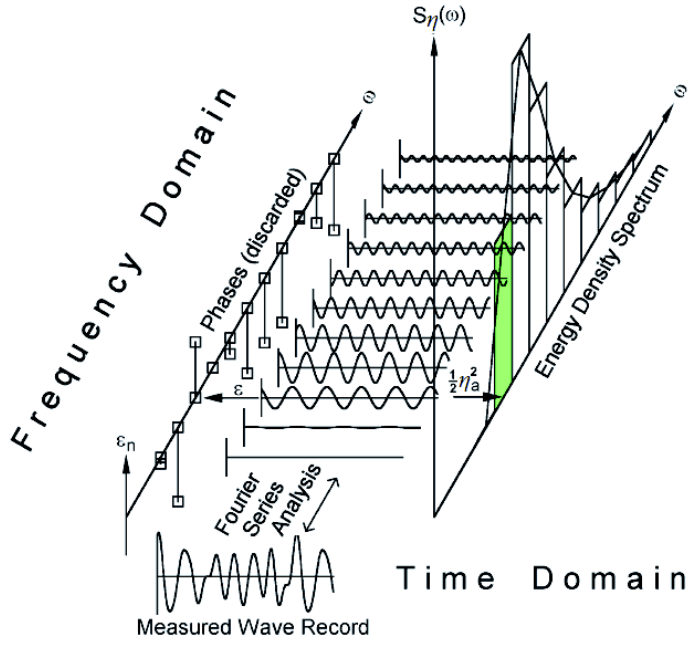

Fig. 2.25: Wave record analysis according to [6]

This complete record analysis and the corresponding probabilistic evaluation of wave measurements in form of wave spectra allows a convenient procedure to base the entire design solely on wave height and period. This is simply achieved by determining the moments of the area under the spectrum related to $\omega = 0$. According to (2.96) $m_{0\eta}$ constitutes the area under the spectrum, $m_{1\eta}$ the first order moment or static moment and $m_{2\eta}$ the second order or inertia moment of this area [6].

$$m_n, \eta = \int_0^\infty \omega^n \cdot S_\eta(\omega) \cdot d\omega \tag{2.96}$$

Since the standard deviation or *RMS* of the surface elevation consequently equals the square root of the area under the spectral curve, several statistical relationships can now be withdrawn such as significant wave amplitude or height but also the mean centroid wave period T_1 and the mean zero-crossing wave period T_2, previously termed as T_z.

$$\eta_{a,s} = 2 \cdot \sqrt{m_{0\eta}} \tag{2.97}$$

$$H_{a,s} = 4 \cdot \sqrt{m_{0\eta}} \tag{2.98}$$

$$T_1 = 2\pi \cdot \frac{m_{0\eta}}{m_{1\eta}} \tag{2.99}$$

$$T_2 = T_z = 2\pi \cdot \frac{m_{0\eta}}{m_{2\eta}} \tag{2.100}$$

With respect to the above described advantages of a wave spectrum researchers have put a lot of emphasise on general energy spectra to describe the energy distribution for any sea state. The main idea of those normalized uni-directional wave energy spectra is to let them simply depend on the significant wave height H_s and any average value of the wave period such as T_1 or T_2 [6].

$$S_{\eta(\omega)} = H_s^2 \cdot f(\omega, \bar{T}) \tag{2.101}$$

Nowadays, two different methods prevail whereas the *Bretschneider* approach in (2.102) [6] rather concentrates on the energy distribution for a fully developed sea state in the open sea. Here, the wind speed and direction are generally considered to be constant over several hours [8].

$$S_{\eta(\omega)} = \frac{173 \cdot H_s^2}{T_1^4} \cdot \omega^{-5} \cdot exp\left\{\frac{-692}{T_1^4} \cdot \omega^{-4}\right\} \tag{2.102}$$

For fetch-limited or coastal wind-induced seas [6] recommends the implementation of the *JONSWAP* wave spectrum in (2.103) which requires the peak period T_p and eventually yields a more distinct peak compared to the *Bretschneider* spectrum in Fig. 2.26.

$$S_{\eta(\omega)} = \frac{320 \cdot H_S^2}{T_p^4} \cdot \omega^{-5} \cdot exp\left\{\frac{-1950}{T_p^4} \cdot \omega^{-4}\right\} \cdot \gamma^A \qquad (2.103)$$

where:

γ = peakedness factor as a function of T_p and T_z according to [14]

A = $\exp\left\{-\left(\frac{\frac{\omega}{\omega_p}-1}{\sigma\sqrt{2}}\right)^2\right\}$

ω_p = angular frequency at spectral peak

σ = step function of ω ($\omega < \omega_p \rightarrow \sigma = 0.07$; $\omega > \omega_p \rightarrow \sigma = 0.09$)

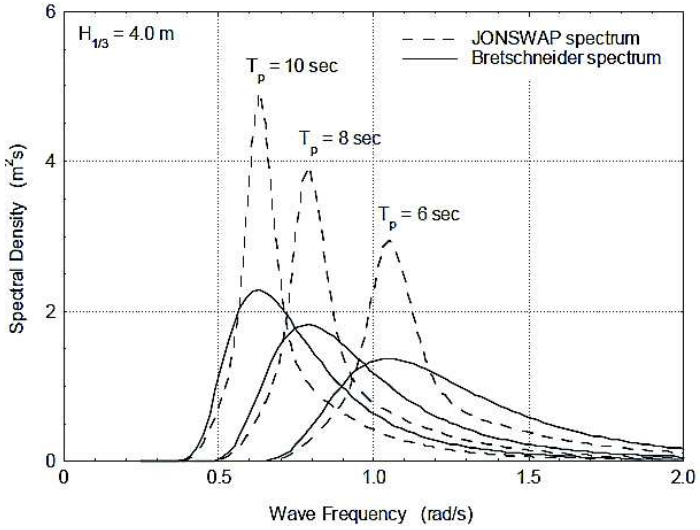

Fig. 2.26: Comparison of Bretschneider and JONSWAP wave spectra for various peak periods [6]

Since monopiles are located in shallow waters and thus closer to the shore, the *JONSWAP* wave spectrum shall be applied for the subsequent simulation of an irregular sea state in 2.5.4.

2.5.3 Transformation to time series

The previously presented statistical processing in form of *Fourier* series analysis and spectrum generation describes the transformation of the irregular wave from the time domain to the frequency domain. But applying a known or generic wave spectrum the irregular wave can be artificially simulated from the frequency domain to the time domain, introducing the inverse problem in wave statistics and availing oneself of the superposition principle [8]. According to *Journeé et al. (2001)* [6] "there is no real need to reproduce the input time record exactly; what is needed is a record which is only statistically indistinguishable from the original signal". So the bottom line is that both the original and the computed wave record should only have the same energy distribution and thus rely solely on the wave amplitude $\eta_{a,j}$ and wave number k_j for each chosen angular frequency ω_j. In case of an equally spaced arrangement of frequency intervals $\Delta\omega$ the wave amplitudes $\eta_{a,j}$ of each regular wave component can be related to the area under the associated segment of the wave spectrum [6].

$$\eta_{a,j} = 2 \cdot \sqrt{S_\eta(\omega) \cdot \Delta\omega} \tag{2.104}$$

Again, the wave number k_j is a function of the angular frequency ω_j and is covered by the *dispersion relationship*. So the only missing part for this transformation to time series involves a new definition of the phase angle ε_j. Here, it is necessary to let the phase angle vary randomly over a range between $0 \leq \varepsilon_j < 2\pi$ as a "statistically identical but in detail different time record" [6] of the irregular wave is anticipated. The differences in the phase angles can be perceived in the below stated illustration of wave record analysis and regeneration in Fig. 2.27.

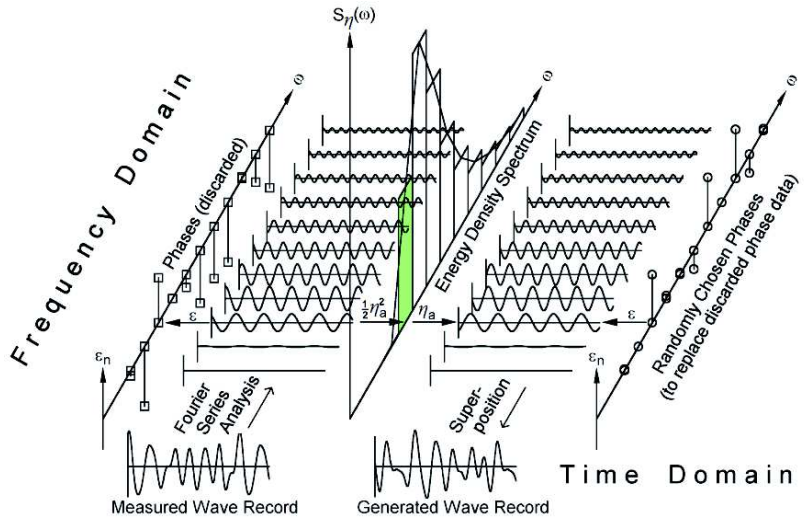

Fig. 2.27: Complete picture of wave data processing and subsequent simulation of irregular sea states [6]

2.5.4 Realisation of an irregular sea state

The realisation and reproduction of a linear irregular sea state constitute the most fundamental groundwork in the design of fixed or floating offshore structures but also for the simulation of ship motions and its sea keeping abilities. The artificially reproduced irregular wave resembles the actual ocean surface most accurately and involves all major location specific properties of the area of application, including wave statistics and water depth. For the definition of wave loads on the monopile the irregular wave is implemented as a background sea state for any extreme case scenario with respect to fatigue life or ultimate strength assessment which shall be explained in more details in the upcoming chapters. On that account, the overall procedure is summarised in the subsequent flow chart in Fig. 2.28 and applied within *Matlab* to produce an irregular wave together with hydrodynamic pressure and wave kinematics.

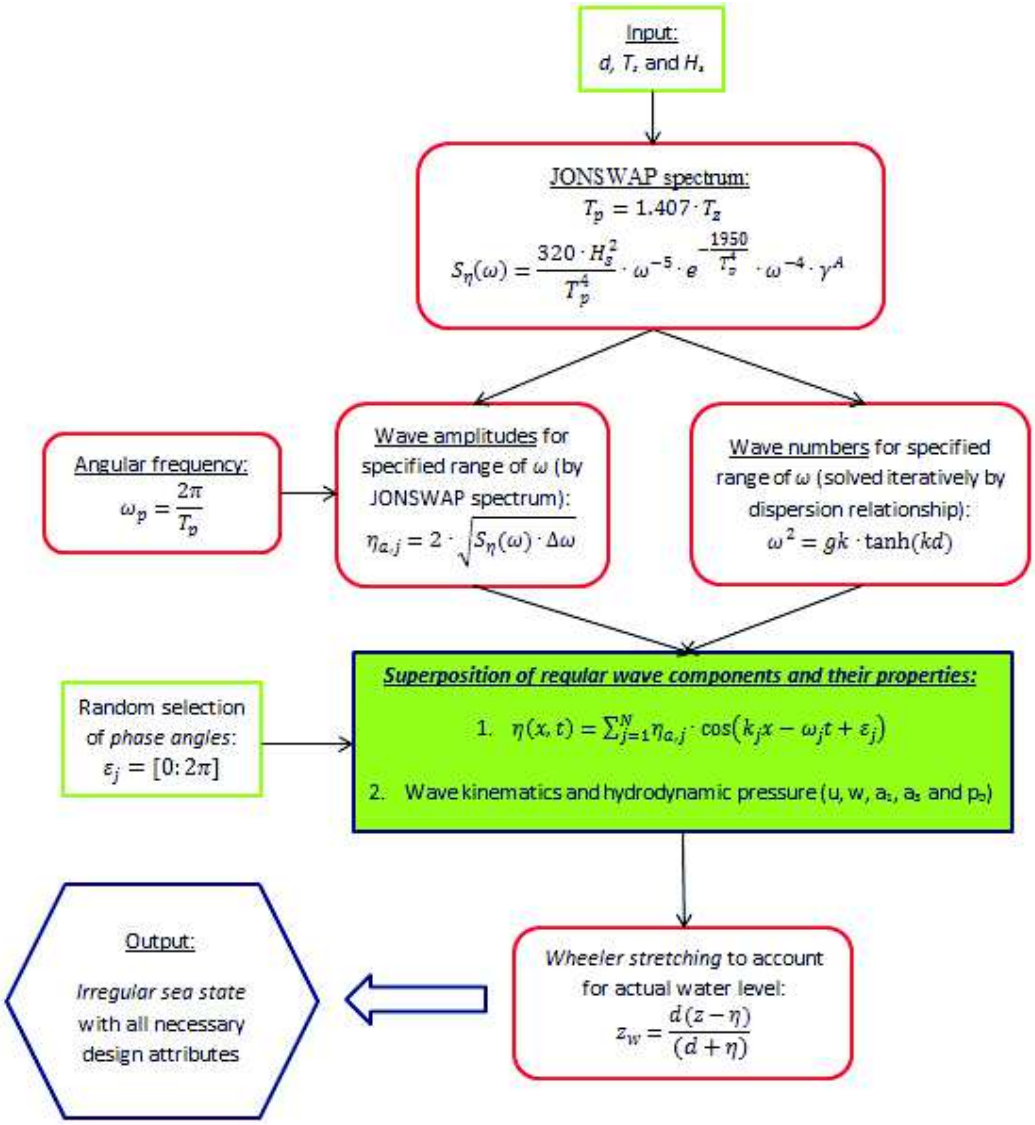

Fig. 2.28: Overview of realising an irregular wave

Implementing the example input parameters in Tab. 2.1, the following irregular wave in Fig. 2.29 can be generated according to the above presented scheme. A *JONSWAP* spectrum for coastal waters is used as the statistical background for this sea state which is compared to the *Bretschneider* approach in Fig. 2.30.

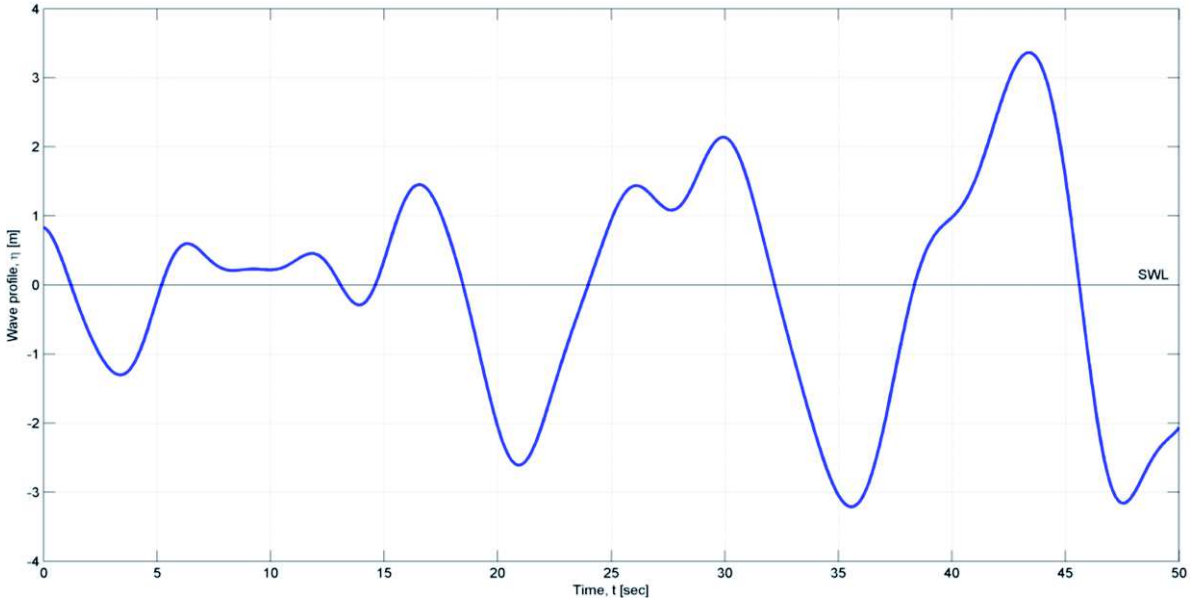

Fig. 2.29: Irregular wave as a sum of regular components

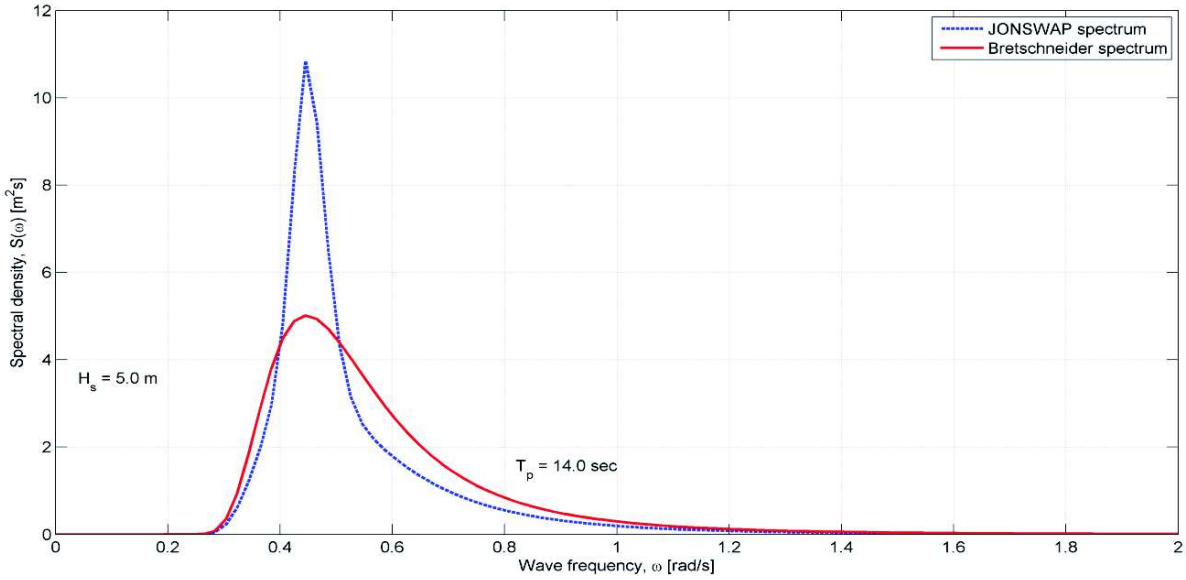

Fig. 2.30: Wave spectra for the generation of the example irregular wave

At this point a quick check of the process can be conducted as the area under the spectral curves can be related to the inputted significant wave height with reference to (2.98). Both energy distributions yield accurate results regarding $H_s = 5.0\ m$, as seen in Tab. 2.2.

Tab. 2.2: Check of wave spectra with respect to significant wave height

Input, Hs [m]	*JONSWAP, Hs [m]*	*Bretschneider, Hs [m]*
5.0	4.9975	4.9922

The main principle of an irregular wave is depicted in Fig. 2.31 where exemplarily four regular wave components are shown compared to the final superimposed surface elevation. The superposition of wave kinematics and hydrodynamic pressure is illustrated subsequently in Fig. 2.32 at *SWL*.

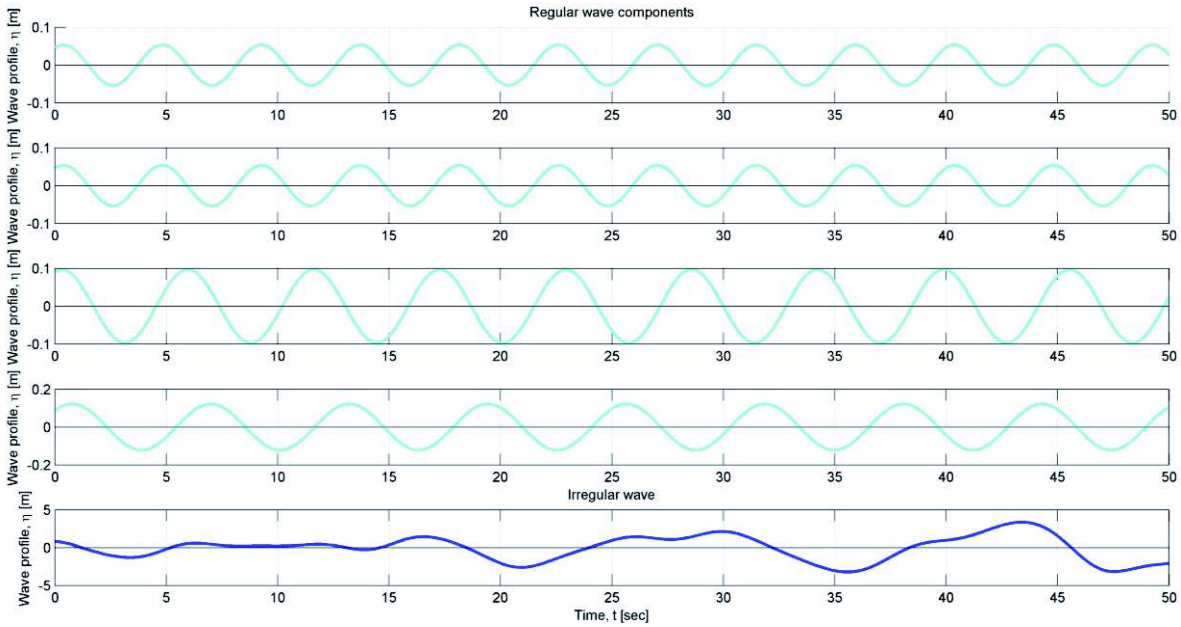

Fig. 2.31: Superposition theory of an irregular wave

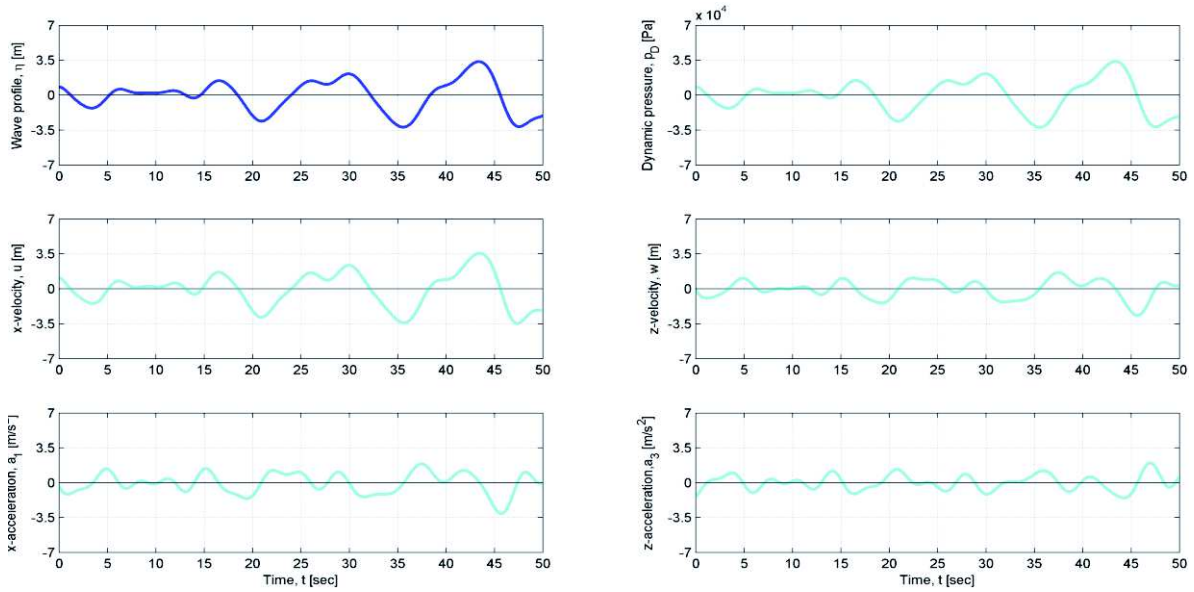

Fig. 2.32: Wave kinematics and hydrodynamic pressure of irregular wave at SWL

By looking closer for instance at the *x*-component velocity one is able to observe the same depth influences as for the regular wave theory discussed previously in 2.4.2. It is clearly visible in Fig. 2.33 how the velocity follows the surface elevation in the direction of propagation but as well how the velocity oscillations are reduced closer to the sea bed at *d = -10.0 m*.

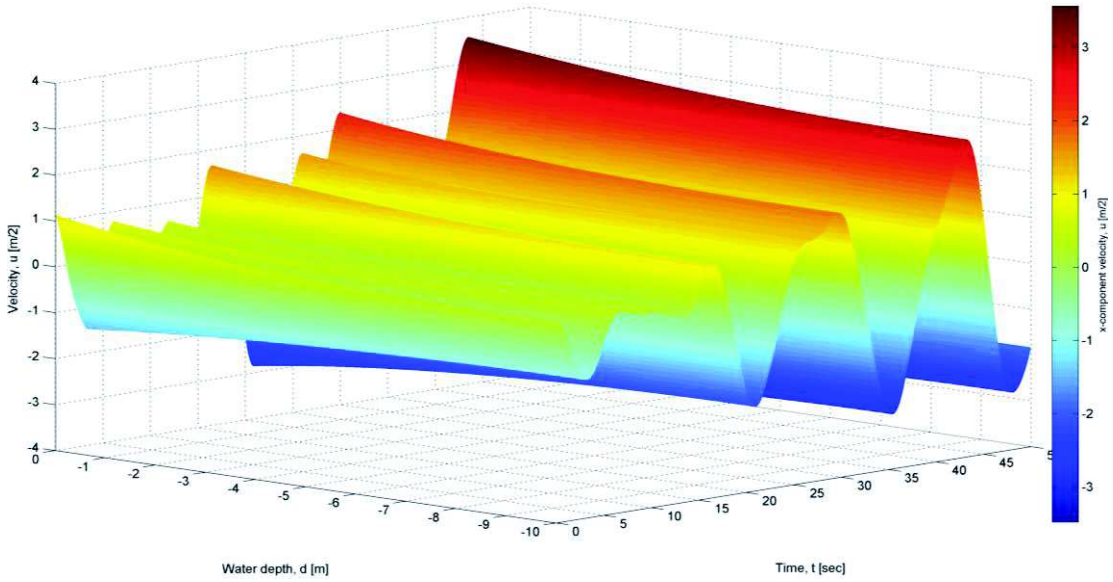

Fig. 2.33: Surface plot of x-component velocity of irregular wave

The final step before the wave kinematics can be deployed for determining wave loads is the implementation of the profile extension method. Again, the *Wheeler* procedure in Fig. 2.34 is performed which eventually results in the adjusted and now surface level dependent velocity and acceleration plots in Fig. 2.36 and Fig. 2.38, revealing the typical and expected water particle motion under wave crests or troughs respectively.

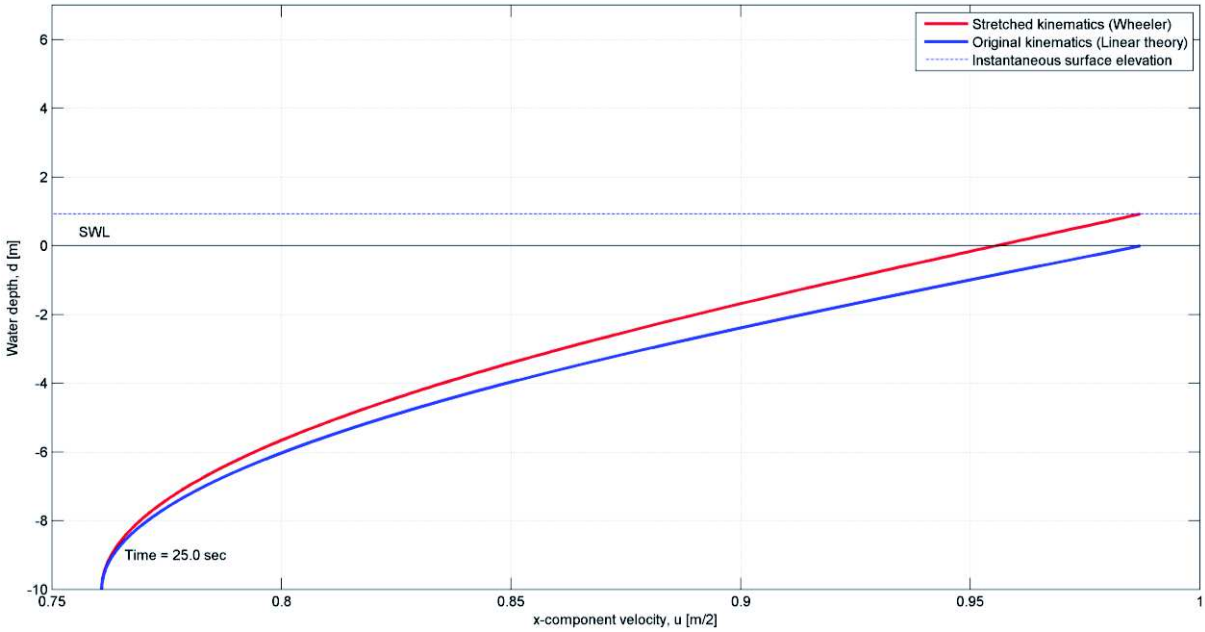

Fig. 2.34: Wheeler stretching for the correct irregular wave kinematics

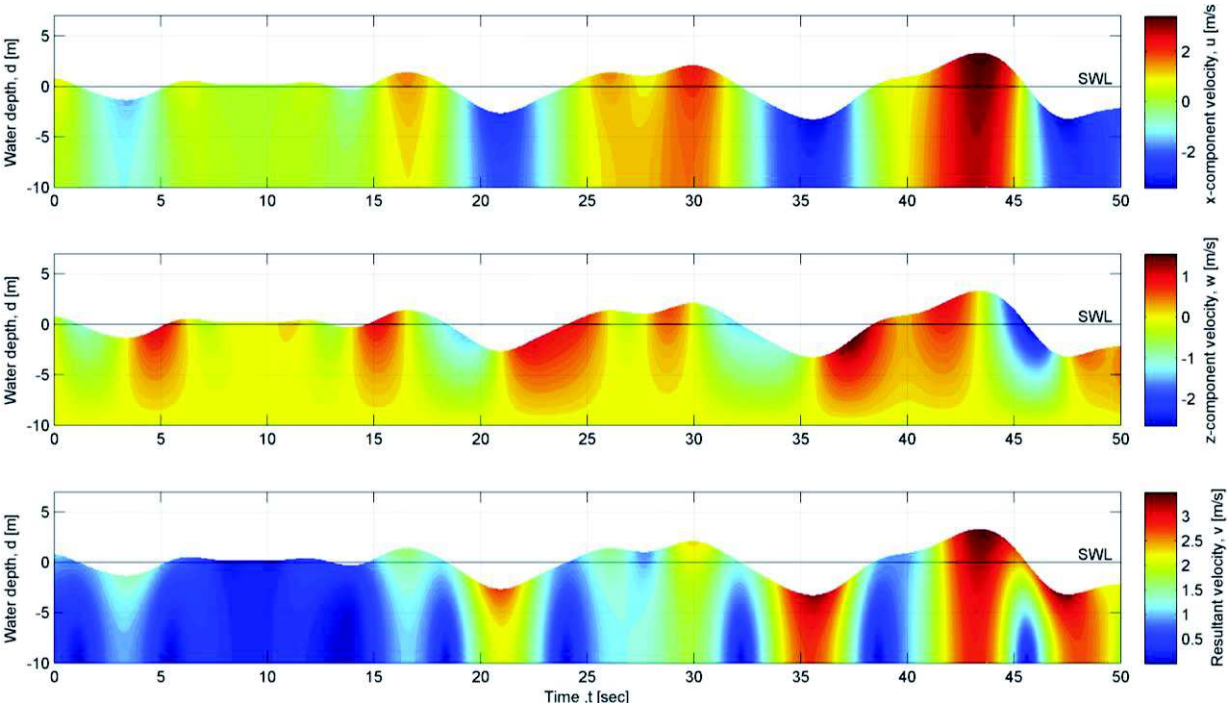

Fig. 2.35: Contour plot of water particle velocity

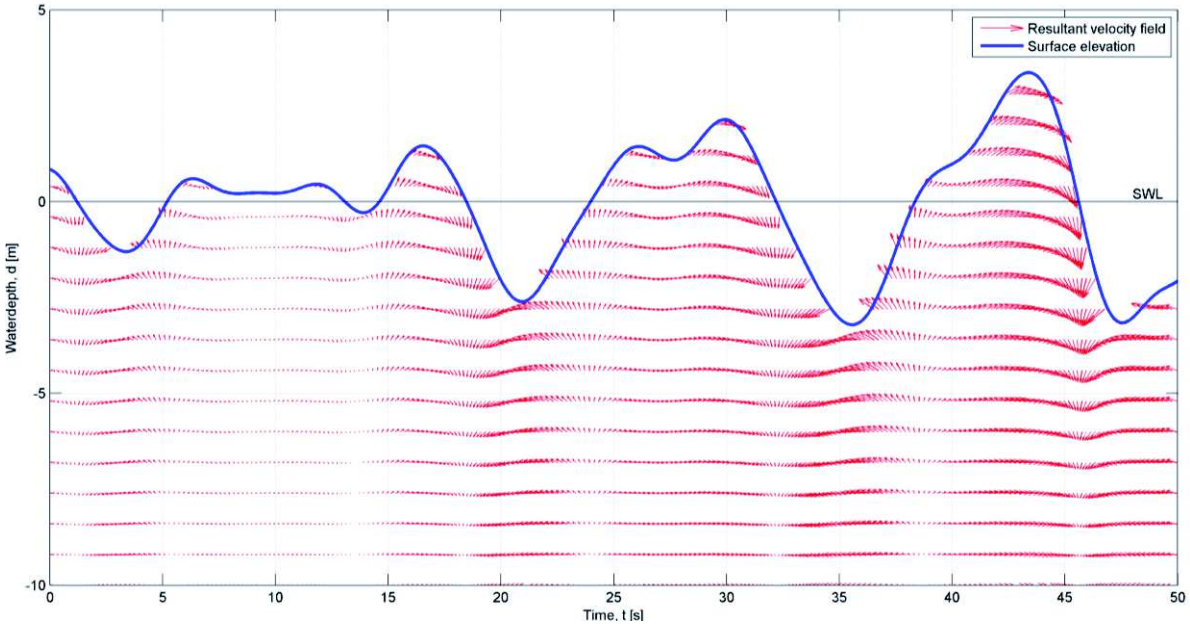

Fig. 2.36: Resultant velocity field under an irregular wave

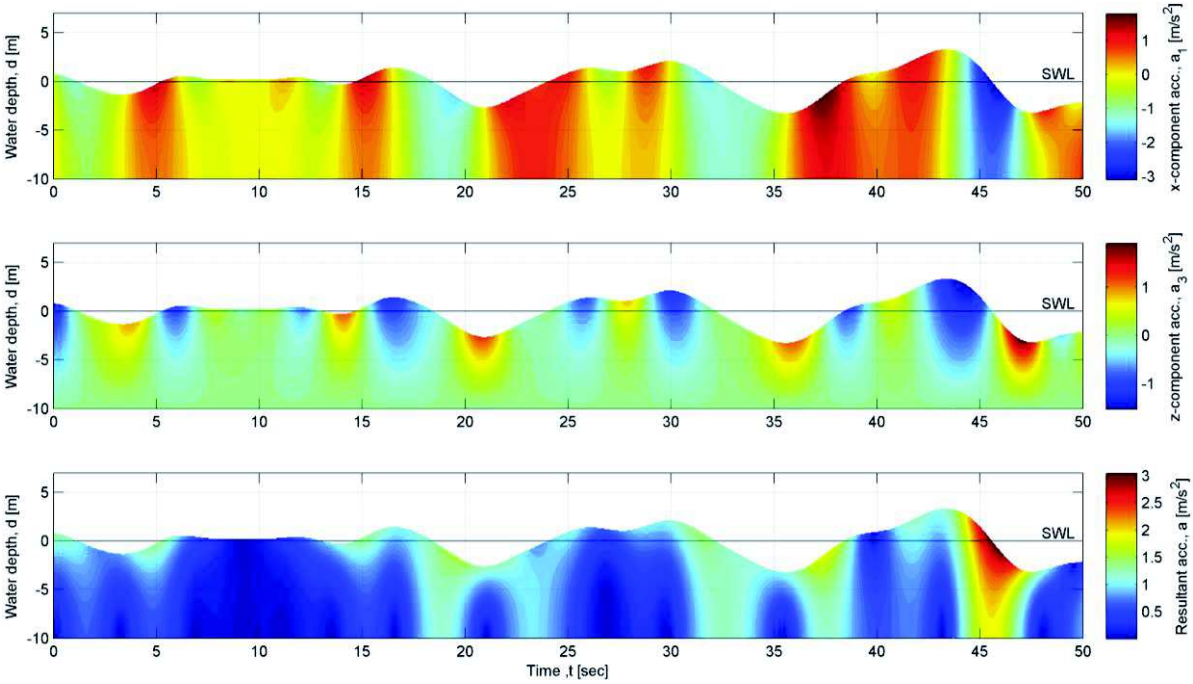

Fig. 2.37: Contour plot of water particle acceleration

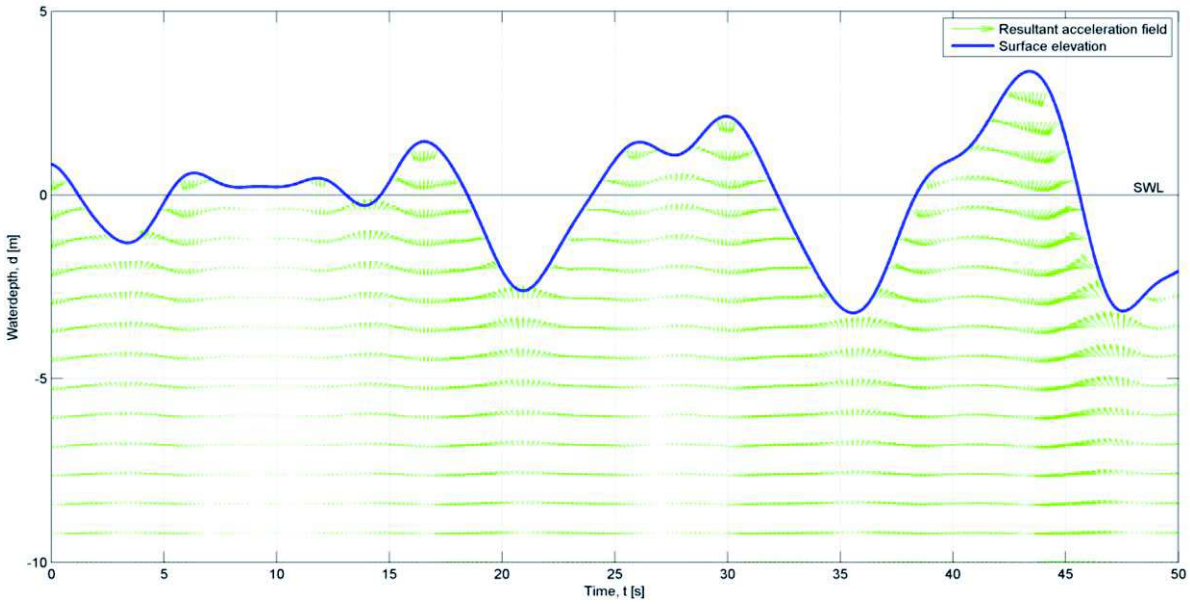

Fig. 2.38: Resultant acceleration field under an irregular wave

2.6 Non-linear wave theories

So far the wave theory requires a linearisation of the *free surface boundary condition* by simply neglecting all higher order terms as described in 2.4. But there are several approaches to include those non-linear contributions in the boundary conditions of the potential flow problem. On that account, wave height and the corresponding steepness can still be small but no longer infinitesimal, representing more realistic waves of finite height. Compared to the small amplitude theory non-linear waves have a more severe impact on its own properties for example in case of third orders the wave propagation speed is not only affected by the water depth but also by the wave height, as seen in (2.123). A more pronounced difference is noticeable by examining the surface elevation, as illustrated in Fig. 2.39 for small amplitude and non-linear waves. Here, the asymmetric shape of the wave around *SWL* is clearly visible as the crest is higher and shorter whereas the trough is less deep and longer. This, of course, has also a considerable impact on wave kinematics as the water particle trajectory does not follow a closed elliptic form any more [12].

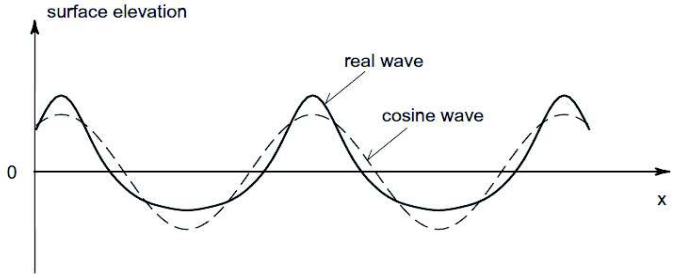

Fig. 2.39: Comparison of a linear and non-linear wave [13]

The *Stokes'* wave theory and the stream function wave are seen as the two most commonly applied non-linear wave simulations which shall be presented in the following. There are additional solutions if for instance the wave length turns out to be much larger than the water depth. In this case, the *Stokes'* application is rather limited and it is recommended to consider long wave definitions, denoted as *cnoidal wave theories*. This wave type changes to the rather simple and so-called *solitary wave* if infinitely long wave length and period are assumed. However, this scenario and the general form of the *cnoidal* oscillation shall not be discussed further because it cannot be implemented for an irregular sea state nor is it classified as an extreme case for the monopile design. It is important to say that all the above mentioned solutions obey the fundamentals of *perturbation methods* and increase in difficulty with higher order of approximation [12].

2.6.1 *Stokes'* finite amplitude waves

In order to include non-linear terms relating wave height and length in the *kinematic boundary conditions Stokes'* main idea implies a series expansion of all important wave characteristics such as surface elevation, kinematics and dynamic pressure, following the principle in (2.105) and (2.106) with the order of magnitude o of the expression in the parenthesis [13]. Using the example of the velocity potential ϕ the second term ϕ_2 can be seen as a correction to the first expression ϕ_1 due to non-linear contributions [12].

$$\phi = \phi_1 + \phi_2 + \phi_i + \cdots \tag{2.105}$$

$$o\left(\phi^{(i+1)}\right) = o\left(\phi^{(i)} \cdot \frac{H}{L}\right) = o\left(\phi^{(i-1)} \cdot \left(\frac{H}{L}\right)^2\right) = \cdots = o\left(\phi^{(i-1)} \cdot \left(\frac{H}{L}\right)^2\right) \tag{2.106}$$

If those series of order i are implemented in the *Laplace equation* in (2.48) and the boundary conditions in 2.3.3, non-linear terms can be solved by applying results from the previous lower order. According to *Brorsen (2007)* [13] this procedure implies that "all terms having a factor $(H/L)^n$ (where $n \geq i$) on their order of magnitude" are discarded. Taking equation (2.106) i-th terms are considered in (2.105) in a *Stokes'* theory of i-th order whereas the first contribution always refers to the results obtained by linear or first order theory [13]. Through this approach it is possible to satisfactorily estimate the non-linearities so that even higher order solutions can be computed exactly. In principle, waves of finite height always include a linear proportion which yields the mathematical basis to account for the additional and non-linear steepness dependency of the wave. The *Stokes'* second order shall be explained in more details and outputs of a

fifth order wave shall be provided for comparison reasons [12]. Due to the asymmetric oscillation of the free water surface about *SWL* the wave height must be adjusted accordingly, as in (2.107) [13].

$$H = \eta_{max} - \eta_{min} \tag{2.107}$$

According to [12] the *dispersion relation* is not affected by the second order approximation, yielding the same phase velocity, wave length, wave number and phase angle as found for small amplitude waves. As wave celerity and length remain independent of the wave height, the second order approach is readily applicable [5]. In contrary to higher order solutions, the wave height of the linear term and the non-linear expression do not differ and thus is twice the amplitude of the first order part [12]. *Stokes'* second order wave can be derived as follows, starting with (2.108) and (2.109) [13].

$$\phi = \phi_1 + \phi_2 \tag{2.108}$$

$$\eta = \eta_1 + \eta_2 \tag{2.109}$$

As the linear contribution ϕ_1 is already known from 2.4, the remaining velocity potential ϕ_2 is obtained by solving the partial differential equations *(PDE)* with the given constraints whereas the undefined surface elevation is treated by a *Taylor* series expansion at $z = 0.0$ of the *dynamic* and *kinematic boundary conditions* which is exemplified in (2.110). But now only quantities with an order of $o((H/L))^2$ times the leading terms shall be erased [13].

$$\left(\frac{\partial \phi}{\partial z} - \frac{\partial \eta}{\partial t} - \frac{\partial \phi}{\partial x}\frac{\partial \eta}{\partial x}\right)_{z=0} + \eta \frac{\partial}{\partial z}\left(\frac{\partial \phi}{\partial z} - \frac{\partial \eta}{\partial t} - \frac{\partial \phi}{\partial x}\frac{\partial \eta}{\partial x}\right)_{z=0} + \cdots = 0 \tag{2.110}$$

If the *Taylor* series expansion of the boundary conditions are applied to the superposition equations in (2.108) and (2.109) and neglecting all small terms, the second order term ϕ_2 can be dissolved, resulting in the combined boundary condition in (2.111) at $z = 0.0$ and in Fig. 2.40 [13].

$$\frac{\partial \phi^{(2)}}{\partial z} + \frac{1}{g}\frac{\partial^2 \phi^{(2)}}{\partial t^2} = -\frac{3}{4k} \cdot (kh)^2 \cdot \frac{\sin[2(\omega t - kx)]}{\sinh(2kd)} \tag{2.111}$$

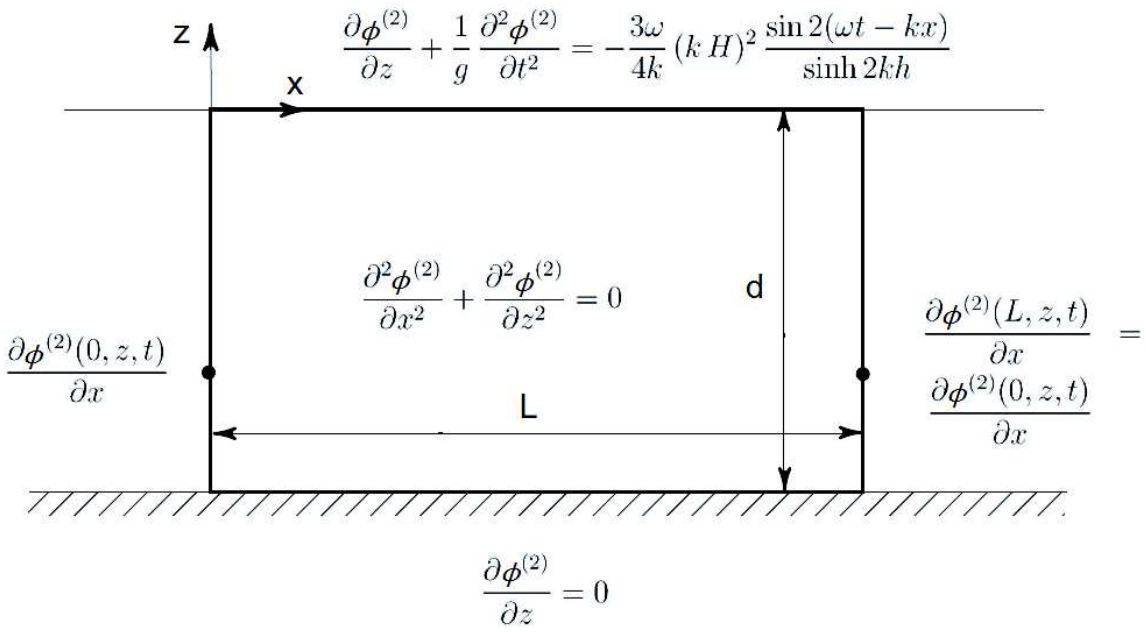

Fig. 2.40: Potential flow problem for 2nd order velocity component ϕ_2 [13]

After restructuring the above and with reference to [14] the following velocity potential in (2.112) can be attained. The wave profile, kinematics as well as dynamic pressure can be determined according to the regular approach by differentiating and including constraints.

$$\phi ST2 = \phi_1 + \frac{3}{8} \cdot \frac{\pi H}{kT} \cdot \frac{\pi H}{L} \frac{\cosh[2k(z+d)] \cdot \sin(2\theta)}{\sinh^4(kd)} \tag{2.112}$$

With respect to the surface elevation in (2.109) *Stokes'* second order solution constitutes a summation of a first order or linear result from 2.4.1 and the second order term in (2.113) [14]. According to [14] the *Stokes'* theory is "an expansion of the surface elevation in powers of the linear wave height *H*".

$$\eta_2 = \frac{\pi H^2}{8L} \cdot \frac{\cosh(kd)}{\sinh^3(kd)} \cdot [2 + \cosh(2kd)] \cdot \cos(2\theta) \tag{2.113}$$

By looking at the composition of the second order surface elevation in Fig. 2.41 one can perceive that the non-linear share describes an oscillation twice as fast the first part and that the wave crest and trough are both superimposed by $\Delta\eta$, reasoning the deviation in crest A_C and trough amplitude A_T [13].

$$\eta_{max} - \eta_{min} = \left(\frac{H}{2} + \Delta\eta\right) - \left(-\frac{H}{2} + \Delta\eta\right) = H \tag{2.114}$$

The asymmetry of a *Stokes'* second order wave is described by the amplitude difference between crest and trough in the scale of $1 + \pi H/2L$ [14], visualised in Fig. 2.41.

$$A_C = \eta(\theta = 0) = \frac{H}{2}\left(1 + \frac{\pi H}{2L}\right) \tag{2.115}$$

$$A_T = \eta(\theta = \pi) = \frac{H}{2}\left(1 - \frac{\pi H}{2L}\right) \tag{2.116}$$

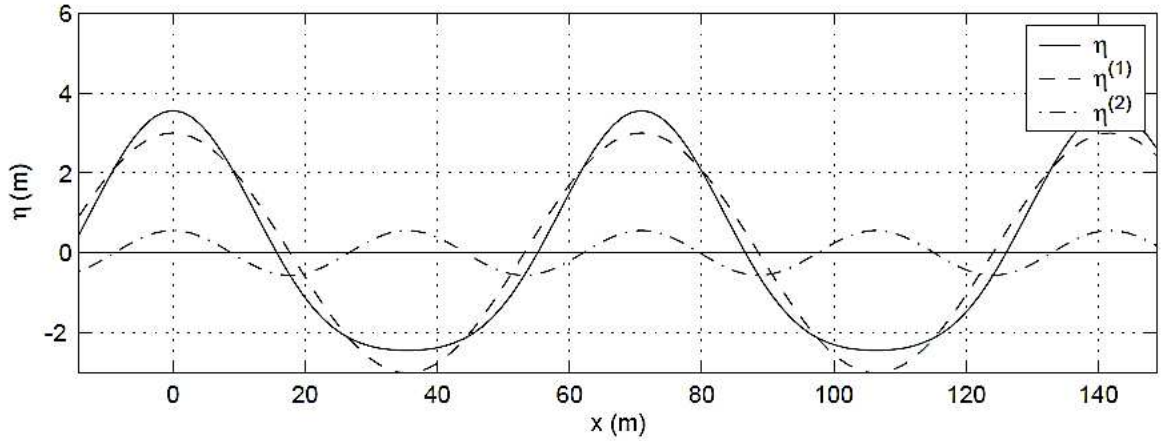

Fig. 2.41: Superposition of 1st and 2nd order surface elevation [13]

Since it is assumed that $\eta_2 << \eta_1$ and that η_2 is proportional to the first order amplitude times the steepness, *Svendsen et al. (1967)* [12] describes the development of a small secondary crest or local maximum in the wave trough if the second order amplitude exceeds one fourth of the linear amplitude. All *Stokes'* orders except the first one face this problem in shallow water *(d/L << 1)* as it is assumed that *o(d/L)* equals one in the evaluation of the individual orders [13]. As this singularity contradicts reality, the prerequisite in (2.117) is considered as the validity restriction of the *Stokes'* second order wave [12].

$$\eta_{a,2} = \frac{1}{4}\eta_{a,1} \tag{2.117}$$

By differentiating with respect to space and time the velocity potential in (2.112) together with the first order contribution yields the following expressions for the wave kinematics and hydrodynamic pressure of a *Stokes'* second order wave.

$$u = u_L + \frac{3}{4} \cdot \frac{\pi H}{T} \cdot \frac{\pi H}{L} \cdot \frac{\cosh[2k(z+d)]}{\sinh^4(kd)} \cdot \cos(2\theta) \tag{2.118}$$

$$w = w_L + \frac{3}{4} \cdot \frac{\pi H}{T} \cdot \frac{\pi H}{L} \cdot \frac{\sinh[2k(z+d)]}{\sinh^4(kd)} \cdot \sin(2\theta) \tag{2.119}$$

$$a_1 = a_{1,L} + \frac{3\pi^2 H}{T^2} \cdot \frac{\pi H}{L} \cdot \frac{\cosh[2k(z+d)]}{\sinh^4(kd)} \cdot \sin(2\theta) \tag{2.120}$$

$$a_3 = a_{3,L} - \frac{3\pi^2 H}{T^2} \cdot \frac{\pi H}{L} \cdot \frac{\sinh[2k(z+d)]}{\sinh^4(kd)} \cdot \cos(2\theta) \tag{2.121}$$

$$\begin{aligned} p_D = p_{D,L} &+ \frac{3}{4} \cdot \rho g H \cdot \frac{\pi H}{L \cdot sinh(2kd)} \cdot \left\{ \frac{\cosh[2k(z+d)]}{\sinh^2(kd)} - \frac{1}{3} \right\} \cdot \cos(2\theta) \\ &- \frac{1}{4} \cdot \rho g H \cdot \frac{\pi H}{L \cdot sinh(2kd)} \cdot \{\cosh[2k(z+d)] - 1\} \end{aligned} \tag{2.122}$$

Since the water particles do not follow a closed circle any more, they experience a gradual or so-called second order drift in the wave propagation. This drift or mass-transport velocity should not be disregarded in the further design. Again, the second order wave is quite susceptible to small water depths as the general condition $H/d << (kd)^2$ for $kd < 1$ pertains, rather recommending non-linear shallow wave theories under specific site conditions or higher orders [5].

If the order of a *Stokes'* wave increases one will ascertain a celerity dependency on the wave height which will complicate the implementation dramatically. For example a third order wave holds the following expression in (2.123) for the phase velocity c on the basis of zero mean *Eulerian* velocity which now depends on the wave height [5] [14].

$$c^2 = \frac{g}{k} \cdot \tanh(kd) \left\{ 1 + \left(\frac{kH}{2} \right)^2 \left[\frac{9 - 8\cosh^2(kd) + 8\cosh^4(kd)}{8\sinh^4(kd)} \right] \right\} \tag{2.123}$$

Comparing the wave celerity obtained by (2.123) to the results of the linear wave theory, one can clearly see the differences and the higher grade of complexity between linear and non-linear approaches in case of a constant wave period. The former is simply independent of the wave height while the latter includes the wave height in the determination of wave length and speed. On that account, the wave properties are reproduced more accurately as the wave becomes faster and longer with an increase in height with reference to Tab. 2.3.

Tab. 2.3: Comparison between linear and non-linear wave celerity

Wave celerity [m/s]	*Wave height [m]*	
	5.0	*7.0*
Linear	9.24	9.24
3rd order	10.38	11.79

Thus, a growing order number is always accompanied with a jump in effort and computational time, although there are several attempts to generalise higher order *Stokes'* wave. Here, *Skjelbreia and Hendrickson (1960)* [5] have elaborated a fifth order solution to the non-linear theory which is exerted frequently in engineering disciplines. According to [5] the velocity potential in (2.124) implies a superposition of five terms which eventually yields the wave profile in (2.125) in the same way together with the wave celerity in (2.126).

$$\frac{k\phi}{c} = \sum_{n=1}^{5} \phi'_n \cdot \cosh[n\,k(z+d)] \cdot \sin(n\theta) \tag{2.124}$$

$$k\eta = \sum_{n=1}^{5} \eta'_n \cdot \cos(n\theta) \tag{2.125}$$

$$c^2 = C_0^2(1 + \lambda^2 C_1 + \lambda^4 C_2) \tag{2.126}$$

The quantities ϕ'_n and η'_n rely on the parameter λ and the remaining coefficients A, B and C which shall all not be presented in details but can be found in [5]. Generally, they depend on the dimensionless form of kd whereas λ and k can be determined iteratively by means of the two following expressions.

$$\frac{1}{kd} \cdot [\lambda + B_{33}\lambda^3 + (B_{35} + B_{55}) \cdot \lambda^5] = \frac{H}{2d} \tag{2.127}$$

$$kd \cdot \tanh(kd) \cdot [1 + C_1\lambda^2 + C_2\lambda^4] = 4\pi^2 \frac{d}{gT^2} \tag{2.128}$$

So if the design wave can be clearly defined by wave height, period and water depth, equations (2.127) and (2.128) can be solved numerically to obtain λ and kd. Eventually, each value of ϕ'_n and η'_n can be derived and it is possible to determine wave kinematics and hydrodynamic pressure at any given point under a *Stokes'* fifth order wave [5].

With respect to the exemplary wave in Tab. 2.1 the depth sensitivity of the *Stokes'* second order wave is clearly visible as this rather shallow water of *10.0* metres causes the above mentioned singularity in form of a secondary crest in the wave trough. Hence, the water depth is increased to *20.0* metres to receive a reasonable picture of this wave type, as seen in Fig. 2.42. Furthermore, one can perceive how the asymmetric wave profile differs from the linear or small amplitude wave model, following $A_C > A_T$.

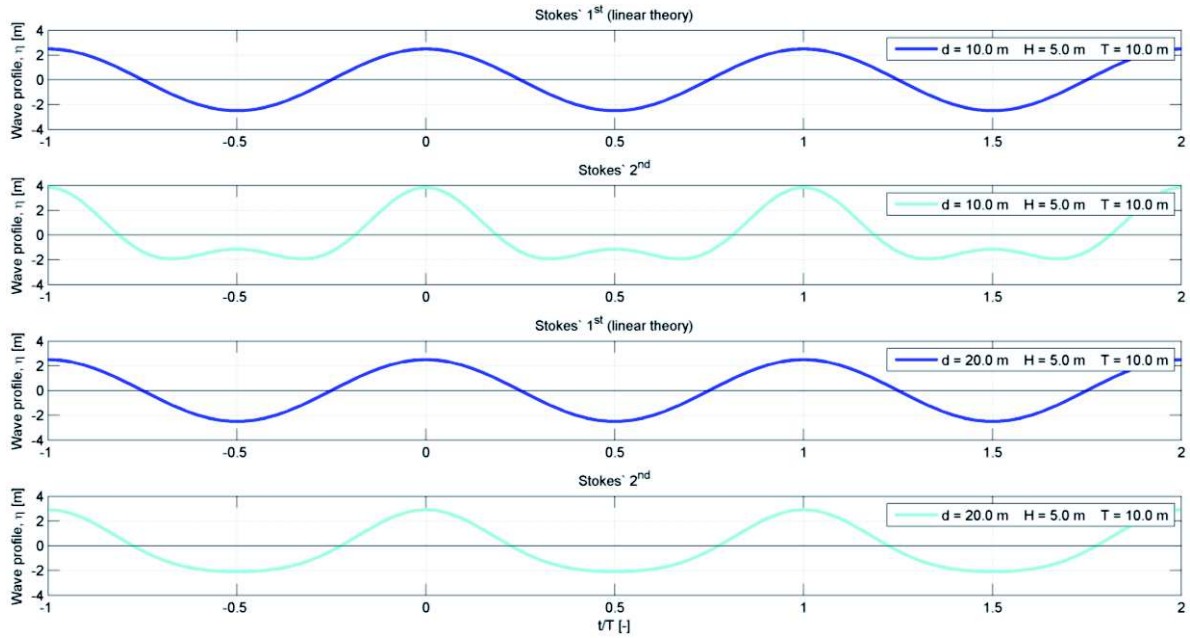

Fig. 2.42: Comparison of different water depths for Stokes' 1st and 2nd order waves

Since the exemplary wave is invalid for the *Stokes'* second order wave, the following wave kinematics and the hydrodynamic pressure shall refer to the deeper scenario with *d = 20.0 m*. Fig. 2.43 demonstrates the same correlation between velocity, acceleration, pressure and wave propagation at *SWL* as the linear wave in 2.4, but the influence on the wave properties of the more pronounced peak and stretched trough becomes obvious, in particular for the acceleration components.

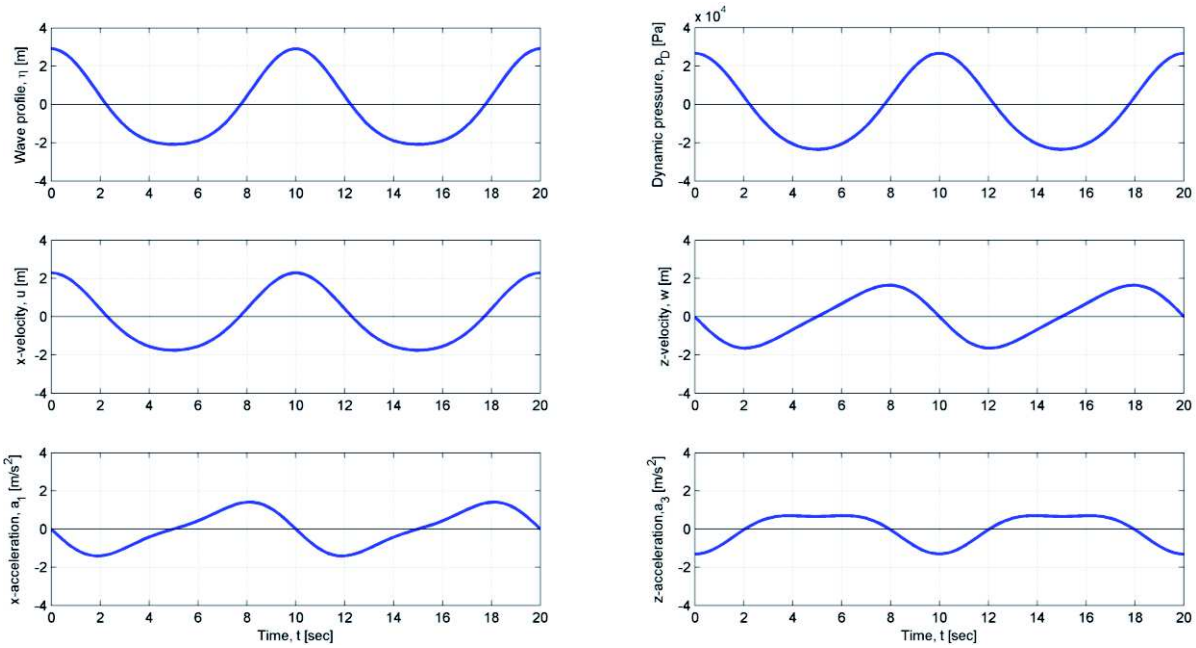

Fig. 2.43: Wave kinematics and hydrodynamic pressure for a Stokes' 2nd order wave

As previously mentioned, the non-linear wave obtained by *Stokes'* second order still requires an adjustment of wave kinematics and dynamic pressure to the instantaneous surface elevation. After *Wheeler* stretching the velocity and acceleration field is revealed in Fig. 2.44.

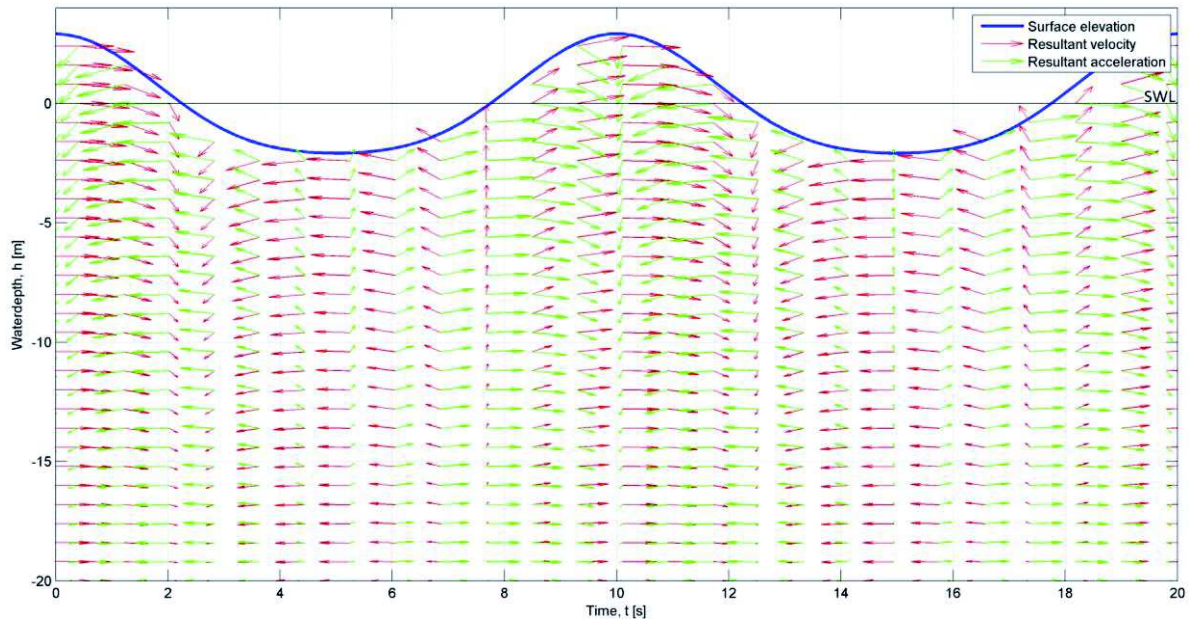

Fig. 2.44: Velocity and acceleration field under a Stokes' 2nd order wave

A fifth order solution is implemented in *Matlab* to investigate the advantageous of increasing the number of non-linear terms. In case of a sufficient water depth, as applied in the previous second order simulation, the higher order wave does not yield any differences, as displayed in Fig. 2.45.

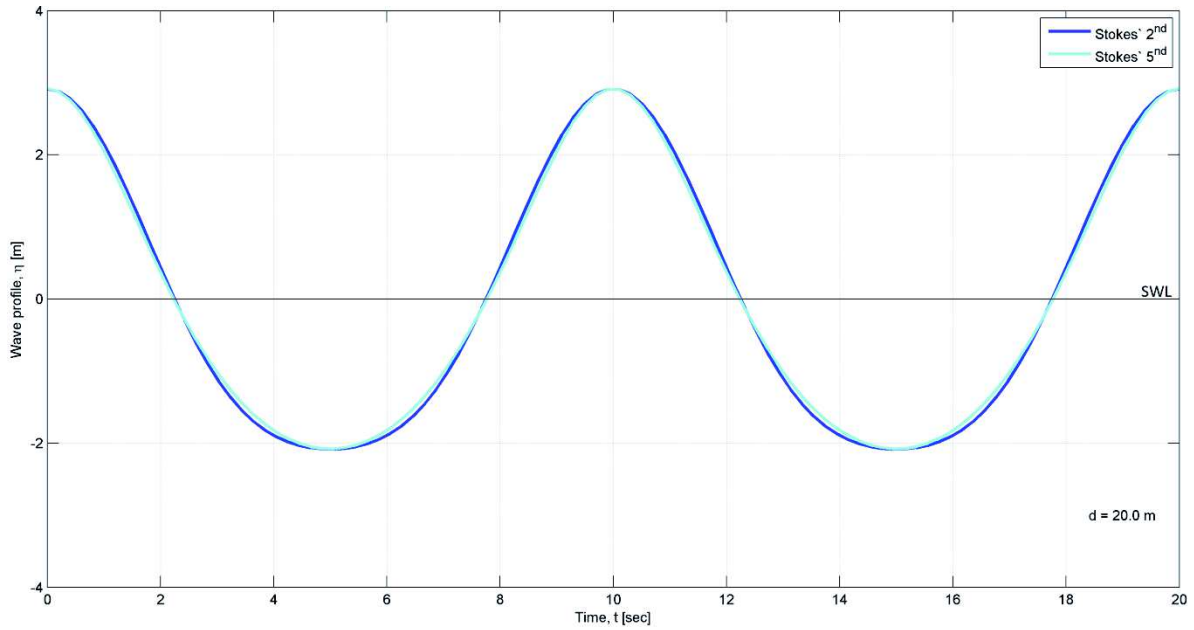

Fig. 2.45: Stokes' 2nd and 5th order wave in deeper water

But if one returns to the former exemplary linear wave in rather shallow water, one is able to see how higher terms in the *Stokes'* approach allow smaller water depths to get fairly accurate results. The same two waves, although for *d = 10.0 m*, are plotted in Fig. 2.46, where the deviations between orders are immense regarding the overall wave profile as well as shape of wave crest and trough. The second order output in Fig. 2.46 definitely exemplifies an incorrect and a non-recommendable wave simulation.

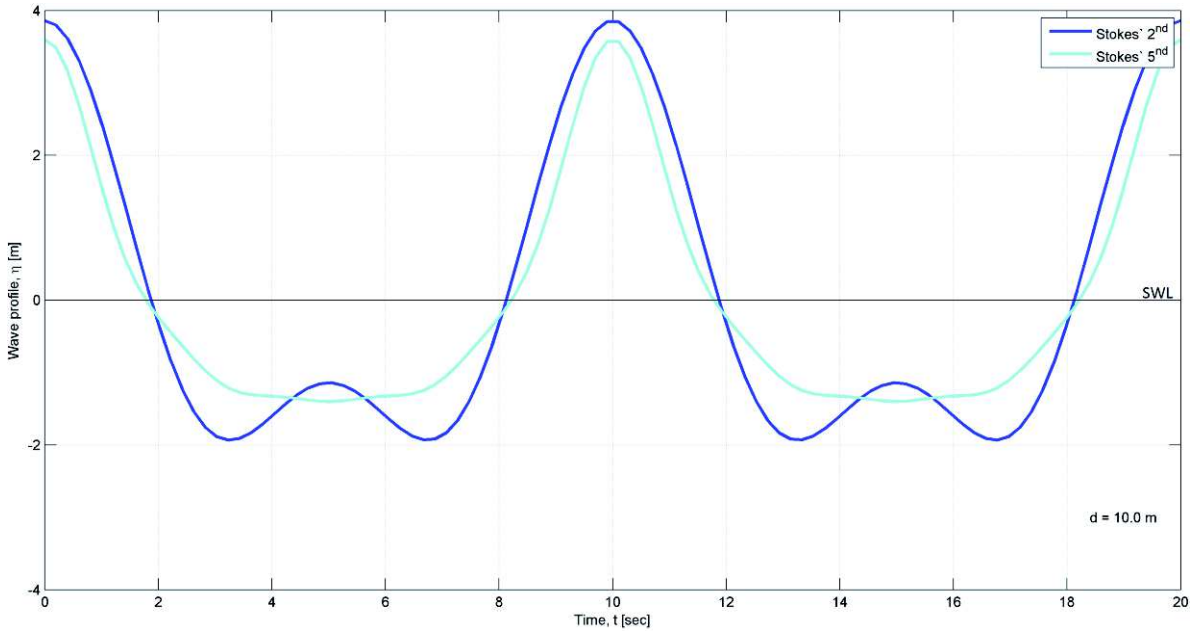

Fig. 2.46: Stokes' 2nd and 5th order wave in shallow water

2.6.2 Stream function waves

The stream function representation has been established by *Dean (1965)* [5] in order to numerically simulate two-dimensional wave properties. The following description of this wide-spread theory shall be reduced to a rather simple problem of constant free surface pressure and without any underlying current. A steady and two-dimensional flow can principally be described by a stream function ψ which also meets the *Laplace* requirement within the fluid in case of irrotationality [5].

$$\frac{\partial^2 \psi}{\partial x^2} + \frac{\partial^2 \psi}{\partial z^2} = 0 \tag{2.129}$$

If the known *bottom* and *free surface boundary conditions* in (2.130) to (2.132) are still prescribed, the stream function adopts the following expression in (2.133) which constitutes an even function of kx with a symmetrical surface elevation and N as the theoretical order of the wave [5].

$$\frac{\partial \psi}{\partial x} = 0 \quad at\ z = -d \tag{2.130}$$

$$w = u\frac{\partial \eta}{\partial x} \quad at\ z = \eta \tag{2.131}$$

$$\frac{1}{2}(u^2 + w^2) + \eta = Q \quad at\ z = \eta \tag{2.132}$$

$$\psi(x,z) = cz + \sum_{n=1}^{N} X_n \cdot \sinh\big(nk(z+d)\big) \cdot \cos(nkx) \tag{2.133}$$

Due to the *kinematic free surface boundary condition* the values of the stream function along the surface elevation $\psi(x,\eta)$ remain constant, relating η and ψ_η at $z = \eta$ in (2.134).

$$\psi_\eta = c\eta + \sum_{n=1}^{N} X_n \cdot \sinh\big(nk(\eta+d)\big) \cdot \cos(nkx) \tag{2.134}$$

The *dynamic free surface boundary condition* is used to retrieve the wave number k, the surface value of the stream function ψ_η and the coefficients X_n. Here, *Sarpkaya et al. (1987)* [5] recommends to designate the unknown wave number as X_{N+1} and to calculate initial values for the unknowns X_n by means of small amplitude wave theory, so that all

X_n except X_1 and X_{N+1} equal to zero. Any numerical technique for further convergence such as *Newton-Raphson* is now applicable whereas the stream function theory focuses on the minimum error in approaching the *dynamic free surface boundary condition* [5].

$$E = \frac{1}{I} \cdot \sum_{i=1}^{I} (Q_i - \bar{Q})^2 \tag{2.135}$$

The subscript i runs from one to I as the input value x shall cover an entire wave length. Q_i is the respective *Bernoulli* constant at the position x and $\bar{Q}$ denotes the mean or actual quantity of the *Bernoulli* constant [5].

$$\bar{Q} = \frac{1}{I} \cdot \sum_{i=1}^{I} Q_i \tag{2.136}$$

By looking at the j-th cycle of the iteration process an approximated relationship in (2.137) can be found between Q_i and the corresponding values of X_n with X'_n as an adjustment to the actual X_n in every computation loop [5].

$$Q_i^{(j+1)} = Q_i^{(j)} + \sum_{n=1}^{N+1} \frac{\partial Q_i^{(j)}}{\partial X_n} X'_n \tag{2.137}$$

$$X_n^{(j+1)} = X_n^{(j)} + X'_n \tag{2.138}$$

If (2.137) is implemented in (2.135) and $\bar{Q}$ is considered to be constant, the error $E^{(j+1)}$ can be adjusted, as in (2.139). On that account, the set of X'_n shall then be obtained by the least squares criterion, prescribing E to be a minimum. The needed values X_n can be determined by means of (2.138) [5].

$$E^{(j+1)} = \frac{1}{I} \sum_{i=1}^{I} \left\{ \left(Q_i^{(j)} + \sum_{n=1}^{N+1} \frac{\partial Q_i^{(j)}}{\partial X_n} X'_n \right) - \bar{Q} \right\}^2 \tag{2.139}$$

Concerning the surface elevation it is now possible to proceed with equation (2.133) to receive an impression of $\eta^{(j+1)}$ at $z = \eta$ by implementing $X_n^{(j+1)}$ and $\psi_n^{(j)}$which are obtained in the latest iteration step [5].

$$\eta^{(j+1)} = \frac{1}{c}\left\{\psi_\eta^{(j)} - \sum_{n=1}^{N} X_n^{(j+1)} \cdot \sinh\left(nk\left(\eta^{(j)} + d\right)\right) \cdot \cos(nkx)\right\} \qquad (2.140)$$

This procedure allows a revision of the surface stream function $\psi_n^{(j+1)}$, although requiring a zero mean value of $\eta^{(j+1)}$.

$$\psi_\eta^{(j+1)} = \frac{1}{L}\int_0^L \left[\sum_{n=1}^{N} X_n^{(j+1)} \cdot \sinh\left(nk\left(\eta^{(j+1)} + d\right)\right) \cdot \cos(nkx)\right] dx \qquad (2.141)$$

Consequently, the x- and z-component velocities can also be defined with the help of the above stated expression for the current stream function at the water surface. One major advantage compared to previous wave theories is the fact that the wave characteristics already refer to the instantaneous surface elevation, discarding any stretching methods [14]. As the $(j+1)$-th loop is completely described by now, including a new Q_i and $Q_i^{(j+1)}$ with the help of (2.132), the iteration process can be continued for higher accuracy [5].

In case of a specific wave related problem the stream function approach can be modified in a way that the wave height is inputted as a governing parameter. The above described numerical procedure is expanded and then relies on the difference between the numerically generated wave height and the given magnitude [5]. In this way, the stream function theory is effectively implemented to gain access to reasonable results for wave lengths and kinematics, especially in shallow waters where other wave theories are rather limited. The approach does not show any subjection to H/L or d/L simply because the assessment of various terms and the elimination of small orders is not required [13]. The required order of the stream function theory refers to the steepness parameter S and the shallow parameter η given in 2.7. Similar to *Stokes'*, for $N = 1$ the stream function wave resembles the results of the linear wave theory. If the wave height enters the wave breaking ambit, more terms or respectively higher orders are needed for a sufficient reproduction of the wave [14]. An overview of the necessary order number to reduce the error in maximum velocity and acceleration below one per cent is presented in Fig. 2.47.

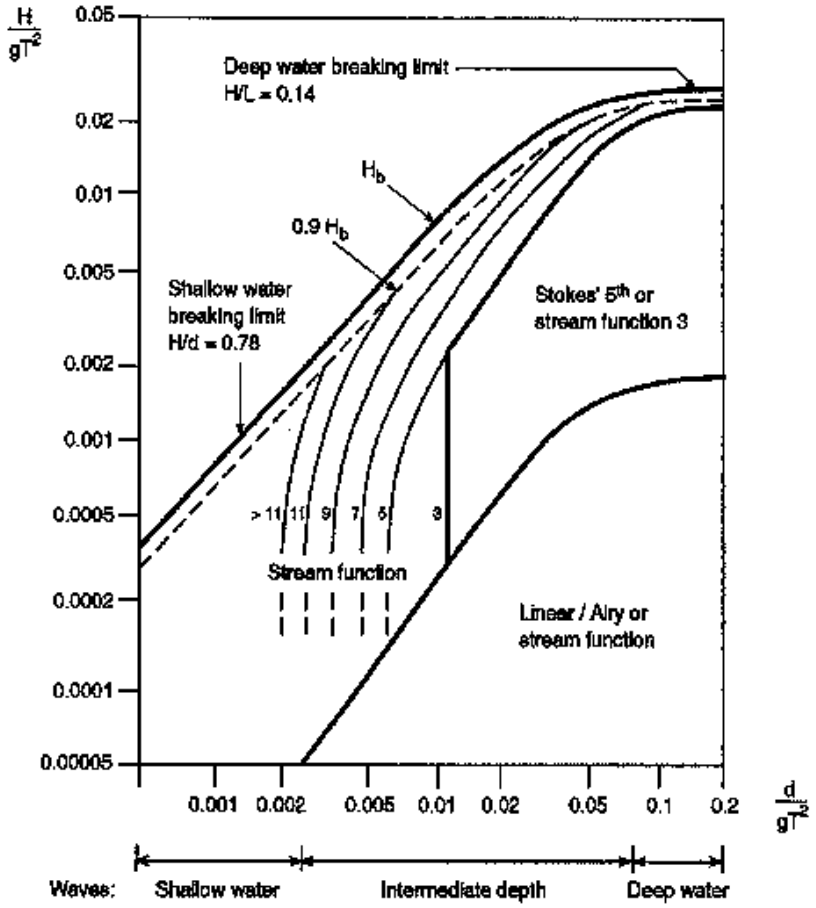

Fig. 2.47: Overview of required order for the stream function wave [14]

Due to its extreme steep profile exemplified in Fig. 2.48 and the large range of validity the stream function is frequently exposed to offshore structure to assess their ultimate strength capabilities. The explicit application of such a non-linear wave and its implementation in a spectrum-generated irregular sea state shall be discussed later. However, the differences to the small amplitude wave are remarkable, especially concerning the shape of wave crest and trough. It is obvious how the individual crest and trough amplitudes differ from each other and thus are responsible for the extreme asymmetry. The pronounced and more slender peak embodies one of the main characteristics of this modelling technique and the reason for the more realistic reproduction of wave kinematics.

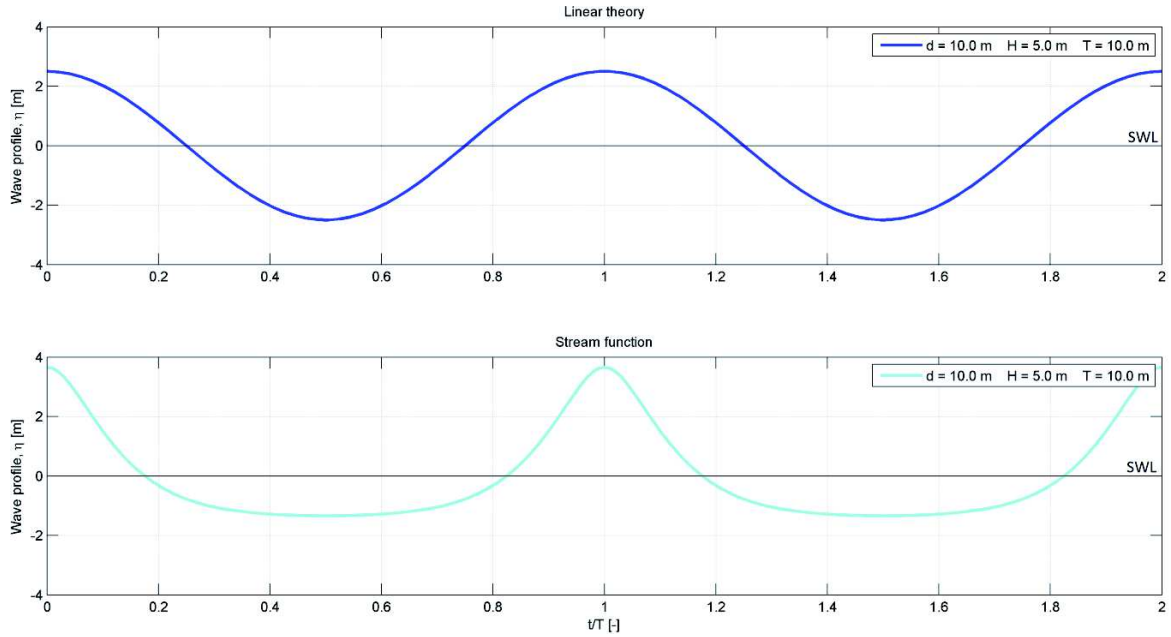

Fig. 2.48: Example of a 20th order stream function wave compared to linear theory

2.7 Validity and comparison of wave theories

As presented in the previous paragraphs, there are various approaches for wave simulations and it is important to say that their application highly depends on the wave and environmental conditions as well as on the interested output values. Generally, it is necessary to distinguish between linear and non-linear theories. This already implies the purpose of the wave for example the generation of one single extreme wave or an irregular sea state as only regular wave components can readily be superimposed. Unequal solutions by means of different wave theories with the same input parameters such as wave height, period and water depth always call for a closer look on validity and applicability. This can clearly be seen in the comparison of the above presented wave models in case of the example in wave in Tab. 2.1 and shallow water. Fig. 2.49 explicitly depicts the severe effect of the water depth on the surface elevation and thus on the validity of each theory. The linear theory simple yields a smooth sinusoidal oscillation with symmetric amplitudes due to the negligence of the distance to the sea floor while the *Stokes'* waves show more or less severe problems, in particular the second order approach. With respect to the additional crests in the wave trough and the considerably larger wave crest and trough this simulation basically fails under the given shallow water conditions. On the other side, the stream function wave stands out if one looks at the consistent and proper progress of the surface elevation even in small water depths.

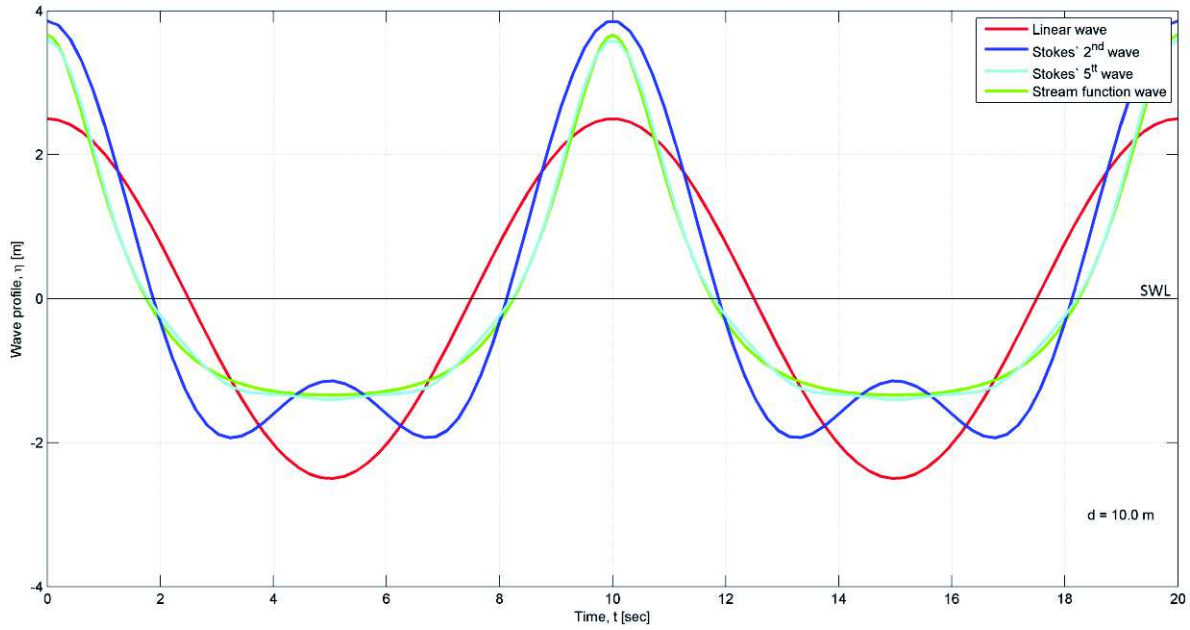

Fig. 2.49: Comparison of the discussed wave models for shallow water

Of course, the initial choice is associated with an assessment of time and effort related to the main design objective. It needs to be weighed whether availability and simplicity of certain approaches constitute the governing factors against more accurate results. On that account, different opinions on the application and deviations among the theories shall be presented to attain a more comprehensive understanding for the upcoming application on a monopile structure and result assessment.

A rough limitation of the individual wave theories is based on the following three non-dimensional parameters which help to define the range of validity for specific scenarios. These are the already mentioned wave steepness S, the shallow water parameter μ and the so-called *Ursell* number U_R [14].

$$S = 2\pi \cdot \frac{H}{gT^2} = \frac{H}{\lambda_0} \tag{2.142}$$

$$\mu = 2\pi \cdot \frac{d}{gT^2} = \frac{d}{\lambda_0} \tag{2.143}$$

$$U_R = \frac{HL^2}{d^3} \tag{2.144}$$

Here, the quantities λ_0 and k_0 represent the linear deep water wave length and wave number associated to the given wave period T and it is worth mentioning that the above stated parameters correlate with each other, yielding the relationship in (2.145).

$$U_R = \frac{S}{\mu^3} \tag{2.145}$$

The limits for each major wave theory can be taken from Fig. 2.50 where steepness on the vertical axis is plotted against the shallowness on the horizontal axis. At the first glance it shows a dissociation of the mentioned theories to wave breaking phenomenon and how the water depth sets clear boundaries for each theory. *Stokes'* approach and linear simulation in form of *Airy* prevail in deep seas whereas the cnoidal approach dominates shallower regions. But concerning the subsequent monopile design and its ultimate strength assessment the stream function theory performs considerably well over the main range of water depths, displayed by the single symbols of simulated laboratory test data. In the particular case of $U_R \sim 30$, only the stream function theory is able to represent reasonable results while an *Ursell* number greater than thirty also allows an application of *cnoidal* wave theory [14].

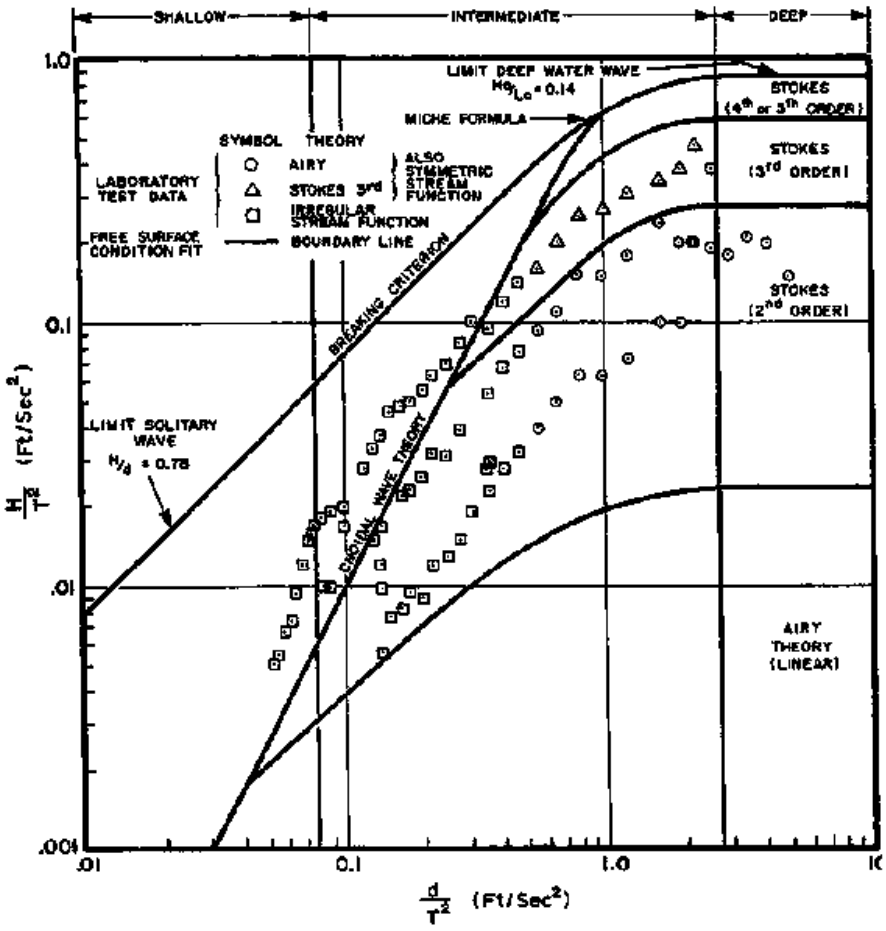

Fig. 2.50: Range of validity for various wave theories [14]

The following investigations and researches proof the above statements about applicability and validity presented for the sake of completeness and verification. One of the main similarities among all common wave theories is the compliance with the

Laplace equation and the seafloor boundary condition. Thus, *Dean (1970)* investigated the "closeness of fit of the predicted motion to the complete problem formulation" or in other words he compared the grade of approximation of the two non-linear *free surface boundary conditions* of the small amplitude wave theory, *Stokes'* third and fifth order solution, *cnoidal*, solitary and stream function realisation. With reference to Fig. 2.51 it is concluded that the first order cnoidal, the linear, the *Stokes'* fifth order and the stream function wave embody the most suitable method in the prescribed range, although without stipulating one final master solution as the main focus lies on low order wave simulations [5].

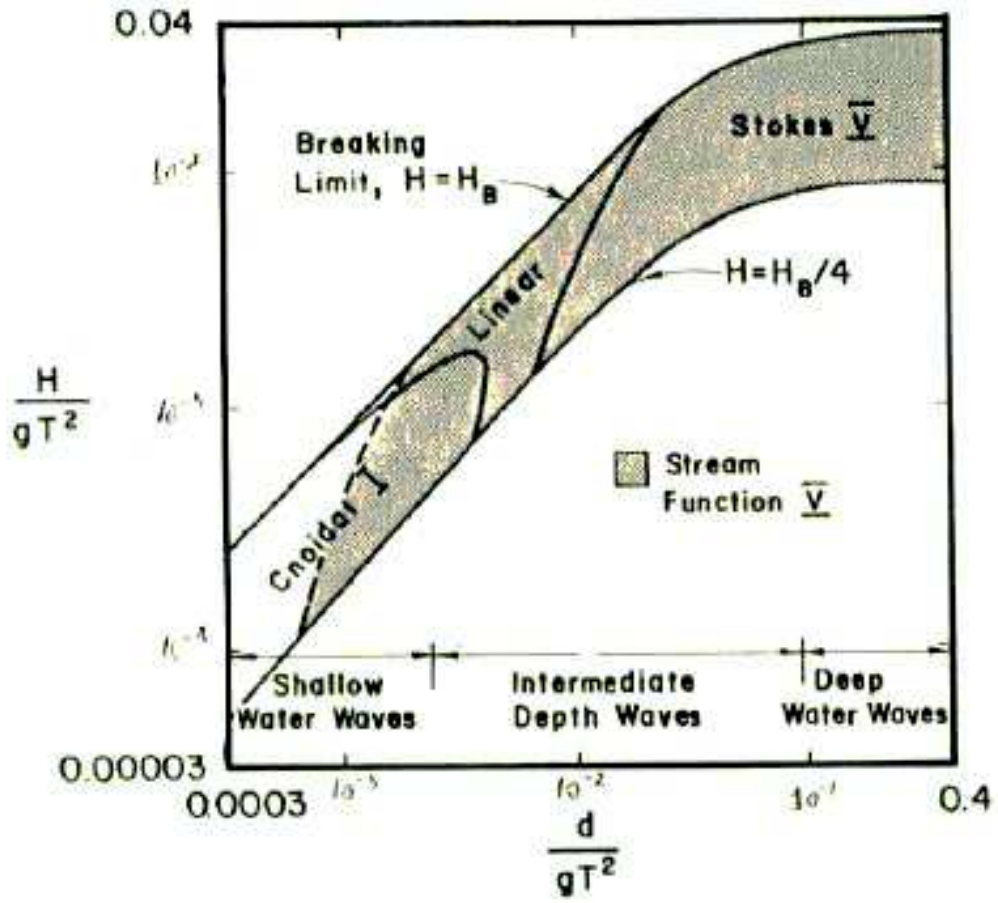

Fig. 2.51: Range of wave theories regarding best fit to the dynamic free surface boundary conditions [5]

Another attempt is conducted by *Le Méhauté (1976)* and presented in Fig. 2.52 where he displays the range of validity for the above mentioned wave theories as a function of the dimensionless water depth but on a rather arbitrary basis due to lack of quantitative verification. However, it can be seen that higher waves in shallow water should be treated in a cnoidal way whereas an increase in water depth reasons the application of *Stokes'* higher order expressions which in principle agrees with the results by *Dean (1970)* [5].

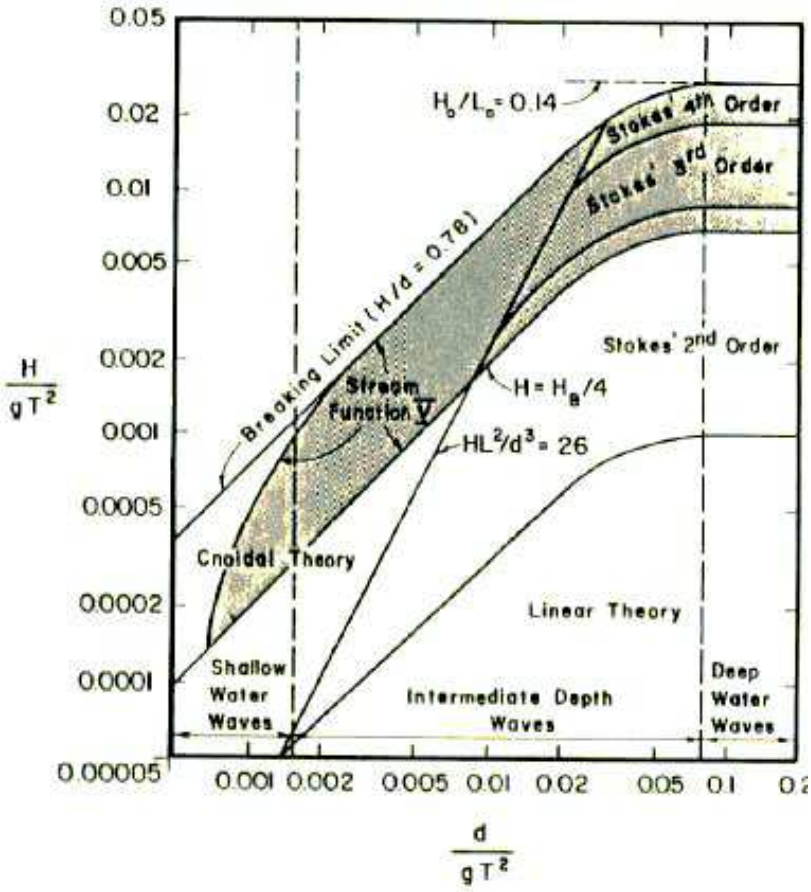

Fig. 2.52: Validity range for different wave theories by Le Méhauté [5]

For simulating maximum wave or extreme steepness characteristics *Stokes'* fifth order and the stream function theory have proven to be quite effective and suitable in marine engineering [5]. In case of regular steep waves when $S < S_{max}$ and $U_R < 30$ applies, the fifth order compared to other *Stokes'* waves is recommended while the maximum crest to wave height relationship for general *Stokes'* orders is *0.635* [14]. By comparing those two approaches the water depth can be considered as the crucial parameter in terms of application and validity. In deep waters both methods reveal reasonable results but in case of decreasing distance to the sea floor *Stokes'* waves begin to show those previously mentioned local maximums in the wave trough. In coastal regions it is even likely that those waves develop a third crest, characterising the validity limit of this theory or order number. *Ebbesmeyer (1974)* examined this phenomenon further and could declare the following boundaries in Fig. 2.53 particularly for *Stokes'* fifth order wave where region *a* constitutes the smooth or satisfactory realm, region *b* the occurrence of a secondary crest and region *c* the triple-crested appearance or no solution [5]. In order to avoid such singularities *Brorsen (2007)* [13] suggests a range of $d/L > 0.10 - 0.15$ while lower order waves are susceptible to larger values of *d/L*. In contrary to and in conformity with Fig. 2.51, the stream function theory is rather stable and applicable over the entire given depth range.

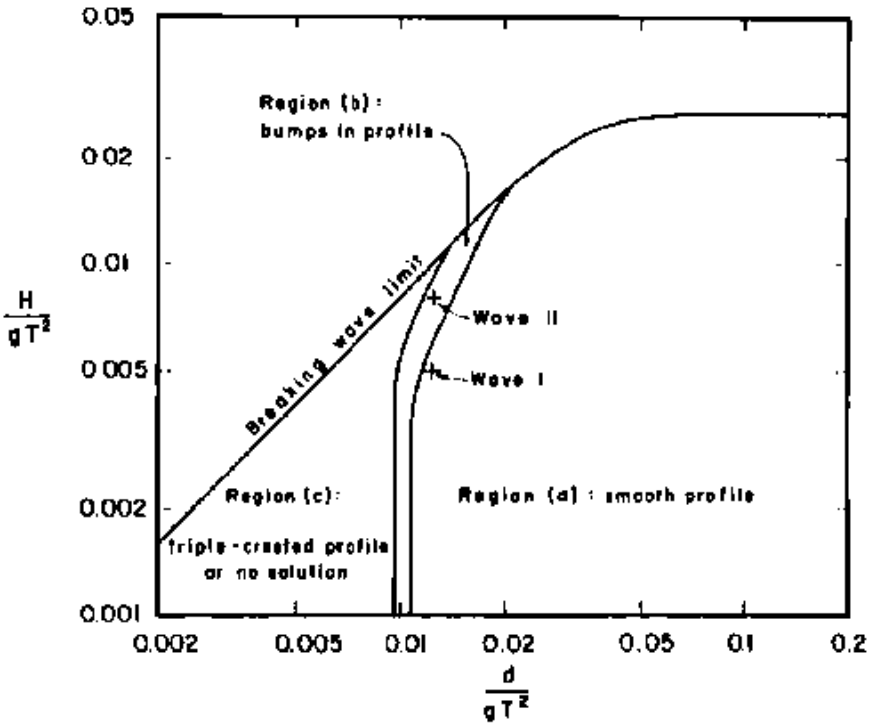

Fig. 2.53: Occurrence of local maximum in case of Stokes' 5th order wave [5]

One can state that with respect to simple but distinct input values in form of wave height, period and water depth a sufficient range of wave types, wave interactions and other environmental influences can be predicted with the here discussed theories. *Sarpkaya et al. (1967)* comes to the conclusion that the obtained accuracy corresponds well to any other engineering field "compared to the somewhat arbitrary choice of celerity definition used and to the unreliabilities in design wave selection or in other steps of the entire design process" [5]. If the relatively simple implementation and availability of most common wave theories are included in the overall evaluation, then the main advantages and reliability cannot be denied. The small amplitude wave theory for the realisation of an irregular sea state and the *Stokes'* fifth order or stream function wave as maximum representations are to be mentioned in particular. Generally for single regular waves, it can be stipulated that *Stokes'* waves, in particular the fifth order approach, are rather found in deep waters as they lose validity with decreasing water depth. An increase of the order number can provide redress but preferably the *cnoidal* wave theory should be deployed. However, in today's maritime engineering the stream function theory is considered as the most common and effective procedure in wave modelling as it provides the most realistic reproduction of wave kinematics and covers more or less any water depths. Only wave breaking is seen as an upper boundary for the method, although this phenomenon must be investigated separately and applies for any other theory as well. The small amplitude wave is hardly ever used nowadays, only for the generation of an irregular sea state due to its superposition merits.

On the other side, it is essential to emphasise that the computation of wave loads eventually requires a profound knowledge of water particle velocities, accelerations and pressure variance because experiments have shown that all wave theories somehow experiences difficulties to reproduce experimental data sufficiently in accordance to [5].

3 Wave forces on cylindrical structures

In the last years today's offshore wind industry has entered water depths which majorly call for hydrodynamically driven constructions. That means that compared to wind and current waves represent the largest contribution to the overall loading on bottom-fixed offshore structures. On that account, it is of substantial importance to completely as well as correctly transfer wave motions and its associated kinematics into loads and moments. For this design step *Morison's* equation represents the most commonly applied and well-evaluated method, providing horizontal forces along the *z*-axis of the structure on the basis of geometry, water particle velocity and acceleration. Besides water density the output also depends on semi-empirical in-line force coefficients which shall be discussed in more details in the following. The total shear force obtained by *Morison et al. (1950)* [17] at each z-position together with the corresponding distance to the sea floor yield the so-called *OTM* which is seen as the prime design parameter for the global dimensions of monopiles. Basically, this structure type can be viewed as a vertical cantilever constrained at the sea floor and exposed to a varying line load. Consequently, it is required to feature a sufficient section modulus to oppose this *OTM* to avoid complete collapse. An integration of each single force component and the corresponding *OTM* over the water depth at a given point in time eventually produces the overall time series of wave loads on circular marine foundations.

This chapter shall neglect the consideration of lift forces on the structure and shall solely cover the derivation of *Morison's* equation and its load components. Furthermore, the main focus shall be on the determination of the previously mentioned force coefficients and their sensitivity to the surface roughness of the cylinder. As a conclusion the in 2.4 and 2.6 presented various wave simulations, including their different surface elevation and wave kinematics are integrated in *Matlab* to simulate wave loads on a simple vertical pile.

3.1 In-line force components

Due to the symmetric shape and the vertical alignment of the cylinder in the water only in-line forces shall be considered and the lift forces, as depicted in Fig. 3.1, are neglected in the following. So in contrary to flexible and very long risers, monopiles are rather seen as rigid and passive structures and with respect to the small water depth they do not witness any severe vortex induced motion or vibration. Generally, a wave scenario constitutes an oscillatory flow with respect to the orbital motion of the water particle and thus causes three main contributions to the in-line forces in (3.1), acting horizontally on the fixed pile.

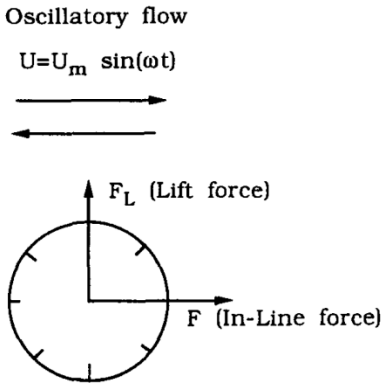

Fig. 3.1: Main forces in an oscillatory flow acting on the cylinder [18]

Similar to steady currents, the pile responds with a resistance against the incoming flow given by the first part in (3.1) where the velocity is separated in two terms to guarantee that the drag force always follows the velocity with the right sign. But due to the oscillatory flow two additional forces are witnessed and added to the total force in (3.1). Here, the second term is denoted as the *hydrodynamic mass* force and the last expression as the so-called *Froude-Krylov* force [18].

$$F = \frac{1}{2}\rho C_D D u|u| + m'\dot{u} + \rho V\dot{u} \tag{3.1}$$

where:

ρ	=	Water density
C_D	=	Drag coefficient
m’	=	Hydrodynamic mass of the cylinder
D	=	Diameter of the cylinder
V	=	Volume of the cylinder
u	=	Water particle velocity due to by wave motions
ů	=	Water particle acceleration due to by wave motions

Referring to *Sumer et al. (2006)* [18] the *hydrodynamic mass* "is defined as the mass of the fluid around the body which is accelerated with the movement of the body due to the action of the pressure". That means that the total force not only depends on the general resistance but also on the surrounding water mass which is excited by the object. On that account, the orientation of the body plays an essential role which is illustrated by means of a simple plate in a straight flow in Fig. 3.2.

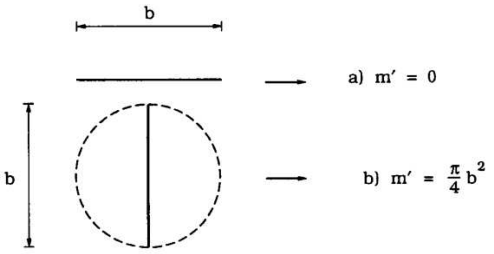

Fig. 3.2: Movement of the plate a) in its own plane and b) perpendicular to the incoming flow [18]

For the calculation of the *hydrodynamic mass* it is common to ignore frictional interactions between the body and the water mass, only considering equilibrium between pressure and inertia of the fluid forces [18]. Therefore, it is possible to define the flow field between the accelerated body and fluid by applying potential flow theory. So if the body is accelerated through the water, it will create a pressure gradient around itself, resulting in the *hydrodynamic mass*. The flow field around the cylinder can then be determined which is used to obtain the pressure on the surface of the pile. Eventually, the calculated pressure gives indications of the forces on the body [18]. *Sumer et al. (2006)* [18] provides the solution for the required force to accelerate a circular cylinder in a still fluid in (3.2).

$$F = ma + \rho r_0^2 \pi a = (m + m')a \tag{3.2}$$

Generally, the hydrodynamic mass is expressed as in (3.3) where A is the cross-sectional area of the body and C_m the *hydrodynamic mass coefficient* which usually equals to *1.0* [18].

$$m' = \rho C_m A \quad with\ C_m = 1.0 \tag{3.3}$$

However, the cylinder is generally considered as stationary and the water is accelerated in reality. Consequently, the body is not only affected by the above explained *hydrodynamic mass* force but also by the effect that the motion of the fluid in the outer-flow region causes an additional pressure gradient in (3.4). This leads to the previously mentioned *Froude-Krylov* force where U represents the velocity far from the cylinder [18].

$$\frac{\partial p}{\partial x} = -\rho \frac{dU}{dt} \tag{3.4}$$

This third force component introduced by the far-field pressure gradient can be acquired by integrating the pressure on the surface of the body S in (3.5) although as a volume integral from the *Gauss* theorem in order to include the term in (3.4) [18]. As the pressure gradient is assumed to be constant the *Froude-Krylov* force F_p can be simplified in terms of the water acceleration $\mathring{U}$ far from the body, presented in (3.6).

$$F_p = -\int_V \frac{\partial p}{\partial x} dV \tag{3.5}$$

$$F_p = \rho V \dot{U} \quad with\ \dot{U} = \frac{dU}{dt} \tag{3.6}$$

For the considered cylinder with a unit length the volume is expressed by means of the cross-sectional area A in (3.7), similar to the *hydrodynamic mass* force [18]. It becomes clear that the *Froude-Krylov* force vanishes as soon as the body starts to move through still water because there will be no accelerated outer flow and thus no additional pressure gradient.

$$F_p = \rho A \dot{U} \tag{3.7}$$

3.2 *Morison's* equation

The drag force, the *hydrodynamic mass* force and the *Froude-Krylov* force in 3.1 make up the total in-line force induced by an accelerated flow and applied on a stationary cylinder from the sea floor upward above the wave profile, summarised in (3.8). By introducing the inertia coefficient C_M the total in-line force can be simplified and eventually assumes the well-known form of *Morison's* equation in (3.10) [18].

$$F = \frac{1}{2}\rho C_D D U|U| + \rho C_m A \dot{U} + \rho A \dot{U} \tag{3.8}$$

$$F = \frac{1}{2}\rho C_D D U|U| + \rho (C_m + 1) A \dot{U} \tag{3.9}$$

$$F = \frac{1}{2}\rho C_D D U|U| + \rho C_M A\dot{U} \quad with\ C_M = C_m + 1 \tag{3.10}$$

The second and modified expression in (3.10) now constitutes the inertia force where C_M amounts to *2.0* for a circular cylinder in an oscillatory flow with small *Keulegan-Carpenter (KC)* numbers in most general cases. The reason is that the flow is not separated yet and thus the potential value of C_m equals to 1.0 according to [18]. So to sum up there is the drag force proportional to the square of the horizontal water particle velocity which is generally described by the drag coefficient depending on *Re* and *KC* numbers. Secondly, the cylinder is exposed to a virtual mass force proportional to the horizontal water particle acceleration which acts on the water mass displayed by the body [17]. Additionally, it is important to mention that the here described approach only refers to unbroken wave scenarios and does not cover any breakers or incipient breakers. This impulsive force usually turns out to be much greater than the drag component although only over a substantially short time period [17].

Generally, *Morison's* load formula is limited to the following condition in (3.11) which relates the wave length L and the diameter D. However, the major assumption which has to be kept in mind during design is the fact that the cylindrical structure does not change the wave. That means that the foundation has no effects on the propagation, celerity and shape of the incident wave before and after the contact. In other words the monopile is seen as a hydrodynamically transparent structure compared to bluff bodies like ships which influence the wave characteristics and cause transformations. According to *DNV (2014)* [14] the end-effects are discarded "when the length of the member is much larger than the transverse dimensions", allowing the simple superposition of each cross-sectional force along the structure. In case of a combination of wave and current the water particle velocities shall be enlarged respectively by vector summation [14].

$$L > 5 \cdot D \tag{3.11}$$

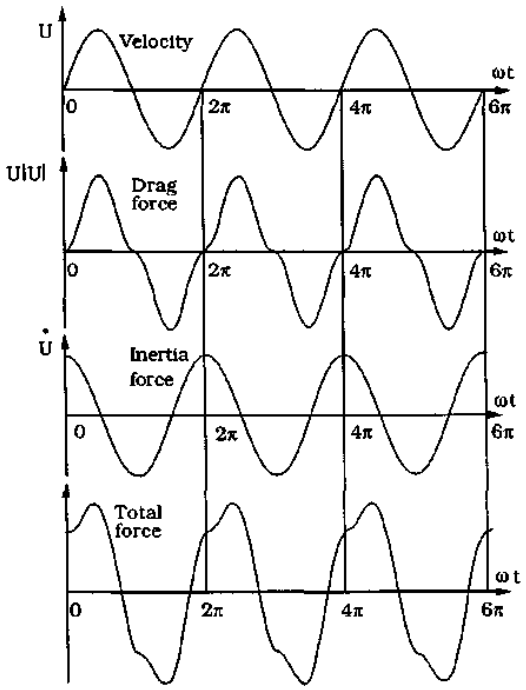

Fig. 3.3: Time series of the drag and inertia forces of Morison's equation [18]

Referring to (3.10) and Fig. 3.3 the *90°* phase shift between each maximum of the drag and inertia force becomes visible which must be borne in mind for the determination of the total in-line load. The ratio between each force component can be expressed as in (3.12) while for small *KC* numbers the ratio is reduced to (3.13) assuming $C_M = 2$ and $C_D \cong 1$ [18].

$$\frac{F_{I,max}}{F_{D,max}} = \frac{C_M \frac{\pi}{4} D^2 \omega U_m}{\frac{1}{2} C_D D U_m^2} = \pi^2 \frac{D}{U_m T} \frac{C_M}{C_D} = \frac{\pi^2}{KC} \frac{C_M}{C_D} \tag{3.12}$$

$$\frac{F_{I,max}}{F_{D,max}} = \frac{20}{KC} \tag{3.13}$$

So under the condition of small *KC* numbers the inertia force exceeds the drag component, although with increasing *KC* values the resistance continues to gain more relevance due to the initiation of flow separation. *Sumer et al. (2006)* [18] denotes the range $0 < KC \ll 20 - 30$ as the *inertia-dominated* regime and the range $KC > 20 - 30$ as the *drag-dominated* regime. According to [17] and referring to (3.10) it can be declared that there is a faster decay of the drag force with increasing depth than for the inertia component and that the total in-line force reaches its peak before the wave crest whereas the angle or time of advance grows with the above provided ratio. Investigations also underline that inertia loads take up a superior role in case of growing cylinder diameter, particularly in relation to wave height and length [18].

Morison's equation is implemented in *Matlab* and avails itself of the previously presented wave kinematics of the example wave in Tab. 2.1 to transfer them in wave loads and the corresponding *OTM*. Here, it is important to mention the below stated results refer to the incident wave impact or more precisely to a static force and not the structural response which of course can be calculated subsequently from a static or dynamic perspective. The pile with a diameter of two metres is considered as fixed at the sea floor and the horizontal water particle velocity and acceleration for each z-coordinate at any time position are implemented. As a result Fig. 3.4 displays the depth dependency of each load component, featuring the familiar parabolic degradation from the instantaneous water surface elevation to the sea floor.

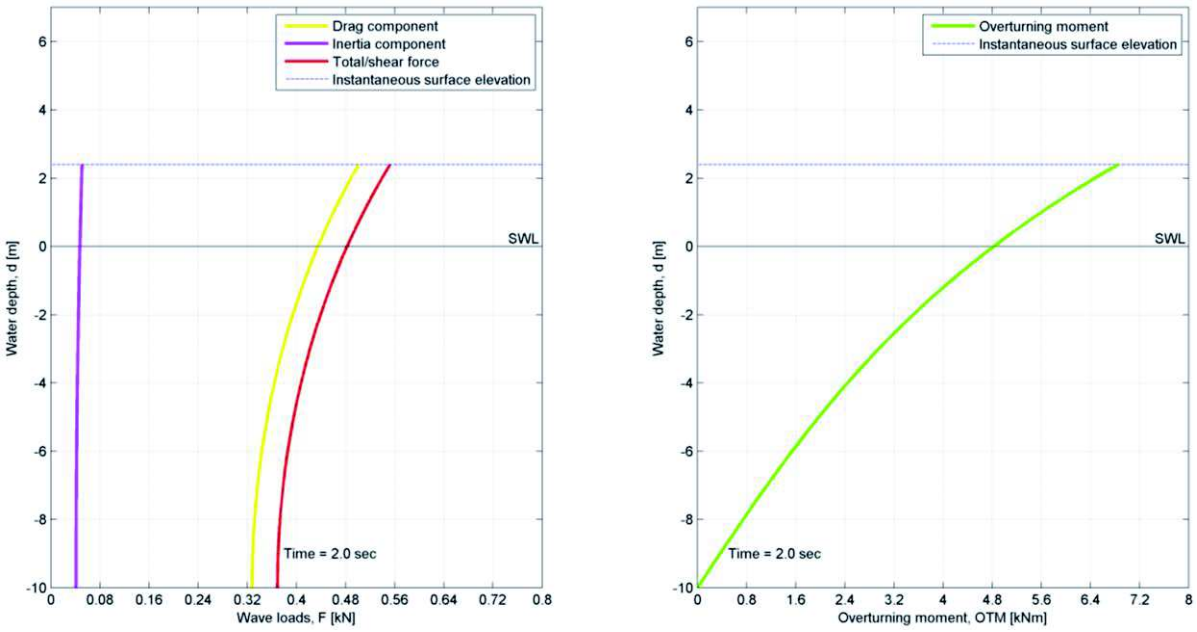

Fig. 3.4: Wave loads for a specific point in time induced by a linear wave

As described in 2.4 and 2.6 various wave theories provide different results for surface elevations as well as water particle properties, revealing alternative outputs in Fig. 3.5 to Fig. 3.7. Here, the previously mentioned phase shift between each force and the propagating wave is clearly visible. The drag component simply follows the wave surface, having the same positions of peaks and lows. However, the inertia force and due to its substantial difference to the drag the total shear force respectively show a delayed response towards the incoming wave. Additionally, the inertia contribution reaches its maximum when the acceleartion peaks as well. The same applies for the *OTM* as it is always in line with the accumulative horizontal in-line force at the same point in time.

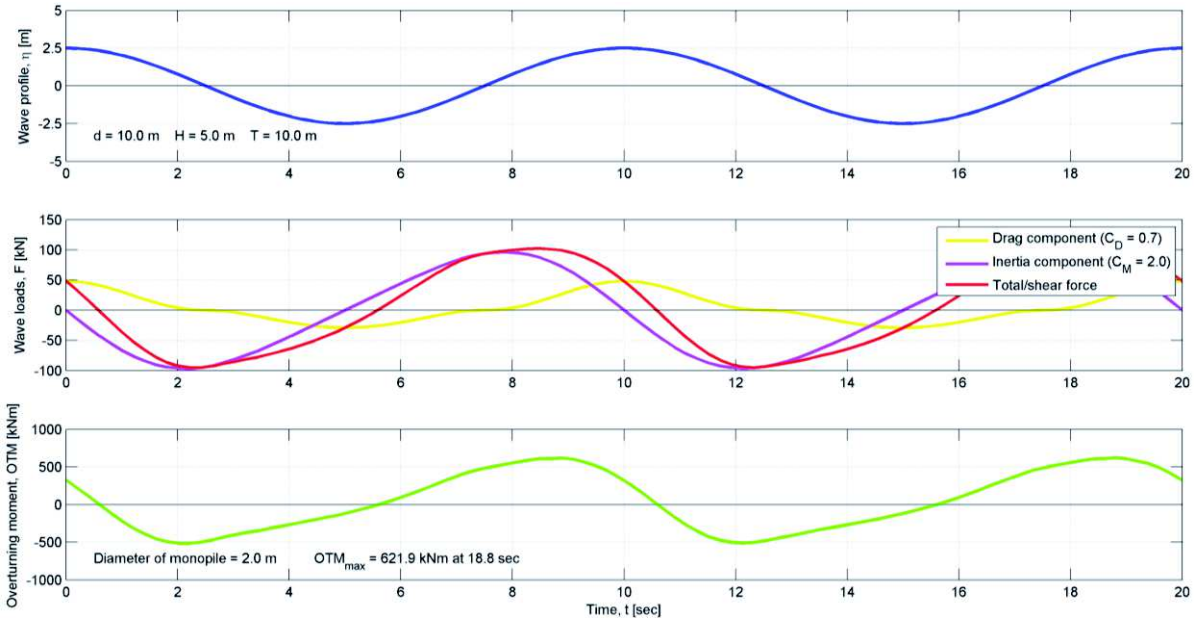

Fig. 3.5: Wave loads and overturning moment induced by a linear wave

As already discussed in 2.7, the main difference between linear and non-linear wave theories is mostly remarkable in the asymmetric shape of the surface elevation with respect to *SWL*. The degree of asymmetry around the horizontal axis severely accelerates the water particles and structural consequences become apparent by looking at the maximum *OTM* while its point in time remains pretty constant. Tab. 3.1 shows that the non-linear approaches more or less yield an *OTM* which is double the one received by linear theory and also enhanced by the larger lever arm between the mudline and the more pronounced wave crest. The slight reduction in case of order increase traces back to the higher accuracy of the *Stokes' 5th* order wave, especially in such shallow waters where the second order wave rather provides unreliable results. A confrontation in Fig. 3.8 emphasises the considerable deviation between the below applied wave realisations.

Tab. 3.1: Overview of different OTMs obtained by various regular waves

Wave loads	*Linear wave*	*Stokes' 2nd order*	*Stokes' 5th order*
OTM [kNm]	621.9	1427.9	1319.4
Point in time [sec]	18.8	9.3	9.5

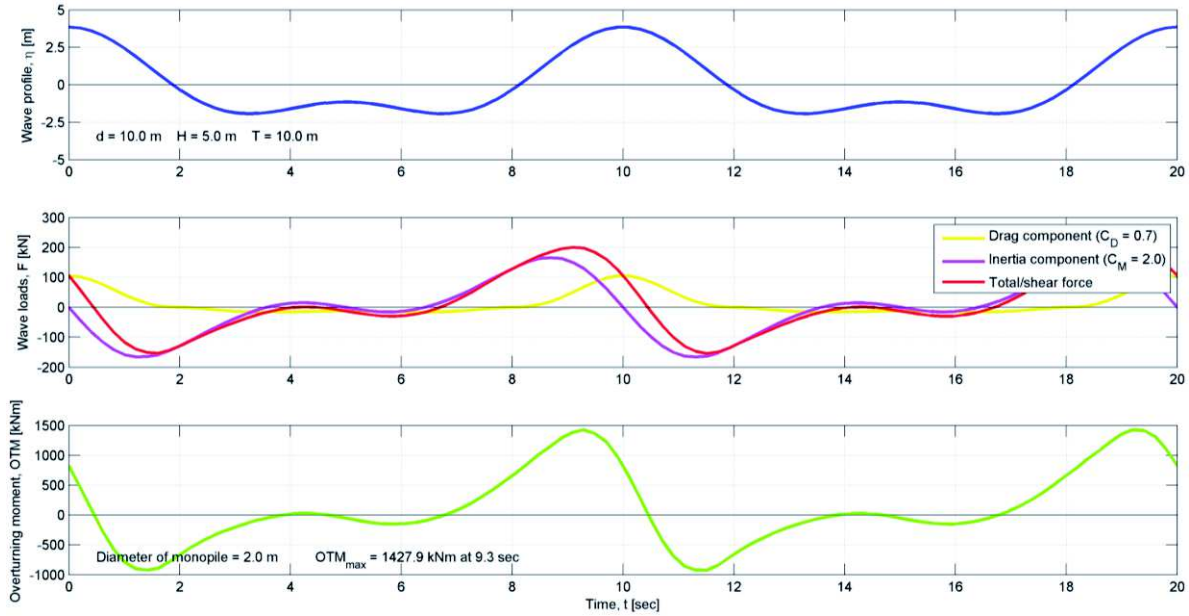

Fig. 3.6: Wave loads and overturning moment induced by a Stokes' 2nd order wave

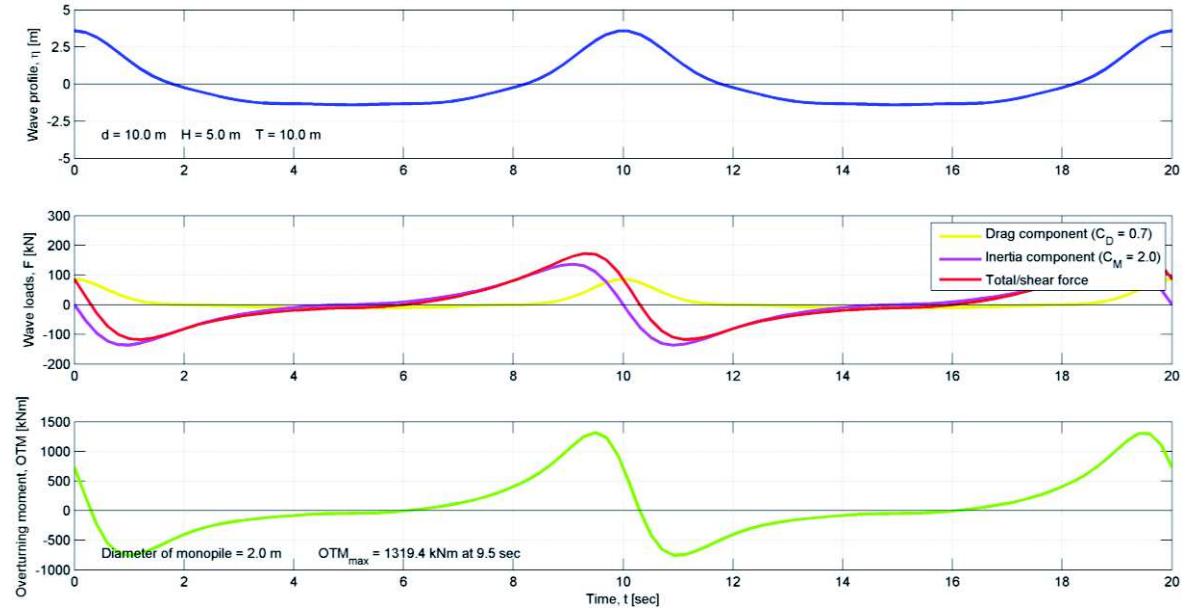

Fig. 3.7: Wave loads and overturning moment induced by a Stokes' 5th order wave

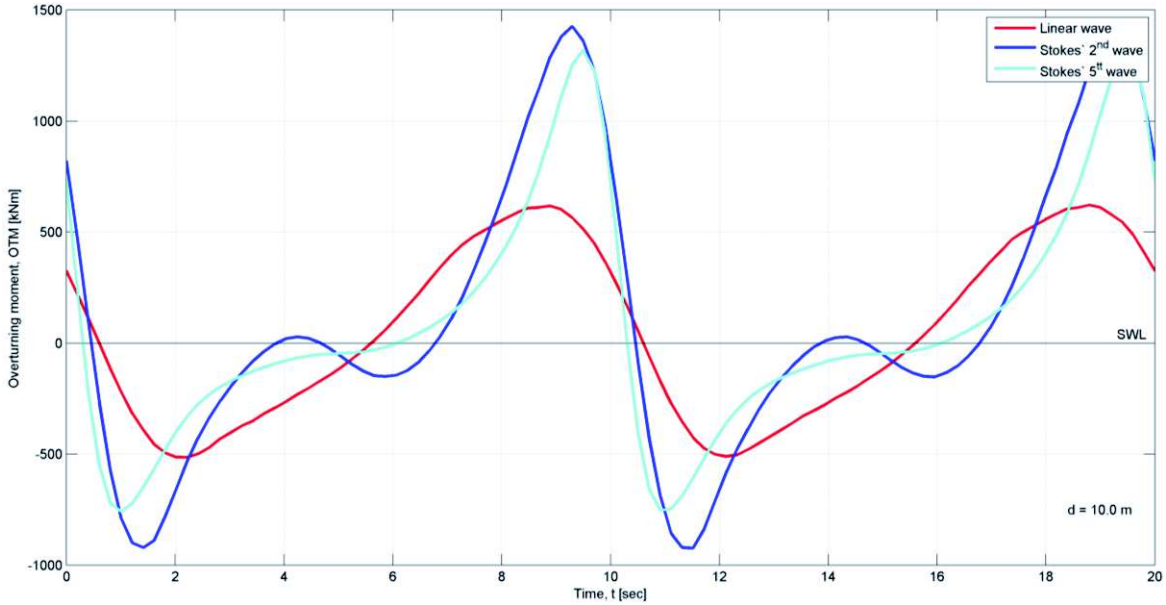

Fig. 3.8: Comparison of overturning moment obtained by different wave theories

3.3 In-line force coefficients

The determination of drag and inertia coefficients is governed by the following non-dimensional numbers, especially the already mentioned *Keulegan-Carpenter* value. In case of an additional current interference the *Re* number refers to the maximum velocity $v = v_c + v_m$ whereas the *KC* number is based on the maximum orbital velocity v_m and the current flow velocity ratio a_c [14].

$$Reynolds\ number \qquad Re = \frac{v \cdot D}{\nu} \tag{3.14}$$

$$Keulegan - Carpenter\ number \qquad KC = \frac{v_m T}{D} \tag{3.15}$$

$$Relative\ surface\ roughness \qquad e = \frac{k}{D} \tag{3.16}$$

$$Current/wave\ velocity\ ratio \qquad \propto_c = \frac{v_c}{v_m + v_c} \tag{3.17}$$

where:

k = Average roughness height
v_m = Maximum orbital velocity
v = Kinematic viscosity
v_c = Current velocity in the direction as the wave

There are different perceptions of the deployed period in the *KC* number, depending on the presence of the current. For a pure wave motion the full wave period is taken which is generally accepted in *ISO 19902 (2007)* [19]. Alternatively, a half wave cycle is considered as the reference period for combined wave and current conditions.

For the definition of drag and inertia coefficients it is possible to resort to standards for example by the classification society *Det Norske Veritas AS (DNV)* or the *American Petroleum Institute (API)* which also complies with the international standards (*ISO*). Thus, the values can be calculated individually for every time step and velocity component, specifically adapted to the instantaneous wave profile. However, in this work and in general design processes it is common to apply constant values for the coefficients found in textbooks or from model tests which are then only adjusted with respect to marine fouling and appurtenances. Indicative hydrodynamic coefficients for cylindrical structures can be taken from Tab. 3.2.

Tab. 3.2: Standard values for drag and inertia coefficients [19]

Surface	C_D	C_M
Smooth	0.65	1.6
Rough	1.05	1.2

With respect to the drag coefficient it is important to mention that it must generally be distinguished between steady and oscillatory flow. For the former flow condition experimental data in Fig. 3.9 reveal that the drag coefficient remains rather constant in the main part of the sub-critical flow regime. In this region of *Re* numbers between *300.0* and *300,000.0* the boundary layer and separation exhibit a laminar behaviour while the wake is fully dominated by turbulences. In the event of a transition from the sub-critical to the critical or super-critical regime the drag coefficient experience a severe collapse [18]. Offshore structures usually end up in the post-critical regime of *Re* numbers larger than 10^6.

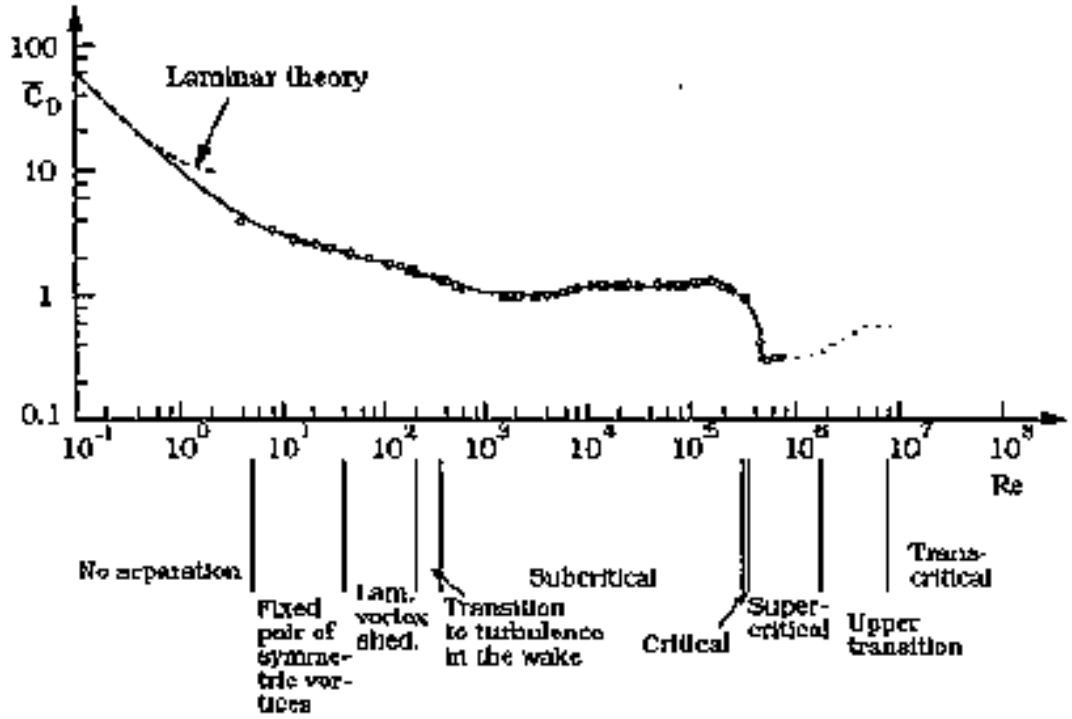

Fig. 3.9: Drag coefficient for a smooth cylinder for varying Reynolds numbers [18]

Concerning steady but oblique flow experiments in [18] reveal that the flow direction adjusts itself close to the cylinder till an almost perpendicular orientation to the pile axis. On that account, kinematics, drag coefficients and the corresponding forces can still refer to the flow component normal to the cylinder, following a rather conservative idea. But it is essential to mention that this simplification is only valid up to a critical angle of attack in the range of *55.0* degrees and for structures of circular cross-section. Due to separation and resulting vortex shedding the drag coefficients for constructions with sharp edges must be considered independent of *Re* numbers and in case of non-circular shapes independent of the surface roughness [18].

With reference to [14] and the range of application the inertia coefficient is usually generalised to the theoretical amount of two for sub-critical *Re* numbers and *KC* values below three for both rough and smooth cylinders. If the inertia coefficient is expressed as a function of the *KC* number larger than three *DNV (2014)* [14] provides general expressions for smooth and rough cylinders for large *KC* numbers.

It is crucial to conclude that the different formulations of force coefficients are quite susceptible to the cylinder alignment or orientation. Since wave motions cause a rather elliptical trajectory of the water particle the validity range is limited to vertical or slightly slanted cylinders with a maximum deviation of *15.0* degrees from the *z*-axis [18].

3.3.1 Roughness influence

The surface roughness severely affects the flow around the cylinder and its overall behaviour in the water. An evolving asymmetry always leads to hydrodynamic instabilities in form of vortex shedding due to lift forces. But the texture also influences the separation angle, the turbulence level and the diameter which simply increase the projected area and thus the overall resistance [18]. Conventionally, the roughness effects are considered in the in-line force coefficients which were investigated extensively by *Justeen (1989)* [18]. Since his experiments were conducted under equal environmental and flow conditions and he only altered the surface roughness, he was able to correlate the variation in force coefficients to the increase in roughness.

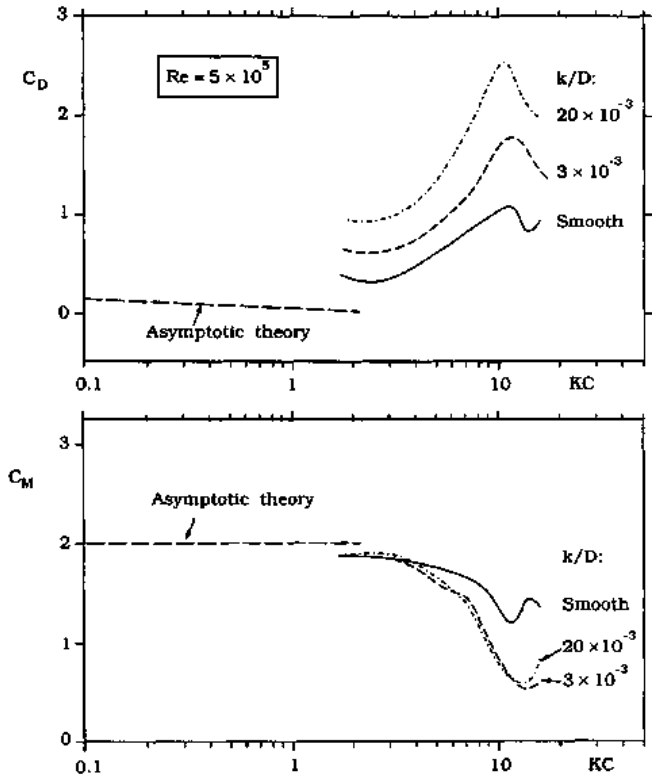

Fig. 3.10: Roughness effects on in-line force coefficients [18]

Fig. 3.10 reveals that the drag coefficient rises in case of a surface alteration from smooth to rough by $k/D = 3x10^{-3}$ whereas the inertia coefficient is reduced. One possible reason for the decreasing inertia coefficient can be related to the non-linear connection between vortex shedding and the hydrodynamic mass which is much more pronounced for rough cylinders due to the greater change in C_M than for smooth surfaces. If the surface conditions continue to aggravate, it can be perceived that C_D follows the same trend which mainly traces back to the fact that the experiments were performed under post-critical Re numbers. On the other side C_M remains rather unchanged with increasing roughness [18].

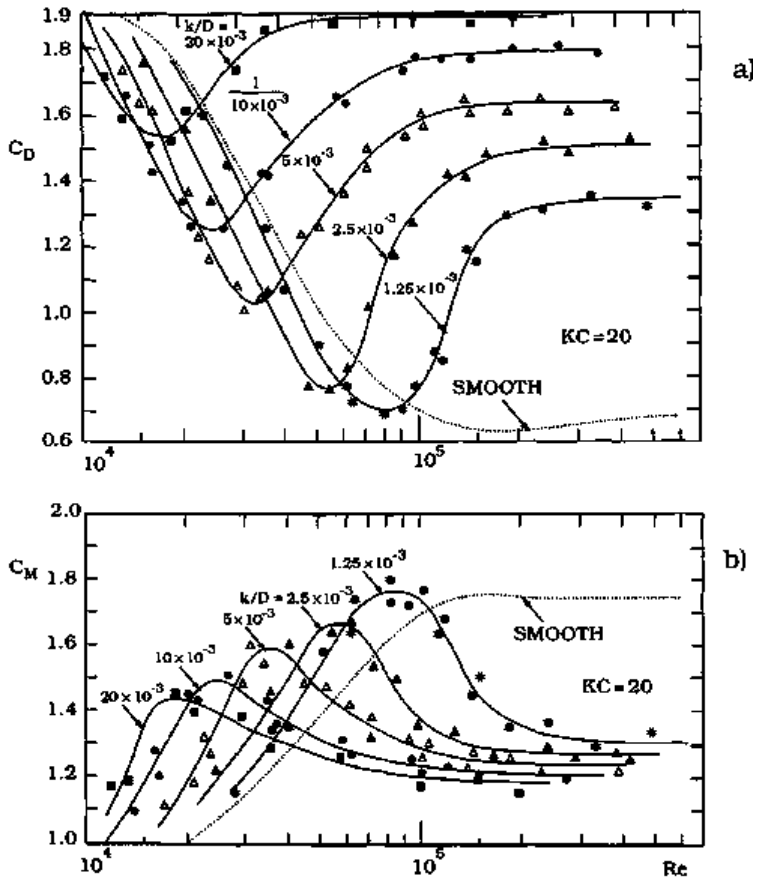

Fig. 3.11: Variation of C_D and C_M as a function of the Reynolds number for different roughness grades [18]

In Fig. 3.11 the *KC* number is kept constant and *Re* changes which typically illustrates how the in-line force components behave reversely with an increasing grade of turbulences. Generally, at low *Re* numbers the viscous forces are predominant, leading to laminar flow while high *Re* values represent a turbulent flow which is mainly characterised by inertia forces. The increase in drag due to higher surface roughness is also clearly visible in Fig. 3.11 accompanied by a reduction of C_M. Normally, the surface is considered to be adverse if the relative roughness *e* exceeds *0.01* or the roughness height *k 0.01D* with k summarised in Tab. 3.3 [14].

Tab. 3.3: Surface roughness for various materials [14]

Material	*k [m]*
Steel, new uncoated	5×10^{-5}
Steel, painted	5×10^{-6}
Steel, highly corroded	3×10^{-3}
Concrete	3×10^{-3}
Marine growth	5×10^{-3} to 5×10^{-2}

In the offshore industry the deterioration of the surface conditions is mainly affected by marine growth which causes a surge in wave loads on the pile. This simply traces back to the enlargement of the effective diameter of the cylinder in (3.18) and the magnitude of force coefficients, as seen above and in Fig. 3.12. The variable D_C denotes the "clean" outer diameter of the structure and t the thickness of marine growth. As marine growth can easily spread out to approximately *10.0* centimetres, most cylinders in the marine environment feature rough surfaces.

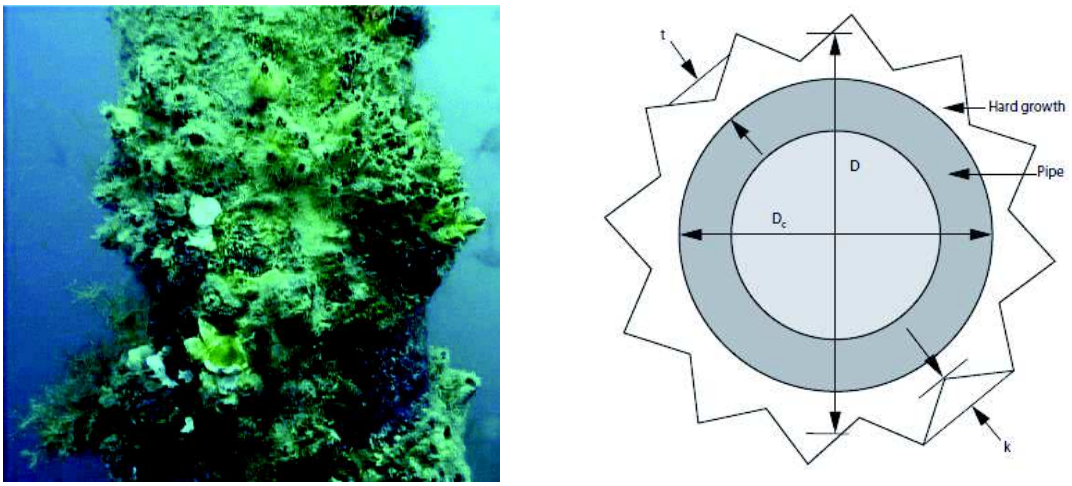

Fig. 3.12: Marine growth[2] and its geometrical consideration according to [20]

The thickness of marine growth is considered to be location dependent and to increase linearly to the specified value over two years after installation. It is said that this influencing parameter develops rather quickly compared to the overall lifetime of a monopile and requires large diameters of at least five metres in order to meet smooth surface conditions. The average density of marine growth has jointly been set to *1325.0* kg/m^3 and a general guideline of possible thicknesses is provided by *NORSIK N-003* in Tab. 3.4 [14].

$$D = D_C + 2t \tag{3.18}$$

Tab. 3.4: Reference marine growth thickness according to NORSOK N-003 [14]

Water depth [m]	*Thickness [mm]*	
	56 to 59	*59 to 72*
+2.0 to -40.0	100	60
Below -40.0	50	30

[2] Image source: Rambøll Denmark AS

3.4 Wave loads induced by irregular waves

As presented in 2.5, an irregular sea state is realised by superimposing regular wave components which are generated by an inverse *FFT* of an energy density spectrum. The wave profile and corresponding kinematics can be obtained using the same procedure. However, problems arouse regarding the necessary flow parameters such as *Re* and *KC* numbers. There are different attempts to sufficiently determine those values for the final irregular wave. For example it is possible to use characteristic or global properties from the wave spectrum and led the significant or maximum wave height and the wave period be the governing variables for the determination of *Re* and *KC* values. Unfortunately, this could not be established as the more calm parts of the corresponding time series for the irregular sea state are not represented correctly.

In contrast to this the flow characteristics can be extracted locally from the time series where a wave can be clearly defined. Here, the time from a zero-crossing until another two zero-crossings in the same point of space can be considered as appropriate. Another possibility could imply the distance between three zero-crossings, two zero-up-crossings or two zero-down-crossings for a specified time to define the wave dimensions. All other required inputs such as time series of water particle velocities and accelerations are already available and thus can be directly implemented to identify maximum kinematics and eventually force coefficients. Of course, this method engages more computational resources and it shows difficulties concerning vortex shedding and the derived properties may not fully develop towards a stationary laboratory state in a sudden transition between calm and more rough parts of a time series. But compared to greater uncertainties within the former approach, the determination of local values prevails and shall be applied in the upcoming generation of wave loads induced by irregular waves.

For the in 2.5 realised sea state the subsequent time series of the wave loads and the *OTM* is generated in Fig. 3.13 and despite the great randomness of the water surface the typical correlations between drag, lift and shear force become evident as well.

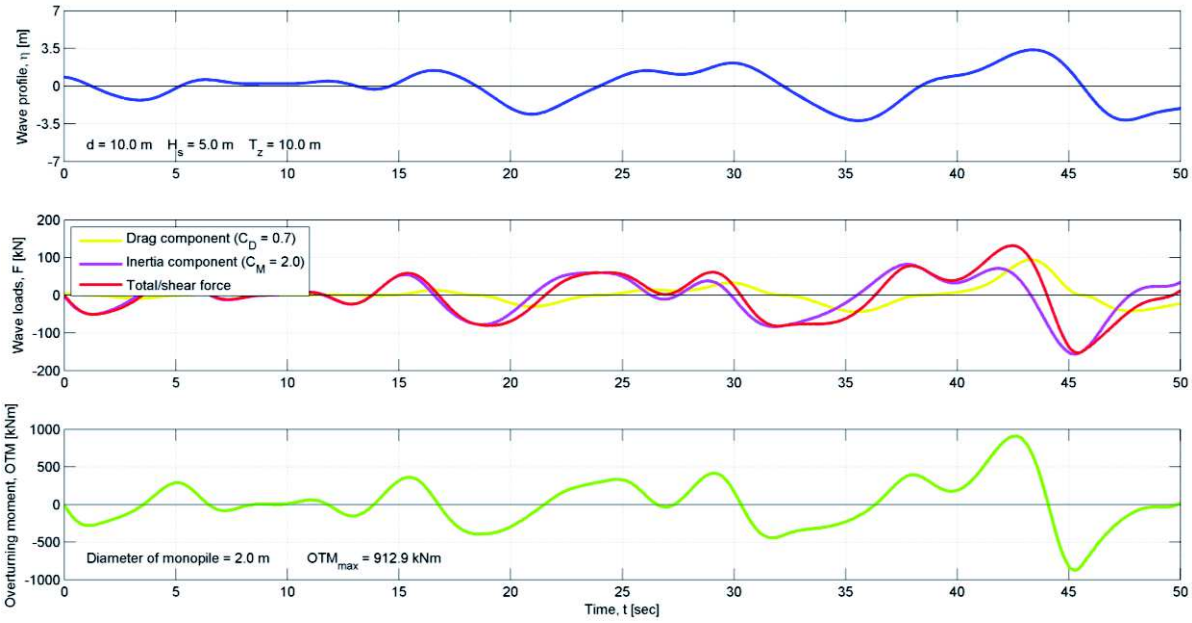

Fig. 3.13: Wave loads and overturning moment induced by an irregular sea state

Part III – Software applications

4 Software description

After major wave theories are extensively examined in the previous chapter in terms of boundary conditions and governing equations, the here applied programs shall now be presented in more details. First of all, *Rambøll's* in house wave simulator named *WAVGEN* shall be explained. As it solely relies on the theory in 2 the focus shall be more on variation and input parameters for the generation of various linear or non-linear regular and irregular waves. The new software *OCW3D* developed by *Engsig-Karup et al. (2009)* [21] is considered as a coastal engineering tool for the realisation of non-linear surface waves. On that account, the theoretical principles behind *OCW3D* and necessary settings shall be understood thoroughly in order to guarantee an accurate handling and interpretation of obtained results.

As the *OTM* shall be the final assessment criterion for the subsequent comparison and plausibility study, the applied beam solver shall be discussed as well. In order to comprehend the complete *ULS* design process and to detect any difficulties regarding the wave kinematics transfer *Rambøll's* strength analysis software called *ROSA* is described. Eventually, exemplary simulation and calculation runs shall confirm the correct interaction between all programs and its engineering application.

4.1 *WAVGEN*

If bottom fixed and transparent offshore foundations shall be exposed to hydrodynamic loads in *Rambøll's* structural analysis software, the program *WAVGEN* is generally deployed to generate velocities, accelerations of water particles and excess pressure in a rectangular grid for waves and current. The following paragraph shall cover the main calculation principles and theoretical background of this tool to be able to clearly identify the differences to the new *OCW3D* approach. In essence, *WAVGEN* constitutes an advanced analytical solver which completely avails itself of the theory discussed in 2.4, 2.5 and 2.6. The program outstands by providing higher order solutions for *Stokes'* waves and by sufficiently simulating stream function waves. Additionally, an extreme wave crest by means of the *NewWave* theory can be generated according to a chosen wave spectrum. An irregular sea state based on wave spectra can either be assessed under unidirectional or directional spreading. All in all, *WAVGEN* is able to handle the following single waves or sea states in Tab. 4.1 and to produce the corresponding kinematics stored in wave files for *Morison's* equation in *ROSA*. The input is made on simple text basis and hierarchically structured by input

cards for example describing environmental parameters or the applied wave theory. Generally, the tool accepts an alphanumeric or text, integer or fixed point format and depends on a strict column observance.

Tab. 4.1: Summary of possible wave theories and spectra in WAVGEN

Regular waves	*Spectra for irregular sea states*
NewWave	*Pierson- Moskowitz (PM)*
Stokes' 5th order	*ISSC* – modified *PM*
Sinusoidal (small amplitude theory)	*ITTC* – modified *PM*
Deep water sinusoidal	*DS449* – modified *PM*
Stream function wave (order between 3 and 42)	*JONSWAP*
	J449 – modified *JONSWAP*
	Ochi-Hubble
	User defined

As the above wave theories or sea state simulations are implemented in the program and in general only rely on significant wave height, wave period and water depth, the main work within *WAVGEN* includes the exact definition of the examination area to correctly compute all necessary wave kinematics for the water column below the instantaneous surface elevation. Thus, the wave data is computed at chosen reference points in a rectangular grid. The vertical grid lines are symmetrically aligned around the origin with a specified and constant distance. In contrary to this, the horizontal grid lines can either show a uniform or varying spacing. The latter shall be defined between the sea floor and the highest wave elevation for absolute z-coordinates, as depicted in Fig. 4.1. The origin of regular waves is placed at the wave crest at $x = 0.0\ m$ whereas the associated x-coordinate for irregular sea states can vary arbitrarily [15].

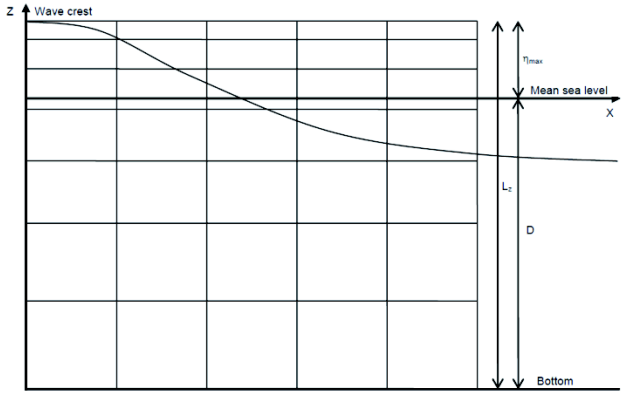

Fig. 4.1: Grid system with absolute z-coordinates [15]

For a viewing window with relative *z*-coordinates, the horizontal grid lines are situated regularly in a relative coordinate system from the bottom to the sea level which can be seen in Fig. 4.2. However, if any profile extension described in 2.4.4 is applied the grid becomes irregular when the actual water level is considered in Fig. 4.2. For the later implementation in *ROSA* it is important to point out that the coordinate systems in both programs are completely independent of each other as only the wave direction angle is used to define the direction of the incoming wave with respect to the position of the monopile foundation [15].

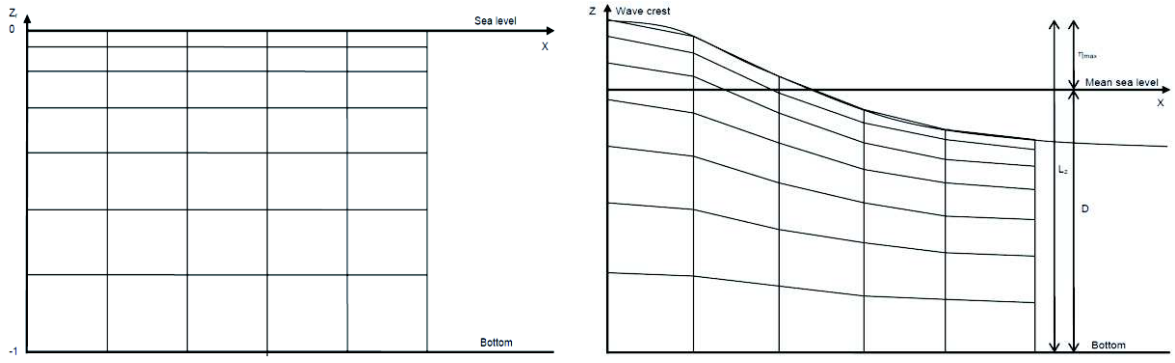

Fig. 4.2: Grid system with relative z-coordinates (left) and after stretching to absolute coordinates (right) [15]

The geometry data constitute a very important input parameter as the accuracy of the wave loads later in *ROSA* highly depend on the chosen spacing method in the *z*-direction of the grid. Besides constant spacing the depth variation can either be performed by an arithmetic or geometric progression which are both generally more accurate compared to an equally spaced grid. The former simply relies on a common difference D_z so that each number varies from the previous one by a constant value. The geometric approach describes a sequence of numbers with a constant or common ratio R_z between them [15].

One major component of *WAVGEN* is the possibility of replacing certain parts of a selected irregular wave with a regular wave with specified properties. This helps to clearly define and control an extreme sea state (*ESS*) within an irregular wave system which is essential in time series for *ULS* analyses and the key aspect of *Rambøll's* conventional approach presented more precisely in 5.3.

WAVGEN is also able to include different currents and to import user-defined wave surface elevations but for the subsequent comparison study all other external influencing factors shall be disregarded. Fig. 4.3 and Fig. 4.4 show possible wave simulations in deep and shallow waters for the metocean data in Tab. 2.1 whereas a comparison to the analytical solution with *Matlab* is presented in 4.4.1.

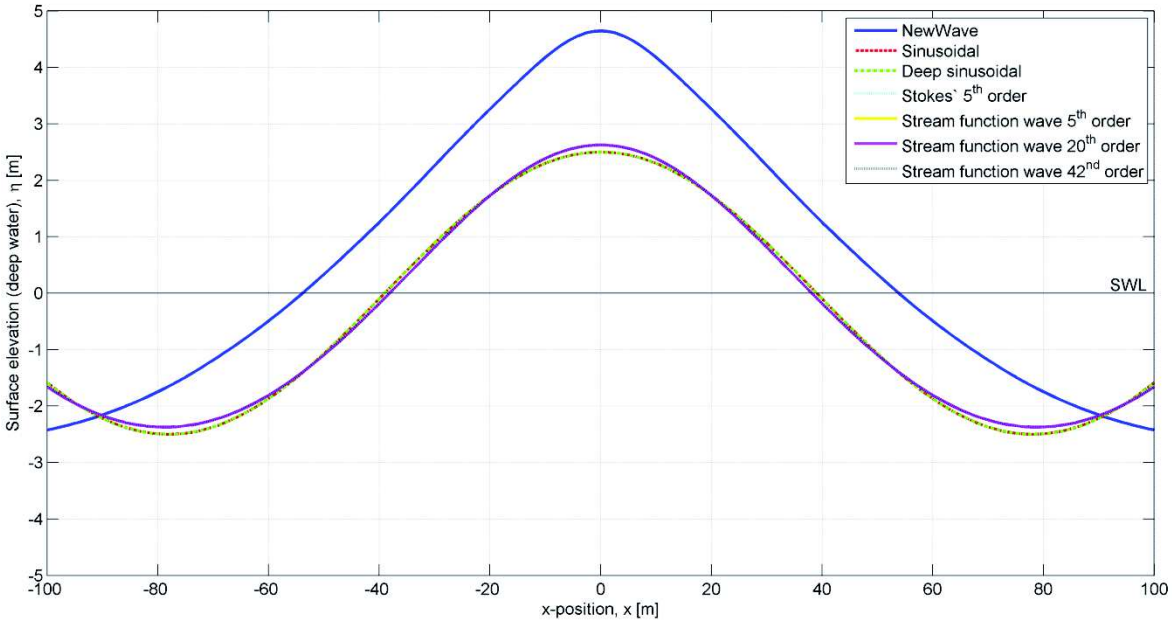

Fig. 4.3: Exemplary wave in deep water by means of different wave theories provided by WAVGEN

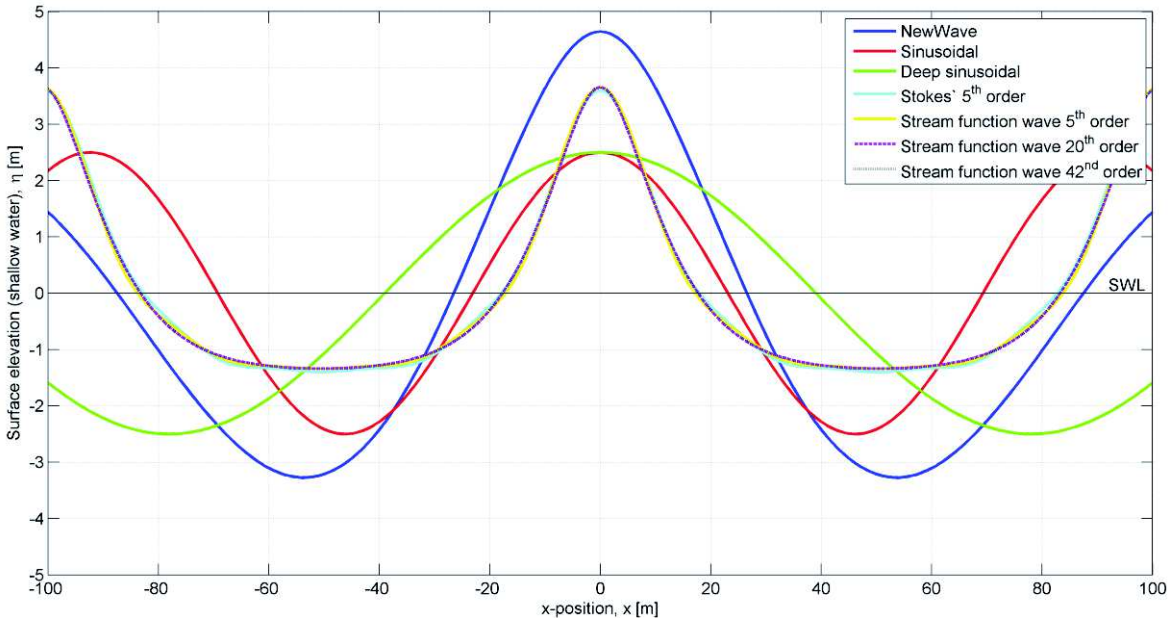

Fig. 4.4: Exemplary wave in shallow water by means of different wave theories provided by WAVGEN

4.2 *OceanWave3D*

In contrast to the analytical solution by *WAVGEN* based on the theory in 2, *OCW3D* focuses on numerical wave modelling which is built mainly upon the evaluation of gradients and time integration. The former or the spatial discretisation is handled in a prescribed computational net which follows the principle that more grid points yield an advanced approximation of the gradient for a defined Δx and a faster solution convergence for a decreasing Δx. Higher order discretisation contrarily may affect the stability of the process negatively [22].

The temporal discretisation and associated time integration can either be conducted in explicit or implicit form. The explicit method provides a solution at a later time step solely by using information from the current state. For wave simulations this means that the free surface η poses the main unknown and limiting parameter as the water surface may only feature simple shapes and cannot handle any overturning events shown in Fig. 4.5.

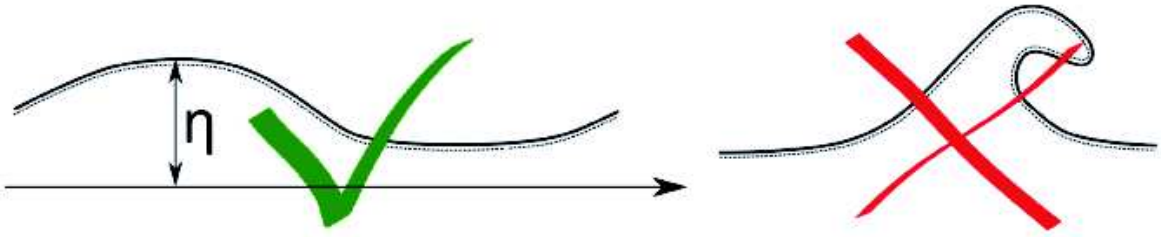

Fig. 4.5: Pro and con of explicit time integration for the water surface [22]

However, an implicit form includes not only the actual time step but also the later one to solve the system of equations. This allows much greater time steps but of course accompanied by larger computational effort. Here, the implicit solution to the location of the free surface is determined by means of an indicator field but with the drawback of a surface elevation with no sharp interface. One major advantage is the correct implementation and realisation of breaking waves and its overturning behaviour as illustrated in Fig. 4.6 [22].

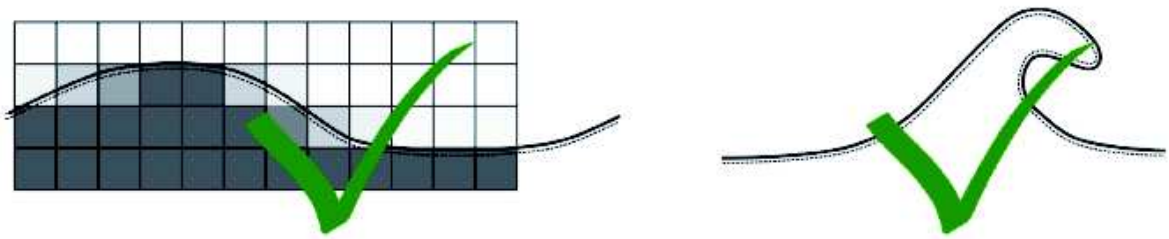

Fig. 4.6: Properties of the implicit solution to the free water surface [22]

OCW3D avails itself of the explicit solution approach to record the free surface and in order to make the grade of a complete numerical wave tank it also must account for wave generation and absorption. Together with the validity limits of common wave theories the following methods to generate and absorb waves in Tab. 4.2, Tab. 4.3 and Fig. 4.7 define the main boundary conditions of *OCW3D's* numerical wave tank.

Tab. 4.2: Methods to numerically generate waves [22]

Method	*Description*	*Advantages*	*Disadvantages*
Directly at boundary (Dirichlet-condition)	Prescribe velocity field at boundary	Simple implementation of analytical or external wave data Low computational effort	Possible volume build-up due to wave induced mass fluxes for long simulations
Wave paddle	Accelerate boundary similar to physical paddle	Readily comparable to laboratory tests No volume build-up due to impermeable paddle	Complex conversion of analytical wave theory into paddle motion Increase of computation, roughly *20%* to *40%*
Relaxation zone	Implement a weighting between a target and computed field	No volume build-up due to constant *SWL* in the relaxation zone Simple integration	Increase of computation due to minimum length for the relaxation zone as long as the wave

Tab. 4.3: Methods to numerically absorb waves [22]

Method	*Description*	*Pros*	*Cons*
Correction to incident wave signal	Correct velocity field by constant scalar	Simple integration Larger validity range in case of higher order corrections although more difficult to compute	Valid reflection compensation only in shallow waters Reflection coefficients of *10%* to *15%* possible
Correction to paddle motion	Correct motion of wave paddle	Readily comparable to laboratory tests Possible implementation of existing control system of actual wave tank	Increase of computation, roughly *20%* to *40%* Difficult integration if no control system available
Relaxation zone	Implement a weighting between a target and computed field	Efficient double function Integration of target solution with *SWL* at outlet boundaries (sponge layer)	Increase of computation due to minimum length for the relaxation zone twice the wave

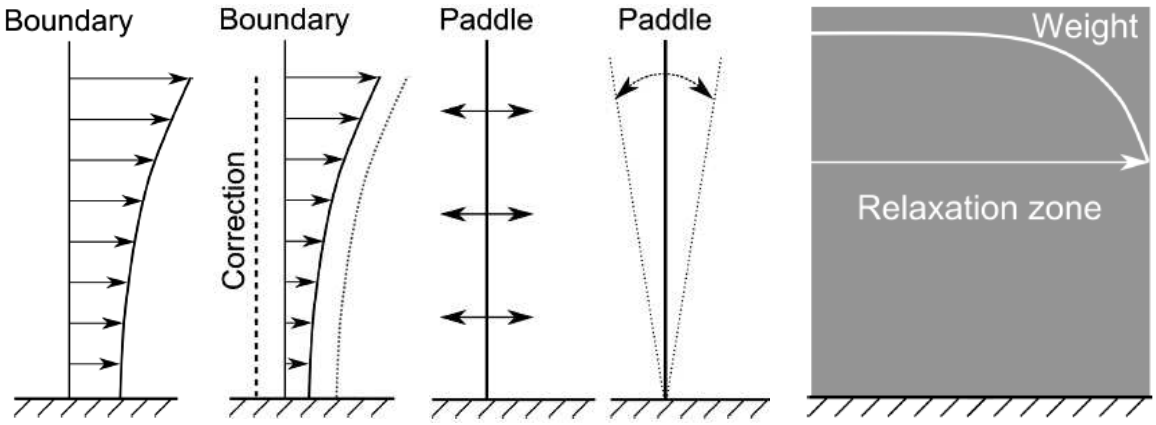

Fig. 4.7: Visualisation of wave generation methods (1. prescribed velocity field, 2. correction to velocity field, 3. wave paddle with correction, 4. relaxation zone)

In essence *OCW3D* represents a numerical wave tank which solves for and tracks the free water surface whose oscillation is excited by a wave generation zone at the first boundary and dissipated in an absorption zone in the end, visualised in Fig. 4.8. More details on the actual solution method and the governing equation shall be given in the subsequent paragraph followed by a closer, more practical look on input parameters and output files.

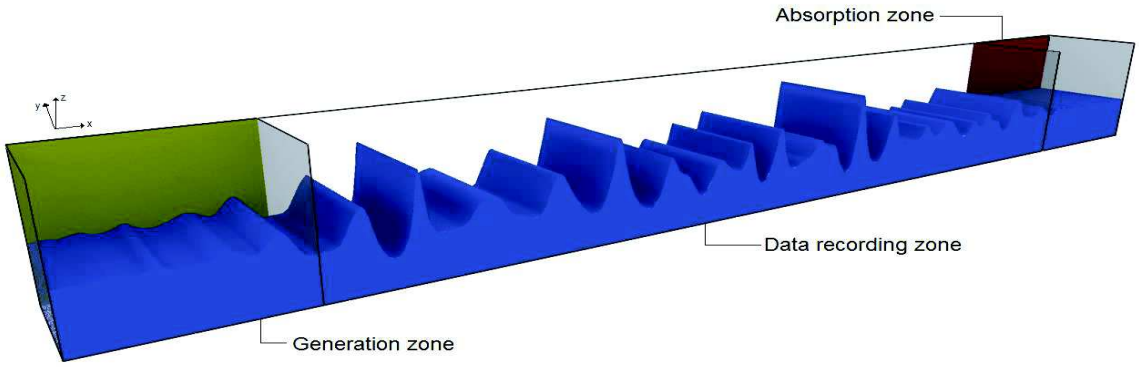

Fig. 4.8: Physical principle behind OCW3D's numerical wave tank

4.2.1 Background and governing equations

The core of the numerical wave tank in *OCW3D* is a three-dimensional fully non-linear potential flow solver which describes the generation as well as propagation of non-linear regular and irregular waves. Until wave breaking is expected a considerable numerical efficiency and remarkable accuracy is assured by implementing the three-dimensional *Laplace* equation which according to *Paulsen (2013)* [2] "is discretized by higher order finite difference stencils in a time-invariant computational domain". The potential flow solution for non-breaking free surface waves concentrates on a scalar velocity potential Φ and the surface elevation η with respect to *SWL*, assuming an inviscid and incompressible fluid [23]. As previously stated, the gradient of the velocity potential in (4.2) with the horizontal gradient operator ∇_H is used to define the physical fluid velocities in (4.1) [2].

$$(\boldsymbol{u}_H, w) = (u, v, w) \tag{4.1}$$

$$(\boldsymbol{u}_H, w) = (\nabla_H \Phi, \partial_z \Phi) \quad with \quad \nabla_H = (\partial_x, \partial_y) \tag{4.2}$$

Similar to conventional wave theories the *kinematic free surface* condition which prevents water particles from penetrating the free surface is integrated as in (4.3) by means of free surface quantities in (4.4) [2].

$$\partial_t \eta = -\nabla_H \eta \cdot \nabla_H \widetilde{\Phi} + \widetilde{w}(1 + \nabla_H \eta \cdot \nabla_H \eta) \tag{4.3}$$

$$\widetilde{\Phi} = \Phi(x, \eta) \quad and \quad \widetilde{w} = \Phi(x, \eta) \tag{4.4}$$

The integration of the momentum equation yields the *Bernoulli* equation for an unsteady fluid which eventually takes up the form in (4.5) if pressure equals zero at the free surface for $z = \eta$. Consequently, the *dynamic free surface* condition is obtained.

$$\partial_t \widetilde{\Phi} = -g\eta - \frac{1}{2}\left(\nabla_H \widetilde{\Phi} \cdot \nabla_H \widetilde{\Phi} + \widetilde{w}^2(1 + \nabla_H \eta \cdot \nabla_H \eta)\right) \tag{4.5}$$

Due to the non-linear properties the above presented boundary conditions in (4.3) and (4.5) do not provide a closed form solution and thus are approximated numerically in time by a fourth-order *Runge-Kutta* method [23]. On that account, the vertical velocity at the free surface $\widetilde{w}$ must be available which is achieved by determining the velocity potential in the fluid volume for each time step. So in order to receive indications on the surface elevation the *kinematic bottom* condition in (4.8) which prohibits sea floor penetration of the water particles is introduced and the *Laplace* equation in (4.7) "is solved by a flexible order finite difference scheme in a time-invariant *(x,σ)*-domain", following *Paulsen (2013)* [2].

$$\Phi = \widetilde{\Phi} \quad at\ z = \eta \tag{4.6}$$

$$\nabla_{\mathrm{H}}^2 \Phi + \partial_{zz}\Phi = 0 \quad at - d \le z < \eta \tag{4.7}$$

$$\partial_z \Phi + \nabla_H d \cdot \nabla_{\mathrm{H}} \Phi = 0 \quad at\ z = -d \tag{4.8}$$

In this case, the water depth d accounts for the distance from the sea floor to *SWL* whereas vertical borders for the numerical solution comply with *Neumann's* homogeneous boundary conditions. The non-conformal transformation σ in (4.9) is used to define and convert the examination grid from the physical to the computational domain which should be clustered near the surface due to the expected presence of larger gradients.

$$\sigma = \frac{z + d(x)}{\eta(x,t) + d(x)} \tag{4.9}$$

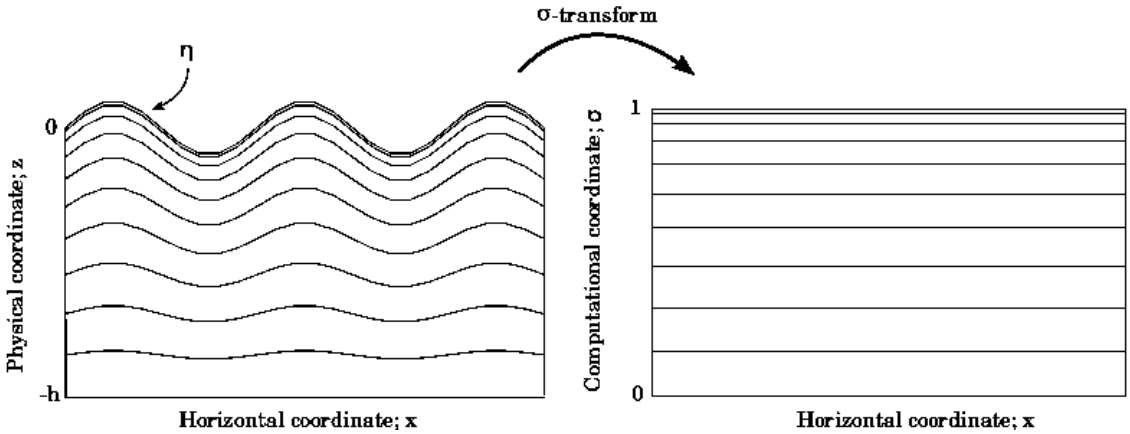

Fig. 4.9: Physical grid versus computational σ-domain in OCW3D [2]

The computational grid is displayed in Fig. 4.9 and by looking at the expression in (4.9) it is argued that the transformation can only be applied for a surface elevation represented by a single valued function. That implies that wave breaking would cause an abort of the numerical modelling, requiring an extra stability control for the solver. Therefore, *OCW3D* uses a function which considers wave breaking by decreasing the energy content within the wave simulation. The effect of the breaking filter shall be evaluated more precisely in 5.3.2 but it is taken into account by defining the following user defined strength parameter in (4.10). In other words it simply reduces the energy of waves whose vertical water particle acceleration exceeds a certain gravitational fraction [23].

$$\frac{dw}{dt} < \gamma g \quad with \quad \gamma \in [0.4; 1] \tag{4.10}$$

Subsequently, the chain rule in (4.11) and (4.12) is implemented in *OCW3D* to transfer the velocity potential Φ in the computational σ-domain into physical velocities $\{\boldsymbol{u}_H(\boldsymbol{x},z);(w(\boldsymbol{x},z)\}$ [2].

$$\boldsymbol{u}_H(\boldsymbol{x},z) = \nabla_H \Phi(x,\sigma) + \nabla_H \sigma \partial_\sigma \Phi(x,\sigma) \tag{4.11}$$

$$w(\boldsymbol{x},z) = \partial_\sigma \Phi(x,\sigma) \partial_z \sigma \tag{4.12}$$

With respect to the summary of wave generation and absorption methods in Tab. 4.2 and Tab. 4.3 a line source relaxation approach presented by *Larsen & Dancy (1983)* is preferred for the potential flow solver in *OCW3D*. At the beginning of the numerical wave tank a relaxation zone is defined where a specified target solution is applied. The same procedure can be taken for absorbing waves to avoid any perturbations of reflected or refracted waves. By introducing an inhomogeneous time varying *Neumann* constraint at the tank inlet the surface oscillation can be directly excited without installing a relaxation zone. The boundary conditions of the *Laplace* expression in (4.7) respectively is set to the requirement in (4.13) [2].

$$\frac{\partial \Phi}{\partial x} = u\,(z,t) \tag{4.13}$$

This generation option has proved itself, especially with respect to reproducing laboratory measurements. In that case, u is adjusted in line with the velocity of the wave paddle. This is done in the following comparison between *OCW3D* and actual tank tests provided by *Deltares (2016)*. The surface elevation in Fig. 4.10 is equivalent to a significant wave height of *8.10* metres, a peak period of *13.0* seconds and a water

depth of *30.15* metres. By implementing the same paddle signal in *OCW3D* the numerical wave tank reveals an almost perfect replica of the recorded water surface, validating and emphasising the stable as well as extremely profitable abilities of this fully non-linear potential flow solver. Additionally, the software is confirmed in terms of grid convergence for two- and three-dimensional wave scenarios in accordance to [23] whereas the computational effort is investigated further in the work by *Engsig-Karup et al. (2009)*.

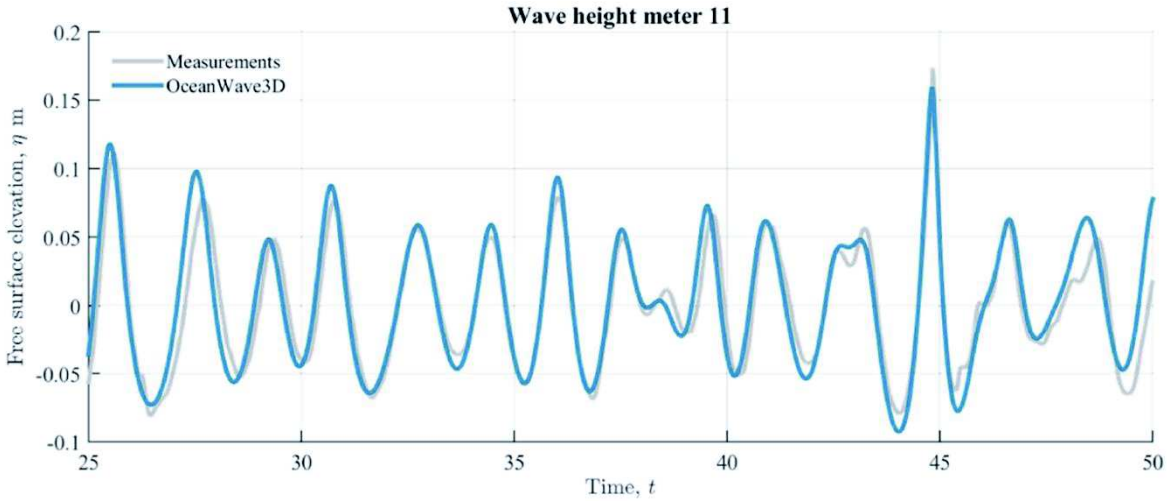

Fig. 4.10: OCW3D versus tank measurements, providing a very satisfying validation of the fully non-linear potential flow solver [23]

4.2.2 Variation and input parameters

The following chapter shall give a brief hands-on introduction to the new software and its working environment. Although the most stable and properly validated version runs in a *LINUX* environment, the available graphical user interface (*GUI*) in Fig. 4.11 and the implemented potential flow solver provide a comprehensible and user friendly application, once a virtual box ensures a sufficient connection between *LINUX* and *WINDOWS*. All variation parameters are defined within the *GUI* and stored in an input file which is read by the solver. As a result, the software yields a binary file containing all wave properties as well as kinematics and a certain amount of *FORTRAN* files which show the complete surface elevation along the *x*-axis for each specified time step. A built-in tool filters the attained wave kinematics for the wave profile and calculates wave loads by means of *Morison's* equation, converting the complex binary file into handy text documents for further processing. Additionally, this add-on enables a transfer of all wave kinematics from a binary format to a more structured and commonly used *FLEX5* output file which however shall be presented in more details in 4.3.1.

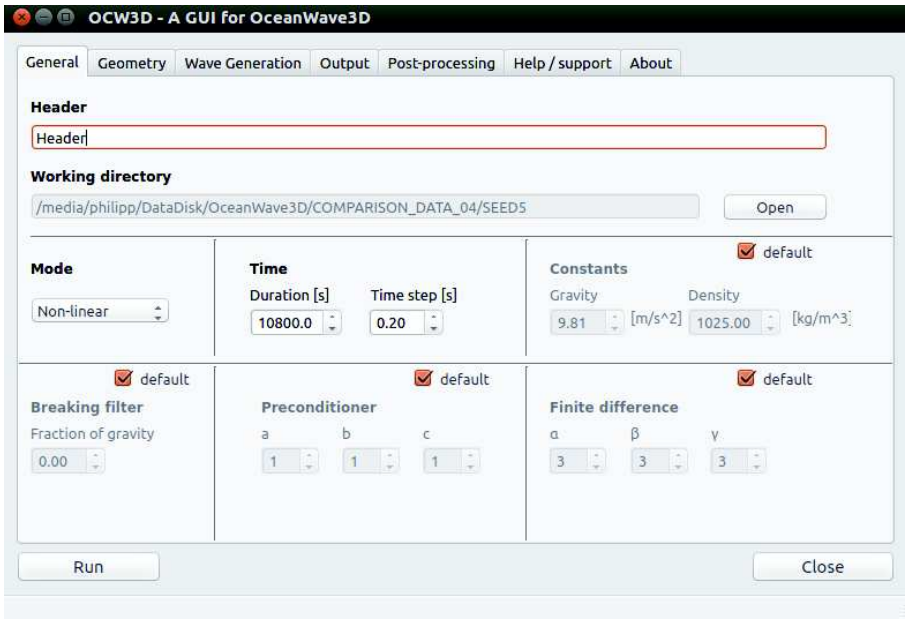

Fig. 4.11: Graphical user interface of OCW3D

After temporal and spatial resolution are defined in terms of spacing and total length to meet the requirements of the non-linear potential flow solver in 4.2.1, *OCW3D* is capable of realising a regular or irregular wave whereas the latter can be based on a *JONSWAP* or *PM* wave spectrum and executed under linear or non-linear conditions. The non-linear regular wave is generated by means of the previously explained stream function theory. As the realisation of a complete non-linear sea state shall be explained thoroughly in the course of the subsequent comparison and feasibility study, only a validated stream function wave shall be tested to illustrate and specify necessary input parameters in the new program.

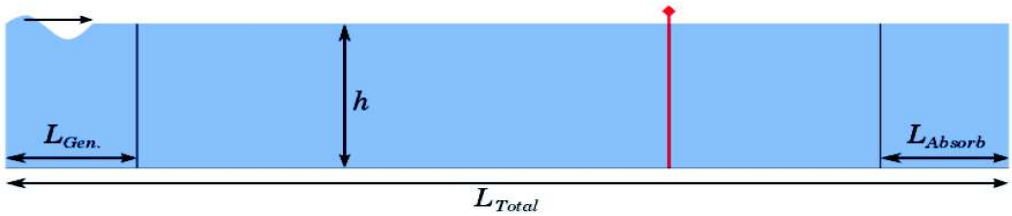

Fig. 4.12: Division of numerical wave tank in OCW3D [22]

For the realisation of a *40.0* metres long and *1.0* metre high stream function wave [22] provides the following recommendations on the most important settings. They assure a stable and accurate numerical solution of the *PDE* whereas the *Courant-Friedrichs-Lewy* (*CFL*) number in (4.14) describes the ratio between spatial and temporal spacing for solving *PDE* numerically.

$$CFL = \frac{u \cdot dt}{dx} \leq 1.0 \quad with \quad u = u_{max} = \sqrt{\frac{g}{d}} \cdot H_{max} \tag{4.14}$$

Recommended settings:

- Activated *vertical stretching* to cluster grid points near the free surface for improved accuracy
- More than ten points per leading order wave length for *horizontal resolution*
- Ten to fifteen points along the *z*-axis for *vertical resolution*
- *CFL* number below one for the *time step* definition
- *Generation length* as long as deep water wave length
- *Absorption length* twice as long as deep water wave length

The summarised input parameters in Tab. 4.4 yield the example stream function wave in Fig. 4.13. The number of grid points in the horizontal direction represents fifteen points per wave length whereas one point along the *y*-axis limits the simulation to a two-dimensional problem.

Tab. 4.4: Input parameters to simulate a stream function wave in OCW3D

Input parameter	*Value*
Time duration, T_{dur} [sec]	200.0
Time step, dt [sec]	0.1
Total length, L_{total} [m]	600.0
Generation length, L_{gen} [m]	100.0
Absorption length, L_{abs} [m]	100.0
Number of grid points, [n_x, n_y, n_z]	[226, 1, 10]

By looking at the displayed data in Fig. 4.13 one can easily recognise the resemblance of *OCW3D* to an actual wave tank as the surface elevation recorded at different positions along the numerical simulation heavily differs in amplitude and propagation. The further away the position is to the generation zone or the specified paddle signal respectively the more time is elapsed to record any oscillations. Right in the generation zone the wave paddle is responsible for a fast and persistent excitation of the water surface along the complete timeline from the beginning on. Subsequently, the wave signal takes a spell to proceed along the horizontal axis and shortly after *40.0* seconds the first surface variation is detected at $x = 300.0$ metres. Naturally, the signal requires even more time to reach the last extraction point which is placed right in the absorption zone. Here, it is clearly visible how the previously mentioned boundary conditions of the relaxation zone dissipate the energy in the system and immensely reduce the wave height, eventually resulting in a complete fading away of the initial signal.

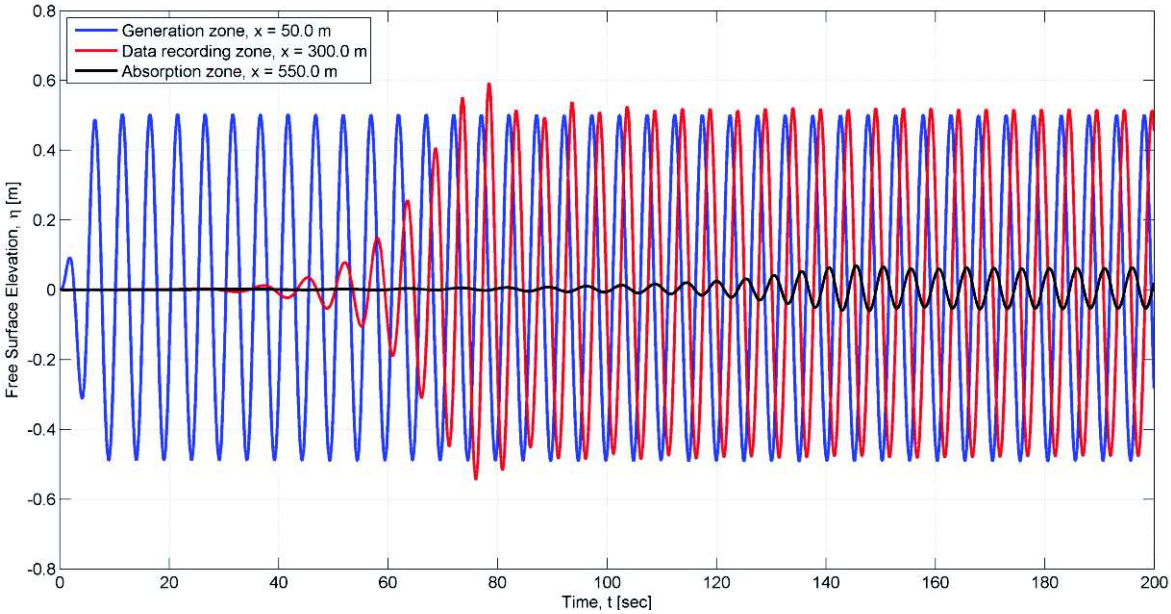

Fig. 4.13: Surface elevation of a stream function wave extracted at different positions along the numerical wave tank

The same behaviour can be seen within the spatial domain in Fig. 4.14. At the start of the simulation the water surface is completely calm and after *50.0* seconds the first elevation is developed by the paddle and propagates through the numerical wave tank. At the final time step it is possible to perceive a fully developed stream function wave which enters the absorption zone after *500.0* metres. Here, the amplitude starts to descend and finally abates a couple of metres before the end of the artificial wave tank.

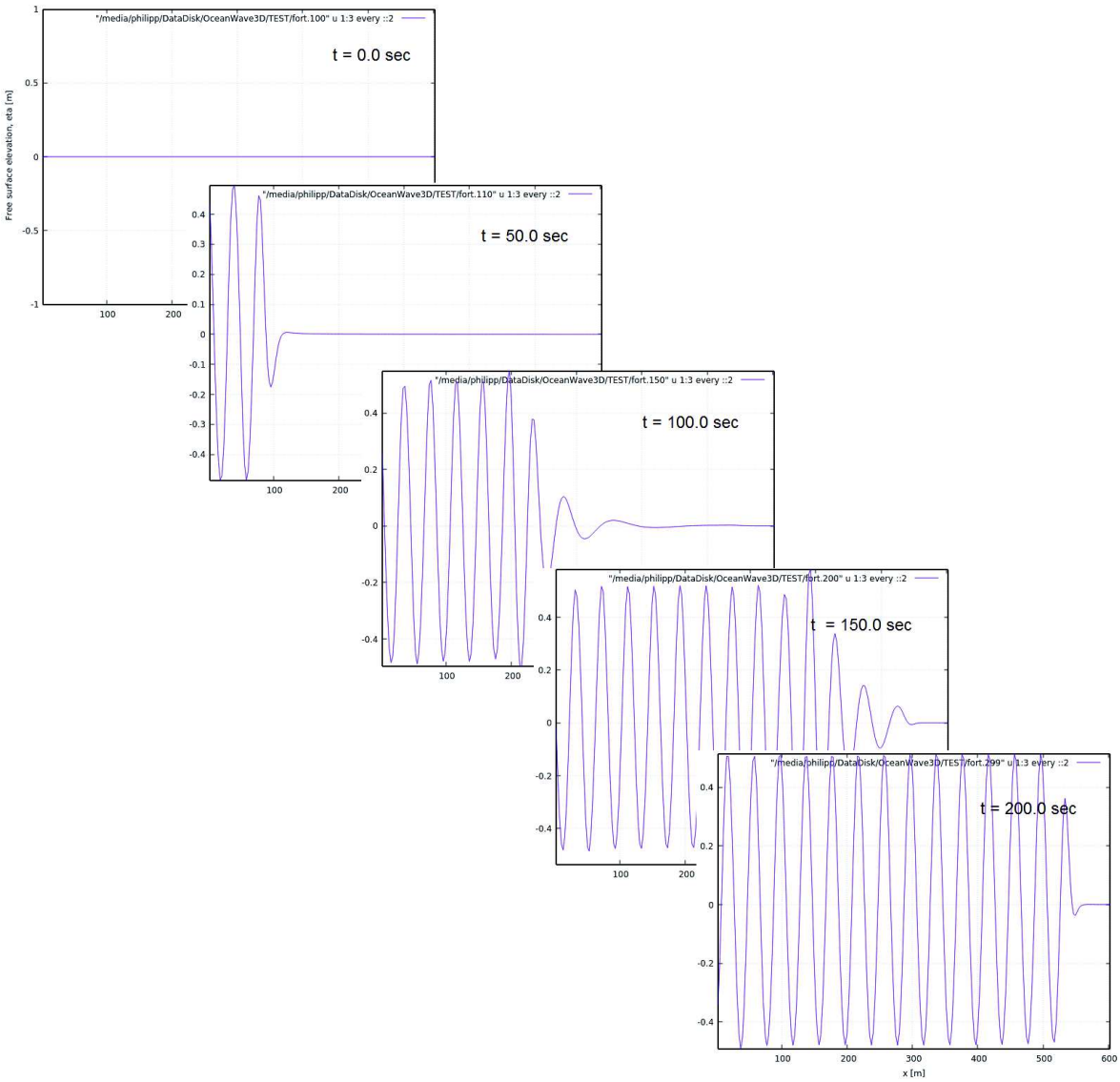

Fig. 4.14: Spatial description of OCW3D's numerical wave tank

Since the horizontal resolution plays a crucial role in the accurate application of the fully non-linear potential flow solver, the differences between varying amounts of grid points shall be exemplified in the following graphs in Fig. 4.15 and Fig. 4.16. Here, it can generally be stipulated that convergence is achieved with approximately ten points along the x-axis in both the temporal as well as spatial domain. The surface elevation plotted in yellow appears deceptive or inaccurate which derives from the rather coarse net of grid points along the horizontal axis. It is important to keep in mind that a low spatial resolution does not imply a low temporal resolution. Again one is able to distinctively identify the difference in the surface elevation in the spatial or temporal resolution while the latter illustrates the effect of the generation zone and the former the energy reduction of the absorption zone.

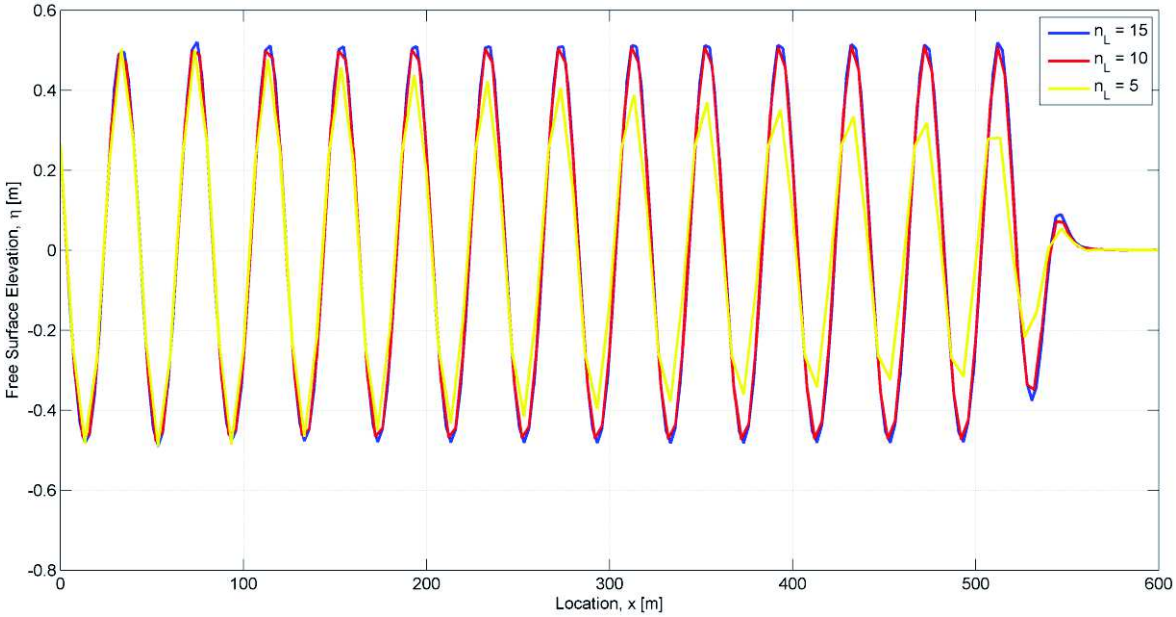

Fig. 4.15: Different spatial resolutions for the surface elevation in space

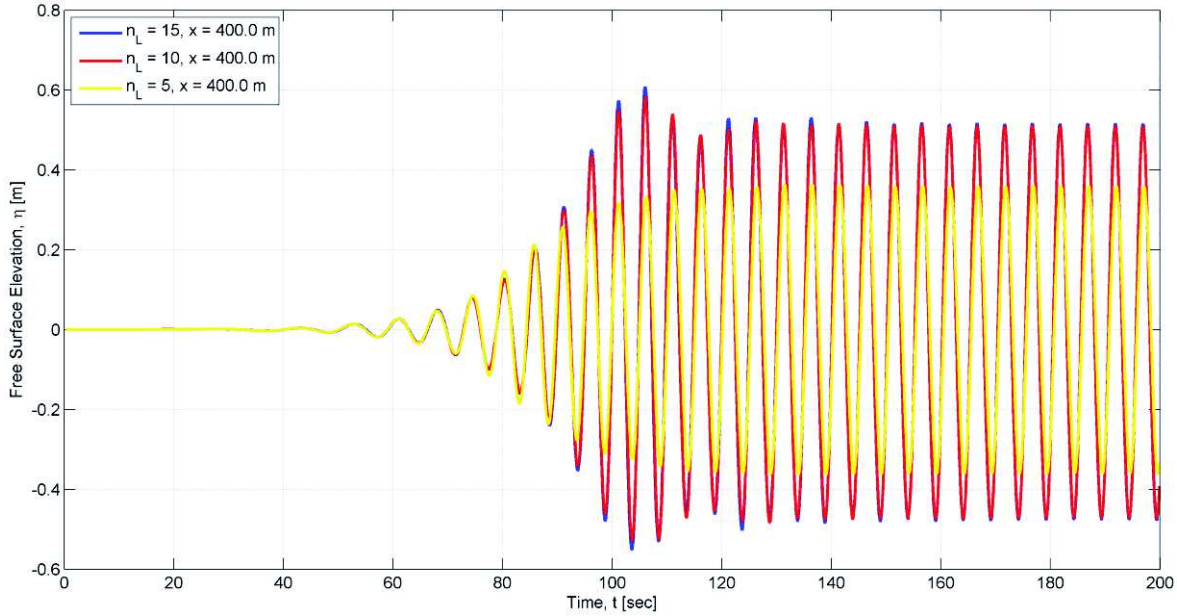

Fig. 4.16: Different spatial resolution for the surface elevation in time

The here obtained knowledge of the *OCW3D* approach shall help to understand the differences to the analytical solver in *WAVGEN* and shall be used to emphasise the exceptional abilities of this fully non-linear potential flow method. More details on the realisation of an irregular sea state within *OCW3D* and a corresponding study on the temporal resolution with respect to water surface accuracy shall be discussed in 5.3.2.

4.3 *ROSAP/ROSA*

The *Ramboll Offshore Structural Analysis programs (ROSAP)* have been developed by in-house experts and designers to provide unique, stable and up-to-date tools for the design, assessment and lifetime extension of onshore as well as offshore steel installations. The entire package includes static and dynamic analyses of spatial frame structures exposed to hydrodynamic, wind and constant forces or accelerations in line with commonly accepted standards. This chapter shall contain a brief description of the solution methods, in- and output format whereas a second focus shall be on how the program reads wave kinematics and transfers them into wave loads. The model layout and the implementation of the foundation shall be discussed in more details in 5.2.

ROSA constitutes the main *FE*-solver which can be supplemented with various add-ons for example with *FATIMA* for fatigue calculations or *RONJA* for non-linear analyses with large displacements and non-linear elasto-plastic material behaviour. Additionally, results in form of stresses and deformations as well as the entire *FE*-model can be visualised in the so-called *STRECH* program. The numerical description and calculation is based on *FORTRAN*, resulting in a console application controlled via *Windows* command line in the project directory [24]. Generally, the complete package is deployed for evaluating jackets, topsides, offshore bridges and risers. *ROSA* particularly focuses on static and dynamic analysis of spatial frames, truss structures and piping systems under a great variety of different loads. Here, it differs between linear and non-linear systems for which it makes use of appropriate time integration methods for the final solution. The dynamic response of a linear model with n degrees of freedom follows the main principle in (4.15) where the dot expresses the differentiation with respect to time and all matrices remain constant during the solving procedure [24].

$$\boldsymbol{M}\ddot{x} + \boldsymbol{C}\dot{x} + \boldsymbol{K}x = h(t) \tag{4.15}$$

where:

$\mathbf{M}$ = structural mass matrix
$\mathbf{C}$ = structural damping matrix
$\mathbf{K}$ = structural stiffness matrix
h(t) = external forces

In case of non-linear systems the stiffness and damping contributions are substituted by non-linear internal forces $\boldsymbol{g(x,\dot{x})}$ in (4.16).

$$\boldsymbol{M}\ddot{d} + \boldsymbol{g}(\boldsymbol{x}, \dot{\boldsymbol{x}}) = h(t) \tag{4.16}$$

In contrary to the static solution with a load step approach the dynamic calculation is governed by time and the time increment Δt in (4.17) may either be constant or shall be adjusted in accordance to the number of needed equilibrium iterations. The initial conditions in *ROSA* are computed according to the loading at time zero when velocities and acceleration are usually set to zero as well.

$$t_{n+1} = t_n + \Delta t \tag{4.17}$$

Due to the considerable non-linearity of possible extreme waves within irregular sea states and the high susceptibility to vibrations the monopile foundation shall be assessed under dynamic conditions applying the generalised α-method. This helps to correctly transfer the non-linear wave kinematics into respective structural responses. In order to fulfil (4.15) and (4.16) *Rayleigh* damping shall be applied using the values in 5.1 and resulting in a constant damping matrix as a linear combination of mass and stiffness matrix, as expressed in (4.18) with (4.19) and (4.20). The damping ratios ξ_1 and ξ_1 are assumed for the two cyclic eigenfrequencies ω_1 and ω_2 [25].

$$C = \alpha_1 M + \alpha_2 K \tag{4.18}$$

$$\alpha_1 = \frac{2\omega_1\omega_2}{\omega_2^2 - \omega_1^2}(\xi_1\omega_2 - \xi_2\omega_1) \tag{4.19}$$

$$\alpha_2 = \frac{2(\xi_2\omega_2 - \xi_1\omega_1)}{\omega_2^2 - \omega_1^2} \tag{4.20}$$

For comparison and validation reason the structure shall also be examined under quasi-static conditions. Here, the wave loading is of primary interest whereas the response of the structure plays an inferior role. All dynamic effects in terms of inertia and damping are ignored similar to the static analysis although determining loads with respect to time increments. Consequently, the nodal velocities and accelerations equal to zero during the solution [24].

Besides directly applied node or beam loads it is possible to automatically define environmental loads in form of gravity, acceleration, rotation, temperature, pressure, buoyancy, wave, current and wind, reducing the amount of input as well as the risk of errors [24]. In case of sea loads the tool is able to determine the position of the wave and structure to yield the most critical impact and thus maximum load sum. Wave and current forces are computed in accordance to *Morison's* equation, including water

particle velocities and accelerations, as described in 3.2. The required in-line load coefficients are set to default values and if necessary adjusted by surface roughness influences. The change of buoyancy loads due to additional excess pressure caused by the wave motion is considered by *WAVGEN* and thus in the resulting wave loads. As the main area of application refers to bottom fixed installations the program excels with simultaneous solutions for a linear beam model and a non-linear pile foundation, not depending on any other single software and their input. Boundary elements or structural support represented as springs can be exposed to prescribed displacements or loads and link elements allow the coupling of two structural nodes to simulate a constructive connection between two parts [24]. Those modelling approaches shall be described more precisely by means of the actual monopile model in 5.2.

4.3.1 Interface adaptation with *OceanWave3D*

For the computation of wave loads *ROSA* relies on a wave file which contains velocities and accelerations along the specified coordinates and grid points. This may be generated by *WAVGEN* or provided by any other source for example in this case *OCW3D*. Depending on the wave theory and the increasing complexity of an irregular sea state compared to a regular wave the kinematics data must either be packed in an *ASCII* or binary format. For the conventional approach all software packages are attuned in such a way that *ROSA* is able to directly call *WAVGEN* with certain input parameters and reads its produced wave file to initiate *Morison's* equation. However, the interaction between *ROSA* and the foreign *OCW3D* requires additional work for post-processing and validating to ensure that all kinematics are transferred flawlessly.

Due to the close cooperation of *Rambøll* with major players in the offshore wind industry the possibility of importing external wave files have already been developed to facilitate the data and result exchange in the course of joint projects. This existing interface shall be used as the initial basis for integrating *OCW3D* in *Rambøll's* working process. Additionally, it has been agreed to focus on the data structuring and recording way conducted by the open source code *FLEX5*. This console application has been written by *DTU* and is used to simulate any loads on off- and onshore wind turbines. Due to the easy accessibility and distinct output format the *FLEX5* approach is considered as an appropriate solution for the wave kinematics transfer. As described in 4.2.2, the definition of the grid in *OCW3D* is decisive for the scale and structure of the generated *FLEX5* file. Each line in the data represents a single time interval and contains the associated wave kinematics in form of vertical and horizontal velocities as well as accelerations for a specified amount of relative depths.

Those are extracted for a certain number of points denoted as α in the spatial domain around the centre line of the structure. However, this plays a more important role for the design of jacket foundations because then the x-coordinates of the grid and the α-value can be set in a way that they match the position of examined cords and braces of such complex structures. For the monopile it is only necessary to extract wave kinematics at the centre line because *Morison's* equation takes the structural extent into account automatically. As seen in Fig. 4.17 showing a simplified model and the resulting file scheme, each kinematics block is divided by the respective wave elevation η at the considered point in the x-direction.

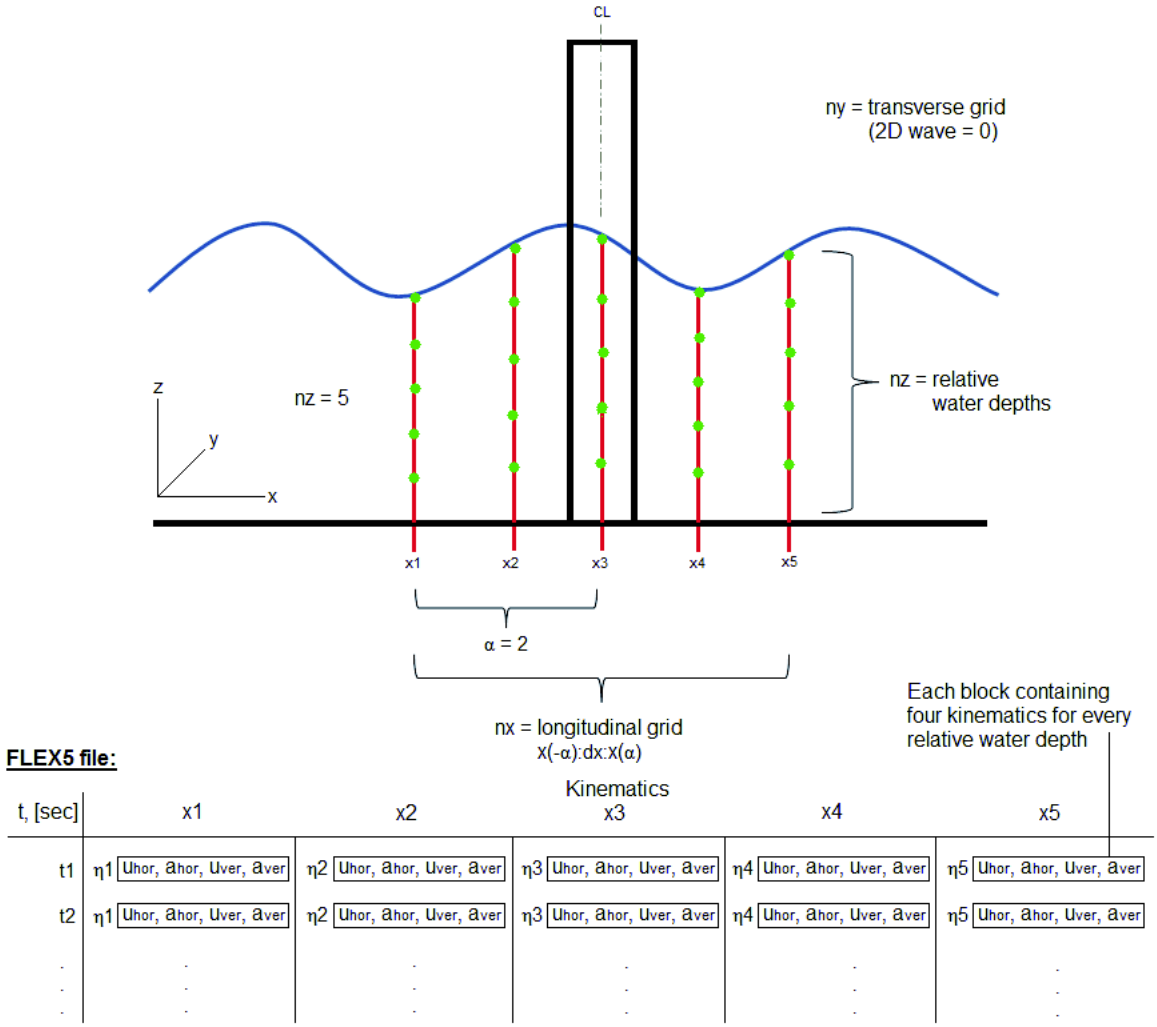

Fig. 4.17: Simplified OCW3D model and corresponding structure of FLEX5 file

The newly developed converter in *OCW3D* satisfactorily yields the desired structure and complete data set of the wave kinematics for the specified grid. Unfortunately, it shows some difficulties if the wave increases to a size where the corresponding wave height or kinematics exceed double digits. As a consequence, the *FLEX5* file loses its strict order and certain columns change positions, as seen in the example in Fig. 4.18.

955	187.40	3.48	3.94	3.85	3.61	3.28	2.92	2.59	2.30
956	187.60	5.50	6.35	6.22	5.85	5.30	4.65	4.01	3.42
957	187.80	7.67	8.13	7.99	7.58	6.94	6.15	5.30	4.48
958	188.00	9.43	9.29	9.14	8.69	8.00	7.12	6.16	5.21
959	188.20	10.29	9.82	9.66	9.20	8.49	7.58	6.59	5.59
960	188.40	10.09	9.63	9.48	9.04	8.36	7.51	6.56	5.62
961	188.60	9.05	8.73	8.59	8.18	7.57	6.82	6.01	5.22
962	188.80	7.63	7.07	6.96	6.65	6.19	5.64	5.07	4.51
963	189.00	6.23	5.12	5.06	4.90	4.67	4.39	4.09	3.77
964	189.20	5.05	3.53	3.53	3.51	3.48	3.41	3.30	3.15

Fig. 4.18: Extract of false kinematics file due to shifted column order

As *ROSA* is considerably sensitive to exact column observance, the program does not accept this false wave file and terminates the calculation without any results. However, it is possible to manually restore the alignment by "right justifying" all characters in the file which of course retards the work immensely but can easily be fixed in a new software update. So despite this rather inefficient bug the load transfer works smoothly and *ROSA* does not show any severe difficulties in handling such a massive amount of data which is produced for a non-linear irregular sea state as in 5.3.2. For a successful calculation of the monopile by importing the externally generated wave file the only step which is left is to adjust the time parameters in the specific *ROSA* card for the dynamic analysis so that end time and time step match the kinematics in the *FLEX5* file.

4.4 Application and validation

In the end, the report shall provide a profound comparison and evaluation of an analytical and numerical wave simulation tool. On that account, it is of great importance to ensure a solid and proper understanding of the differences between both approaches but also a proven handling of the software. The previously presented theory and the description of each program shall now be used to guarantee a correct application for the upcoming feasibility study. Therefore, the analytical simulation is tested by *Matlab* and *WAVGEN* followed by a first confrontation with *OCW3D*. For this purpose, the already known example wave in Tab. 2.1 is implemented to generate surface elevations in line with available theories and the simple cylinder in Tab. 4.5 is loaded with corresponding wave kinematics to compare the resulting *OTM*. As in 3.2 the foundation in Fig. 4.19 is represented by regular beam elements fixed at the sea bottom.

Tab. 4.5: In-line load coefficients and pile diameter of the example cylinder

Drag coefficient, C_D [-]	*Inertia coefficient, C_M [-]*	*Diameter [m]*	*Length [m]*	*Thickness [mm]*
0.7	2.0	5.0	30.0	50.0

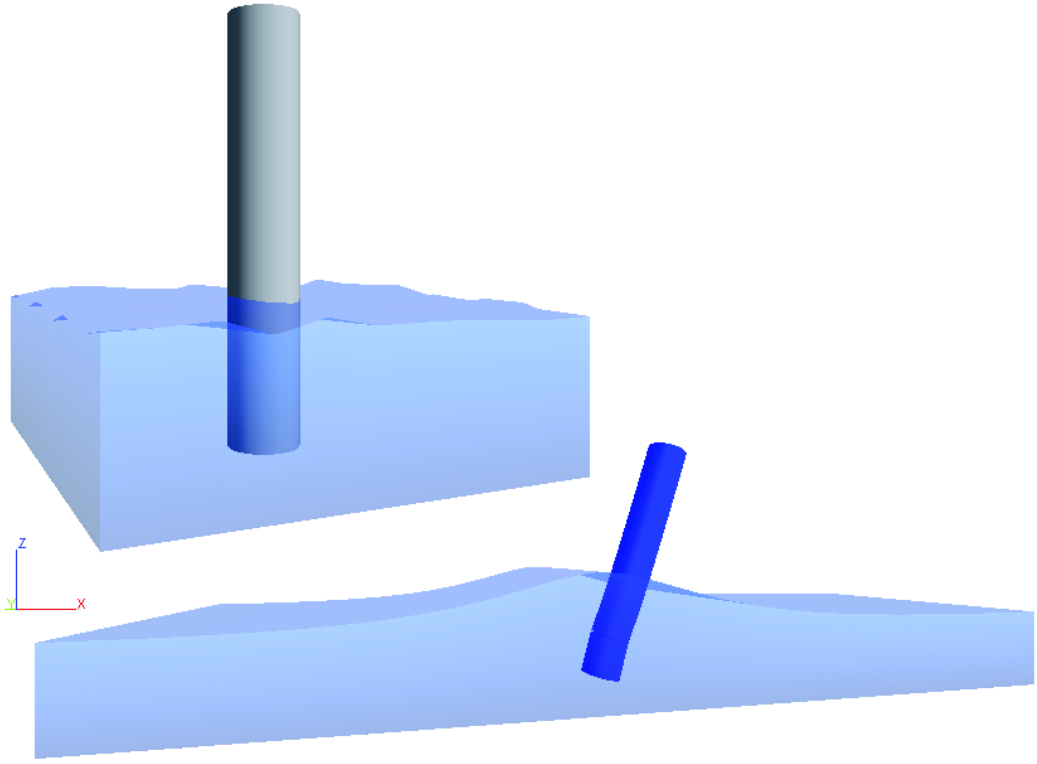

Fig. 4.19: Bottom fixed cylinder and upscaled impact of stream function wave

4.4.1 *Matlab* vs. *WAVGEN*

The already mentioned *Matlab* scripts shall now be taken to verify the analytical solution provided by *WAVGEN*. Therefore, a regular linear as well non-linear wave shall be produced by means of small amplitude theory and *Stokes'* fifth order method. In order to provoke a high degree of non-linearity and sea floor interference a water depth of only *10.0* metres is prescribed. By looking at Fig. 4.20 and Fig. 4.21 *Matlab* and *WAVGEN* yield a proper consensus of the water surface, thus revealing a correct analytical solution.

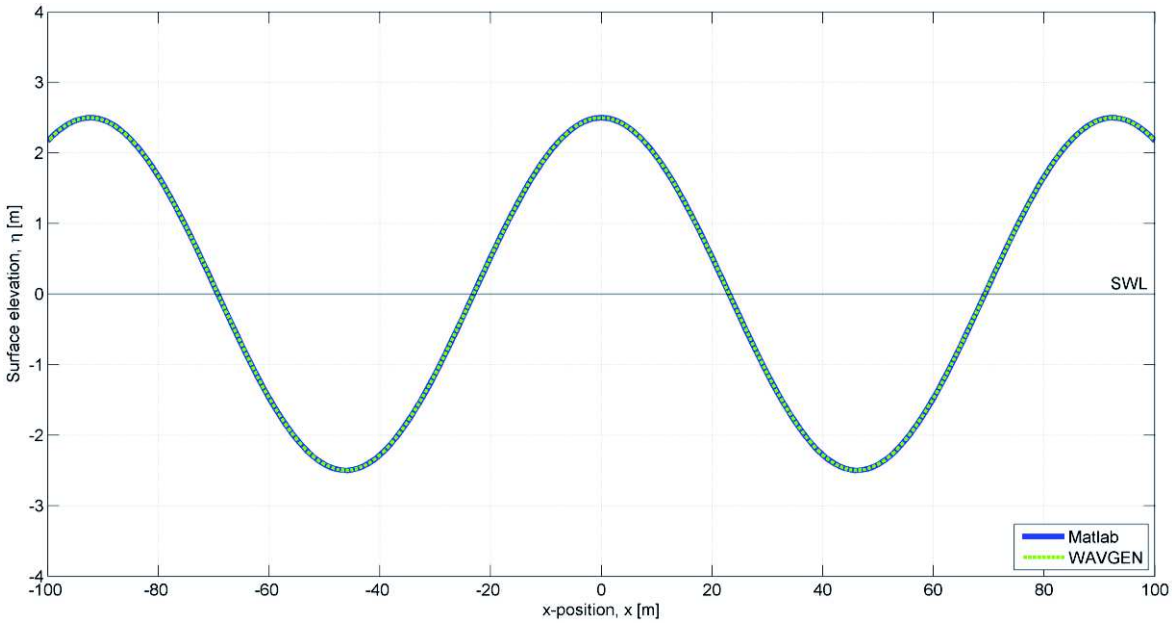

Fig. 4.20: Linear wave by Matlab and WAVGEN

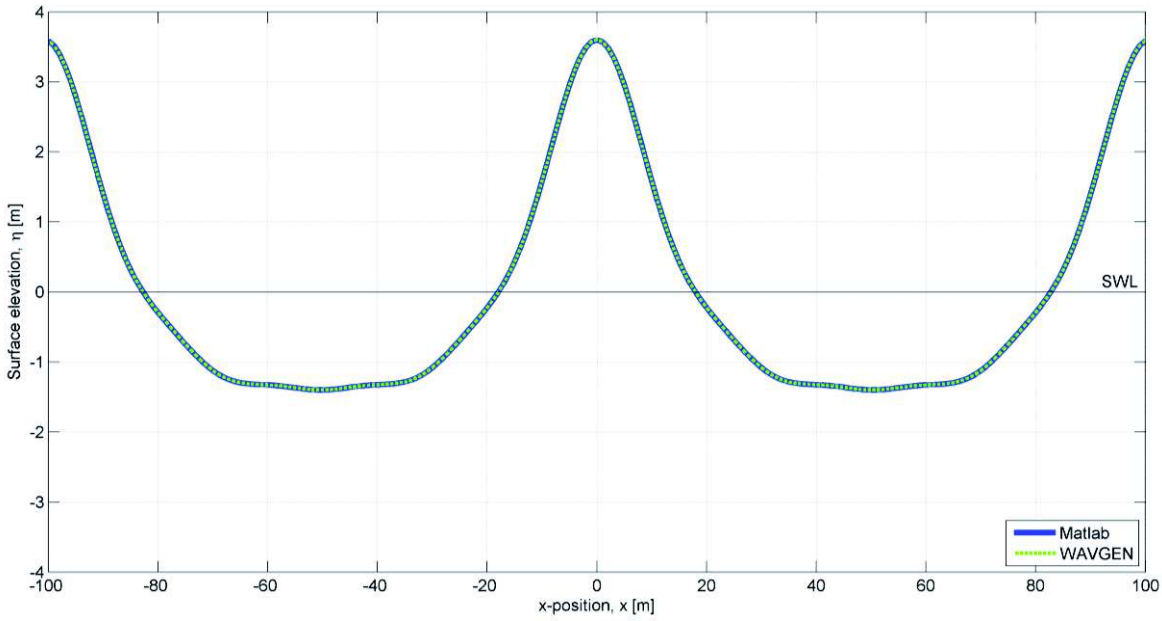

Fig. 4.21: Stokes' 5th order wave by Matlab and WAVGEN

The generation of horizontal water particle velocities and accelerations by both codes together with the *ROSA* transfer works as well since corresponding wave loads cause the same structural response of the cylinder induced by a linear and *Stokes'* fifth order wave.

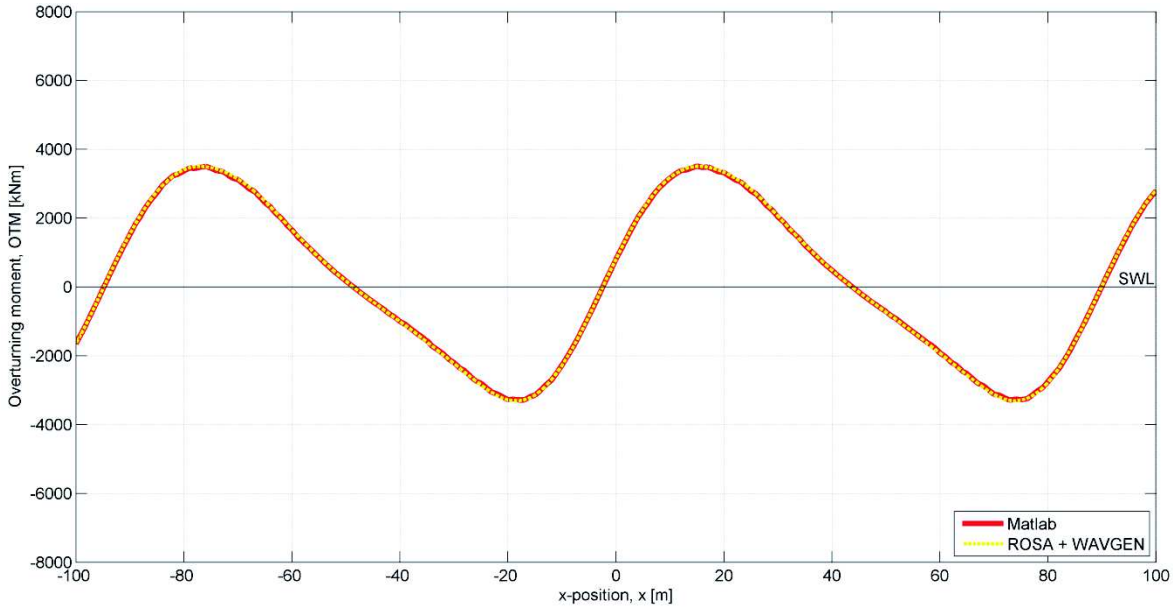

Fig. 4.22: OTM induced by linear wave with Matlab and WAVGEN plus ROSA

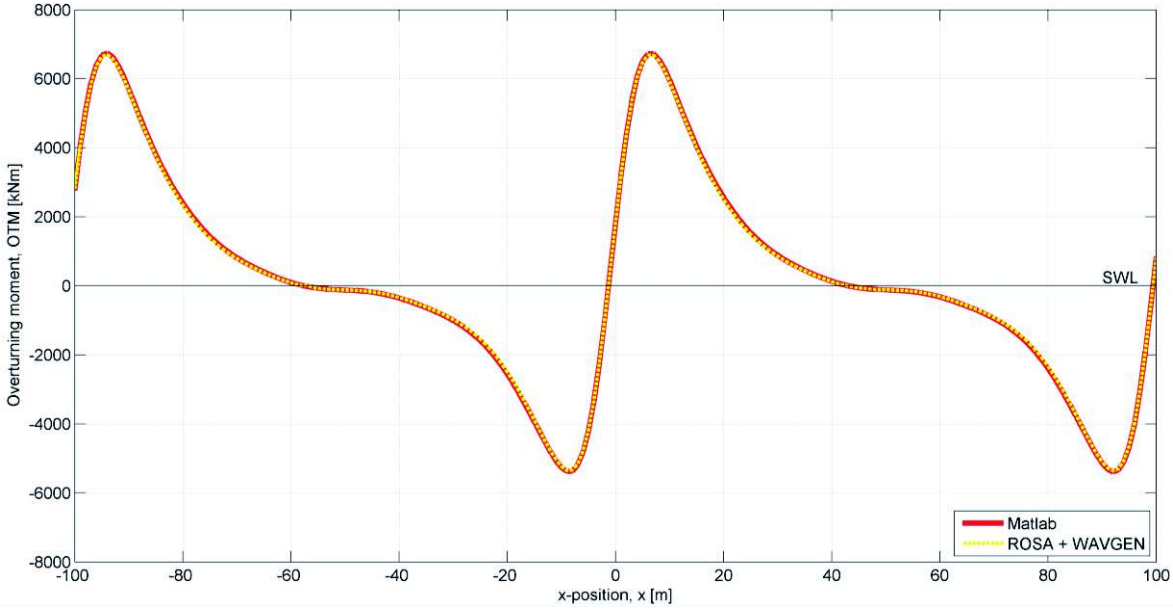

Fig. 4.23: OTM induced by Stokes' 5th order wave with Matlab and WAVGEN plus ROSA

4.4.2 *WAVGEN* vs. *OceanWave3D*

As *WAVGEN* and the interaction with *ROSA* are successfully validated by hand-written codes, the next step is to test *OCW3D,* including its variation parameters, output file and most important the conversion of its wave kinematics into a *FLEX5* format. This comparison is also considered as a verification of the later described new approach as the connection between *ROSA* and *OCW3D* can be revised and evaluated. After satisfying all boundary conditions in 4.2.2 and transferring the particle velocities and accelerations in accordance to 4.3.1 *OCW3D* numerically realises the following non-linear stream function wave. The water depth shall vary and respectively demonstrate deep or shallow conditions in order to detect any computational difficulties. *WAVGEN* delivers the expected confirmation in Fig. 4.24 and Fig. 4.25 and the small deviations of the surface elevations at the crest and trough in Tab. 4.6 are more than acceptable and consequently imply a correct simulation and operating procedure.

Tab. 4.6: Deviations in surface elevation for the crest and trough between analytical and numerical approach

Water depth	*Deviations*	
	Crest	*Trough*
Deep	0.7 %	2.3 %
Shallow	0.8 %	1.1 %

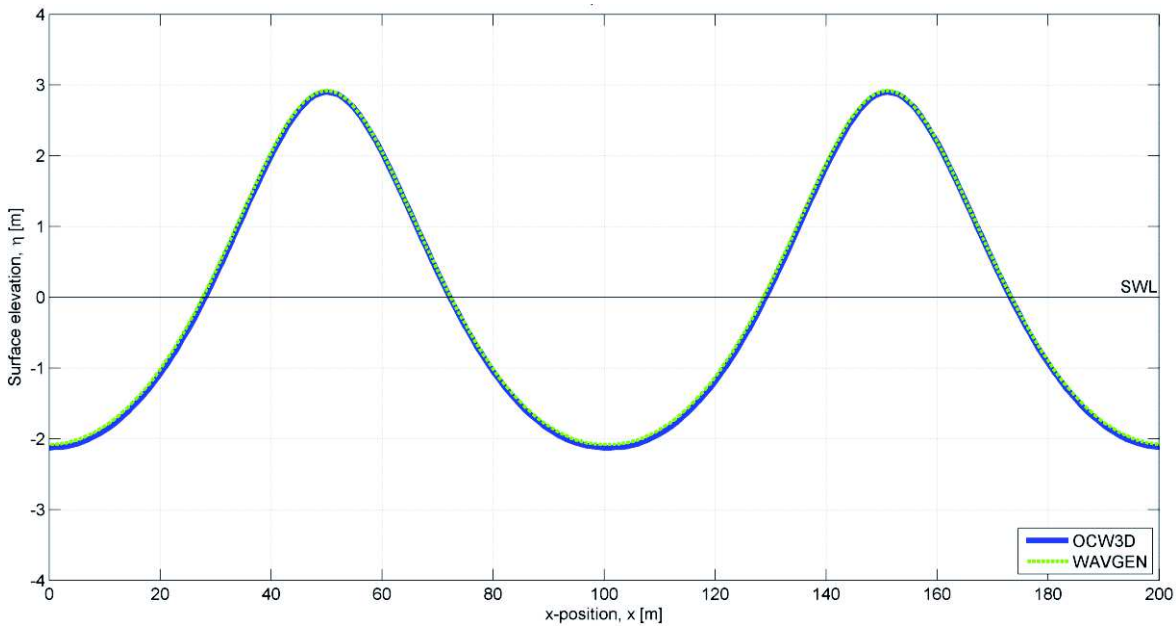

Fig. 4.24: Stream function wave in deep water by OCW3D and WAVGEN

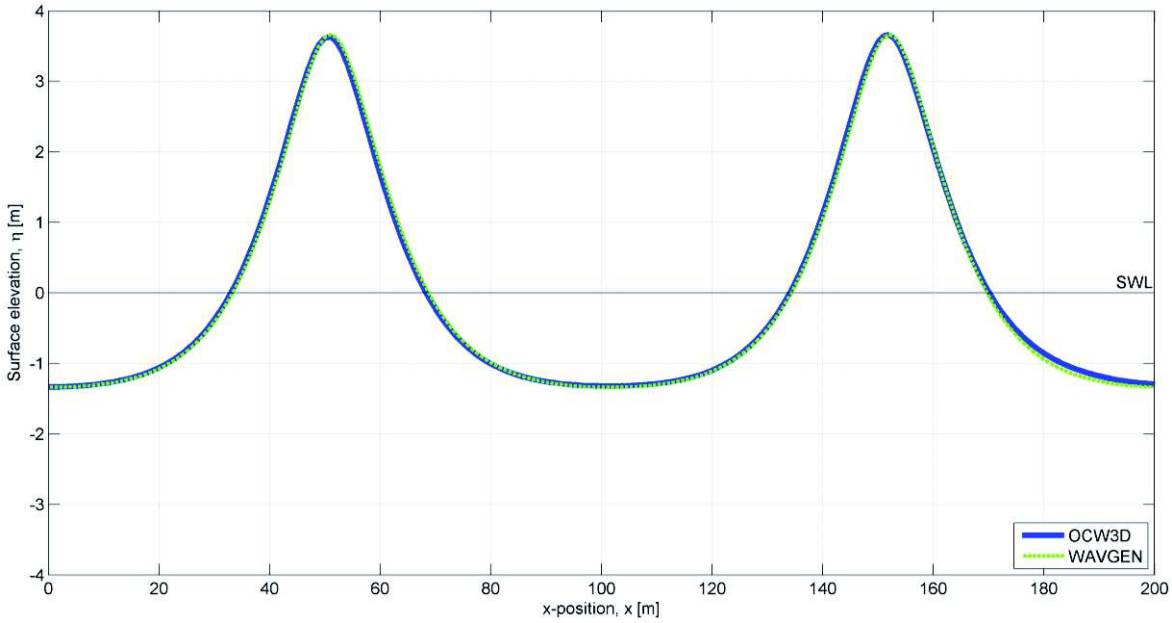

Fig. 4.25: Stream function wave in shallow water by OCW3D and WAVGEN

The minor numerical discrepancy, especially in the trough area might indicate a more realistic representation by *OCW3D*. The numerical solution of all boundary conditions for the potential flow problem might cover more influencing parameters in particular the small water depth. Only genuine tank tests or investigations of a large range of depths could, however, support this assumption.

Interestingly, despite almost identical surface elevations *OCW3D* reveals higher wave kinematics as the resulting *OTM* amounts to a greater response of the cylinder in Fig. 4.26 and Fig. 4.27. The *OTM* time series obtained by the numerical method exceed maxima and minima of the *OTM* induced by *WAVGEN* whereas the water depth shows a severe influence on the results. An increase of almost eight percent compared to deep water is perceived according to Tab. 4.7. That means that *OCW3D* includes a more pronounced elliptical trajectory and thus a greater acceleration of water particles due to the smaller distance to the sea floor. As a conclusion, it is expected that the comprehensive solution process and the integration of further governing conditions in *OWC3D* eventuate a more accurate output of wave kinematics, especially in case of considerable non-linearity in form of finite water depth and asymmetric steep waves. This possible limitation of the common wave theory agrees with its validity range described in 2.7.

Tab. 4.7: Deviations in surface elevation for the crest and trough between analytical and numerical approach

Water depth	*Deviations*	
	Crest	*Trough*
Deep	2.6 %	2.1 %
Shallow	10.9 %	9.5 %

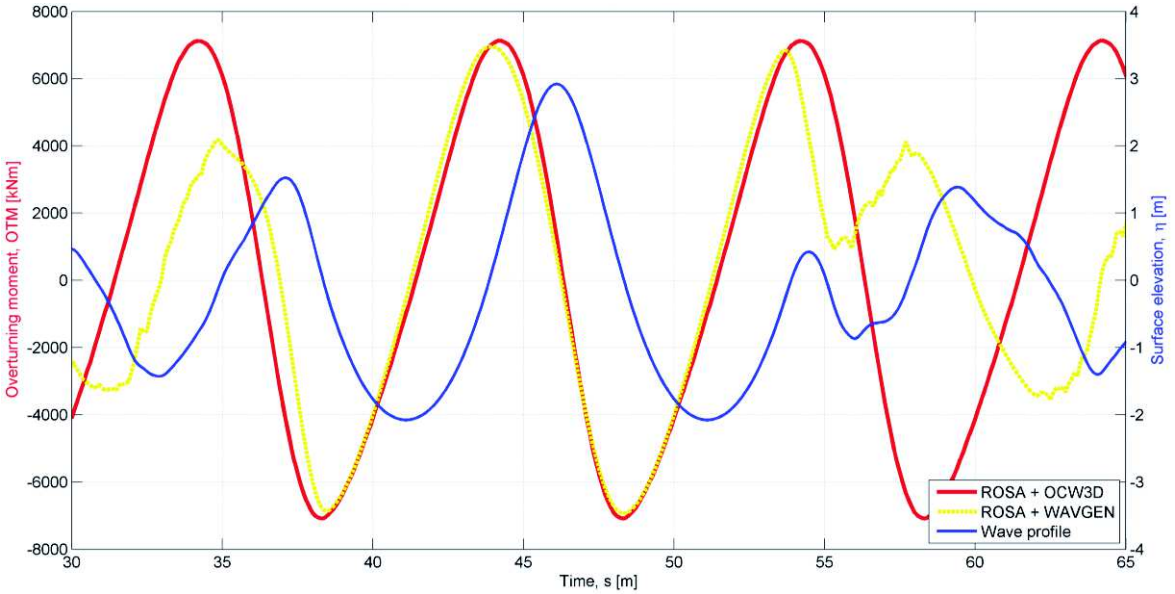

Fig. 4.26: OTM induced by stream function wave in deep water with OCW3D and WAVGEN

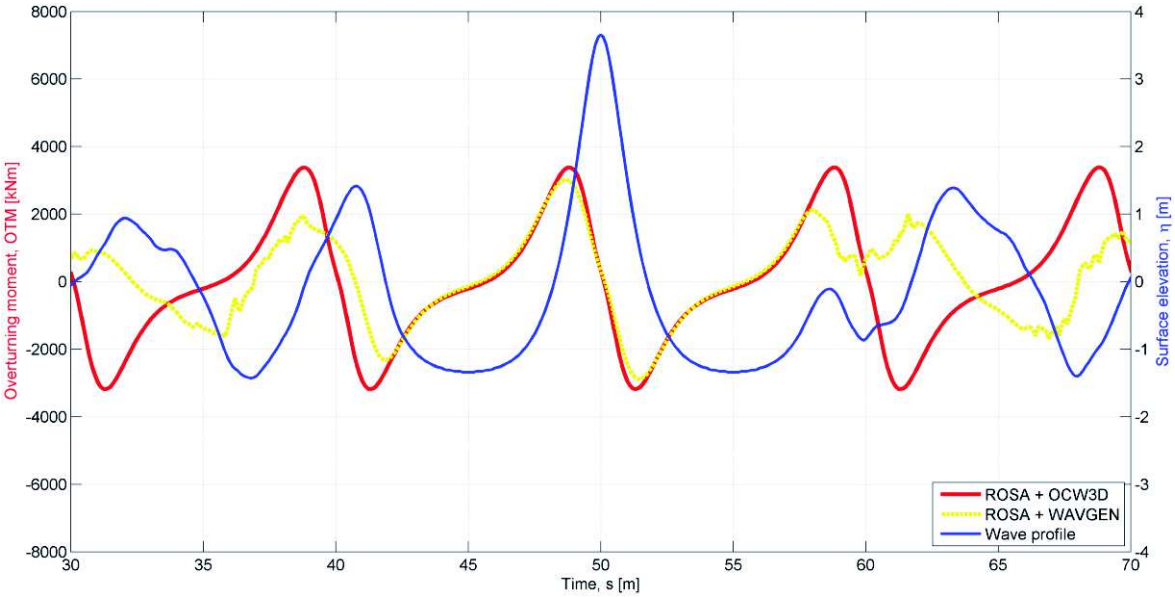

Fig. 4.27: OTM induced by stream function wave in shallow water with OCW3D and WAVGEN

Despite the small divergence in the *OTM* progression the overall process of numerically developing a non-linear wave scenario which is applied on a monopile related structure in *ROSA* can hereby be confirmed. This lays the foundation for the subsequent problem and final evaluation of the conventional and new design process. It is important to point out that the interface between *ROSA* and *OCW3D* does not pose any problems any longer and can be considered as successfully implemented.

5 Comparison study

The following chapter composes the main part of the thesis as it provides the prime answer to the objectives stated in 1.3. For that reason the comparison study includes the comprehensive description of the conventional and new approach applying either *WAVGEN* or *OCW3D* as the wave kinematics solver. Before results like wave properties and structural response of an actual offshore foundation are evaluated, the design scenario and the *FE*-model of the monopile shall be presented. The necessary input variables like geometry of structure or turbine, environmental conditions, metocean and geotechnical data form the common ground for the comparison study and shall remain constant throughout all calculation runs. In the end, the comparison between different wave scenarios and *OTMs* shall yield the basis for the final evaluation of both programs and the entire project.

5.1 Design scenario

It is important to begin by saying that the following details of the design scenario refer to genuine conditions and that the structure of the offshore foundation is inspired by an actual industry project. However, due to the involvement of third parties and their corporate input confidentiality and disclosure agreements have to be respected. This virtually affects the topside concept, including the tower and the wind turbine as well as site specific information obtained by geotechnical investigations. For the comparison and feasibility study of the new software all necessary information can be presented and it can generally be said that the considered monopile shall be deployed in the southern North Sea.

Consequently, this results in the environmental and locational parameters in Tab. 5.1. The water depth d, significant wave height H_s and wave peak period T_p are based on an one hour sea state and return period of *50.0* years. In order to account for the ultimate strength limit of the monopile the conventional approach includes an *ESS* in form of a stream function wave using equations in (5.1) and (5.2) [26].

$$H_{max} = 1.86 \cdot H_s \tag{5.1}$$

$$T_{max} = 14.3 \cdot \sqrt{\left(\frac{H_s}{g}\right)} \tag{5.2}$$

Tab. 5.1: Sea state and extreme wave conditions with respect to LAT

Return period [years]	*d [m]*	*H_s [m]*	*T_p [s]*	*H_{max} [m]*	*$T_{max,upper}$ [s]*	*Wave direction [deg]*
50.0	27.0	9.0	13.0	16.7	13.7	0.0

Other specified parameters can be taken from Tab. 5.2 whereas the given default in-line load coefficients shall be adjusted by the roughness increase due to marine growth which is applied from mudline up to one metre above the lowest astronomical tide (*LAT*). Although an existing current changes the wave kinematics, this influencing parameter shall be disregarded due to simplicity. Usually, it must be included as a current in an opposing wave direction leads to larger and steeper surface elevations because of wave-current refraction and energy conservation. On the other hand, a following current allows a higher wave to exist, increases its celerity and consequently yields higher hydrodynamic loads. Any other perturbations like sea level or tidal variances shall be neglected as well in this report.

Tab. 5.2: General and environmental design parameters

Safety factor [-]	*Water density [kg/m3]*	*Air density [kg/m3]*	*Gravity constant [m/s2]*	*Drag coefficient [-]*	*Inertia coefficient [-]*	*Marine Growth [mm]*
1.00	1025.0	1.234	9.81	0.65	2.00	1.00

As the monopile is considered to be fixed at the sea floor, the soil constitutes the major boundary condition and requires a distinct numerical reproduction. The realistic definition of the soil is essential for the pile-soil interaction and the resulting *OTM* with respect to mudline. Eventually, this gives indications on the main structural dimensions and the needed penetration depth of the monopile in the ground under the specific local conditions. In order to determine the total deflection of the structure in accordance with the soil resistance the lateral soil resistance-deflection (*P-Y*) curve, the axial load transfer (*T-Z*) curve for skin friction and the tip load-displacement (*Q-W*) curve for the pile tip resistance must be calculated by means of Fig. 5.1. Unfortunately, soil properties are highly sensitive and vary considerably from site to site or between different sample depths. Thus, only an exemplary output of a geotechnical analysis is presented to show which soil properties are needed and how they are layered. In case of estimating the utilisation ratio of structural components, natural frequency or fatigue analyses safety factors are set to

unity, while the here discussed extreme event approach considers plastic soil conditions in order to examine the minimum pile penetration, applying greater safety factors for soil properties according to Tab. 5.3 [20].

Tab. 5.3: Safety factors for soil capacity

Material parameter	*Characteristic soil*	*Plastic soil*
Angle of internal friction, φ	1.00	1.15
Cohesion, c	1.00	1.25
Axial load-carrying capacity of piles	1.00	1.25

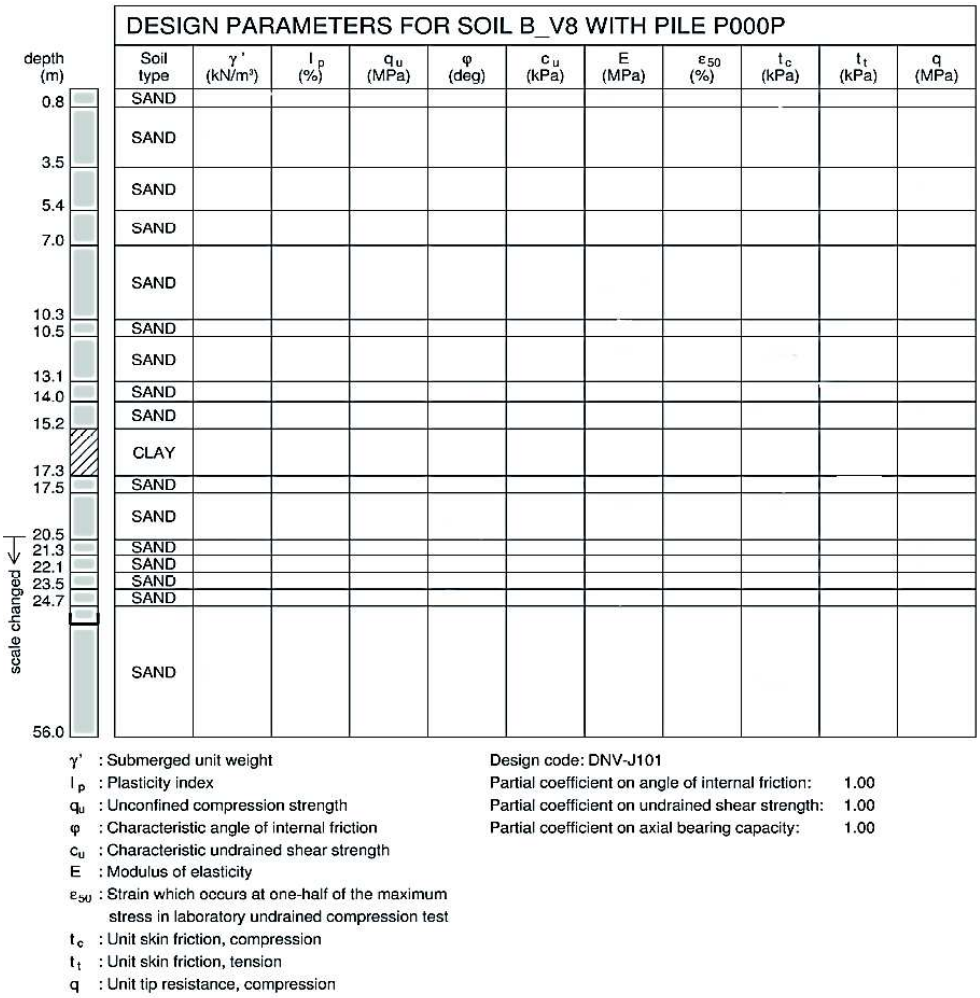

Fig. 5.1: Applied soil data to calculate the soil-pile interaction curves

The global dimensions of the examined *MP* and *TP* can be found in the drawings in appendix A.1 and are summarised in Tab. 5.4. The technical specification of the rotor-nacelle-assembly (*RNA*) and other tower equipment shall be simplified and refer to a standard wind turbine which is already commissioned in today's wind parks.

Tab. 5.4: Foundation dimensions

Data	*Value*
Weight (*TP* + *MP*), [t]	1049.0
Centre of gravity (*MP*) w.r.t. *LAT*, [m]	-28.31
Centre of gravity (*TP*) w.r.t. *LAT*, [m]	12.44
Outer bottom diameter,[mm]	7000.0
Outer top diameter, [mm]	5500.0
Total length (*MP*), [m]	61.80
Total length (*TP*), [m]	19.72
Total length (tower), [m]	64.48
Targeted penetration depth, [m]	58.60

In the course of subsequent *FE*-calculations it is recommended to initially include any additional loadings induced by so-called secondary steel components i.e. boat landing bumpers, internal *J*-tubes as cable foundations and sacrificial anodes. Those structural elements indeed contribute to wave areas, masses and stress concentration factors but do not affect the global stiffness of the structure. Externally installed appurtenances must be treated in the same way as primary steel, possibly changing surface conditions from rough to smooth and adjusting force coefficients. In this design case two boat landing bumpers are arranged along the structure which shall be orientated perpendicular to the wave propagation so that the worst scenario for the increased resistance and thus hydrodynamic loading is achieved. Furthermore, four anodes are applied outside the cylinder. The effect of external appurtenances on the structure can be withdrawn from Tab. 5.5.

Tab. 5.5: Properties of external appurtenances

Item	*Mass [kg/m]*	*Buoyancy [m3/m]*	*Wave area [m2/m]*	*Start elevation w.r.t. LAT [m]*	*End elevation w.r.t. LAT [m]*
Boat landing bumpers	800.0	0.196	0.5	-2.0	10.0
Anodes	205.0	0.026	0.4	-2.4	2.2

Of course, the entire installation holds further structural elements to facilitate the installation and operation of the wind turbine which consequently have to be added to

the total mass. Due to classified tower details the remaining masses of working platforms, cable tracks or grouting in Tab. 5.6 form one sum together with the tower arrangement.

Tab. 5.6: Mass appurtenances properties

Item	*Mass [kg]*	*COG w.r.t. LAT [m]*
External platform Upper platform Equipment platform Internal platform Air-tight platform Grout skirt J-tubes Mass (tower)	81010.0	25.9
Hub	273000.0	89.1

In order to minimise the scope of work corrosion shall not be included in the actual calculations. The same applies to scour protection. Therefore, it shall be assumed that no scour hole development will occur around the pile at mudline. The assessment of the wind turbine foundation and the calculations are carried out in line with *DNV-OS-J101 (2014)*, prescribing general design criteria. It shall be emphasised that the soil penetration of the monopile is defined at the point when the maximum load on the installation equals the soil resistance. It also states that for steel the maximum member *ULS* utilisation ratio should not exceed *1.0* [26]. For the dynamic assessment of the monopile foundation the damping ratios in Tab. 5.7 are assumed on a realistic level according to the natural frequency analysis in 5.2.1 and taken for the *Rayleigh* based damping matrix as presented in 4.3.

Tab. 5.7: Applied damping ratios for dynamic analyses

Damping ratio, [-]	
ξ_1	ξ_2
0.0063	0.240

5.2 Finite element model of monopile

The application of *Rambøll's* in-house program *ROSA* is seen as the joint basis for the subsequent comparison study between *WAVGEN* and *OCW3D*. Since the main objective is to transfer resulting wave kinematics from both codes to *ROSA*, it is important that the *FE*-model of the foundation is distinctly and correctly conceived to eventually detect any deviations or contradictions in the final output. Following this, the beam model is described in terms of material, node and element definitions together with load application and boundary conditions. As already mentioned, the structural model is inspired by an actual industry project and is modified to meet requirements of a simple but safe construction. That means that no stress exceedance and thus no resulting adjustments on components are assumed. In order to guarantee a sufficient safety margin in advance, the interface between *TP* and the tower is raised so that possible extreme wave crests do not hit the topside. The pile penetration and the wall thickness are also increased to a rather conservative level.

Environmental description and general input:

Since the monopile is assessed under wave loads and thus under hydrodynamic conditions, general and environmental parameters need to be set beforehand. All conditions listed in Tab. 5.2 and Tab. 5.3 are implemented whereas the in-line load coefficients shall be adjusted automatically by the influence of marine growth, additional appurtenances and geometry. If marine growth is considered, the input parameter is the marine growth to radius which changes the radius of tubular elements or the equivalent radius of non-tubular parts. The resulting new outer diameter is then taken for the determination of drag and mass forces. The following materials in Tab. 5.8 are used for the *MP*, *TP* and tower whereas the properties are classified in the program as a function of steel section thickness.

Tab. 5.8: Material properties of the lowest upper thickness limits in FE-model

Description	*Name*	*E-Modulus [MPa]*	*Poisson's ratio [-]*	*Mass density [kg/m3]*	*Yield-strength [MPa]*	*Ultimate tensile strength [MPa]*
Flange (MP)	FLA	210000.0	0.3	8150.0	355.0	490.0
Flange (TP)	FL1	210000.0	0.3	8150.0	355.0	490.0
Flange (Tower)	FL2	210000.0	0.3	9600.0	355.0	490.0
MP + TP	N35	210000.0	0.3	7850.0	355.0	490.0
Tower	TOW	210000.0	0.3	7873.0	355.0	490.0

Soil data:

The pile-soil interaction and the influence on *OTM* are governed by the penetration depth and geotechnical data, resulting in the specific pile-soil interaction curves. Those are generated in *ROSA* by means of common design codes and standards. The consideration of each characteristic soil layer is performed in line with [26] and [20] while the safety factors for friction, shear strength and axial capacity refer to Tab. 5.3. Sample drillings at the installation site yield different layers of the sea floor which need to be read separately in the program. It can be chosen between sand, silt, chalk, lime, clay and rock in accordance with [20] and [26]. The submerged unit weight and the depth of each layer as well as the angle of internal friction for frictional soils like sand or clay eventually provide the basis for a reasonable soil profile. The soil in Fig. 5.2 is kept quite simple consisting of twelve different sand compositions and one clay interruption.

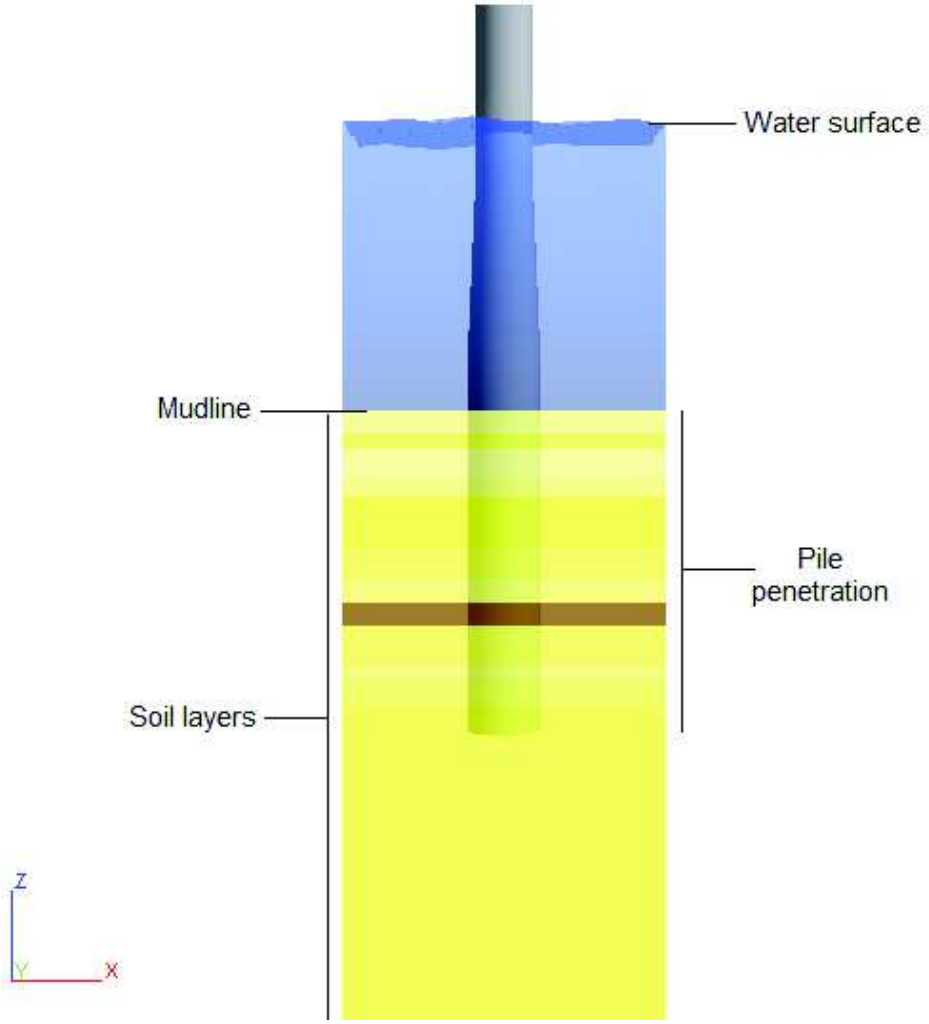

Fig. 5.2: Specific soil profile with various sand (yellow) and clay (brown) layers

Node and element definition:

The node positions in Tab. 5.9 refer to the global dimensions of each structural element and the maximum extent of producible plate sizes which are denoted as can lengths. Here, the *z*-coordinate of each node is given as the entire model is aligned in the centre of the coordinate system. The naming of nodes and elements can be seen in Fig. 5.3 and shall be applied throughout the entire project.

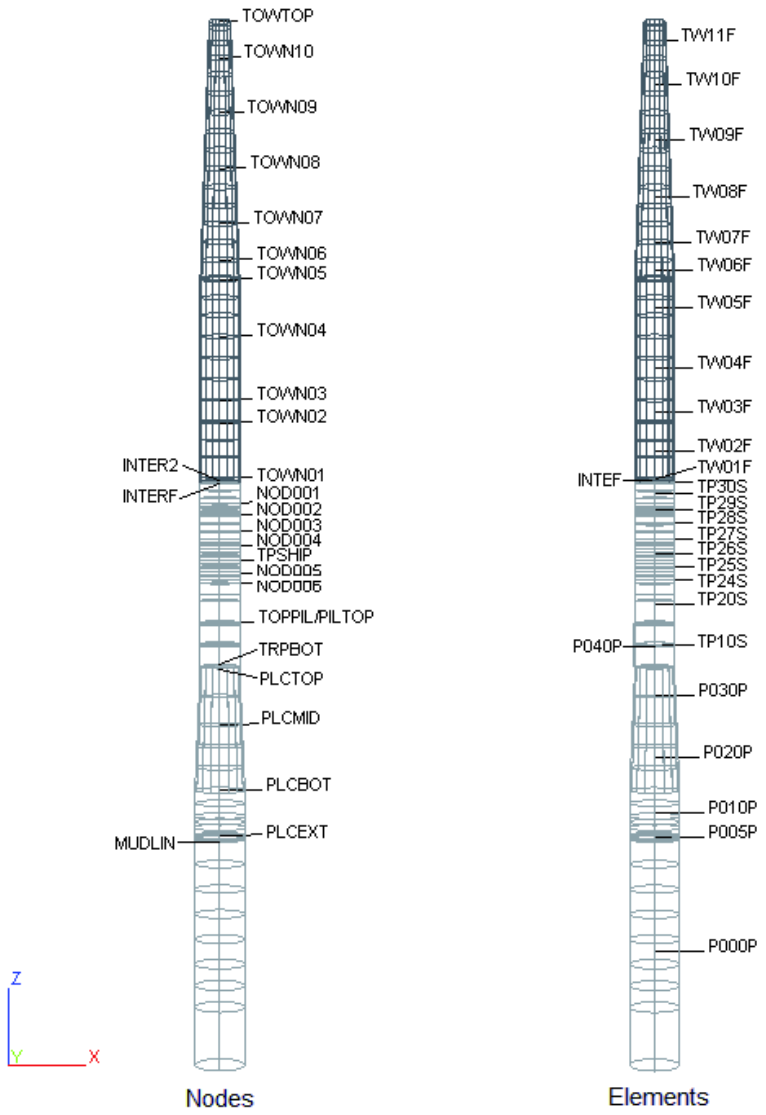

Fig. 5.3: Node and element naming for continuity reasons

For the *TP* and *MP* structure above mudline tubular and conical beam elements are used and equipped with respective sectional properties in terms of outer diameter and wall thickness of each can length. In order to reduce computational time and effort each structural beam can be divided into as many as five sections with different material and sectional properties, as listed in Tab. 5.9.

The part penetrating the ground is made up of a pile element which is seen as a composite structural element, consisting of the pile itself and the surrounding soil. The pile element is treated as a beam although based on a non-linear approach in order to satisfy the non-linear soil properties and to reproduce sufficiently the *P-Y* dependency in contrary to the linear deformation principle of remaining beam elements. The soil provides a lateral and tangential support along the pile as well as an axial bearing at the pile tip [24]. The soil can also limit or prohibit torsion of the pile. For this, the soil stiffness according to Fig. 5.1 is inputted as a set of piecewise

linear curves specified at the top and bottom of each layer. This special element which can be sub-divided in up to 15 components with varying properties follows the same structure in terms of *i*-node and *j*-node whereas the former must correspond to the mudline and the *z*-coordinate of the pile tip must be stated explicitly, as in Tab. 5.10. Alternatively, it is possible to deploy an equivalent linear element. However, the overall stiffness of the pile top would then only comprise the initial spring stiffness for all pile-soil curves and the linear contribution of the pile itself. This would not differ much from general stiffness elements of the support type [24]. Together with the previously described soil profile the pile element constitutes the anchoring of the monopile, hence the only physical boundary condition. Compared to the simple cylinder examined in *Matlab*, the bottom of the structure is not fixed and allows certain rotations and displacements of the degrees of freedom according to the soil resistance. In the end, this simultaneous solution for a linear structure above a non-linear pile foundation saves time and costs as it completely runs within one software package [24].

Tab. 5.9: Nodal positions with respect to LAT and corresponding beam elements

Node	*z-position [m]*	*Element*	*i-Node*	*j-Node*	*Sub-elements*	*Material*
INTERF	22.9	P040P	PILTOP	PLCTOP	3	FLA
NOD001	20.0	P030P	PLCTOP	PLCMID	2	N35
NOD001	18.4	P020P	PLCMID	PLCBOT	3	N35
NOD003	16.0	P010P	PLCBOT	PLCEXT	5	N35
NOD004	14.0	P005P	PLCEXT	MUDLIN	3	N35
TPSHIP	12.0	TP30S	INTERF	NOD001	5	FL1
NOD005	10.0	TP29S	NOD001	NOD002	5	N35
NOD006	8.75	TP28S	NOD002	NOD003	5	N35
TOPPIL	3.20	TP27S	NOD003	NOD004	5	N35
TRPBOT	-2.80	TP26S	NOD004	TPSHIP	5	N35
PILTOP	3.20	TP25S	TPSHIP	NOD005	5	N35
PLCTOP	-3.00	TP24S	NOD005	NOD006	5	N35
PLCMID	-11.0	TP20S	NOD006	TOPPIL	4	N35
PLCBOT	-20.2	TP10S	TOPPIL	TRPBOT	2	N35
PLCEXT	-26.5	INTEF	INTERF	INTER2	1	FL2
MUDLIN	-27.0	TW01F	INTER2	TOWN01	2	TOW
INTER2	23.1	TW02F	TOWN01	TOWN02	3	TOW
TOWN01	23.6	TW03F	TOWN02	TOWN03	3	TOW

TOWN02	31.2	TW04F	TOWN03	TOWN04	3	TOW
TOWN03	34.4	TW05F	TOWN04	TOWN05	3	TOW
TOWN04	43.3	TW06F	TOWN05	TOWN06	3	TOW
TOWN05	51.3	TW07F	TOWN06	TOWN07	2	TOW
TOWN06	54.0	TW08F	TOWN07	TOWN08	3	TOW
TOWN07	59.1	TW09F	TOWN08	TOWN09	3	TOW
TOWN08	66.8	TW10F	TOWN09	TOWN10	3	TOW
TOWN09	74.7	TW11F	TOWN10	TOWTOP	3	TOW
TOWN10	82.3					
TOWTOP	87.4					

Additionally, it is necessary to group elements into flooded and non-flooded members, decreasing or increasing the buoyancy of the structure. As the monopile is non-watertight to a certain level, all *MP* elements below the flange connection overlapped by the flooded *TP* grout skirt are considered as non-flooded. In this way the buoyancy is not included twice.

As described in 1.2, common procedure of connecting *MP* and *TP* includes bolting and subsequent grouting to ensure sufficient corrosion protection of the flange. Numerically, this is achieved by defining a link element which represents different connection types between coincident nodes. Here, it is possible to assign certain spring stiffness values or complete constraints to the six degrees of freedom. So for example in typical seat connection with zero annular space one component is free to translate or rotate around the other component's axis while some forces are only transferred perpendicular to the centreline [24]. In this case the joint between *MP* and *TP* is simulated by a rigid link element, as in Tab. 5.10.

Tab. 5.10: Properties of applied pile and link element

Name	*Element type*	*i-Node*	*j-Node*	*Sub-elements*	*Material*
P000P	Pile element	MUDLIN	-58.6 m	8	N35
				Translations	*Rotations*
LINKT	Link element	PILTOP	TOPPIL	Fixed	Fixed

The soil and thus the pile element shall remain constant throughout all calculation and simulation runs, resulting in the following maximum pile capacities in Tab. 5.11.

Tab. 5.11: Maximum pile capacity for the monopile design

Skin friction		*Tip resistance*		*Capacity*	
Tension [MN]	*Compression [MN]*	*Suction [MN]*	*Compression [MN]*	*Tension [NM]*	*Compression [NM]*
45.891	45.891	0.000	61.536	60.452	103.753

Appurtenances:

The structural components in Tab. 5.5 and Tab. 5.6 do not contribute to the overall stiffness but to the structural load. Thus, they are included in the model by positioning them along beam elements or at specific nodes, implementing mass, area and volume of each secondary steel part. Externally distributed appurtenances in Fig. 5.4 exposed to wave loads like boat landing and anodes not only affect the mass but also the hydrodynamic load area and volume which must be taken into account for any shielding or blocking events and in case of marine growth.

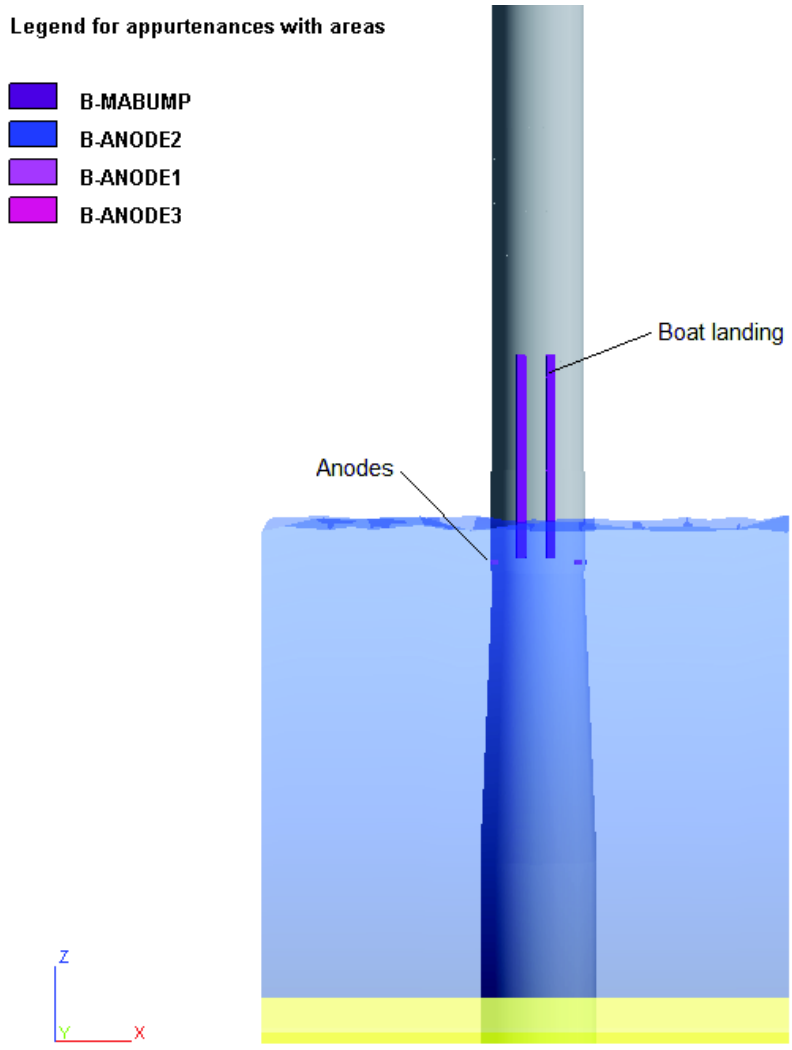

Fig. 5.4: External appurtenances

All remaining appurtenances which do not interfere with the hydrodynamics of the installation are simply defined as additional masses within the foundation, as depicted in Fig. 5.5.

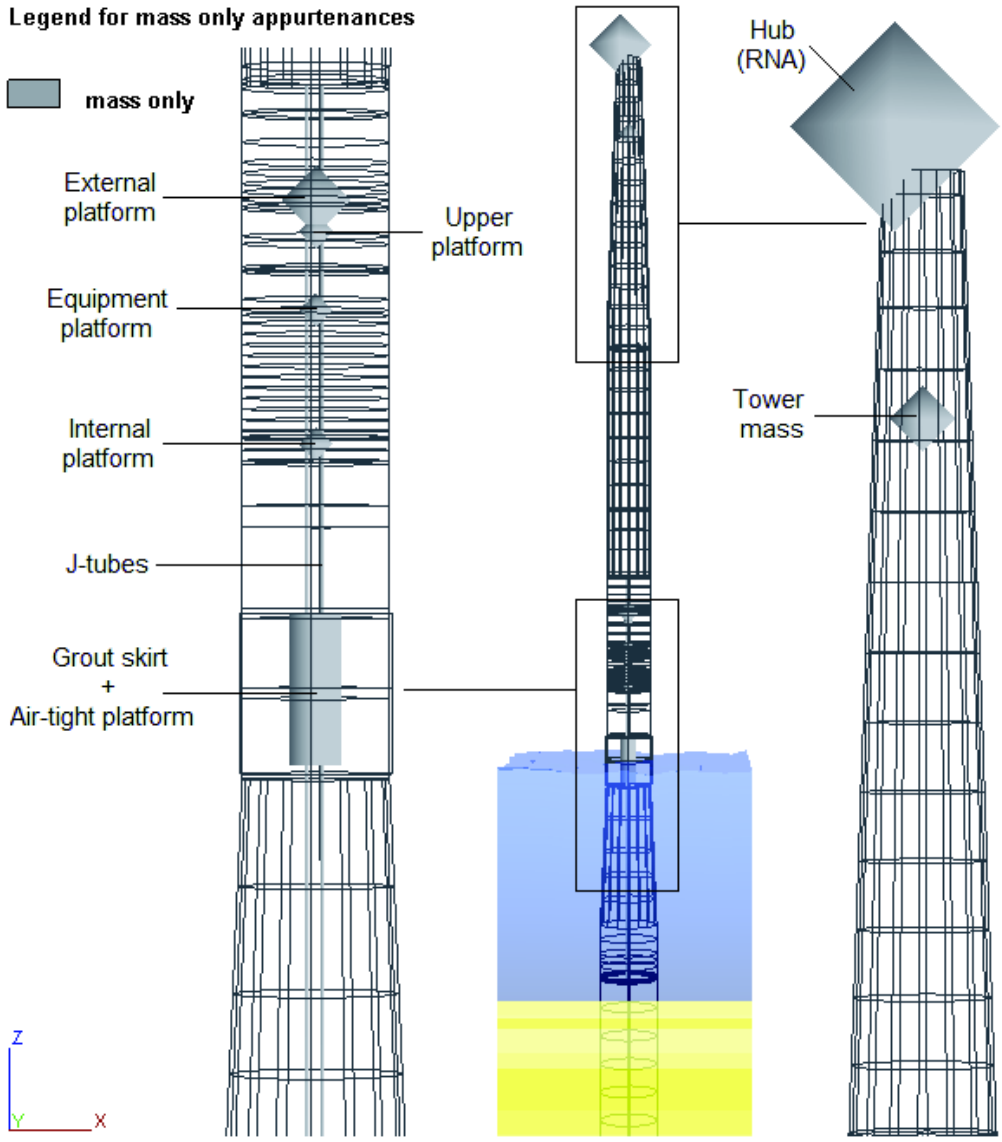

Fig. 5.5: Mass appurtenances

Load cases and application:

Besides directly specified node and beam nodes *ROSA* is able to handle all common environmental loads and in the course of an ordinary design process for a wind turbine foundation wave loads have to be superimposed by current and in particular by wind forces. But as the focus lies on the correct simulation of wave kinematics the here conducted *ULS* analysis shall only include deadweight of the structure, buoyancy and wave impacts, resulting in three separate load cases which are eventually combined for the actual calculation.

The gravity load sums up all structural masses which are automatically generated from the element materials and sectional properties as well as node or beam appurtenances, yielding one total gravitational force. In case of buoyancy loading the hydrostatic pressure with respect to the specified water depth is determined whereas deviations through any wave induced excess pressure is calculated separately and added later. Any details on generating and handling wave loads in *ROSA* are discussed more precisely in 4.3, 5.3 and 5.3.2. So the total load on the structure induced by the self-generated weight and buoyancy are exemplified by the monopile with boat landing and marine growth. The wave load contribution varies with the applied theory and software, hence giving later in 5.3 and 5.3.2.

Tab. 5.12: Example of total load on the structure induced by gravity acceleration and buoyancy

Load case	*Force in*			*Moment about*		
	x-dir. [kN]	*y-dir. [kN]*	*z-dir. [kN]*	*x-axis, [kNm]*	*y-axis [kNm]*	*z-axis [kNm]*
Gravity load	0.00	0.00	-12063.19	606.63	-2395.24	0.00
Buoyancy	0.00	0.00	564.13	-11.96	6.03	0.00

Summary:

For the static and dynamic analysis the *FE*-model of the complete wind turbine foundation summarised in Tab. 5.13 and displayed in Fig. 5.6 shall not be altered in any way as only different wave loads shall be investigated. A natural frequency analysis (*NFA*) shall now be performed to check the model and its displacement behaviour.

Tab. 5.13: ROSA model summary

Number of	*Amount*
Nodes	28
Beam elements	26
Link elements	1
Pile elements	1
Node appurtenances	1
Beam appurtenances	20

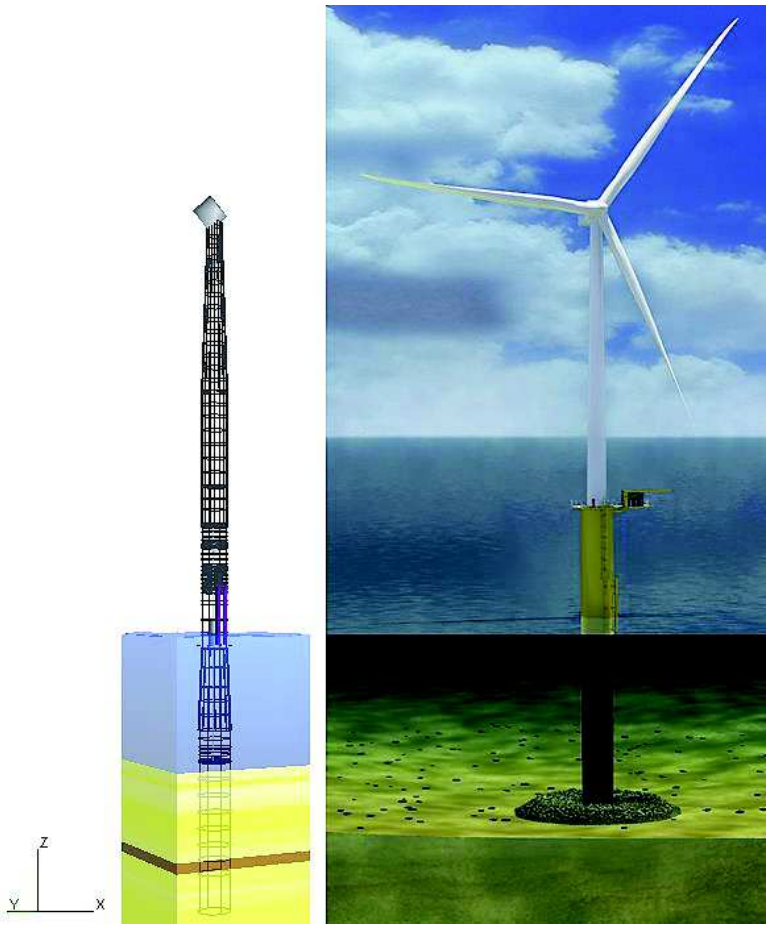

Fig. 5.6: FE-model against rendered image of the wind turbine foundation[3]

5.2.1 Natural frequency analysis

The main objective of natural frequency analyses is to identify the periods for dynamic calculations, to validate the structure and to detect any modelling errors by reproducing the first five eigenmodes. Due to their simple and distinct mode shapes the deformation behaviour of the *FE*-model can readily be assessed. Additionally, a dynamic calculation based on a simple regular wave impact with the parameters in Tab. 5.1 shall be examined more closely to check whether the structure responds in line with the *NFA*. The first five eigenmodes and the associated periods as well as frequencies are listed in Tab. 5.14 and visualised in Fig. 5.7. The results are presented in the *xy*-plane where the second and forth mode shape are rotationally symmetric to the first and third mode.

[3] Image source: Rambøll Denmark AS

Tab. 5.14: Properties of first five eigenmodes provided by NFA

Mode shape	*Cyclic frequency [rad/s]*	*Frequency [1/s]*	*Period [s]*
1	2.0760	0.3304	3.0266
2	7.7232	1.2292	0.8135
3	9.3417	1.4868	0.6726
4	14.3314	2.2809	0.4384
5	25.7014	4.0905	0.2445

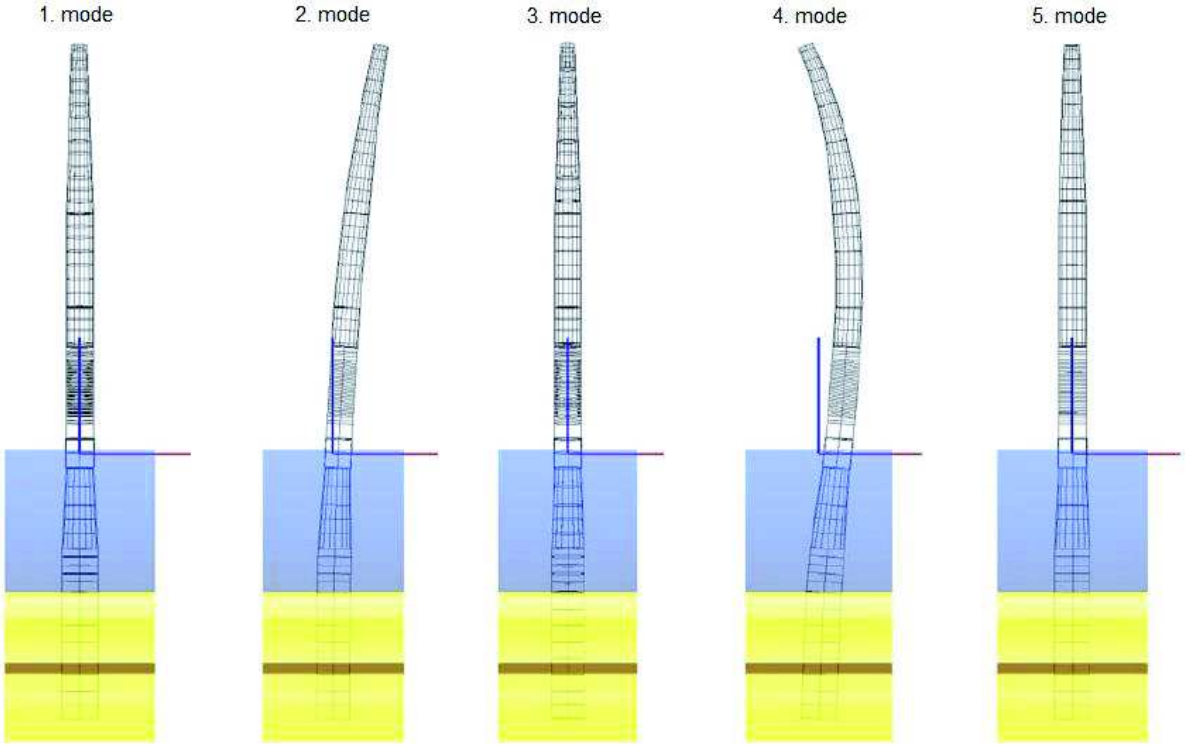

Fig. 5.7: First five mode shapes of wind turbine foundation

If the structure is exposed to an exemplary sea state with T_p equals *13.0 s* in a dynamic analysis, the resulting power spectrum in Fig. 5.8 shows peaks corresponding to the first eigenfrequencies of the foundation and the wave period.

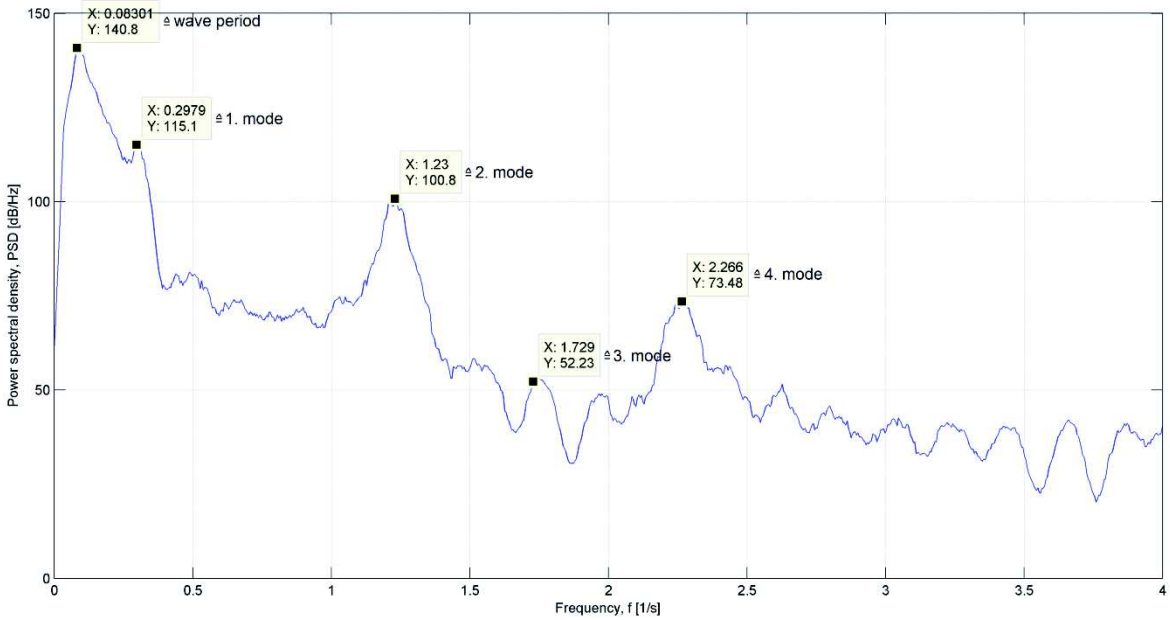

Fig. 5.8: Example power spectrum of the monopile, showing correct matches with eigenmodes and wave peak period of 13.0 seconds

With reference to Fig. 5.7 and Fig. 5.8 the conducted *NFA* yields reasonable results in terms of eigenfrequencies, response and displacement, verifying a sufficient and satisfying *FE*-model. The *NFA* also gives first indications on the global capacity and on the performance of the link element with reference to the maximum stiffness at the connection between *MP* and *TP* in Tab. 5.15.

Tab. 5.15: Maximum stiffness values at selected nodes

Node	*Translation*		*Rotation*	
	Ele. stiffness [kN/m]	*Max. stiffness [kN/m]*	*Ele. stiffness [kN/m]*	*Max. stiffness [kN/m]*
TOPPIL	8.2465E+07	8.2465E+12	8.4518E+08	8.4518E+13
PILTOP	5.4250E+07	5.4250E+12	6.9513E+08	6.9513E+13

5.3 Design process

For the comparison study and the overall evaluation of *OCW3D* one cornerstone of the monopile design shall be simulated and precisely documented. This allows a clear understanding and identification of necessary features an alternative to *WAVGEN* needs to provide. Here, the principle objective is to modify the current workflow as little as possible. Before integrating *OCW3D*, the common procedure shall be conducted based on the design scenario in 5.1. The main focus shall be on *ULS* analyses although the complete engineering additionally prescribes *NFA* and fatigue life state (*FLS*) examinations. Each design case in Fig. 5.9 relies on different loadings and yields specific pile characteristics like soil penetration depth, global dimensions and material thicknesses.

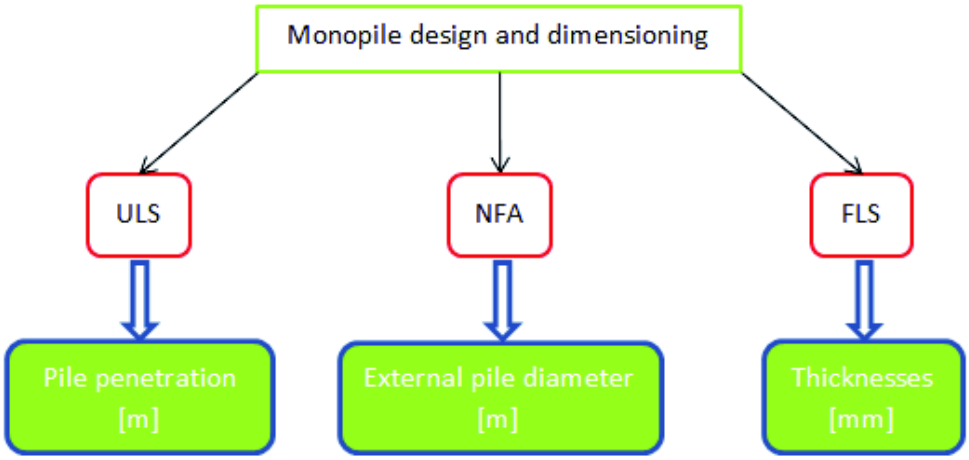

Fig. 5.9: Flowchart of monopile design and corresponding output

The *ULS* assessment constitutes a worst case scenario and thus includes extreme waves in order to give indications on the pile penetration in the sea floor. Usually, several design load cases (*DLC*) are assessed considering also different critical wind models. For this work the influence of aerodynamic forces shall be neglected and solely hydrodynamic effects on the structure shall be compared which are dominant for water depths greater than *25.0* metres in the open sea. The comparison study shall concentrate only on waves and their kinematics, excluding any current interference. Besides the *FE*-model of the monopile described in 5.2 both the conventional and new approach rely on the same input parameters and boundary conditions. For the *ULS* design the metocean data provides a significant wave height and wave peak period for a return period of *50.0* years, underlining the rigorous conditions for this load case. In principle, this exceedance probability states that the specified design wave will only be exceeded once in *50.0* years. In contrast, substations are evaluated under more conservative conditions and a *100.0* years return period is stipulated simply due to the fact that those offshore installations are considered to be manned. Furthermore,

the *ULS* study requires the explicit water depth and soil composition proposed by geotechnical screening on site. The topside of the offshore installation includes the turbine, the tower, working platforms and rotors and the data on their weight, accelerations and stiffness properties complement the governing factors of the monopile design. The starting situation and the common ground for the comparison and plausibility study is summarised in Fig. 5.10 and the subsequent conventional approach describes the continuation with *WAVGEN* whereas the new approach covers the integration of *OCW3D*.

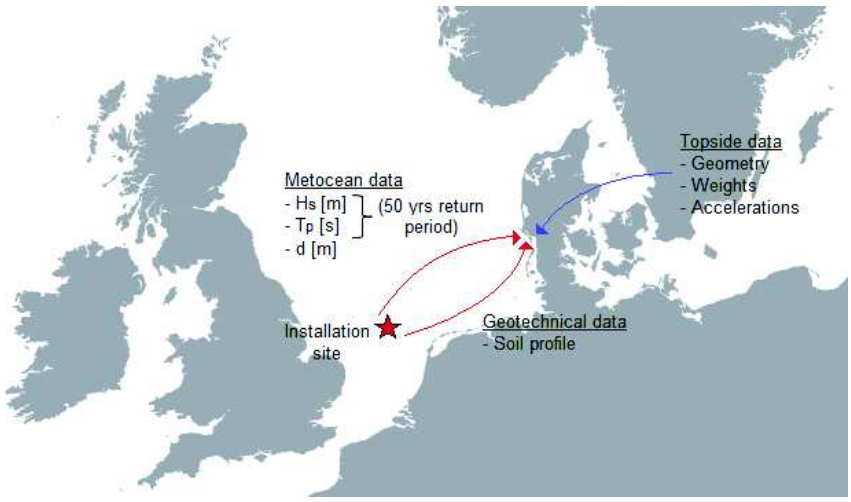

Fig. 5.10: Input and initial situation for the comparison study between WAVGEN and OCW3D

5.3.1 Conventional approach

Following the conventional approach of *Rambøll* the hydrodynamic loading to determine the ultimate strength of the construction is attained by combining two different wave simulations. The common practice is to generate a linear irregular sea state in a reduced time series of around *300.0* seconds, determine its largest single wave and replace it by a stream function wave. The background sea state is based on a *JONSWAP* spectrum implementing significant wave height, peak period and water depth from the previously mentioned metocean data whereas the regular non-linear wave is built upon the maximum wave height and its associated period in (5.1) and (5.2). This embedded stream function wave in an irregular time series allows to control and accurately define the greatest design wave and to cover the non-linearity caused by the shallow water effect to a certain level as well as the randomness of the water surface [27]. Although *ULS* studies solely focus on an extreme event and thus should only rely on the most critical wave which certainly is embodied by the stream function theory, it is very important to include the linear irregular sea state and to observe the wave interactions and the associated structural response. This becomes evident in dynamic analyses as the oscillating reaction of the monopile induced by the

extreme wave can be superimposed by a second wave, possibly yielding a more adverse impact. Among experts this refers to the *lock-in* situation where the structure is heavily exposed to increasing wave loads as waves are approaching in such an interval that they constantly add up along the foundation.

The replacement wave in Fig. 5.11 is symmetrically arranged around the peak of the maximum wave in the irregular background sea state with an extent of half f_r and T_r to each side where T_r is the replacement wave period and f_r the replacement factor. At the beginning and end of this specified interval the transition between the regular wave and the irregular sea state is conducted by a *sine-cosine* transition. Here, the blending interval is defined by T_r and the overlapping factor f_0. In this case, twice the wave length of the design wave is integrated in the irregular wave train to accurately simulate non-linear wave troughs. The transition region is controlled by an overlapping factor of *0.25* times the wave length and the affected surface elevation as well as kinematics are multiplied with *sin(0)* to *sin(π)* and *cos(0)* to *cos(π)* for a smooth blending [27]. So the conventional approach consists of a linear irregular sea state described in 2.5 with an embedded stream function wave as in 2.6.2 and the data in Tab. 5.16 yield the wave in Fig. 5.11 which is applied on the monopile for *ULS* determination.

Tab. 5.16: Sea state and extreme wave conditions with respect to LAT

Return period [years]	*d [m]*	*H_s [m]*	*T_p [s]*	*H_{max} [m]*	*T_r [s]*	*Wave direction [deg]*
50.0	27.0	9.0	13.0	16.7	13.7	0.0

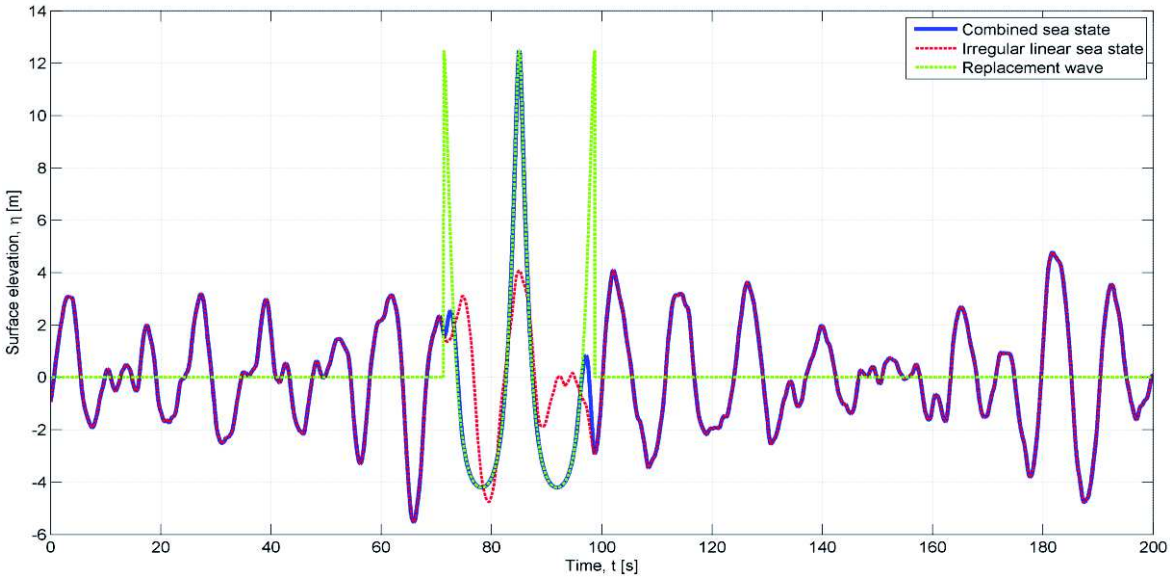

Fig. 5.11: Design wave of conventional approach obtained by WAVGEN for ULS analysis

The magnified extract of the above sea state in Fig. 5.12 clearly illustrates the common procedure of replacing the most pronounced linear wave in the random time series in red by a very steep and highly non-linear wave in green, yielding the combined sea state in blue.

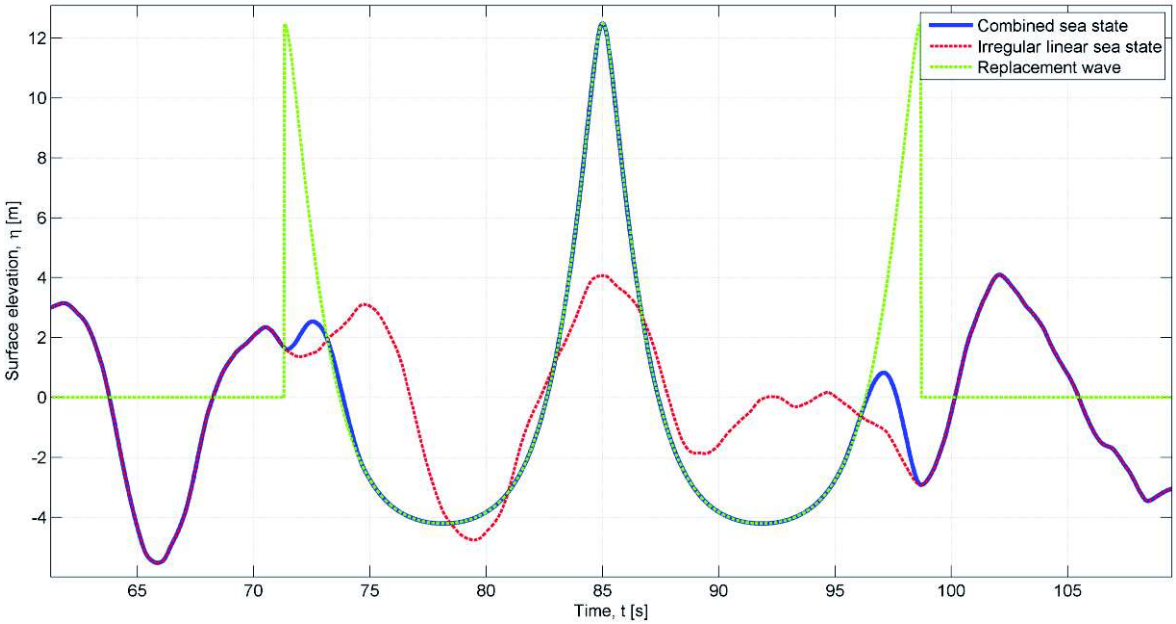

Fig. 5.12: Extract of the worst case scenario for the monopile in the conventional approach

In order to reach the objective of identifying the maximum *OTM* the monopile foundation is generally examined under different conditions and constellations. Here, the wave direction, the arrangement of external appurtenances and the influence of marine growth (*MG*) are the principle variation parameters as they either enlarge or reduce wave loads. In the subsequent *ULS* assessment the wave direction is set to zero and the orientation of anodes and boat landing (*BL*) is defined in a way to attain highest impacts due to the increased area of attack. So to foresee the consequences of those influencing factors the monopile shall be considered without and with a boat landing or marine growth, resulting in three models for quasi-static (*QS*) and dynamic (*DYN*) analyses. The impact of the stream function wave of the monopile can be seen in Fig. 5.13 and the responsible wave load and resulting *OTM* for each case are summarised in Tab. 5.17.

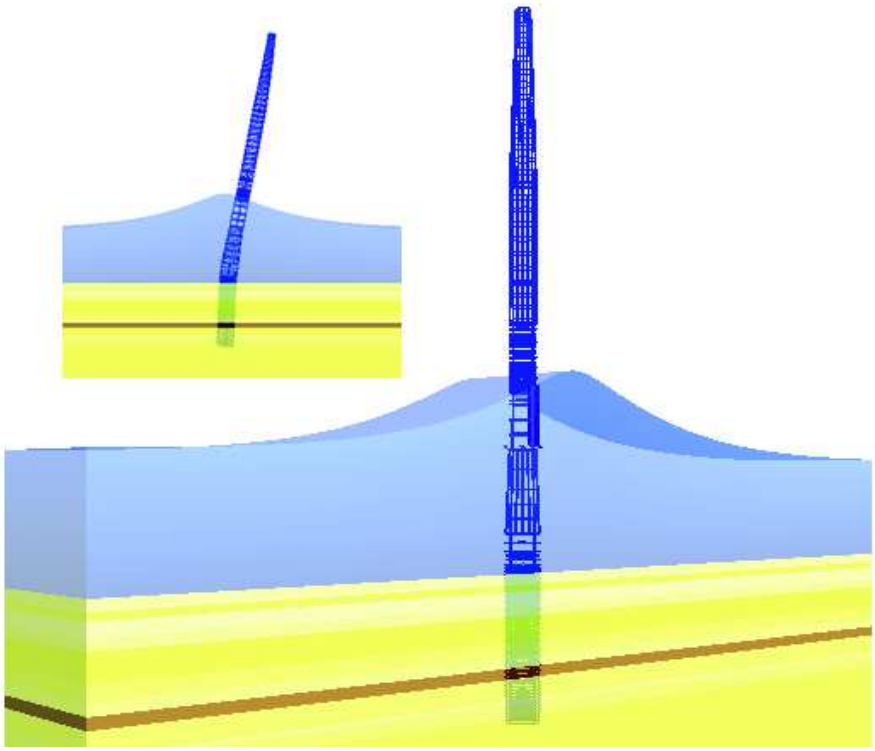

Fig. 5.13: Upscaled deflection of monopile and depiction of stream function wave

Tab. 5.17: Final results of conventional ULS assessment of monopile structure

	*No BL & No MG**		*BL & No MG*		*No BL & MG*	
	QS	*DYN*	*QS*	*DYN*	*QS*	*DYN*
Shear force [kN]	4735.7	4953.0	5184.0	5426.4	5323.1	5573.1
OTM w.r.t. mudline [kNm]	103786.0	124325.0	122717.0	142989.0	114665.0	135645.0

* Reference values for comparison study

The above presented results truly reveal the surge of wave loads and thus a greater *OTM* if the boat landing is arranged perpendicular to the wave propagation and marine growth is considered. It also shows that the accentuation of the surface roughness due to marine growth results in a greater shear force but in a smaller *OTM* than the enlarged load area in the impact zone of the wave. Additionally, one can surmise the interaction of consecutive waves and a certain extent of *lock-in* because the dynamic analyses uniformly produce greater wave loads and eventually greater reaction moments. However, the increase of wave loads by roughly *8.6 %* due to external appurtenances and by *11.0 %* due to marine growth do not turn out to be as striking as expected which can also be perceived in Fig. 5.14. On that account and to reduce the time effort and any errors the naked monopile shall be used for the comparison and plausibility of *OCW3D* only.

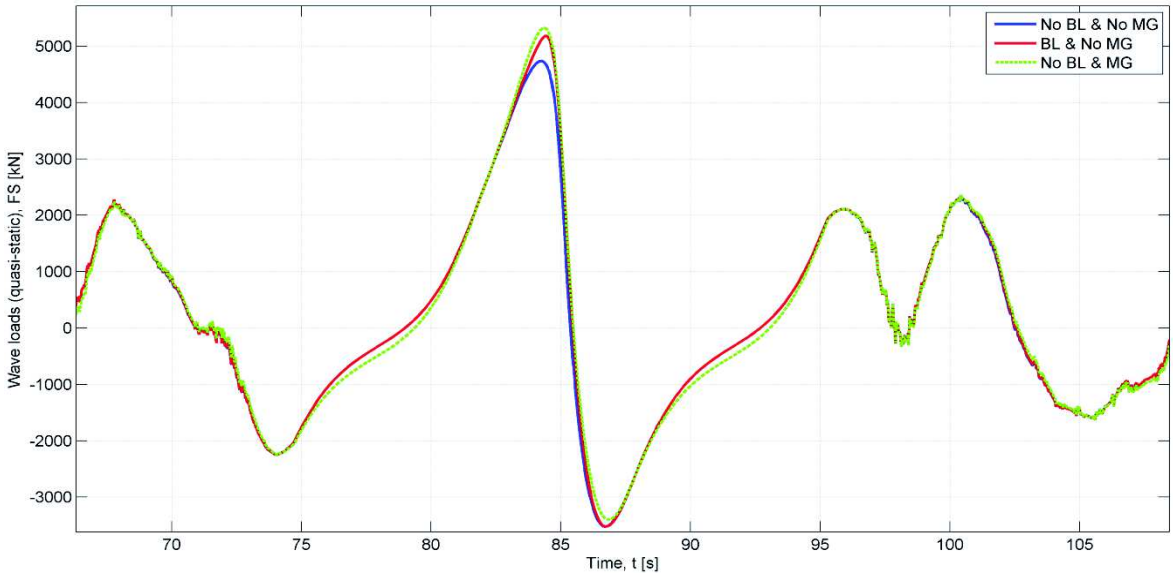

Fig. 5.14: Comparison of quasi-static wave loads for the three different design constellations in the time of ESS

Eventually, the *OTM* results for the first design case in Tab. 5.17 shall be used as a reference value for the new approach. A closer look on the complete time series and the detailed view on the embedded stream function in Fig. 5.15 and Fig. 5.16 show the difference between quasi-static and dynamic response as the latter causes extreme oscillations of the *OTM* after the extreme wave hits the monopile. Furthermore, the results match the assumptions and the knowledge received in 3.2 as the *OTM* progression correctly follows the *WAVGEN* sea state with a slight phase shift due to inertia effects. The output values as well as temporal propagation of wave and *OTM* are indicative of a proper monopile modelling, wave generation and *ULS* computation, providing a solid basis for the upcoming comparison.

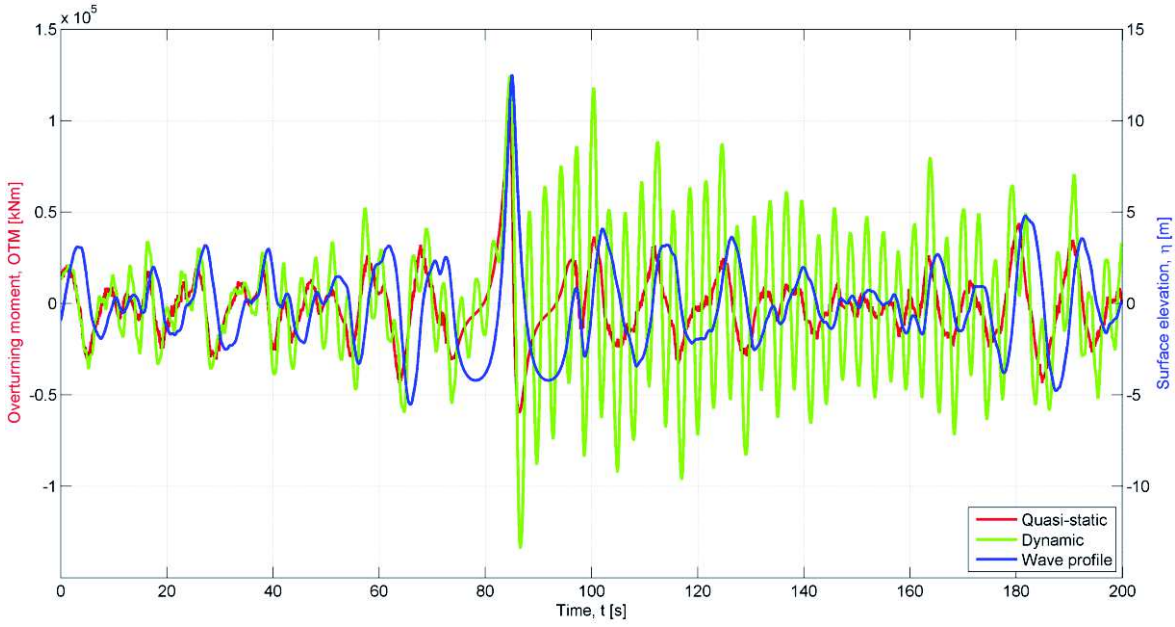

Fig. 5.15: Overall time series of OTM for the first design (No BL & No MG)

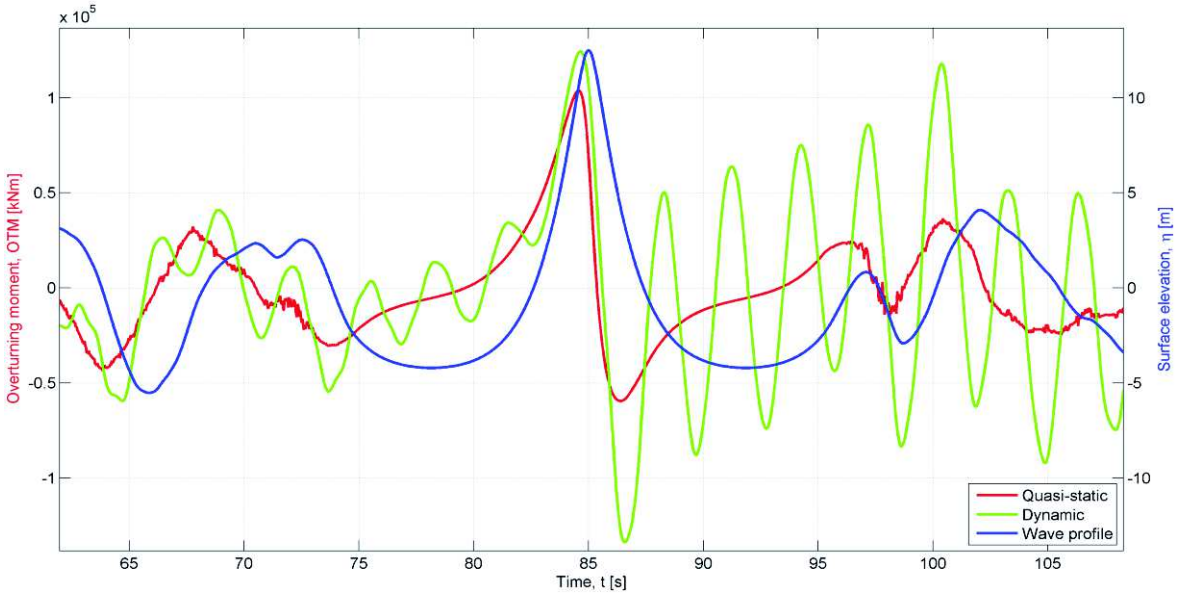

Fig. 5.16: Closer look on the OTM time series in line with wave propagation

5.3.2 New approach

The new approach of integrating *OCW3D* entails the following properties and in particular stands out with the fact that the depth interference is considered for the complete irregular sea state. As the background water surface in the conventional approach is composed of regular linear wave components which only depend on the amplitude and *sine* expression in 2.5.3 the final water profile is entirely unaffected by the distance to the sea floor. The non-linear solution in *OWC3D* does not only account for this essential influence but also for the correct and immediate computation of wave kinematics to the instantaneous water level. Thus, there is no need for any profile extension method for the wave kinematics. But in contrast to the embedded stream function wave, the new approach is solely based on a spectrum and thus random sea state, resulting in an uncontrollable extreme wave with an unpredictable maximum wave height. In order to tackle this challenge it is crucial to conduct multiple realisations and to generate fully developed sea states. Here, [14] recommends to record data from a one hour time series in order to receive reliable results presented more precisely in the following chapter. The main focus shall be on the correct dealing with input variables and output options in *OCW3D*, starting with the spatial and temporal resolution for the non-linear computation of an irregular water surface.

As described in 4.2 *OCW3D* represents a numerical wave tank which requires a clear description of both the time and space domain. *Paulsen et al. (2015)* [22] provides rules of thumb on the computational grid for a converging numerical solution based on the cut-off frequency f_{cut}. This input parameter refers to the upper bound of

the frequency range until the *JONSWAP* spectrum is valid as the previously mentioned paddle signal shall resemble reality as good as possible and thus simply cannot produce waves with extremely short periods. Different α-values and the corresponding cut-off frequencies are illustrated in Fig. 5.17 whereas for the new approach α is set to three.

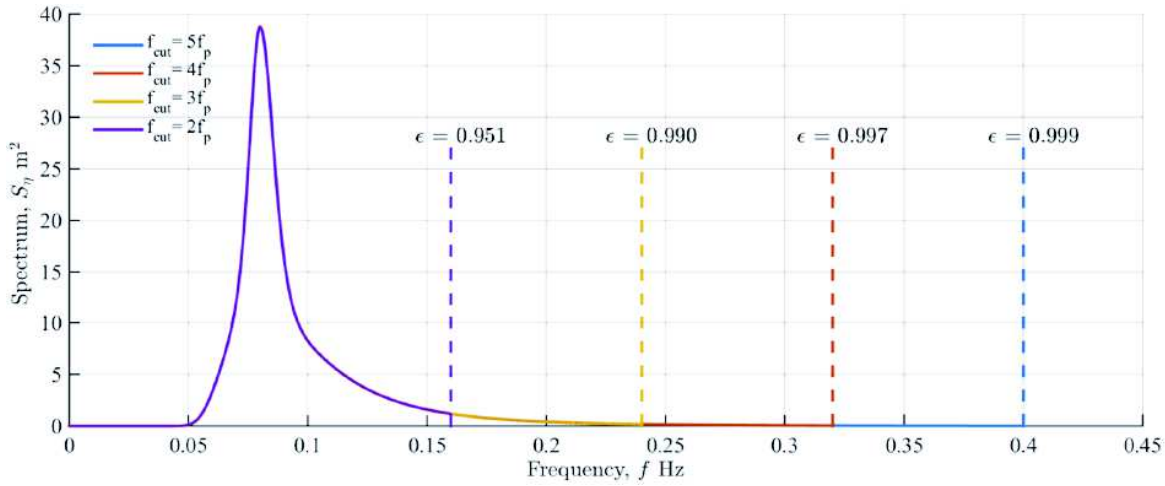

Fig. 5.17: Different truncation frequencies for the input spectrum [22]

According to [22] the grid should feature at least five points per leading order wave length in the x-direction and *10* to *15* points for the vertical resolution. Together with f_{cut} in (5.3) and the maximum wave number k_{cut} in (5.4) the shortest wave length L_{cut} can be determined according to (5.6) which is then accurately described by five grid points, resulting in the following horizontal spacing in (5.7).

$$f_{cut} = \alpha \cdot f_p = \frac{3}{13.0} = 0.23\ Hz \tag{5.3}$$

$$k_{cut} = \frac{(2\pi \cdot f_{cut})^2}{g} = \frac{(2\pi \cdot 0.23)^2}{9.81} = 0.21 \frac{1}{m} \tag{5.4}$$

$$kh_{max} = 0.21 \cdot 27.0 = 5.67 \approx 6 \tag{5.5}$$

$$L_{cut} = \frac{2\pi}{k_{cut}} = \frac{2\pi}{0.21} = 29.3\ m \tag{5.6}$$

$$dx = \frac{L_{cut}}{5} = \frac{29.3}{5} = 5.8\ m \approx 5.9\ m \tag{5.7}$$

The entire numerical wave observation visualised in Fig. 5.18 shall be over a distance of *1500.0* metres so that there is enough space for generating and absorbing waves. As already mentioned in 4.2 the generation zone shall be as long as the wave length corresponding to the specified T_p which amounts to *196.45* metres by means of the dispersion relationship for the wave in 5.1 under deep sea conditions whereas the dissipation area at the end is extended by an additional wave length to avoid any perturbations of reflected or refracted waves.

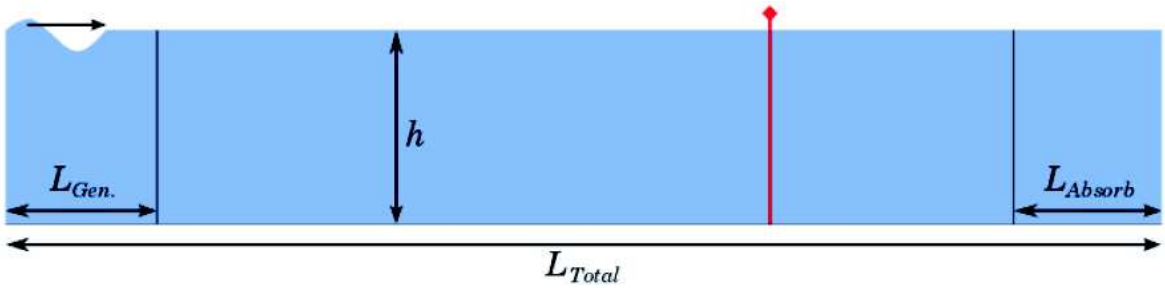

Fig. 5.18: Length division of numerical wave tank in OCW3D [22]

As the monopile only depends on one x-position compared to a jacket structure and as the structural response shall be presented in the time domain, the temporal resolution plays an even bigger role for the accuracy and numerical concept in *OCW3D*. For a start the *CFL* number can be used which describes the ratio between spatial and temporal spacing for solving partial differential equations numerically. For proper convergence the time step has to satisfy a *CFL* value below one.

Fig. 5.19 shows a *CFL* of *0.8* in red, of approximately *0.5* in blue and an extremely small time step of *0.1* seconds in green with $dx = 5.0$ metres. First of all, one can clearly perceive how the choice of time step alters the surface elevation. This traces back to the solution code as the time steps govern the number of *Fourier* steps, resulting in alternating water levels at certain points in time. Additionally, the accuracy or the smoothness of the water surface in the detail window obviously depends on the time step. Due to the non-linear characteristics of the *OCW3D* sea state a time step of *0.4* seconds is considered to be too coarse whereas everything below *0.2* seconds causes a computational and storage overflow. On that account and with respect to numerical precision the temporal resolution is set to *0.2* seconds, yielding *18000.0* data sets for a one hour sea state simulation in *OCW3D*.

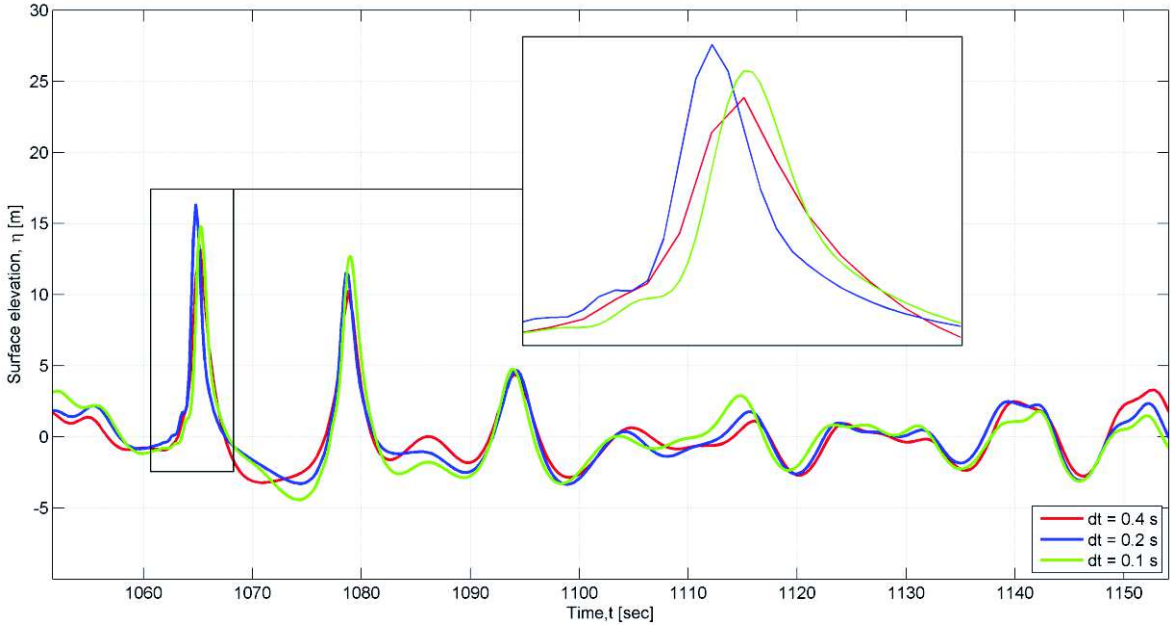

Fig. 5.19: Temporal resolution study for a non-linear sea state in OCW3D

Because of the non-linear handling of the boundary conditions in *OCW3D* not only the more realistic waves with an anticipated asymmetric shape around its vertical and horizontal axis evolve but also waves with radical heights and steepness can be found in the outputted sea state. However, those waves would normally not exist as the built-up energy would be so high that the waves would actually break under genuine conditions. In order to account for this behaviour a breaking filter (*BF*) can be adjusted, constituting one of the most important input parameter of the new software. This application implies a smoothing of waves whose vertical water particle acceleration exceeds a certain gravitational fraction. Although this approach is seen as a rather simple wave breaking model, investigations provided by *Harry B. Bingham* (*PhD, Associate Professor* at *DTU*), show that a value of *0.4g* reveals a considerable good representation of the actual energy dissipation of breaking waves under hydrodynamic consideration. In essence, the breaking filter searches the non-linear sea state for waves with vertical accelerations greater than the specified limit, takes away the excess energy and polishes the surface elevation. Based on the comparison study on an exemplary sea state in Fig. 5.20 exposed to different breaking filters a more reserved assumption of *0.9g* shall be applied for the first calculation runs.

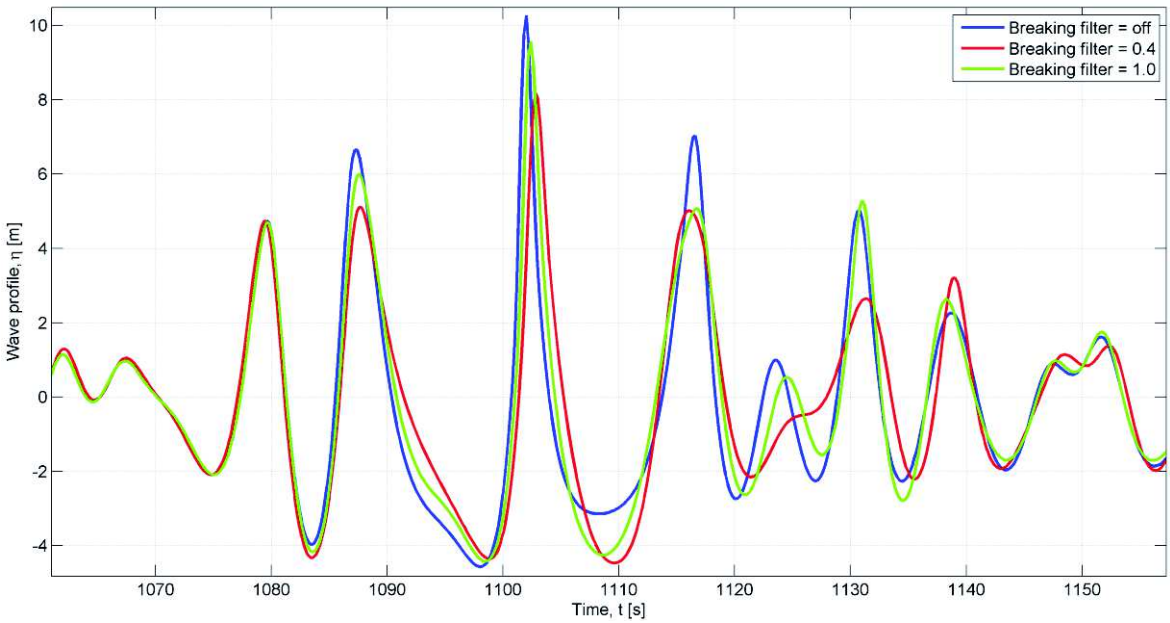

Fig. 5.20: Different breaking filters on a non-linear irregular sea state

As the main objective is to identify a wave within the non-linear irregular sea state which corresponds to the embedded stream function wave with an equal structural impact and hydrodynamic properties, it must be ensured that ample data is available for a statistically stable evaluation. Since *OCW3D* in principle resembles a numerical wave tank it is possible to extract wave kinematics at different positions along the tank and record them over the entire time frame. So picturing the one hour sea state at varying x-coordinates would basically yield a various amount of wave realisations. In order to account for the different energy levels caused by the applied breaking filter it is agreed to collect data right behind the generation zone, before the absorption zone and at a position between both, as visualised in Fig. 5.21.

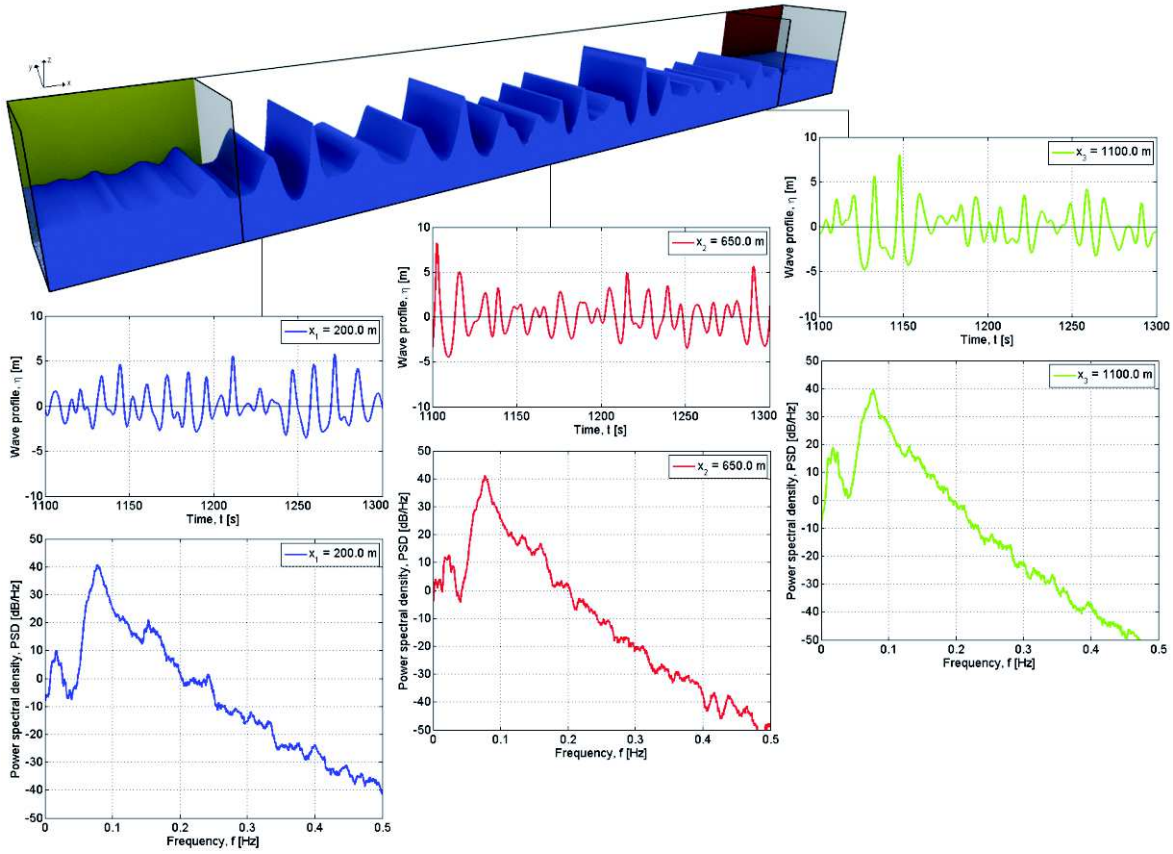

Fig. 5.21: Graphical description of OCW3D's numerical wave tank and the agreed extraction points

If the surface elevations at $x = [200.0\ m,\ 650.0\ m,\ 1100.0\ m]$ and the associated spectral energy distributions from above are plotted together in Fig. 5.22 and Fig. 5.23, the deviation and the development of the non-linear wave train along the wave tank become evident.

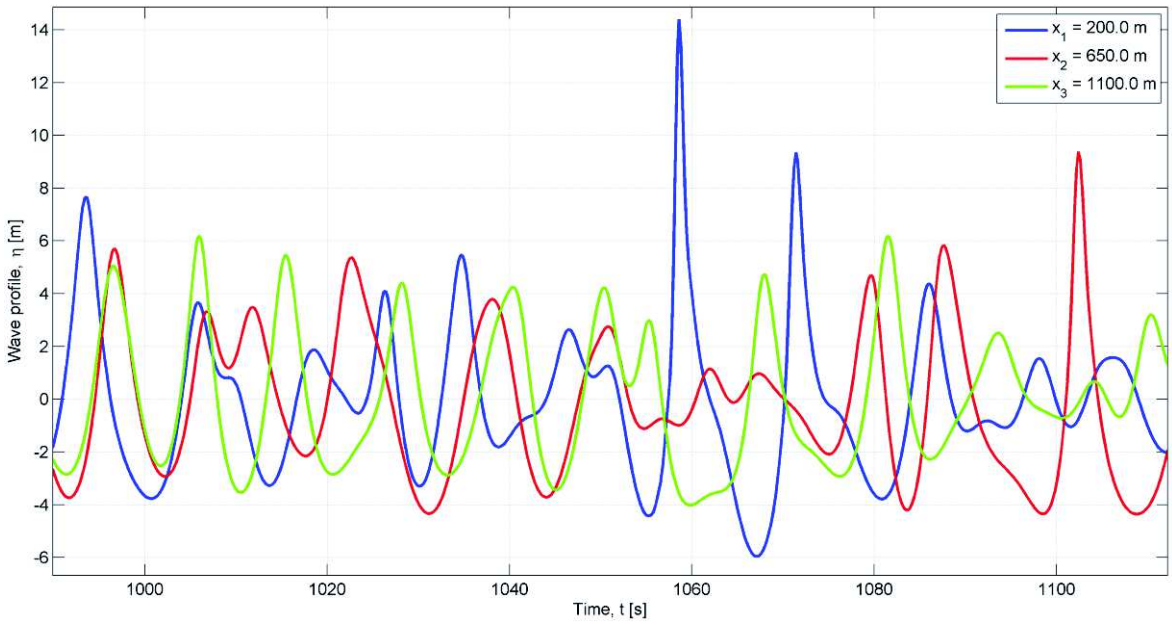

Fig. 5.22: Extract of non-linear irregular sea states at three different x-positions

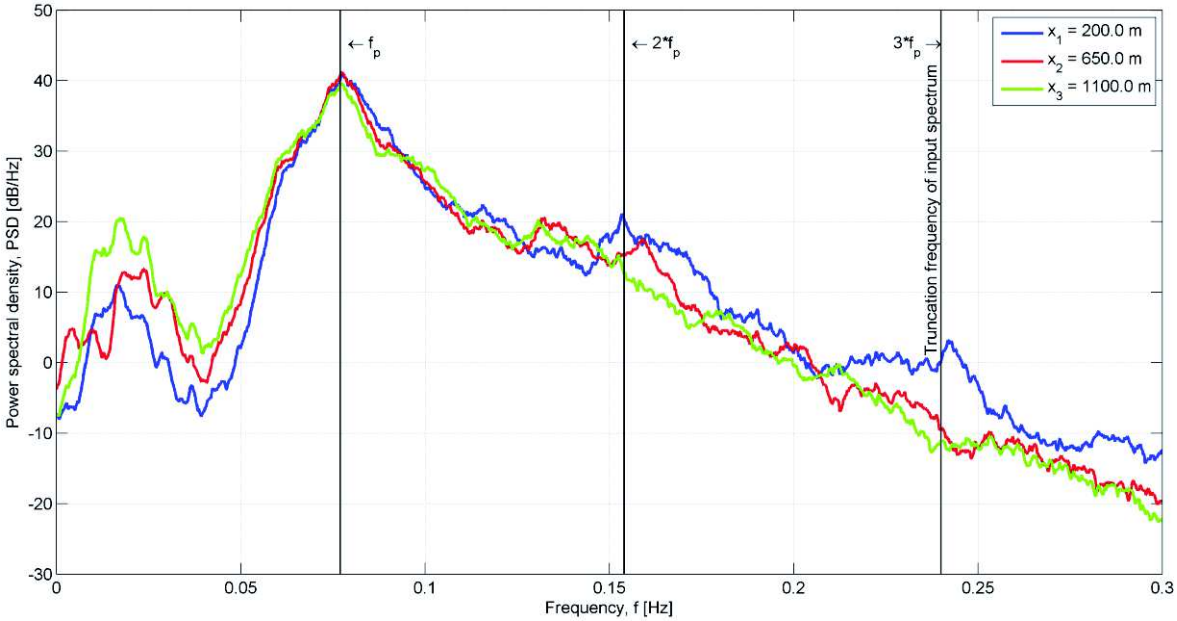

Fig. 5.23: Power spectral density of the surface elevation at the specified points

As mentioned before, the non-linear solution method of *OCW3D* is responsible for the development of very steep and asymmetric waves with a considerably high energy potential. By looking at Fig. 5.23 those non-linear effects and the corresponding higher orders are clearly visible in the peaks which are particularly pronounced at the first position behind the generation zone. Here, it can be said that the paddle is inducing energy without being reduced by the breaking filter yet. At the second position where the wave train has already travelled *450.0* metres after the generation zone the third peak at around *0.24 Hertz* vanishes. The numerical breaking filter has resembled natural wave breaking and thereby a reduction of steepness/energy around the third order peak. Compared to reality the large and very steep waves from the first position dissipated their energy through breaking. This is confirmed by investigating the final position at the end of the regular part of the wave tank before absorption is initiated. Here, the spectral power density exemplified by the green line in Fig. 5.23 shows a considerable energy loss and thus a decrease of non-linearity, eliminating all deceptive waves within the sea state. In the end, it is assumed that the sea state has reached a fully developed and stable condition basically with limited wave breaking and thus without unrealistic wave formations right before the absorption zone.

In order to increase the amount of evaluable material *OCW3D* offers the possibility to generate up to five different seeds for irregular sea states based on the same wave spectra. With reference to 2.5.2 an irregular sea state is simulated by means of a wave spectrum and arbitrarily chosen phase shifts. So in order to reproduce results and to guarantee different sea states phase information are stored under the so-called seed

number. As a starter three diverse seeds are computed, shown in Fig. 5.24 and together with three recording positions along the *x*-axis nine non-linear sea state realisations are applied on the monopile and compared to the conventional approach.

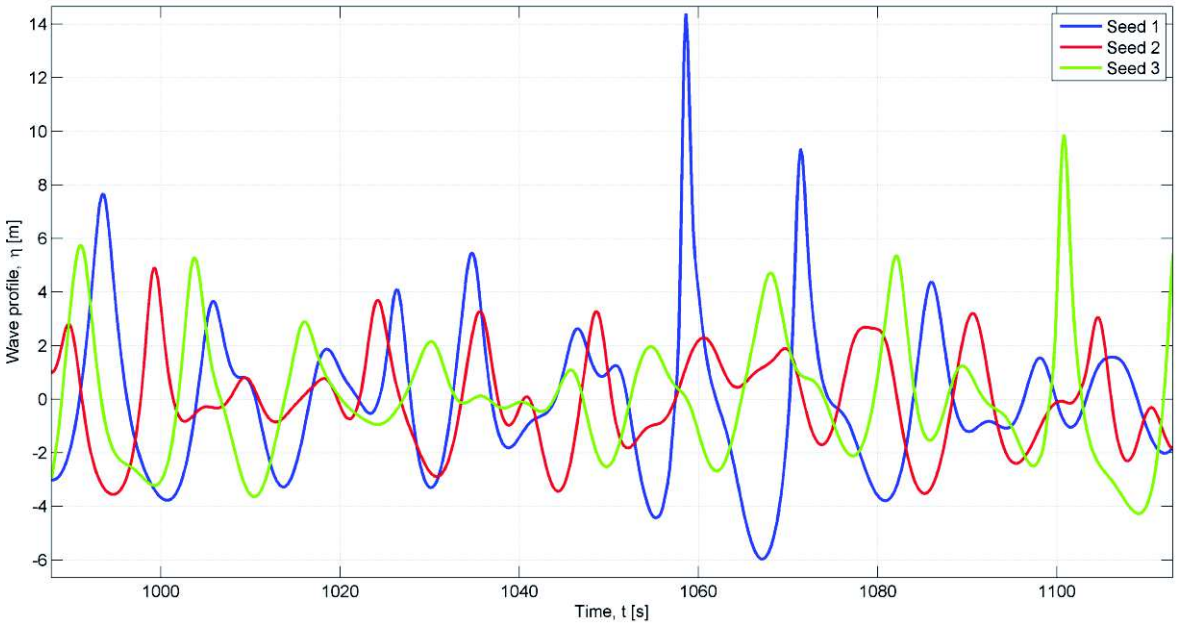

Fig. 5.24: Segment time series of surface elevation for three different seeds at the same extraction position along the numerical wave tank

To sum up and upon consultation again with *Harry B. Bingham* and *Bo Terp Paulsen* (*PhD, advisor and researcher at Deltares*) the above presented and from now on applied non-linear surface elevations are based on the input parameter in Tab. 5.18 for *OCW3D*. A complete time series of the first seed behind the generation zone at $x = 200.0$ metres with the generalised labelling *S1_X1* and the highest wave in the magnification can be seen in Fig. 5.25. Here, the blow-up nicely reveals the outstanding ability of *OCW3D* to produce realistic water surfaces as the presented wave features a complete random shape and greatly exemplifies the asymmetry around its principle axes.

Tab. 5.18: Summary of OCW3D input

Input parameter	*Value*
Significant wave height, H_s [m]	9.00
Peak period, T_p [s]	13.0
Water depth, d [m]	27.0
max(kh)	6.0
Seeds	3
x-spacing, dx [m]	5.0
Total length, L_{tot} [m]	1500.0
Generation length, L_{gen} [m]	200.0
Absorption length, L_{abs} [m]	400.0
Time span, t [s]	3600.0
Time interval, dt [s]	0.2
Data at x-position, x [m]	[200.0, 650.0, 1100.0]
Breaking filter, [m/s²]	0.9g

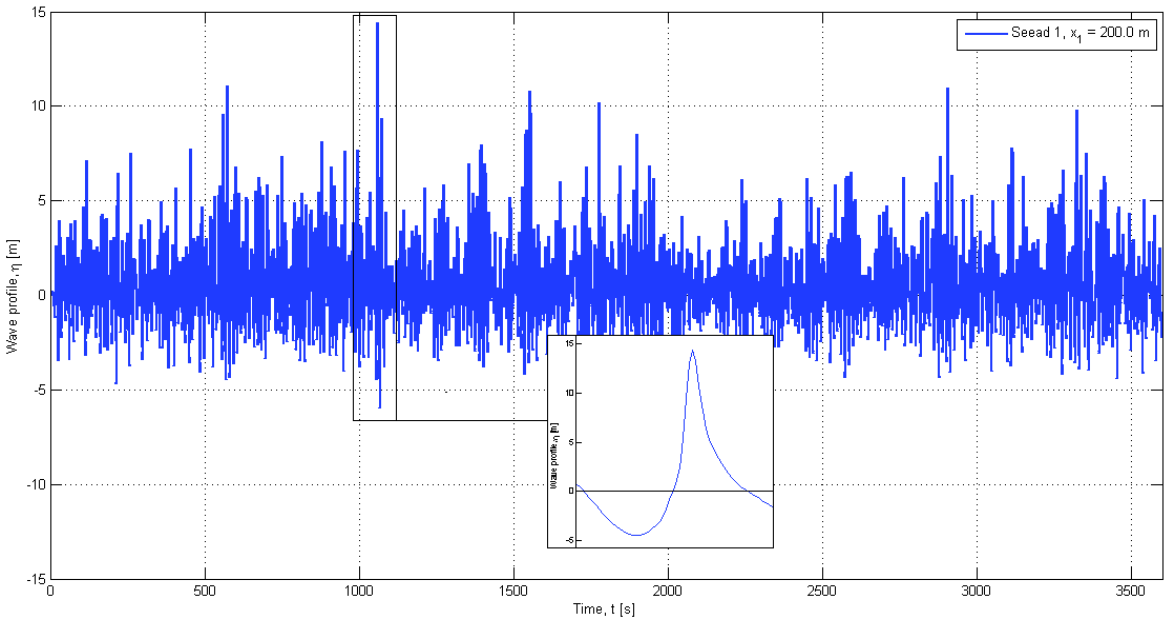

Fig. 5.25: Complete time series of a one hour non-linear irregular sea state with extreme wave in the detail

If the *FLEX5* output file is converted and corrected according to 4.2.2, all nine non-linear sea states are implemented in *ROSA* to load the monopile model. The expected distribution of the structural response obtained by quasi-static and dynamic analyses is demonstrated in Fig. 5.26 and Fig. 5.27 and the resulting maximum *OTMs* are summarised in Tab. 5.19.

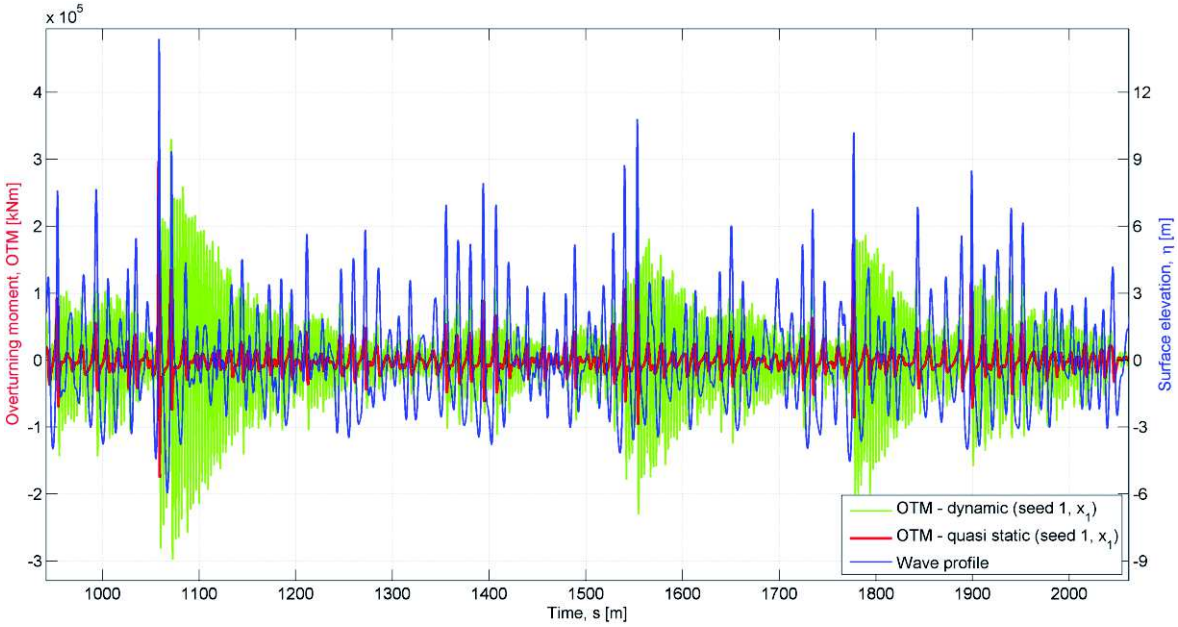

Fig. 5.26: Longer time series of OTM for the first seed at the first position

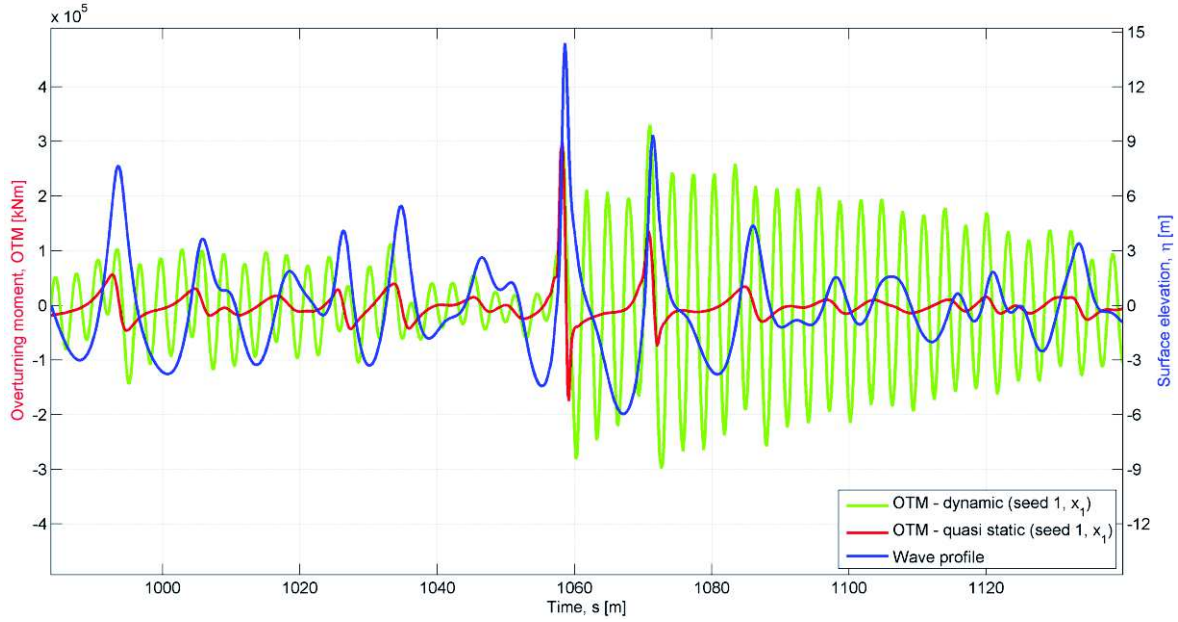

Fig. 5.27: Extract of the above to show structural response induced by the most extreme wave in the first seed

Fig. 5.28 illustrates the difference in the structural response of the monopile foundation if exposed to the third seed in *OCW3D*. Compared to the above the extreme wave does not turn out as big as in the first seed and occurs later in time.

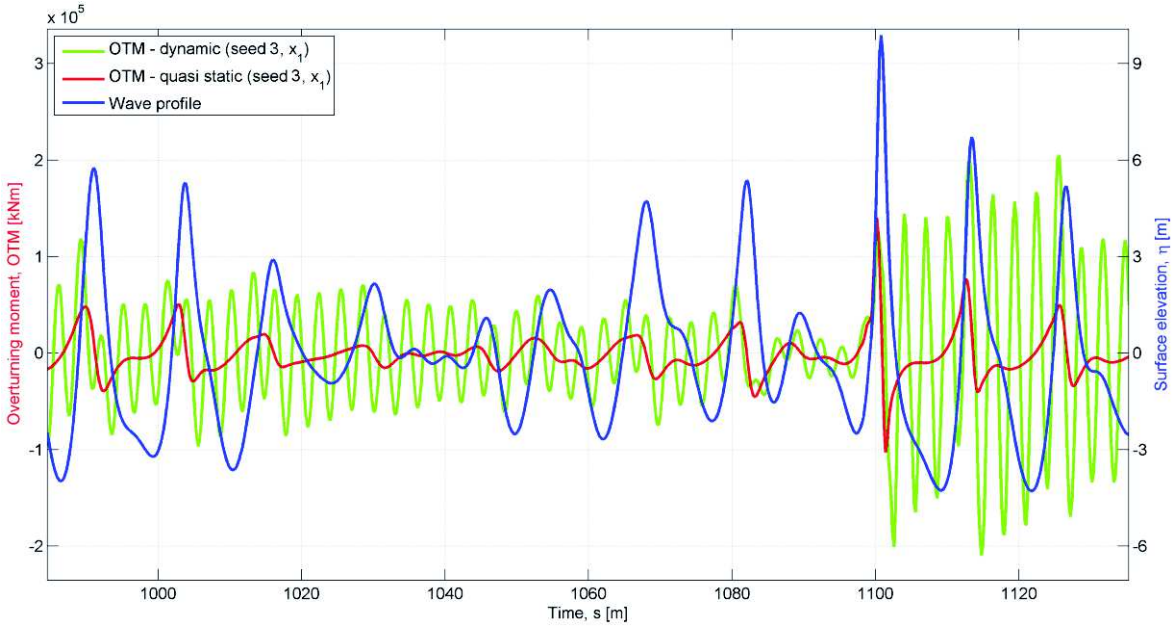

Fig. 5.28: Extract of the structural response induced by the most extreme wave in the third seed

Tab. 5.19: Final results of new ULS assessment of monopile structure

Description [S = seed; X = position]	*Shear force [kN]*		*OTM [kNm]*	
	QS	*DYN*	*QS*	*DYN*
S1_X1	12436.7	14718.8	297851.0	330388.0
S1_X2	6417.1	6630.1	136069.0	130218.0
S1_X3	6907.1	7130.4	162541.0	199219.0
S2_X1	6474.4	7229.8	136245.0	179203.0
S2_X2	5471.8	5077.2	118199.0	162415.0
S2_X3	6977.3	7560.7	154901.0	162084.0
S3_X1	7849.9	8333.6	168591.0	263696.0
S3_X2	7533.5	7886.3	170314.0	243105.0
S3_X3	7007.3	6902.7	163377.0	166185.0

In Tab. 5.19 one can perceive how the wave scenarios produce different results based on the random phase shifts and on which power the wave in the beginning of the tank possesses. In particular, the first seed right behind the generation zone

produces an extreme wave which creates a high response compared to the remaining seeds and positions. However, as these results represent maximum values and rely on metocean data for a return period of *50.0* years, the output data shall be assessed further in the subsequent chapter for the final comparison with the maximum *OTM* received by *ROSA* and *WAVGEN*.

5.4 Results and assessment

It is important to begin by saying that a breaking filter of *0.9g* yields overly conservative results with respect to wave elevation and kinematics as seen in the later course by means of the structural response of the monopile. On that account, it shall only be considered as a reference value for the upcoming comparison and the more realistic value of *0.4g* shall be adopted, of course following the exact same procedure described in 5.3.2. Additionally, it becomes apparent that the dynamic analyses may distort the structural response due to *lock-in* effects in a way that the *OTM* cannot distinctly be affiliated to one specific wave. This could be impeding and elusive for the comparison study and thus only quasi-static conditions shall be evaluated from now on.

So far the previously presented steps reveal one single maximum *OTM* received by the embedded stream function wave in *WAVGEN* and several maximum *OTMs* for all different wave scenarios generated in *OCW3D*. However, in order to answer the initial question whether the non-linear sea state solution produces a single wave that exceeds the embedded stream function wave and its respective structural response the output by *OCW3D* requires further post-processing. Here, a single wave assessment shall be performed to explicitly identify wave characteristics and their impact on the foundation. Therefore, a tool is applied which separates single waves within the non-linear time series from *OCW3D* by filtering zero-down crossings of the surface elevation and determining the corresponding wave height and period. The resulting *OTM* with respect to the associated time frame is found in *ROSA* output files by *Matlab*. Eventually, this aggregates approximately *300* waves within each non-linear sea state realisation. As the lower breaking filter is now appraised as the baseline value the seed number shall be increased to enlarge the data record, eventuating in an analysed wave quantity of *4722* for a breaking filter of *0.4g* (*5* seeds, *3* positions) and of *2825* for *0.9g* (*3* seeds, *3* positions). This single wave description allows a clearer and organised data handling for the comparison between both approaches and yields the following distribution of occurring waves for a breaking filter of *0.4g* in Fig. 5.29 to Fig. 5.31. Fig. 5.31 nicely displays the expected

cluster of waves around a mean zero crossing period between *10.0* to *11.0* seconds, underlining a reasonable wave simulation with respect to the inputted peak period of *13.0* seconds.

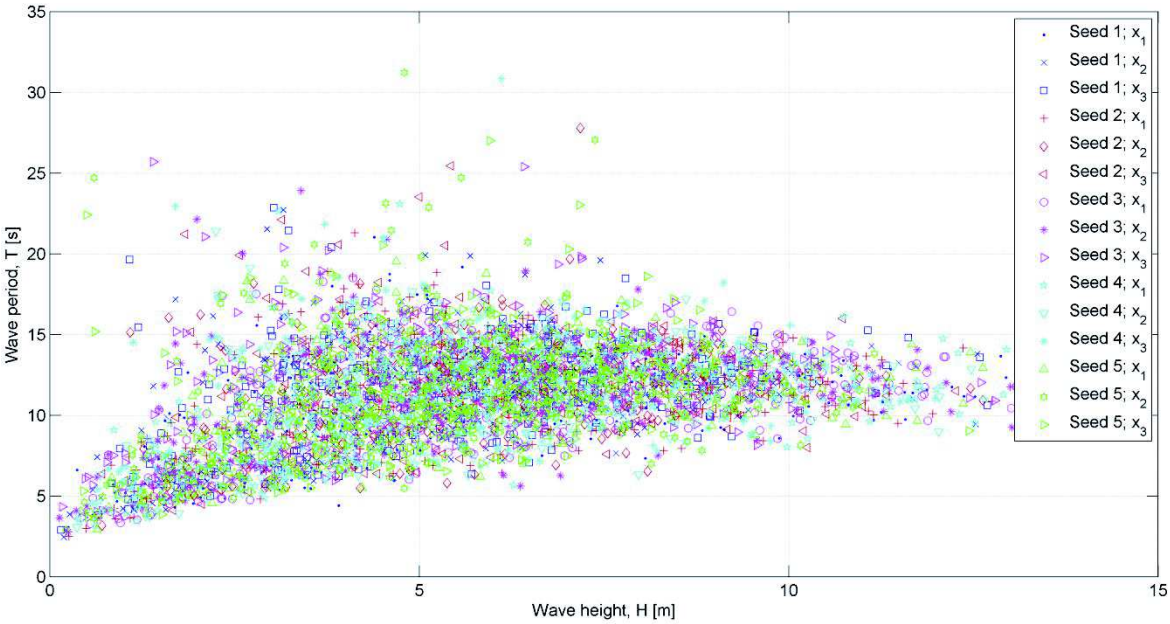

Fig. 5.29: Distribution of occurring wave periods as a function of wave height

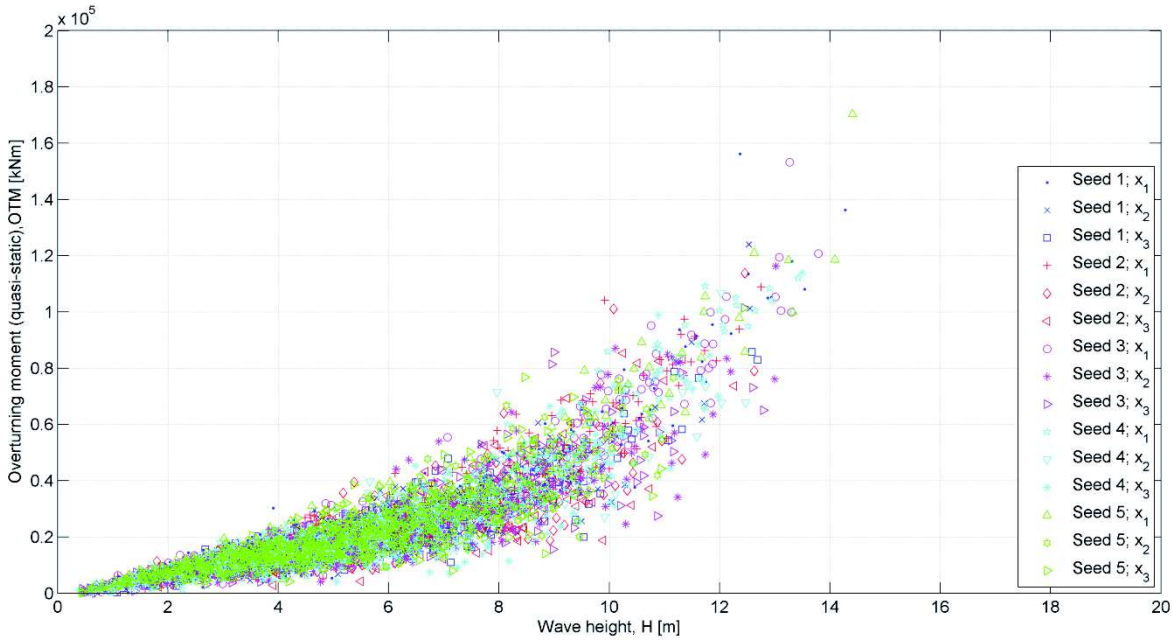

Fig. 5.30: Resulting OTM as a function of recorded wave height

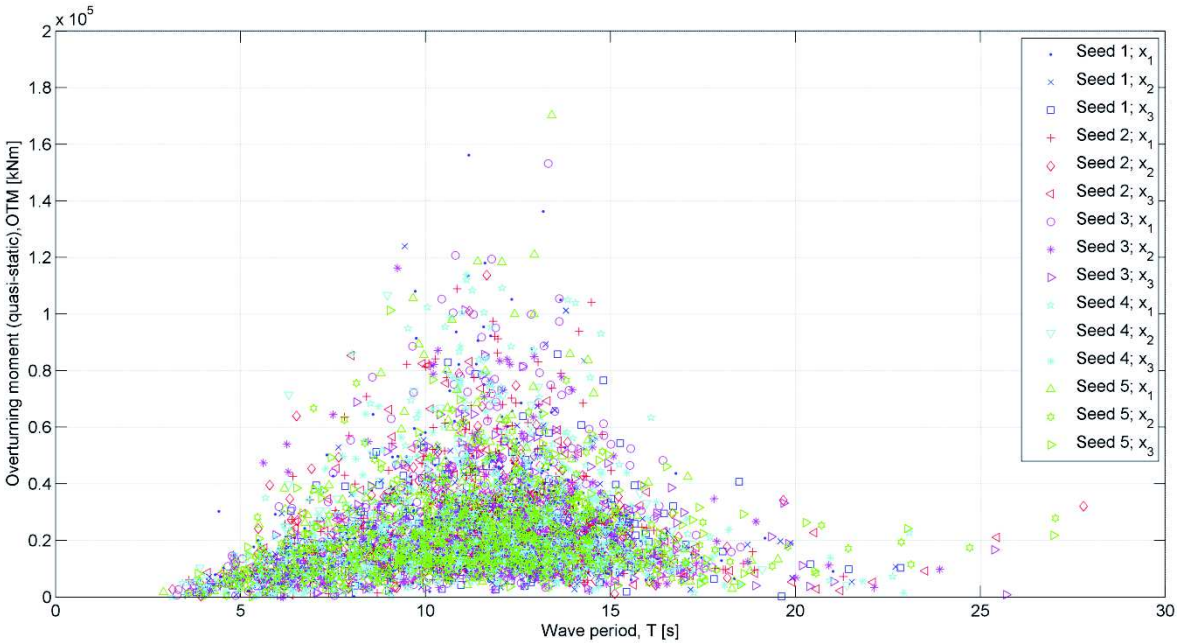

Fig. 5.31: Resulting OTM as a function of recorded wave period

Fig. 5.32 and Fig. 5.34 summarise all findings in one graph by plotting the obtained *OTM* as a function of corresponding wave height and period. All dots represent individual waves from *OCW3D* and their structural response while the red transparent surface and cyan coloured mark stand for the maximum *OTM* caused by the embedded stream function wave in *WAVGEN*. The scatter tables in Fig. 5.33 and Fig. 5.35 reveal the corresponding number of measured single waves within the non-linear sea states as a function of wave height and period.

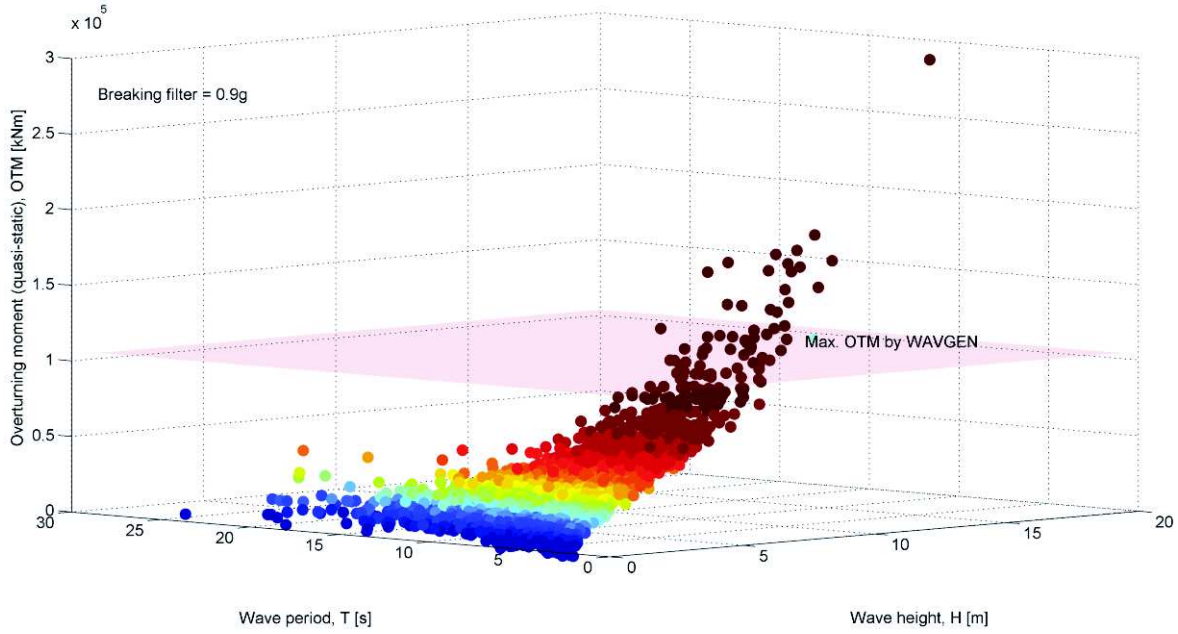

Fig. 5.32: Scatter plot of all OTMs obtained by OCW3D (BF = 0.9g) and compared to WAVGEN

Wave height, [m]	Wave period, [s]															Sum
	< 2	2 - 4	4 - 6	6 - 8	8 - 10	10 - 12	12 - 14	14 - 16	16 - 18	18 - 20	20 - 22	22 - 24	24 - 26	26 - 28	28 - 30	
> 20																0
19 - 20																0
18 - 19					1											1
17 - 18																0
16 - 17																0
15 - 16						1	2									3
14 - 15					1	6	2	1								10
13 - 14				1	1	8	3	1								14
12 - 13					2	15	7	2								26
11 - 12					3	28	19	6								56
10 - 11				1	7	32	46	11	1							98
9 - 10					18	50	56	22	1							147
8 - 9				5	21	67	98	43	6							240
7 - 8				6	31	98	84	49	6	3			1	1		279
6 - 7				15	53	104	134	61	14	4		1	1			387
5 - 6			1	22	59	94	112	62	22	8	1	1	2			384
4 - 5			4	38	74	91	81	65	19	6	3					381
3 - 4			15	70	62	69	61	28	15	6	6	3				335
2 - 3			42	68	40	30	25	7	7	3	2	1				225
1 - 2		6	74	52	31	9	5	5	3	1	2		1			189
< 1		22	18	9				1								50
Sum	0	28	154	287	404	702	735	364	94	31	14	6	5	1	0	2825

Fig. 5.33: Scatter diagram showing the number of waves within non-linear sea state (BF = 0.9g, red circle = max. wave of S1_X1, green box = WAVGEN)

In the above displayed scatter diagram in Fig. 5.33 the most extreme wave for instance from the first seed at the first position in Fig. 5.27 can nicely be identified by the single count circled in red. The embedded stream function wave with *WAVGEN* is also shown by the green mark for completion reasons.

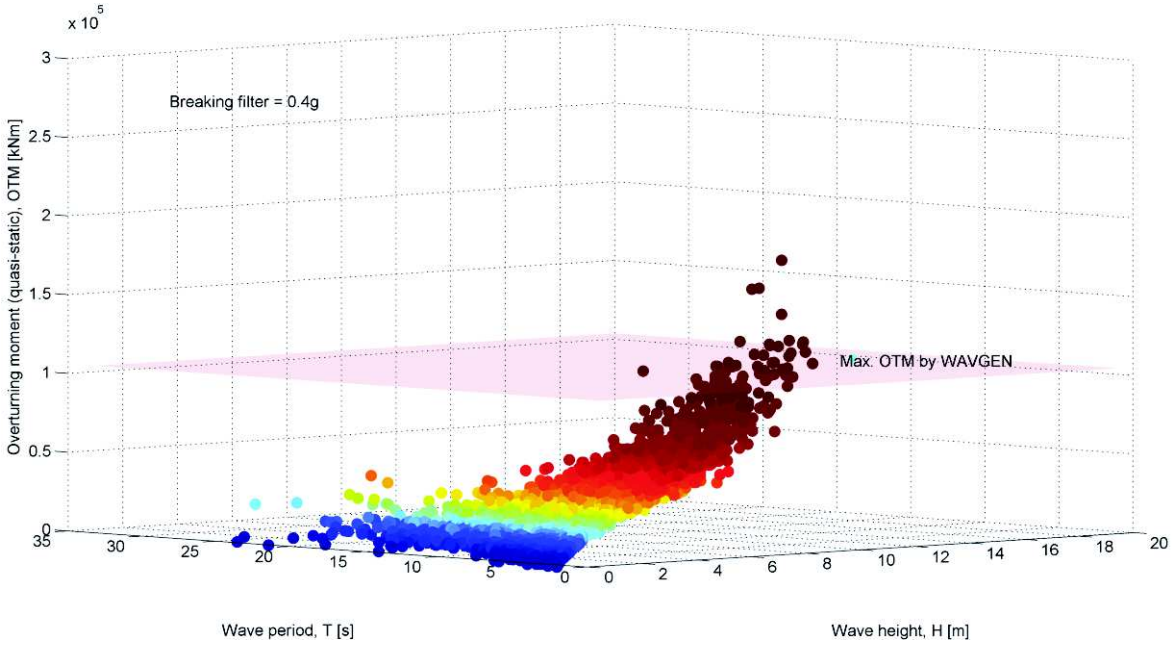

Fig. 5.34: Scatter plot of all OTMs obtained by OCW3D (BF = 0.4g) and compared to WAVGEN

Wave height, [m]	Wave period, [s]															Sum
	< 2	2 - 4	4 - 6	6 - 8	8 - 10	10 - 12	12 - 14	14 - 16	16 - 18	18 - 20	20 - 22	22 - 24	24 - 26	26 - 28	28 - 30	
> 20																0
19 - 20																0
18 - 19																0
17 - 18																0
16 - 17																0
15 - 16																0
14 - 15						1	2									3
13 - 14					2	8	4									14
12 - 13					4	18	12	3								37
11 - 12					7	48	23	5								83
10 - 11					12	64	62	10	1							149
9 - 10					27	87	108	27	1	1						251
8 - 9				8	37	104	150	63	8	1						371
7 - 8				7	52	144	162	90	15	5	1	1		2		479
6 - 7			2	26	80	180	211	123	19	3	1		1			646
5 - 6			1	38	98	180	193	98	45	9	1	2	2	1		668
4 - 5			4	81	137	156	135	94	40	8	7	2				664
3 - 4			19	115	118	116	98	52	28	12	7	5				570
2 - 3			70	107	88	50	41	16	14	5	4					395
1 - 2		14	119	95	36	11	8	8	2	1	1	2	1			298
< 1		34	39	17	1			1				1	1			94
Sum	0	48	254	494	699	1167	1209	590	173	45	22	13	5	3	0	4722

Fig. 5.35: Scatter diagram showing the number of waves within non-linear sea state (BF = 0.4g, green box = WAVGEN)

First of all, it is possible to answer the main part of the principle question as *OCW3D* in fact produces waves which exceed the maximum *OTM* by the conventional approach and thus have a worse impact on the structure. Secondly, one can clearly perceive the distinct difference between both breaking filters by pointing at the maximum wave and *OTM* as well as by the number of exceeding waves. But in general the scatters of the single waves in Fig. 5.32 and Fig. 5.34 are relatively equal along the wave height and period scale. They show almost the same profile for waves with less impact potential whereas the dispersion of the obtained *OTM* values increases after $1.0e^5$ *kNm.*

As *OCW3D* realises more aggressive waves, it is important to have a closer look on the scenarios which cause the severest structural response. Therefore, all maximum *OTMs* and their corresponding wave properties are put together in Tab. 5.20 and Tab. 5.21 for the final comparison between *WAVGEN* and *OCW3D*.

Tab. 5.20: All maximum OTMs for both breaking filters, different seeds and x-positions obtained by quasi-static analyses

Description [S = seed, X = position]	OCW3D = BF (0.4g)			OCW3D (BF = 0.9g)		
	OTM [kNm]	*H [m]*	*T [s]*	*OTM [kNm]*	*H [m]*	*T [s]*
S1_X1	160164.0	12.37	11.18	297851.0	18.82	9.90
S1_X2	127141.0	12.53	9.44	136069.0	13.73	13.68
S1_X3	87984.0	12.59	13.57	162541.0	14.39	14.61
S2_X1	111651.0	12.75	10.85	136245.0	12.88	9.66
S2_X2	116695.0	12.46	11.67	118199.0	12.52	11.61
S2_X3	87543.0	10.25	8.00	154901.0	13.02	7.57
S3_X1	157087.0	13.27	13.32	168591.0	14.72	9.30
S3_X2	119210.0	13.02	9.24	170314.0	14.52	12.14
S3_X3	103973.0	12.45	11.07	163377.0	14.45	10.69
S4_X1	114835.0	13.43	11.12	–	–	–
S2_X2	109326.0	12.03	8.97	–	–	–
S4_X3	116809.0	13.50	11.11	–	–	–
S5_X1	174595.0	14.41	13.42	–	–	–
S5_X2	78474.0	11.16	13.81	–	–	–
S2_X3	103876.0	12.44	9.04	–	–	–
Min.	78474.0	10.25	8.00	118199.0	12.52	7.57
Max.	174595.0	14.41	13.81	297851.0	18.82	14.61
Mean	117957.7	12.57	11.05	167565.3	14.34	11.02

Tab. 5.21: Maximum OTM by embedded stream function wave with WAVGEN

WAVGEN		
OTM [kNm]	*H [m]*	*T [s]*
103786.0	16.74	13.70

By means of this overview it is ascertained that the new approach yields a more drastic structural response concerning a breaking filter of *0.4g* but a smaller wave

height than the semi-empirical extent of the embedded stream function wave, answering the second objective. So the random non-linear wave in *OCW3D* does not reach equal dimensions as the regular non-linear wave in *WAVGEN* if the preferred breaking filter is activated. However, this entails that *OCW3D* calculates wave kinematics in a more aggressive way as the wave loads transferred by *Morison's* equation in *ROSA* turn out be much larger than by means of *WAVGEN*, confirming the conclusion from the validation outcome in 4.4.2. On the other side a smaller wave has an interesting effect on the general monopile design as the interface level could be lowered. This would positively influence the overall construction with respect to engineering and building efforts regarding materials, appurtenances as well as coating. However, with respect to uncontrollable and thus arbitrary wave heights in *OCW3D* the question arouses whether the obtained maximum wave heights in Tab. 5.20 would actually occur under genuine conditions. According to [11] and [28] laboratory tests have revealed relationships in (5.8) and (5.9) which in essence define the point of wave breaking and thus the highest possible wave as a function of water depth. The results in Fig. 5.36 indicates that all maximum wave heights for both breaking filters never exceed the measured limit for solitary waves as well as show the same trend along the governing relationship for irregular sea states whereas the embedded stream function would not exit theoretically.

$$H_{max} = 0.78 \cdot d \quad for\ solitary\ waves \tag{5.8}$$

$$H_{max} = 0.55 \cdot d \quad for\ irregular\ sea\ states \tag{5.9}$$

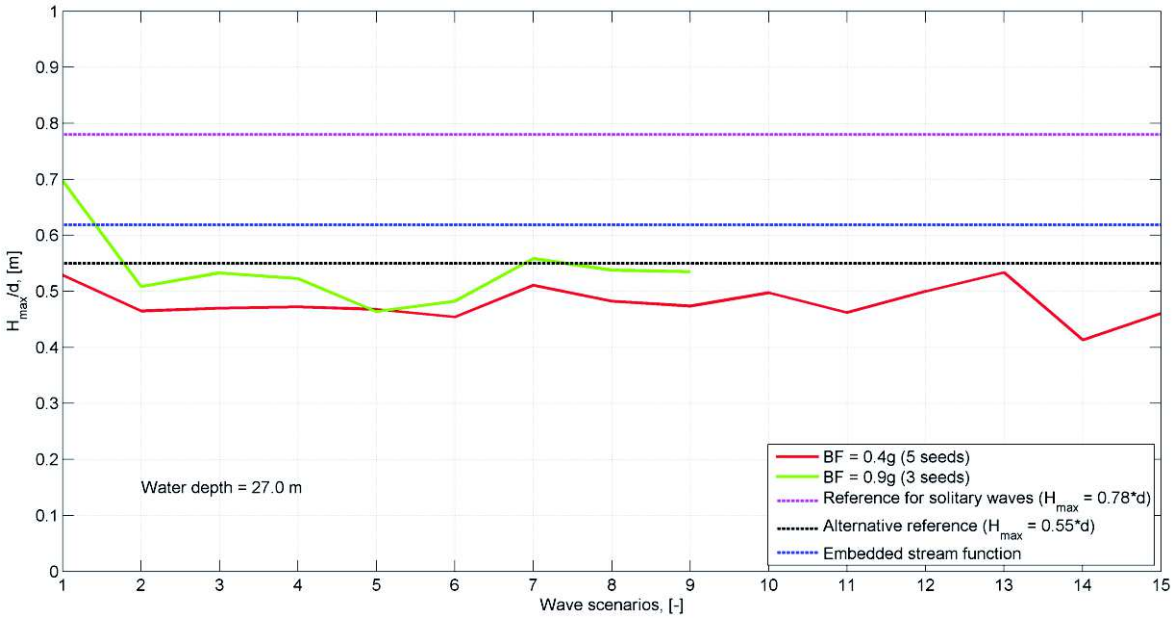

Fig. 5.36: Comparison of maximum wave heights by OCW3D and tank tests

Continuing with the main assessment criterion and thus by examining the running average of all seed *OTM* maxima compared to *WAVGEN's* output in Fig. 5.37 and Fig. 5.38 it can assuredly be claimed that a very satisfying outcome is obtained with a breaking of *0.4g*. The mean value illustrated by the pink line nicely approaches the maximum *OTM* by *WAVGEN*. Again the remarkable deviation between both breaking filters stands out by overserving the highest *OTM* values and their running averages, substantiating the finding that *0.9g* solely represents a reference value and *0.4g* resembles reality most accurately. Furthermore, it can be emphasised that the most dangerous waves and thus the greatest reaction moment is recorded right behind the wave generation zone perceptible by the first of the three values of each seed in Fig. 5.37. This is in accord with the final assumption of the spectral energy analysis in 5.3.2.

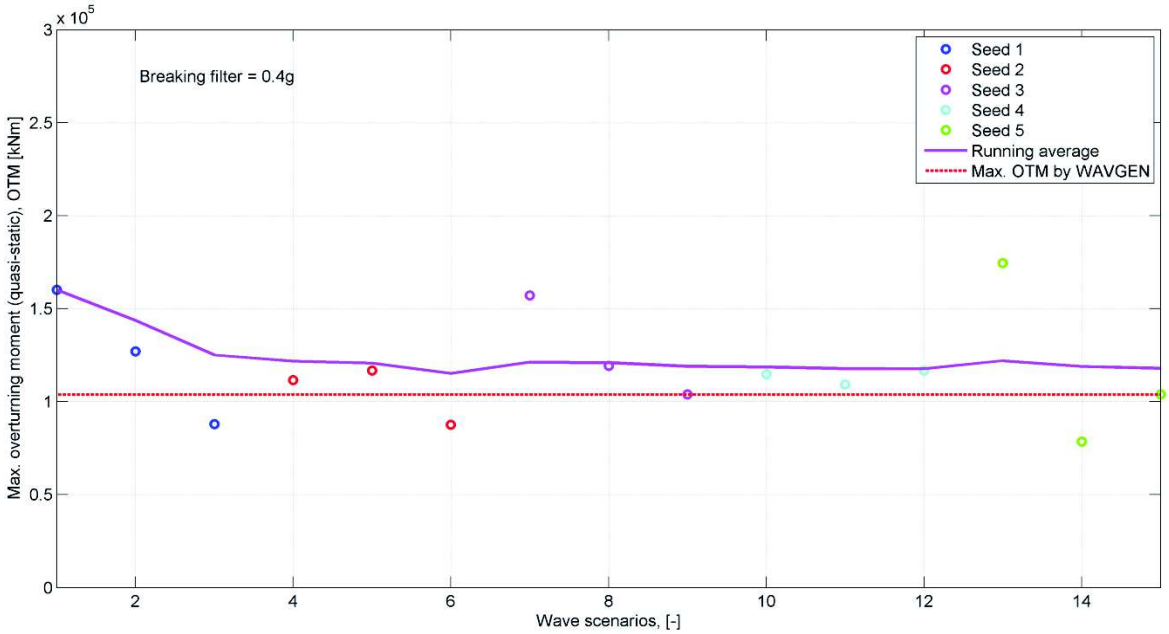

Fig. 5.37: Summary of all maximum OTMs and their running average (BF = 0.4g)

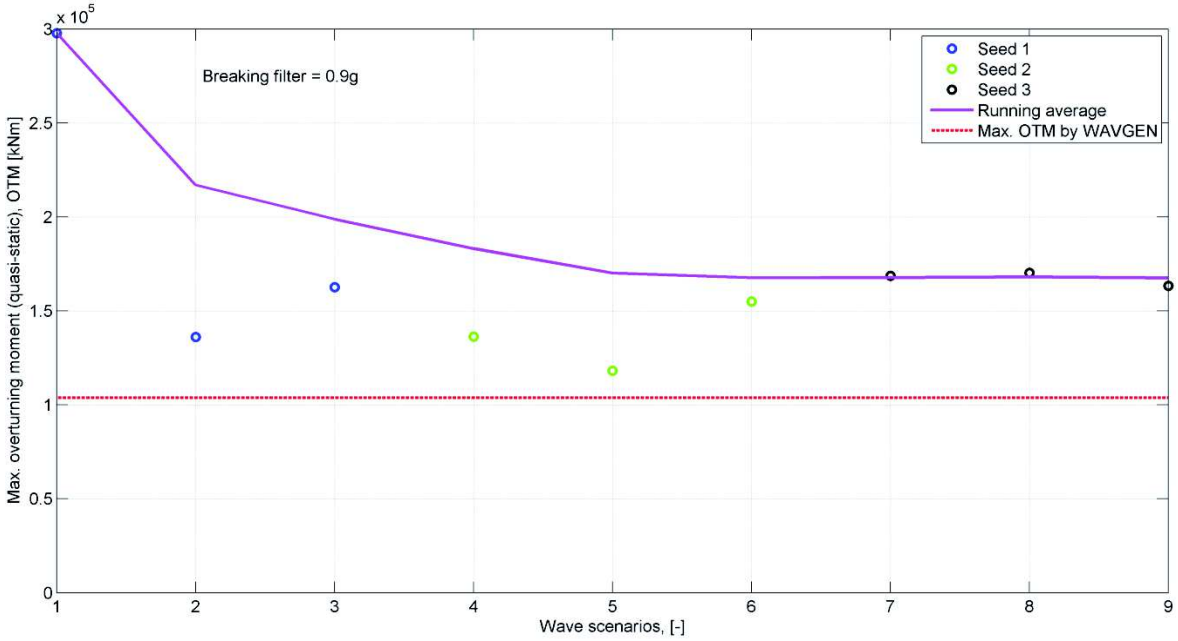

Fig. 5.38: Summary of all maximum OTMs and their running average (BF = 0.9g)

Hence, by observing the energy distribution in 5.3.2 along the numerical wave tank it can be claimed that the most stable and thus realistic wave profile as well as wave kinematics are gauged right before the absorption zone. This appears to be the recommendable extraction position as all the excessive and deceptive energy is dissipated. So if the maximum *OTMs* caused by waves from the first position behind the generation zone are discarded, the running average for the more genuine breaking filter substantially approaches the single maximum value by *WAVGEN,* as depicted in Fig. 5.39. In case of considering only the third position and thus assumingly the most authentic waves the seed averaged *OTM* by *OCW3D* turns out to be smaller than the reference figure from the conventional approach by a difference of *4.0 %.* This final evaluation does not only provide an overall positive assessment of the entire work but also a very interesting basis for discussion and in the end a great outlook for future applications of *OCW3D*.

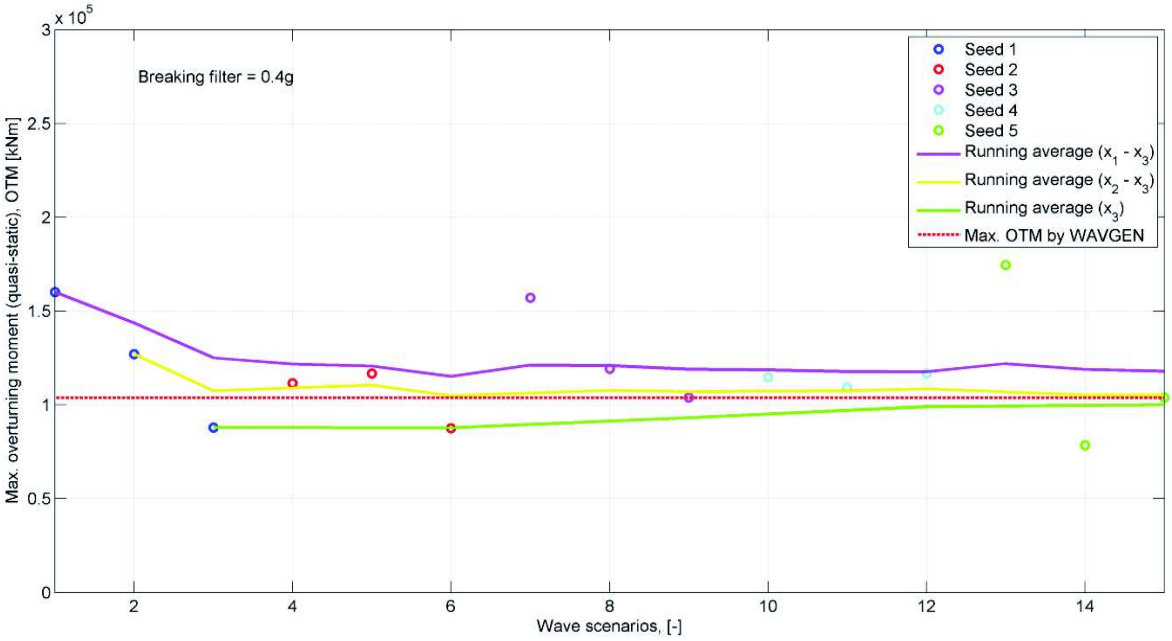

Fig. 5.39: Assessment of maximum OTMs obtained by WAVGEN and OCW3D

The prime conclusion from the comparison and plausibility study between *WAVGEN* and *OCW3D* based on a *ULS* analysis of a monopile foundation under explicit engineering conditions can be summarised as follows.

- More realistic and accurate reproduction of the water surface with *OCW3D*, including wave asymmetry around its horizontal and vertical axis
- Successful implementation of *OCW3D* in a state-of-the-art *ULS* design procedure and functioning coupling with *ROSA*
- Insight in breaking filter influence with respect to the realistic results obtained by a breaking filter of *0.4g*
- Although smaller wave height than the embedded stream function wave, higher mean *OTM* by *OCW3D* due to more aggressive and non-linear wave kinematics
- Concerning *OTM* final deviation between *OCW3D* and *WAVGEN*: *12.0 %* with *BF = 0.4g* and *38.0 %* with *BF = 0.9g*
- From another perspective effective and unprecedented validation of *Rambøll's* common engineering procedure
- In case of considering only the third position and thus assumingly the most authentic waves after a certain distance along the numerical wave tank a *4.0 %* smaller seed averaged *OTM* achieved by *OCW3D* than with WAVGEN

Part IV – Conclusion

6 Evaluation of *OceanWave3D* and *WAVGEN*

Based on the previously described *ULS* design process following the conventional or new approach this chapter shall give a final evaluation of *OCW3D* and *WAVGEN*. The former excels with an extremely realistic and accurate reproduction of the water surface as the program is able to simulate not only an asymmetry of the wave profile around the horizontal but also around the vertical axis. Thus, it can be concluded that *OCW3D* is a very strong, stable and highly recommendable wave simulation tool especially with respect to the growing demand for non-linear sea state realisations. *OCW3D*, including the non-linear simulation over hours or kilometres and the very effective breaking filter implementation, can be considered as a very efficient "*pocket*" wave tank, easily available, open source, comprehensible, fast and almost as reliable as real laboratory set-ups. Depending on certain knowledge in operating systems and computational disciplines *OCW3D* nevertheless constitutes a user-friendly and handy application which provides the necessary interaction potential with other programs due to the in-built kinematics converter. Here, the *Master Thesis* has offered a great opportunity regarding the interaction with *ROSA* to elaborate on wave kinematics and their conversion into wave loads and by looking at the structural response of an actual monopile foundation satisfying and reasonable results are achieved.

Furthermore, it is important to mention that *OCW3D* offers additional features which could max out the full optimisation potential in terms of wave simulation and load definition. One of the most interesting and useful add-ons is the possibility to change the bottom topography and include slopes or other mudline irregularities. Since *OCW3D* constantly considers the water depth in its solution process, the wave simulation is automatically adjusted and shoaling effects are perceptible in the surface elevation as illustrated in the very simple example in Fig. 6.1. This may be beneficial for designing monopiles because they are extremely cost efficient but depth limited. So in case of a more accurate reproduction of the installation site for example on the verge of a bottom slope the potential for monopiles could be fully exploited compared to other software which solely assume a simplified flatbed. It is also possible to generate a three-dimensional sea state with a completely random water surface and multidirectional wave heading.

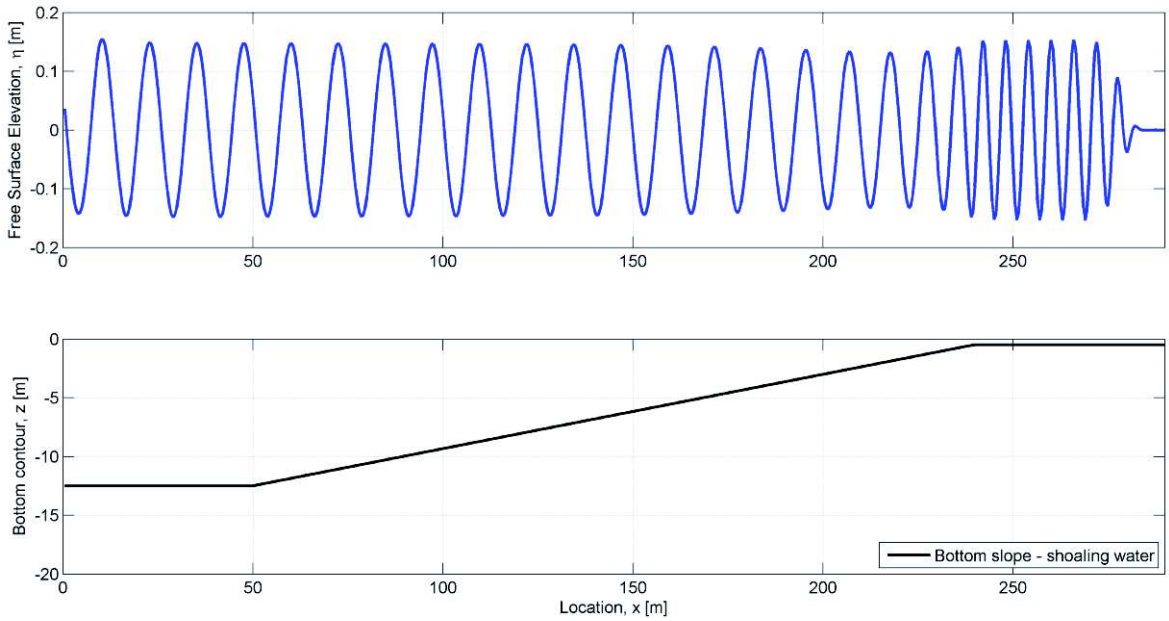

Fig. 6.1: Implementation of a bottom slope in OCW3D for the simulation of a stream function wave

On the other hand, there is *WAVGEN* as a highly advanced analytical solver that stands out by simulating any available wave theory, in particular the comprehensive non-linear methods according to *Stokes'* and the stream function theory. As the code requires only a small amount of input parameters and runs extremely stable, *WAVGEN* is a very efficient wave simulator, especially with respect to the automatic linkage to *ROSA*. This combination and the flawless wave load transfer yields unquestionable results in terms of structural response for the *ULS* design, as proven and validated in this work. Furthermore, in comparison to the new tool *WAVGEN* features a wider range of wave spectra already implemented for the realisation of irregular sea states. Here, the two-peaked and thus more accurate *Ochi-Hubble* wave spectrum is worth-mentioning. So concerning the low expenditures, including costs, time and computational effort, this in-house program together with *ROSA* serves the engineering purpose and immensely facilitates *Rambøll's* design process.

In the end, the question remains whether the numerical wave tank or the analytical implementation of common wave theories is the more suitable tool for realising extreme wave scenarios. Since the new approach reveals a higher *OTM* which would have negative effects on the monopile foundation in terms of steel weight, production and eventually money, and since the embedded stream function wave appears to work sufficiently, the conventional approach is seen as the more efficient working procedure. However, *OCW3D* should not be discounted and rather stay in the drawer, again referring to the final results of the power spectral analysis in 5.3.2 and their interpretation in Fig. 5.39. Further tests now have to verify the

assumption that the third extraction position along the numerical wave tank right before the absorption zone provides the most reliable wave kinematics for transferring loads and applying them on the *FE*-model. Here, not only a more realistic water surface is obtained but also smaller wave heights and thus reduced structural responses are perceived for the current scenario. In case of confirming this potential *OCW3D* would consequently move up and strengthen its abilities under engineering conditions. Although the application of *OCW3D* currently implies additional effort concerning operating system and kinematics transfer, it can still be concluded that this new tool may be helpful and useful for special customer queries or be consulted for example in assessing single damage events. It should definitely be applied in imminent research and development projects by *Rambøll*.

7 Review and future work

With reference to the overall objectives of the *Master Thesis* in 1.3 the major part of the work comprises the correct implementation of two completely different wave simulation approaches and their coupling with an already existing *FEM* program for realistic engineering problems. Depending on the final results the project either provides a profound insight in the applicability of *OCW3D* and a validation and assessment of the conventional approach with *WAVGEN*. As a basis it has been of great importance to avail oneself with the theoretical background and governing equations of both programs. In order to understand the difference between the analytical solver in *WAVGEN* and the fully non-linear potential flow solver in *OCW3D* the literature study and the associated development of own wave codes by means of *Matlab* have been extremely helpful throughout the entire time. Due to the intense involvement in simulating waves and identifying their structural impact on offshore installations from the beginning on it has been possible to discuss and evaluate results diligently and critically. In particular the close collaboration with *Rambøll* colleagues and especially with *Christof Wehmeyer* contributed considerably to the positive and valuable outcome of this *Master Thesis*.

Finally, there is to say that *OCW3D* has been successfully implemented in a state-of-the-art *ULS* design process under genuine conditions. The program has proven its abilities and together with the functioning interaction with *ROSA* offers great opportunities for further studies and applications. Nevertheless, the embedded stream function wave developed in *WAVGEN* remains a solid and fast engineering procedure and the approach is successfully validated by the present study. The final report, including the extensive literature study and the precise description of the design process has been well received internally and viewed as a guideline or summary for future projects, reaching the main objectives of the *Master Thesis*.

Of course, there are a lot of open issues and it is crucial to say that this work should only be seen as an entry point for the consideration of fully non-linear wave impact on offshore structures. The complete process would imply more data, varying input parameters, further simulation and validation runs. In this case the focus has been on the correct understanding of the theory of both programs, the smooth integration in *Rambøll's* engineering process and the associated transfer from wave kinematics to hydrodynamic loads. On that account, it has been initially decided to work with the simpler monopile foundation and to conduct the rather straightforward *ULS* design process. This decision allowed a quick introduction and detection of possible difficulties since the monopile is already seen as structurally optimised with

ample references and the structural behaviour is solely investigated as the response of an extreme sea state, exactly speaking of one single wave impact. Therefore, with respect to the promising outcome of this study future work with *OCW3D* should definitely include more advanced foundations such as jacket structures. Here, the arrangement of chords and braces at different x-positions in the wave propagation direction would challenge the wave kinematics converter in *OCW3D* and require deeper knowledge in the data handling and calculation process in *ROSA*, particularly in terms of blocking and shielding effects.

Another step to increase the degree of difficulty would be the execution of a complete *FLS* assessment. Since *OCW3D* produces a fully developed non-linear sea state over a statistically stable period of time, it is expected that the obtained fatigue life assessment is based on a much more realistic cyclic strain as for the linear irregular sea state generated by common procedures. Due to the non-linear solution and persistent consideration of the water depth the simulation of oscillating wave loads constitutes one of the most interesting future applications of *OCW3D*. Here, it is essential to ascertain the increase of computational effort with respect to the immense data volume since the numerical approach requires a certain refinement in temporal and spatial resolution.

However, before performing analyses with new foundation types or in line with alternative design criteria *OCW3D* should primarily be examined under varying metocean data. For the here discussed case study an already extreme sea state with respect to the considerable significant wave height related to the water depth is considered but in order to evaluate the full operational potential of the new software it is recommended to cover a certain range of varying water depths or wave characteristics. It would be quite relevant to investigate whether *OCW3D* and *WAVGEN* would still yield the same deviation in the *OTM* in deeper water where the non-linearity is not as pronounced as in shallow regions.

Moreover it is advised to completely understand additional features of *OCW3D* for example the capability of defining the bottom topography and of generating three-dimensional sea states. So for the future work one has to decide to comprehend the entire scope of the program or to specifically test it against *Rambøll's* needs and *WAVGEN's* abilities to eventually pave the way for a commonly accepted and commercial utilisation of *OCW3D*.

References

[1] Offshore Wind, “offshoreWIND.biz,” [Online]. Available: http://www.offshorewind.biz/2016/02/11/2015-european-offshore-wind-in-numbers/. [Accessed 21 July 2016].

[2] B. T. Paulsen, “PH.D. Thesis: Efficient Computations of Wave Loads on Offshore Structures,” Technical University of Denmark, Lyngby, 2013.

[3] Offshore Wind, “offshoreWIND.biz,” [Online]. Available: http://www.offshorewind.biz/2016/02/09/europe-powered-by-wind-2015-strong-year-for-offshore/. [Accessed 21 July 2016].

[4] O. B. Leite, “Review of Design Procedures for Monopile Offshore Wind Structres,” University of Porto, Porto, 2015.

[5] T. Sarpkaya and M. Isaacson, Mechanics of Wave Forces on Offshore Structures, New York: Van Nostrand Reinhold Company, 1987.

[6] J. M. J. Journeé and W. W. Massie, Offshore Hydromechanics, Delft: Delt University of Technology, 2001.

[7] K. Garme, “Marine Hydromechanics,” KTH Centre for Naval Architecture, Stockholm, 2011.

[8] A. Rosén, “Introduction to Seakeeping,” KTH Centre for Naval Architecture, Stockholm, 2011.

[9] J. N. Newman, Marine Hydrodynamics, Cambridge: The MIT Press, 1977.

[10] E. Bauer, “Wave Modeling at the Service of Security in marine Enviroment,” Eolss Publishers, Oxford, 2004.

[11] L. H. Holthuijsen, Waves in Oceanic and Coastal Waters, Cambridge: University Press, Cambridge, 2007.

[12] I. A. Svendsen and I. G. Jonsson, Hydrodynamics of Coastal Regions, Lyngby: DEN Private Ingeniørfond Technical University Denmark, 1976.

[13] M. Brorsen, "DCE Lecture Notes: Non-linear Waves," Aalborg University, Dept. of Civil Engineering, Aalborg, 2007.

[14] DNV GL, "Enviromental Conditions and Enviromental Loads (DNV-RP-C205)," Det Norske Veritas AS, Oslo, 2014.

[15] Rambøll Denmark AS, "ROSAP - Program WAVGEN/Wave Generation - User's Guide," Rambøll Denmark AS, Esbjerg, 2015.

[16] O. M. Faltinsen, Sea Loads on Ships and Offshore Structures, Cambridge: Cambridge University Press, 1990.

[17] J. R. Morison, M. P. O'Brien, J. W. Johnson and S. A. Schaar, "The Force Exerted By Surface Waves on Piles," University of California, Berkeley, 1950.

[18] B. M. Sumer and J. Fredsøe, Hydrodynamics Around Cylindrical Structures, Singapore: World Scientific Publishing Co. Pte. Ltd., 2006.

[19] International Standards, ISO 19902 - Petroluem and natural gas industries - Designing and Constructing fixed steel offshore structures, 2007.

[20] American Petroleum Institute, "Recommended Practice for Planning, Designing and Constructing Fixed Offshore Plattforms - Working Stress Design (RP 2A-WSD)," American Petroleum Institute, 1993.

[21] A. P. Engsig-Karup, H. B. Bingham and O. Lindberg, "An Efficient Flexible-Order Model for 3D Nonlinear Water Waves," *Journal of Computational Physics,* p. 228, 2009.

[22] B. T. Paulsen and N. G. Jacobsen, "OceanWave 3D Course Material," Deltares, Delft, 2015.

[23] B. T. Paulsen, H. Bredmose and H. B. Bingham, "An efficient Domain Decomposition Strategy for Wave Loads on Surface Piercing Circular Cylinders," Elsevier - Coastal Engineering, Lyngby, 2014.

[24] Rambøll Denmark AS, “ROSAP - Program ROSA Structural Analysis - User's Guide,” Rambøll Denmark AS, Copenhagen, 2015.

[25] R. Sigbjørnsson and I. Langen, Dynamic Analysis of Structures, Trondheim: Tapir, 1979.

[26] DNV GL, “Design of Offshore Wind Turbine Structures (DNV-OS-J101),” Det Norske Veritas AS, Oslo, 2014.

[27] C. Wehmeyer and J. H. Rasmussen, “Mooring Response of a Floating Offshore Wind Turbine in Nonlinear Irregular Waves,” *IJOPE Paper,* p. 9, 2009.

[28] R. C. Nelson, “Wave Heights in Depth Limited Conditions,” in *6th Australian Conference on Coastal and Ocean Engineering*, Gold Coast, 1983.

[29] A. Techet, “Lecture Notes: Free-Surface Waves,” MIT Dept. Mechanical Engineering, Cambridge, 2005.

Software

The following software has been used for the *Master Thesis*.

- *Microsoft Office Professional Plus 2010*, © 2010 Microsoft Corporation
- *Matlab 2012*, © 1994-2016 The MathWorks, Inc.
- *ROSA 49.0*, © Rambøll Denmark AS
- *SHEILA 49.0*, © Rambøll Denmark AS
- *RONPLT 49.0*, © Rambøll Denmark AS
- *WAVGEN 49.0*, © Rambøll Denmark AS
- *OceanWave3D*, © 2009 Allan P. Engsig-Karup, DTU Compute, Technical University of Denmark

Appendix

A.1 Drawings of monopile and transition piece

Legend

Taper 1/4

COG

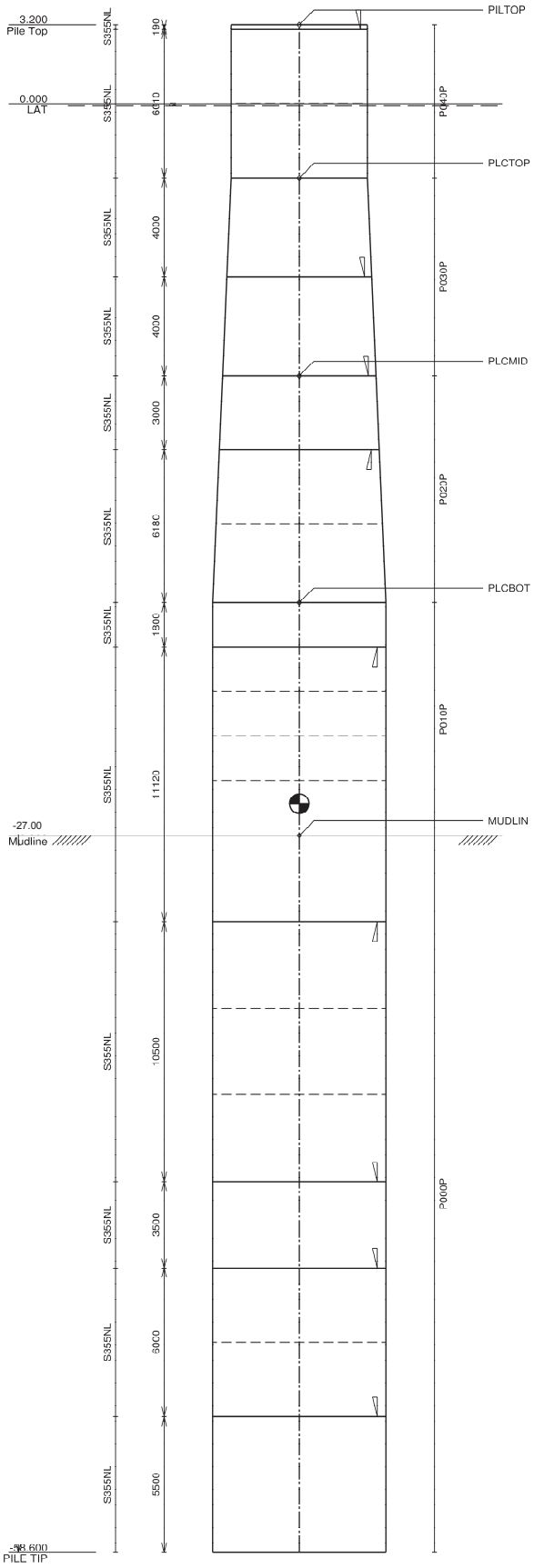

NOTES

1. All dimensions in millimeters.
2. All levels in meters.

Master Thesis - Philipp Schöpfer

Title			
MONOPILE			
Scale	Size	Drawing No.	Rev.
1:196	A3	PAGE 1	

Legend

Taper 1/4

COG

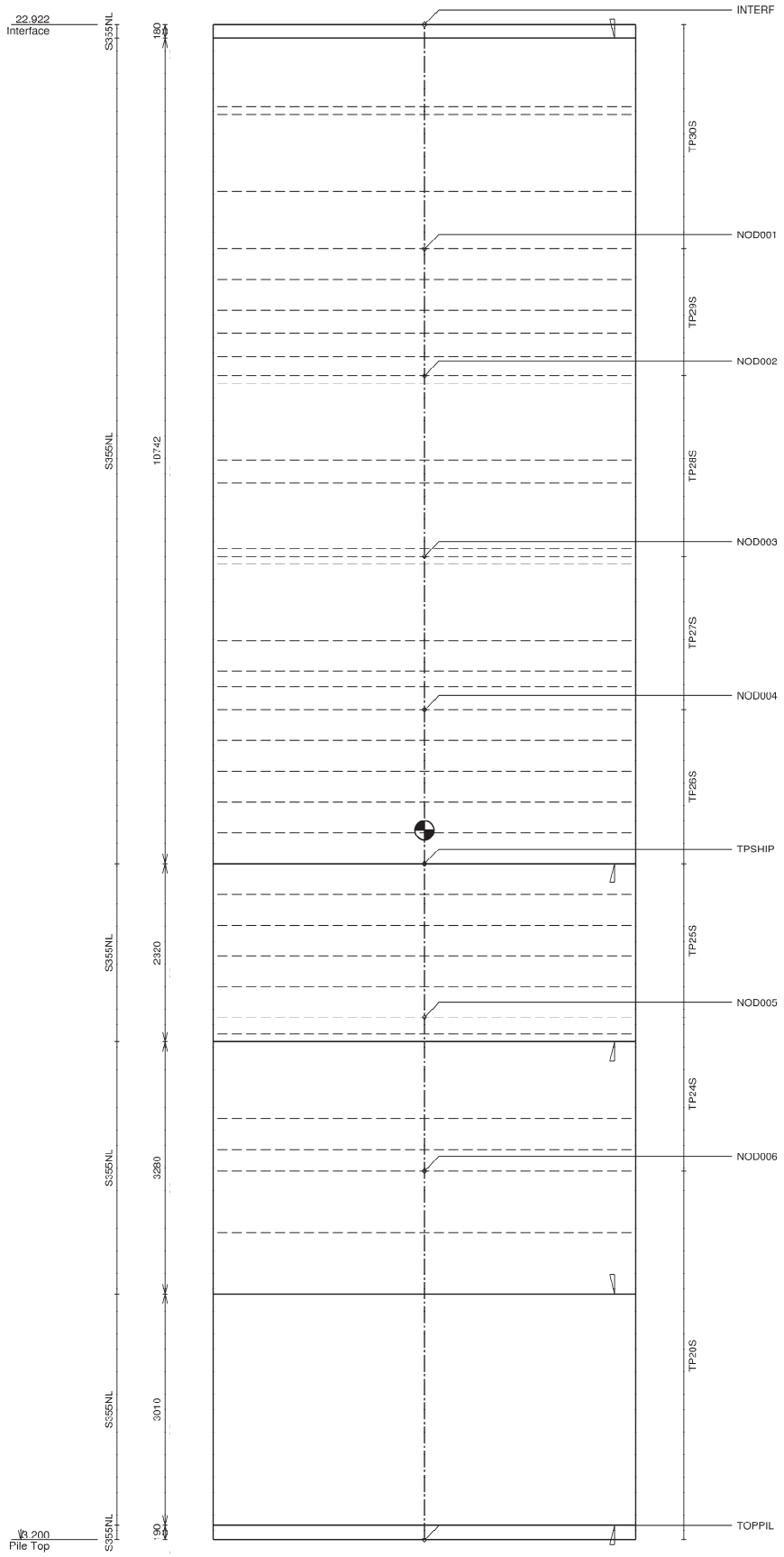

NOTES

1. All dimensions in millimeters.
2. All levels in meters.

Master Thesis - Philipp Schöpfer

Title

TRANSITION PIECE

Scale	Size	Drawing No.	Rev.
1:63	A3	PAGE 2	